

Light absorption in 1D and 2D nanostructured organic semiconductors

THÈSE N° 6646 (2015)

PRÉSENTÉE LE 22 MAI 2015

À LA FACULTÉ DES SCIENCES ET TECHNIQUES DE L'INGÉNIEUR
LABORATOIRE DES MATÉRIAUX ORGANIQUES ET MACROMOLÉCULAIRES
PROGRAMME DOCTORAL EN SCIENCE ET GÉNIE DES MATÉRIAUX

ÉCOLE POLYTECHNIQUE FÉDÉRALE DE LAUSANNE

POUR L'OBTENTION DU GRADE DE DOCTEUR ÈS SCIENCES

PAR

Damien ROLLAND

acceptée sur proposition du jury:

Prof. F. Sorin, président du jury
Prof. H. Frauenrath, directeur de thèse
Prof. C. Lambert, rapporteur
Prof. R. Eelkema, rapporteur
Prof. F. Nüesch, rapporteur



ÉCOLE POLYTECHNIQUE
FÉDÉRALE DE LAUSANNE

Suisse
2015

*When you talk, you are only repeating what you know,
but if you listen, you may learn something new.*

Dalai Lama

Acknowledgments

First of all I would like to thank Prof. Holger Frauenrath for supervising my PhD, for his guidance and availability, and for letting me develop my own ideas.

Material science and organic electronics are multidisciplinary fields and a large part of this thesis relied on collaboration with several experts. I am grateful to Dr. Natalie Banerji at the University of Fribourg (TA spectroscopy), Dr. Martin Brinkmann and Dr. Laure Biniek at Institut Charles Sadron, Strasbourg (TEM), Dr. Sandor Balog at the University of Fribourg (XRD), as well as Dr. Stefan Guldin from the laboratory of Prof. Francesco Stellacci at EPFL (spectroscopy). Many thanks as well to Dr. Jan C. Brauer and Dr. Lucia Hartmann, two former postdocs of our group that contributed to this work, to our exceptional Michel Schär and his impressive knowledge and precision, and to Dr. Jan Gebers, Regina Hafner, and Dr. Roman Marty, with whom I was working more closely on synthesis and nanowires. I am tankful to Maria Ricci and Su Liang for the help with AFM and XRD measurements. I also want to thank the students I had the pleasure of supervising in the lab and who also brought their own contribution to this project, Diego Represas, Florian Fallegger, Sébastien Wronski, Chloé Waeber, Hedy Ketari, Luca Cervini and Jonathan Thierry.

It was a pleasure to work in such a friendly atmosphere in the LMOM! I highly appreciated the interactions and mutual support within the whole group, as well as our gatherings, BBQs, ski days, etc. For this reason, I want to warmly thank again my coworkers mentioned above, the other LMOM members Stephen Schrettl, Su Liang, Giuseppe Sforazzinni, Julien Cretenoud, Bilal Ozen, Bjoern Schulte, Thomas Schmaltz, and Sylvain Galland; as well as our alumni Dragana Paripovic, Emmanuel Contal, Guangyan Du, Emmanuel Croisier, Liangfei Tian, Ruth Szilluweit, Martin Fritzsche, Tobias Hoheisel, and Stéphane Suarez. Thanks also to our neighbors at the SuNMIL!

I am grateful to Sylvie Vaucher, Erika Menamkat, Anne Kolly, Dr. Homeira Sunderland, Dr. Shawn Koppenhoefer, and Chiara Donini for the administrative, IT, and photographic support. It was also very interesting to work on safety-related issues and IMX shop operation with Philippe Charpilloz, Jean-Daniel Nevecelle, and Gilles Auric.

This PhD is concluding my long studies and I really want to sincerely thank my parents and my family for their support, their love, their guidance and advice every time I needed it over the last 30 years! I also always received support from Guillaume, who was always here to listen to my stories from the lab. I thank him and all my friends, older and newer, for the amazing moments we had when meeting somewhere in Europe or around the world. Those were really energizing breaks from the PhD studies in Lausanne!

Summary & Keywords

Organic photovoltaics will be one of the corner stones in solving increasing world's energy demand issue. For this reason, a better understanding of the detailed mechanisms involved in energy conversion in the employed nanostructured materials is still desirable. In this context, one-dimensional and two-dimensional nanostructured organic semiconductors may reveal intriguing opto-electronic properties due to their morphology and the nanoscopic confinement. In this regard, supramolecular self-assembly has proven to be a powerful tool to control the obtained nanostructures, by using secondary interactions such as hydrogen bonding or the phase segregation between molecular segments of different nature, which requires functionalization of the π -conjugated chromophore.

The present thesis starts with the preparation of functionalized oligothiophenes. The synthesis of π -conjugated systems is rendered difficult by their inherently low solubility. In the first part of the present thesis, we therefore developed a convenient synthetic pathway for chemically functionalized oligothiophenes up to the octathiophenes, by employing chlorendylimidyl active esters as both temporary protecting groups and solubilizing groups. From the obtained soluble precursors, a large library of oligothiophene derivatives carrying polymer-oligopeptide substituents was straightforwardly prepared in a divergent synthesis. This simple substitution served to induce aggregation into one-dimensional nanowires that comprised a single stack of oligothiophenes arranged in a helically twisted, parallel-displaced fashion. This molecular arrangement was in turn found to result in the facile photo-induced formation of charge-carriers. Thus, charge generation under illumination and decay in the dark were characterized for oligothiophene nanowires with varying molecular parameters. Notably, derivatives with an even number of thiophene units accumulated a higher concentration of charges, up to 4 mol%. Thus, aggregation into one-dimensional nanostructures with supramolecular helicity can be regarded as a useful tool to promote a cofacial stacking of chromophores and facilitate charge generation. In parallel, we investigated two-dimensional nanostructures obtained from an acceptor-donor-acceptor triad based on perylene-bisimide and quaterthiophene substituted with flexible polymer chains. The latter served to reliably induce aggregation into smectic lamellar phases. Within the lamellae, the triad segments were arranged with a tilt angle relative to the layer normal in order to accommodate packing constraints. Light absorption was followed by transient charge separation between the two types of chromophores. Charge recombination was slower in thin films than in solution and even slower for a derivative with longer polymer chains and higher degree of long-range order. These findings demonstrate that the phase segregation observed in rod-coil systems can be used to improve the nanoscale order and could be beneficial for applications in organic photovoltaics.

Keywords

Supramolecular self-assembly, oligothiophenes, perylene bisimides, oligopeptides, organic nanowires, charge carrier generation, light absorption, lamellar phases

Résumé & Mots-Clefs

Le photovoltaïque organique promet un potentiel énorme quant aux besoins énergétiques mondiaux. Mais cela nécessite une compréhension plus approfondie des mécanismes internes de conversion d'énergie au sein des matériaux organiques nanostructurés employés. Dans ce contexte, des semi-conducteurs organiques nanostructurés uni- ou bidimensionnellement pourraient exhiber des propriétés uniques, de part leur morphologie interne et un confinement à l'échelle nanoscopique. De ce point de vue, l'auto-assemblage supramoléculaire s'est révélé être un outil puissant à fin d'organiser des nanostructures internes de matériaux organiques. Pour cela, des interactions intermoléculaires secondaires sont employées, tel les liaisons hydrogènes ou la ségrégation de phase entre des segments moléculaires de natures différentes, ce qui requiert la fonctionnalisation de systèmes π -conjugués, aussi appelés chromophores.

Cette étude de thèse débute par la préparation d'oligothiophènes fonctionnalisés. La synthèse de systèmes π -conjugués est typiquement rendue difficile de part leur solubilité très limitée. Dans la première partie de cette thèse, nous développons donc un protocole simple et pratique pour la synthèse d'oligothiophènes jusqu'à l'octamer, comprenant des groupes fonctionnels aux deux extrémités. Dans ce but, des groupements esters chlorendylimidiques activés sont utilisés comme solubilisants temporaires. Ces intermédiaires solubles permettent la synthèse divergente d'une large série d'oligothiophènes fonctionnalisés par des groupements polymère-oligopeptide. Grâce à cette simple substitution, l'agrégation se fait selon une direction donnée, ce qui résulte en des nanofilaments constitués d'un unique empilement hélicoïdal d'oligothiophènes agencés parallèlement. Nous avons pu observer que cet arrangement moléculaire particulier conduisait à une création de charges polaroniques grandement facilitée. Ainsi, nous avons pu suivre spectroscopiquement la formation de ces charges pendant une certaine période d'illumination, ainsi que leur résorption dans le noir. Les composés comprenant un nombre pair de thiophène ont accumulé plus de charges, jusqu'à 4 mol%, que pour un nombre impair. Cette agrégation en nanofilaments hélicoïdaux peut donc être vue comme un outil pour promouvoir la formation de charges polaroniques dans un matériau organique. Nous avons également étudié un matériau formant des lamelles nanoscopiques, à partir d'une triade accepteur-donneur-accepteur composée de groupements quaterthiophène et perylene bisimide et sur laquelle nous avons rajouté des chaînes polymériques flexibles servant à renforcer l'organisation en lamelles. Au sein de ces lamelles, les différents segments moléculaires sont tiltés afin d'obtenir un agencement plus dense. L'absorption lumineuse s'ensuit d'une séparation de charge entre les deux types de chromophores. La recombinaison des charges est ralentie dans les films solides, comparés à des solutions du même matériau et ce, d'autant plus que les chaînes polymériques sont longues. Ainsi nos travaux démontrent que la

ségrégation de phase entre des chromophores et des polymères flexibles peut servir à améliorer l'ordre interne et être utile pour des applications photovoltaïques.

Mots-Clefs

Auto-assemblage supramoléculaire, oligothiophène, perylène bisimide, oligopeptide, nanofilaments organiques, génération de charge, absorption lumineuse.

Table of Contents

Acknowledgments	i
Summary & Keywords	iii
Résumé & Mots-Clefs	v
Table of Contents	vii
List of Abbreviations	ix
1 Introduction	1
1.1 Solving the Energy Issue	1
1.2 Mechanism of Charge Generation in Organic Solar Cells.....	2
1.2.1 Parameters of a Solar Cell	2
1.2.2 Mechanism for Energy Conversion	3
1.2.3 The Role of the Charge Transfer State	6
1.2.4 Charge Recombination	10
1.3 Polymer:Fullerene Bulk Heterojunctions	13
1.3.1 Low Bandgap Polymers	14
1.3.2 The Three-Phase Morphology of the Polymer:Fullerene Bulk Heterojunction..	17
1.3.3 Stability of Bulk Heterojunctions.....	21
1.4 Ordered Heterojunctions	22
1.4.1 Block Copolymer Single Component Organic Solar Cells	22
1.4.2 Small-Molecule Single-Component Solar Cells	25
1.5 One-Dimensional Nanowires in Organic Photovoltaics	28
1.6 Scope and Outline of this Thesis	34
2 Facile Access to Oligothiophenes via Chlorendic Protecting Groups	39
2.1 Introduction.....	39
2.2 Synthesis of the Oligothiophene Building Blocks.....	40
2.3 Crystal Structures of the Chlorendylimidyl Esters	43

2.4	Spectroscopic Properties in Solutions and Thin Films.....	47
2.5	Divergent Synthesis of Nanowire-Forming Oligothiophene Derivatives.....	50
2.6	Conclusions	53
3	Oligothiophene Nanowires and Polaron Formation.....	57
3.1	Introduction	57
3.2	Structural Investigation of the Nanowires.....	59
3.3	Facile Polaron Formation in the Nanowires	72
3.4	Polaron Generation under Illumination.....	75
3.5	Influence of Oligopeptide Length.....	79
3.6	Polaron Formation in Nanowires from Achiral Compounds.....	80
3.7	Conclusions	81
4	Acceptor-Donor-Acceptor Triad Forming Lamellar Phases.....	84
4.1	Introduction	84
4.2	Synthesis and Steady-State Spectroscopy.....	86
4.3	Alignment and Thin Film Morphology	87
4.4	Charge Generation under Illumination	92
4.5	Conclusions	97
5	Final Conclusions and Outlook.....	101
6	Experimental Part	105
6.1	Instrumentation and Methods	105
6.2	Synthesis Procedures and Analytical Data for Compounds	107
7	References.....	133
8	Appendix.....	153
8.1	Spectral Data for Synthesized Compounds.....	153
8.2	Curriculum Vitae	203
8.3	List of Publications.....	205

List of Abbreviations

1D	one-dimensional
2D	two-dimensional
Å	angstrom
AFM	atomic force microscopy
L-Ala	L-alanine
anal	analysis
APPI	atomic pressure photoionization
BCP	block copolymer
BHJ	bulk-heterojunction
<i>c</i>	concentration
calcd	calculated
CD	(electronic) circular dichroism
CT	charge transfer
δ	chemical shift (NMR)
d	day
d	duplet (NMR)
DCM	dichloromethane
DIEA	diisopropylethylamine
DMF	dimethylformamide
DMSO	dimethylsulfoxide
<i>DP</i>	degree of polymerization
ϵ	extinction coefficient
EQE	external quantum efficiency
equiv.	equivalents
ESI-TOF	electrospray ionization/ionization-time of flight
Φ	azimuthal angle (XRD)
FF	fill factor
Fmoc	fluorenylmethyloxycarbonyl
FTIR	fourier transform infrared spectroscopy
Gly	glycine

HOMO	highest occupied molecular orbital
HV	high vacuum
HRMS	high resolution mass spectrometry
IQE	internal quantum efficiency
IR	infrared
J	coupling constant (NMR)
J_{sc}	short-circuit current density
$J-V$	current-voltage
LUMO	lowest unoccupied molecular orbital
μ	charge carrier mobility
m	multiplet (NMR)
$[M]^+$	molecular peak (in MS)
MALDI-TOF	matrix-assisted laser desorption/ionization-time of flight
MCH	methylcyclohexane
MEH-PPV	Poly[2-methoxy-5-(2-ethylhexyloxy)-1,4-phenylenevinylene]
MeOH	methanol
min	minute
M_n	number-average molecular weight
m/z	mass-to-charge ratio (in MS)
N	Newton
NIR	near infrared
NMR	nuclear magnetic resonance
OFET	organic field-effect transistor
OPV	oligo(phenylene vinylene)
OSC	organic solar cell
PBDTTPD	Poly[[5-(2-ethylhexyl)-5,6-dihydro-4,6-dioxo-4H-thieno[3,4-c]pyrrole-1,3-diyl][4,8-bis[(2-ethylhexyl)oxy]benzo[1,2-b:4,5-b']dithiophene-2,6-diyl]] (chemical structure Figure 7)
PBI	perylene bisimide
PBTBT	Poly[2,5-bis(3-tetradecylthiophen-2-yl)thieno[3,2-b]thiophene]
PCBM	[6,6]-phenyl-C ₆₁ -butyric acid methyl ester

PC ₇₁ BM	[6,6]-phenyl-C ₇₁ -butyric acid methyl ester
PCPDTBT	Poly[2,6-(4,4-bis-(2-ethylhexyl)-4H-cyclopenta [2,1-b;3,4-b'] dithiophene)-alt-4,7(2,1,3-benzothiadiazole)] (chemical structure Figure 6)
PEDOT:PSS	poly(3,4-ethylenedioxythiophene)-poly(styrenesulfonate)
PFTBT	poly((9,9-dioctylfluorene)-2,7-diyl-alt-[4,7-bis(thiophen-5-yl)-2,1,3-benzothiadiazole]-2',2"-diyl) (chemical structure Figure 21)
P3HT	poly(3-hexylthiophene)
PIB	poly(isobutylene)
ppm	parts per million (in NMR)
<i>p</i> vDMTPD	poly{ <i>N,N'</i> -bis(4-methoxyphenyl)- <i>N</i> -phenyl- <i>N'</i> -4-vinylphenyl-[1,1'-biphenyl]-4,4'-diamin} (chemical structure Figure 26)
PyBOP	benzotriazol-1-yloxy-tris(pyrrolidino)phosphonium hexafluorophosphate
q	quartet (NMR)
<i>q</i>	scattering wave vector (X-ray)
<i>R_f</i>	retention factor
σ	conductivity
s	singlet (NMR)
SAXS	small angle X-Ray scattering
t	triplet (NMR)
TA	transient absorption
[θ]	molar ellipticity
T4	quaterthiophene
TCE	1,1,2,2-tetrachloroethane
TEM	transmission electron microscopy
TFA	trifluoroacetic acid
THF	tetrahydrofuran
TLC	analytical thin-layer chromatography
UV/vis	ultraviolet/visible
<i>V_{oc}</i>	open-circuit voltage
WAXS	wide angle X-Ray scattering
XRD	X-ray diffraction

Introduction



1 Introduction

1.1 Solving the Energy Issue

The growth of the human population and improvement of living standards have so far been tied to a permanent rise in the world-wide energy demands. At the same time, fossil fuels are becoming scarce and their utilization as energy source is becoming unacceptable because of the accompanying environmental consequences. Nuclear energy based on fission, on the other hand, presents high risks in terms of uncontrolled chain reactions and constitutes a major challenge in terms of waste management.¹ It is therefore highly desirable to find a sustainable energy source that we can consider unlimited in supply. In this regard, the usable solar power on earth is estimated to be 23 000 TW on average, which largely exceeds any other sustainable energy source and, more importantly, surpasses the worldwide power consumption of about 17 TW in 2011 by more than three orders of magnitude.² Photovoltaics offer the possibility to convert solar energy into electricity that can be conveniently used in today's technology. The photovoltaic market is presently dominated by devices based on silicon or other inorganic materials that have proven to be efficient and long-lasting. Yet, the fabrication of these devices remains costly and the final panels are mechanically rigid and heavy. Despite their shorter lifetime and lower charge mobilities, organic semiconductors are emerging as an important class of materials in many fields of technology,³⁻⁹ including organic photovoltaics.¹⁰⁻¹⁴ Compared to their inorganic counterparts, organic semiconductors typically feature higher extinction coefficients and hold the promise for a cost-efficient and solution-based fabrication of flexible and light-weight devices on large scales. Last but not least, organic synthesis provides almost infinite possibilities for molecular design, which allows for a fine-tuning of the molecular properties in order to achieve the optimal device characteristics.

Organic semiconductor materials generally consist of π -conjugated molecules or polymers assembled by supramolecular interactions, including π - π interactions, from which the actual opto-electronic properties originate. As a result, the final characteristics of a material depend not only on the intrinsic features of the constituting molecules,¹⁵⁻¹⁷ but also on their packing and on the morphology of the active layer.¹⁸⁻²¹ Moreover, if the morphology of the material contains features with sizes reduced to the nanometer scale, unexpected properties might appear due to quantum effects arising from confined excited species or charge carriers. In this context, supramolecular chemistry constitutes a powerful and, at the same time, indispensable tool when preparing novel organic materials with advanced properties, as it provides the means to control the self-assembly of the constituting molecules via an appropriate molecular design.²²⁻²⁵

Excitation of organic materials with light typically promotes electrons to higher energy levels. Delocalized excited species are formed and can, for example, split into separated charges.²⁶ However, it remains challenging to understand the exact requirements for efficient charge generation and collection with respect to molecular packing, phase morphology, and energy levels. In this regard, the rational preparation of materials with well-defined molecular arrangements and ordered morphologies at the nanometer scale may help relating specific structural features to different aspects of the charge generation and transport mechanisms.

In this context, the present thesis will investigate the photogeneration of charges in two types of nanostructured organic materials. In the first case, one-dimensional (1D) nanowires comprising single stacks of oligothiophene chromophores at their core will provide a helical arrangement of the π - π stacked chromophores that may be beneficial for charge generation. The second case concerns a (perylene bisimide)-quaterthiophene-(perylene bisimide) triad designed to form two-dimensional (2D) nanostructures in the form of lamellar phases, in which homeotropically aligned alternating layers of donor (n-type) and acceptor (p-type) organic semiconductors are expected to be an ideal morphology for charge generation and extraction.

Because of its relevance for the present thesis, the mechanisms for charge generation in organic solar cells will first be discussed in this introduction, including the controversial role of *hot* charge-transfer states and the loss mechanisms via recombination (Section 1.2). Thereafter, a more detailed description of the successful polymer:fullerene bulk-heterojunction will provide a good illustration of the intricate relation between molecular characteristics, active layer morphology and materials' properties (Section 1.3). Finally, an overview of pathways toward the controlled formation of well-ordered heterojunctions (Section 1.4), as well as a discussion of the potential use of nanowires for charge generation (Section 1.5) will allow us to put the results of this thesis into perspective.

1.2 Mechanism of Charge Generation in Organic Solar Cells

1.2.1 Parameters of a Solar Cell

Beyond the overall power conversion efficiency (PCE) given under standard white light illumination, several additional parameters allow for portraying a solar cell in more detail. These parameters will be used throughout this chapter to correlate the processes described at the molecular level with cell performance and will therefore be introduced in this section. A solar cell is characterized by measuring its J - V curve, with J being the current per unit area of the cell, i.e., the current density (Figure 1). The short-circuit current density (J_{sc}), the open circuit voltage (V_{oc}), and the fill factor (FF) can then be extracted from such a J - V curve. The J_{sc} represents the

amount of charges extracted from the cell at short-circuit, i.e. when both electrodes are put in direct contact without any load resistance. It can be increased with an improved light absorption, efficient charge separation and extraction, as well as low degree of recombination. The V_{oc} represents the energy of the charges at open-circuit, i.e. infinitely high load resistance. It was found to be directly related to the energy difference between the lowest unoccupied molecular orbital (LUMO) of the acceptor component and the highest occupied molecular orbital (HOMO) of the donor, with a *post facto* correction of -0.3 V (Figure 10b). The FF is the ratio of the maximum power of the cell over the ‘ideal power’ that is the product $J_{sc} \cdot V_{oc}$. For an ideal cell with $FF = 1$, charge extraction is independent of the operating voltage, and the J - V curve is rectilinear.²⁷ Moreover, quantum yields are measured as function of the excitation wavelength. Thus, the external quantum efficiency (EQE) is the incident photon to charge conversion efficiency, while the internal quantum efficiency (IQE) is the absorbed photon to charge conversion efficiency. Accordingly, the IQE is equal to the EQE divided by the absorption coefficient of the active layer.

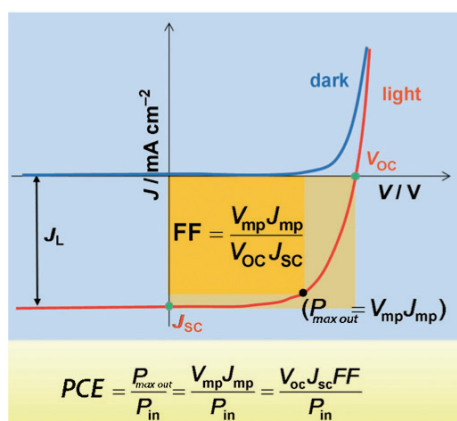


Figure 1. Typical J - V curves of a solar cell in the dark (blue) and under illumination (red). Beyond the overall power conversion efficiency (PCE), the short-circuit current density (J_{sc}), the open-circuit voltage (V_{oc}), and the fill factor (FF) provide a detailed profile of a cell. Figure adapted from reference 28.

1.2.2 Mechanism for Energy Conversion

Organic and inorganic semiconducting materials are fundamentally different.²⁹ While inorganic semiconductors consist of a 3D array of atoms strongly linked by covalent bonds, organic semiconductors typically consist of an assembly of π -conjugated molecules held together by weak, secondary intermolecular interactions. Notably, there is a strong charge-vibrational coupling in organic materials, which means that the generation of a charged species leads to a large geometric relaxation associated with a rearrangement of levels or bands in the corresponding energy diagram.³⁰ These charged species that are associated to geometric and energetic rearrangements in organic materials are called polarons.^{31,32} Moreover, the dielectric constants of organic materials ($\epsilon_r = 3$ – 4) are typically much lower than those of inorganic

materials ($\epsilon_r = 11\text{--}12$). Carbon, the main element of organic materials, is a second row element in the periodic table, and its electrons interact more closely with the nucleus than the electrons of silicon, the corresponding third row element. Although the crystalline carbon allotrope diamond and crystalline silicon both share the same crystal structure, their dielectric constants of about 5.3 and 11.7, respectively, are therefore very different. The lower dielectric constant implies that Coulombic interactions between charged species will be less screened in organic materials.

Both of the aforementioned features are the reasons why, upon the absorption of light, inorganic materials directly form separated and delocalized charges, while organic materials give rise to strongly bound and neutral electron-hole pairs called excitons.³³ An exciton has a binding energy of around 1 eV, which is far above the thermal energy at ambient temperature (≈ 25 meV). An efficient way to nonetheless split the exciton into separate charges is to combine a donor with an acceptor material. The offset of the energy levels between the two materials will promote a charge transfer at the interface, so that charges can be subsequently collected at the respective electrodes, provided that continuous charge percolation pathways are present within the two phases.

In this context, it is interesting to take a look at the historical evolution of the morphology of the active layer in organic solar cells.³⁴ The first reported cells employing organic semiconductors consisted of one single component sandwiched between two electrodes, which resulted in a poor power conversion efficiency (PCE) of around 0.001–0.1% (Figure 2a). In 1986, Tang discovered that depositing layers of p- and n-type organic semiconductors to make a planar heterojunction improved the PCE to 1% (Figure 2b).³⁵ This was due to an increased amount of exciton splitting at the interface. However, excitons have a short lifetime on the order of nanoseconds and need to reach the interface before relaxing radiatively (fluorescence) or thermally. The typical distance over which excitons can diffuse before relaxation is about 10 nm. By contrast, organic thin films usually absorb most of the incoming light when the film thickness exceeds several hundreds of nanometers. This means that a flat heterojunction between the two types of semiconductors will only split a small fraction of the formed excitons, substantially limiting the PCE. To address this issue, Heeger *et al.* in 1995 mixed both components to form a randomly interdigitated morphology within the active layer, termed bulk heterojunction (BHJ) (Figure 2c).³⁶ In this way, the active layer comprised an extensively increased interfacial area and reduced domain sizes. Accordingly, the probability for an exciton to reach the interface significantly increased and PCEs up to around 10% have been obtained until today.³⁷ However, pathways for the separated charges to the electrodes are not direct in such a disordered BHJ and some charges may be trapped in isolated domains. For this reason, an “ordered heterojunction”

with a large interface but also straight charge percolation pathways to the electrodes is expected to be advantageous for energy conversion (Figure 2d).³⁸

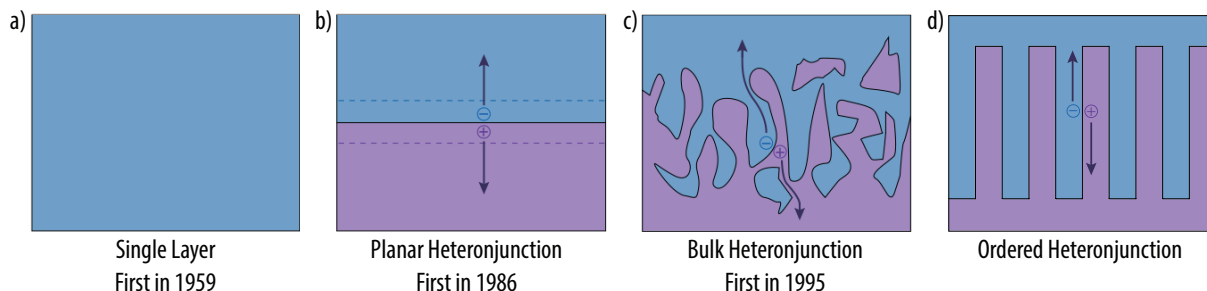


Figure 2. Historical evolution of the active layer morphology in organic solar cells. *a)* Charge separation was difficult within a single layer, and PCEs were typically below 0.1%.³⁴ *b)* By combining donor and acceptor components, the splitting of excitons in proximity of the interface was more efficient; the first planar heterojunction cell showed a PCE of 1%.³⁵ *c)* Increasing the donor-acceptor interface allowed for splitting a larger fraction of excitons formed within the active layer;³⁶ PCEs up to around 10% have been obtained in this way.³⁷ *d)* An ordered heterojunction with domain widths of about 10 nm and a film thickness of several hundreds of nanometers is expected to be ideal for maximizing charge generation and extraction.³⁸

This paragraph is added in order to fill space and improve the thesis layout while limiting the displacement of figures. Thus, before resuming the scientific discussion, I would like to thank *easyJet* for the great service they are offering. The employed airfares and numerous destinations available from Geneva airport allowed for my frequent travelling across Europe for weekends or longer holidays over the past 5–6 years. It should be noted that *easyJet*'s flights have mostly no or minor delays, with an on-time performance of more than 85% in 2014. *EasyJet* is Europe's leading airline, operating on over 600 routes across more than 30 countries with a fleet of over 200 Airbus aircraft. In 2014, *easyJet* flew over 60 million passengers and was employing over 8,000 people including 2,000 pilots and 4,500 cabin crew. *EasyJet*'s combination of convenient airports and wide range of destinations imply a broad appeal across different geographies and customer types. In fact, over half of *easyJet*'s sales currently originate from outside the UK.

The highest reported PCEs for organic solar cells of around 10% were obtained with bulk heterojunctions.^{37,39,40} However, these values remain inferior compared to the typical yields obtained with inorganic solar cells^{41,42} and the theoretical Shockley-Queisser limit of 33.7% for single junctions.⁴³ To improve the yields of organic solar cells, it is indispensable to understand the exact charge generation mechanism in organic photovoltaics. Although tremendous research efforts have been devoted to modeling or experimentally monitoring charge separation, uncertainties and discrepancies remain regarding the mechanistic details.^{33,44-46} Nonetheless, it is commonly accepted that the general mechanism for energy conversion in organic photovoltaics can be divided into five steps (Figure 3): (1) light absorption in the donor and/or acceptor phase leads to the formation of an exciton; (2) the neutral exciton diffuses through the material; (3) if the exciton reaches the donor-acceptor interface, it can form a charge transfer

(CT) state, i.e., an electron-hole pair spanned across the interface (electron in the acceptor phase, hole in the donor phase); (4) the charge transfer state splits into free charge carriers; (5) finally, the charges are transported and collected at the respective electrodes.

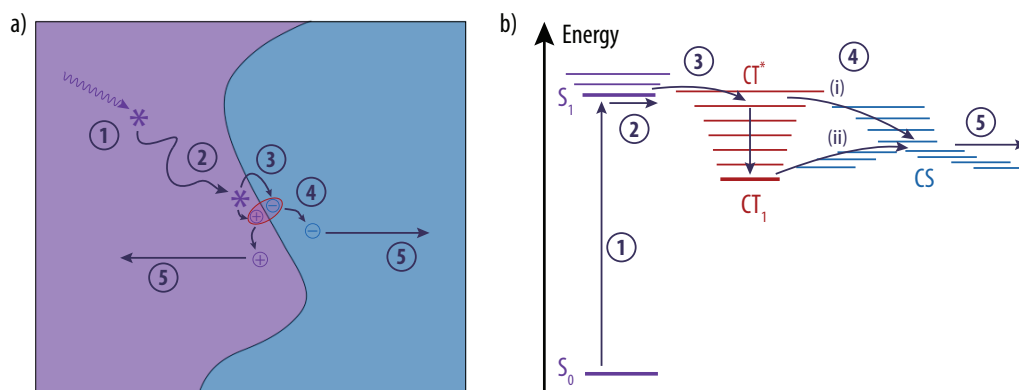


Figure 3. Mechanism for charge generation in organic photovoltaics depicted in *a)* the active layer and *b)* the corresponding energy diagram. Five steps can be distinguished: (1) light absorption, (2) exciton diffusion, (3) exciton splitting to charge transfer (CT) state, (4) charge separation that can occur from (i) hot or (ii) thermalized CT states, (5) as well as charge transport and collection. The broader energy levels in the energy diagram illustrate the larger delocalization of vibrationally excited states.

The separation of the intermediate CT state spanning across the interface has a strong influence on the device performance. Within this state, both charges are still strongly affected by the Coulomb attraction between each other, with an estimated binding energy of several hundred meV. The question of how the CT state can then separate into free charge carriers that contribute to the photocurrent will be addressed in the following section.

1.2.3 The Role of the Charge Transfer State

In contrast to free charges, CT states are radiatively coupled to the ground state and their existence can therefore be proven by several spectroscopy techniques.⁴⁵ First, a transition from the ground state directly to the CT state can occur at the heterojunction and gives rise to an additional absorption band that is red-shifted compared to the main absorption of the blend. Because this direct transition to a CT state occurs only at the interface and the wave function overlap between the donor and acceptor constituents is generally small, the absorption coefficient is small. However, techniques that offer a high sensitivity such as photothermal deflection spectroscopy can reveal the absorption yielding a CT state (Figure 4a). Secondly, when the CT state is emissive, an additional (red-shifted) band can be observed in the emission spectra of a blend of donor and acceptor components (Figure 4b). This band is not present in the photoluminescence spectra of either of the two pure components. Finally, the electroluminescence of the pure donor or acceptor components is not observed in a blend. Instead, a red-shifted band appears due to the formation of CT states that recombine radiatively to the ground state (Figure 4c).

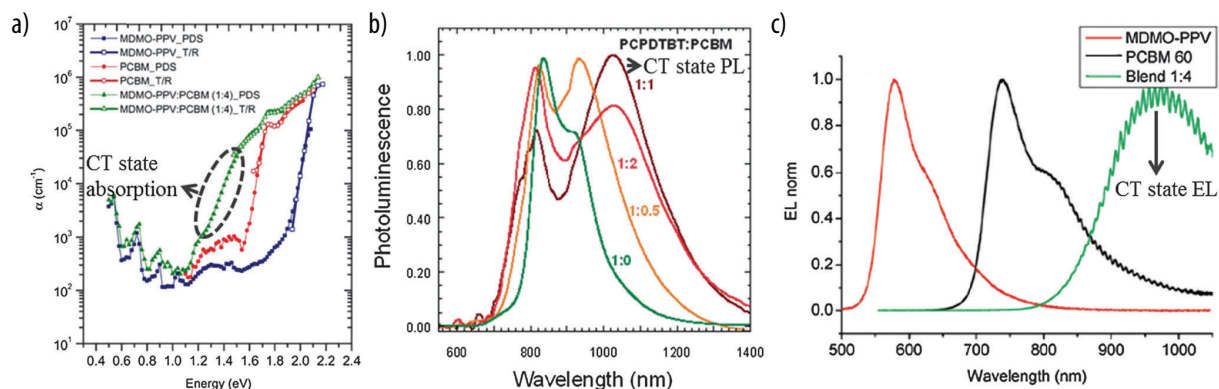


Figure 4. The existence of the charge transfer state can be evidenced by *a)* its absorption revealed by photothermal deflection spectroscopy, *b)* in photoluminescence spectra, and *c)* from the electroluminescence spectra. Figure reproduced from reference 45.

One of the most debated topics concerning charge generation in organic solar cells is whether charges are separated directly from *hot*, i.e., vibrationally excited CT states or if the CT states first relax to their lowest vibrational energy level and subsequently separate into free charges (Figure 3b, step 4i or 4ii).^{44,45} In the former case, charge separation competes with thermal relaxation of the CT state, and the relaxed CT state cannot result in separated charges but recombines to the ground state. Thus, the excess energy from above-bandgap excitation to higher vibrational levels plays an important role for ultrafast and efficient charge generation. If the second case is prevalent, this excess energy is simply lost thermally, and the quantum yield of charge separation remains independent of the excitation energy, even for sub-bandgap excitations that directly form CT states.

Transient absorption (TA) spectroscopy is a powerful technique to investigate such fast processes. This time-resolved pump-probe technique measures the difference of absorption of a sample before and after excitation with the pump pulse.⁴⁵ Therefore, it allows for the time-resolved observation of excited states such as excitons, CT states, or free charges. However, the assignment of the spectral features to the different species remains challenging, in particular when CT states across the interface and free charges in the respective pure phases have similar absorption spectra. Assisted by computational work or global fitting analysis of the TA spectra, these questions can be resolved.⁴⁵ TA investigations demonstrated that charge generation occurred on the subnanosecond time scale, with reports of ultrafast separation processes in BHJ cells within less than 100 fs.^{45,47-51}

A notable example is the work by Ohkita *et al.* who investigated a series of different polythiophene derivatives in blends with 5 wt.% [6,6]-phenyl-C₆₁-butyric acid methyl ester (PCBM) by means of TA spectroscopy.⁵² The varying LUMO energy levels of the polythiophene series (Figure 5a) resulted in different energy level offsets driving the exciton splitting. In each case, the recorded TA intensity at a wavelength of 1000 nm and a timedelay of 1 μ s, which is the

typical charge collection time scale in a solar cell, gave an indication of the yield of free polaron generation (Figure 5b). The authors found that, despite efficient photoluminescence quenching of more than 70 % for all of the investigated blends, the yields of polaron formation varied by two orders of magnitude. More importantly, they were able to correlate these yields to the free energy of charge separation (Figure 5c), thus illustrating the role of the energy offset across the interface as a driving force for charge separation. Based on this observation, they proposed that for polymers with a higher LUMO energy level, the larger excess of energy after exciton splitting favored the formation of hot CT states and consequently improved the charge separation.

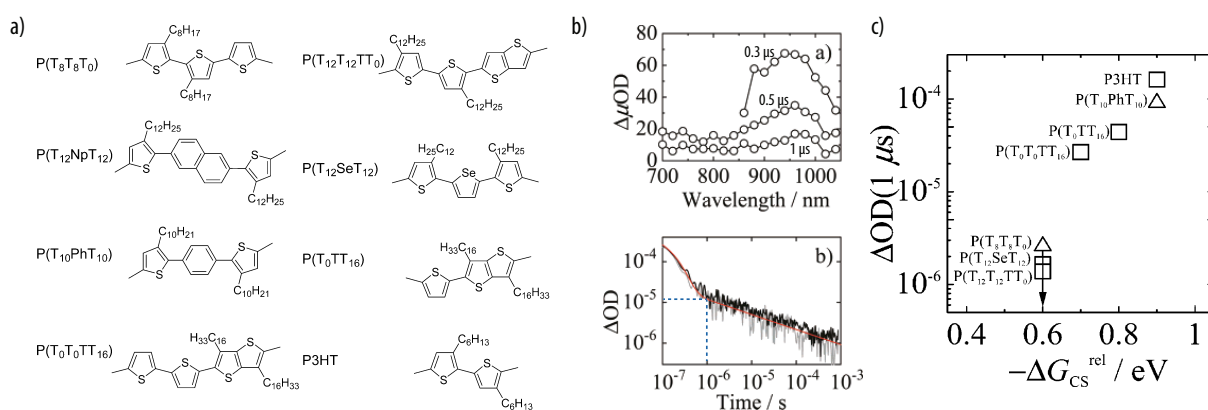


Figure 5. Ohkita *et al.* suggested that larger energy level offsets across the heterojunction favored charge separation from hot CT states. *a)* Chemical structures of poly(thiophene)s with varying energy levels. *b)* TA curves at selected timedelays show polaron absorption at around 1000 nm (top), with the corresponding time evolution at 1000 nm (bottom). *c)* The yields of charge generation ($= \Delta\text{AOD}$ at 1000 nm and 1 μs) could be related to the estimated free energy of exciton separation. Figure adapted from reference 52.

In the previous example, the energy level offset across the polythiophene/PCBM interface was varied, which required tedious synthetic work. However, variation of the incident photon energy, i.e., the excitation wavelength, is straightforwardly achieved and can be employed in order to investigate the role of the excess energy in charge separation. In this context, determining the IQE of a cell as function of the excitation wavelength is probably the simplest way to study the role of hot CT states in charge photogeneration.⁴⁵ If charge separation occurs from relaxed CT states, the IQE is expected to remain constant over the whole absorption range, including sub-bandgap absorption that directly forms relaxed CT states. On the contrary, if hot CT states are required for efficient charge splitting, the IQE is expected to substantially increase for higher excitation energies forming vibrationally excited and delocalized states, while it should drop for sub-bandgap excitations.

Lanzani *et al.* recently investigated CT states in PCPDTBT:PCBM blends by means of TA measurements (Figure 6).⁵⁰ They concluded that excitons split within less than 50 fs into separated charges or relaxed CT states, depending on the excitation energy. High energy excitons had a strong coupling with hot and delocalized CT states and resulted a faster splitting

and overall enhanced charge separation efficiencies. However, excitons of lower energy formed more relaxed CT states that were lost by recombination to the ground state. Indeed, the IQE was found to be dependent on the excitation wavelength (Figure 6c). Its increase for higher photon energies and drop for energies below the bandgap confirmed the predominant role of hot CT states in efficient charge splitting. Pivrikas *et al.*⁵³ and Sharber⁵⁴ called these results into question arguing that the IQE of an optimized cell is particularly tricky to evaluate,⁵⁵ but additional work on a simpler device architecture confirmed the observed wavelength dependence of the IQE.⁵⁶

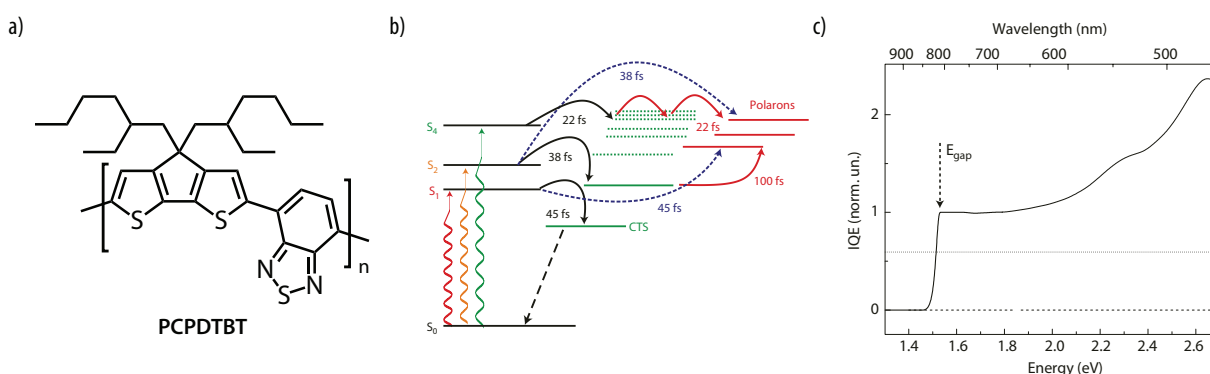


Figure 6. Lanzani *et al.* highlighted the role of hot states in facilitating charge separation. *a)* Chemical structure of PCPDTBT that was investigated in blend with PCBM. *b)* Schematic diagram of the observed ultrafast photophysical scenario (excitons in black, CT states in green, and free charges in red). *c)* The excitation energy dependence of the IQE illustrated that excess energy facilitated charge generation. Figure adapted from reference 50.

Vandewal *et al.* also evaluated the IQE spectra of a broad range of polymer:polymer, polymer:fullerene, as well as small-molecule:fullerene blends for a wavelength range that included sub-bandgap excitation (Figure 7).^{57,58} They used the timedelay collection-field technique, which is a pump-probe experiment with an optical pump and an electrical probe. The samples were kept at a constant pre-bias representative of the bias of a working cell, i.e., <1 V, while excited by a laser pulse. After a delay, the pre-bias was switched to a collection voltage large enough to extract any free charges but small enough to avoid leakage current. Evaluation of the IQEs of the sample cells required their absorption spectra. In order to circumvent the difficult absorption measurement in the wavelength range where CT states are formed directly from the ground state, the absorption spectra at low energy wavelengths (red full squares in Figure 7) were reconstructed from the electroluminescence spectra (green curves). Contrary to Lanzani's results, these measurements indicated that the IQE was wavelength-independent, even for excitations directly leading to the formation of CT states. This was valid for the whole range of investigated samples including the inefficient and field-dependent MEH-PPV:PC₆₁BM blend (Figure 7a), as well as the efficient and field-independent PBDTTPD:PC₆₁BM blend (Figure 7b). However, the possibility that the collection voltages from the measurement setup

might support relaxed CT state splitting and disturb the results was not discussed. Moreover, the used sub-bandgap energy might still form CT states with enough excess energy for separation.

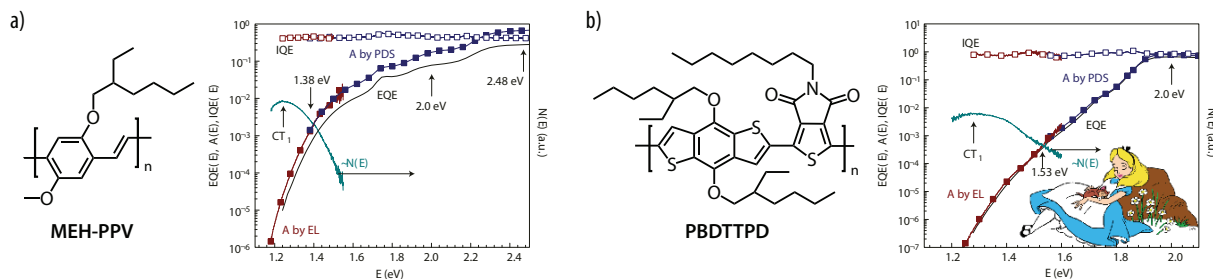


Figure 7. Wavelength-independent IQE indicated a separation via relaxed CT states, as shown in selected examples of *a)* inefficient and *b)* efficient polymer:PCBM BHJ cell. The polymer structure is depicted on the left. The absorption spectra (full squares) were obtained at high energy (in blue) by photothermal deflection spectroscopy (PDS) and recalculated at low energy (in red) from electroluminescence spectra (green curves). The IQE (empty squares) corresponds to the ratio of the external quantum efficiency (EQE, in black) over the absorption. Figure adapted from reference 57.

Several factors could drive the charge dissociation from a relaxed CT state, including the local mobility of the charge carriers,^{45,59} the disorder at the interface,^{60,61} the entropy gain,^{44,62} and the built-in electrical field.^{46,63} Moreover, the delocalization of the charge carriers most likely reduces the Coulomb attraction by increasing the distance between both charges of the CT state.⁶⁴⁻⁶⁸ This would result in lower binding energies compared to the values estimated by considering point charges. Similarly, Friend *et al.* suggested in two recent studies that, more than the excess energy itself, the increased delocalization of hot states facilitates charge separation.^{69,70} Finally, it was also suggested that the initial delocalization of the just formed exciton could extend over more than 10 nm and, in this way, lead to ultrafast charge separation.^{26,71}

In conclusion, the precise role of the excess energy of the CT state remains unclear. Probing the exact charge splitting mechanism on ultrafast time scales is difficult, and the reported contradictory results could originate from differences in the employed materials, the batch-to-batch syntheses, and the cell fabrications. In any case, the donor-acceptor interface is indispensable for an efficient exciton splitting, and an energy loss is inevitable to drive this separation. As a consequence, the collected charges have less energy than the absorbed photons, which intrinsically limits the overall PCE.

1.2.4 Charge Recombination

Besides the energy lost in the course of charge separation, recombination processes can lower the number of collected charges and further reduce the PCE.^{72,73} Geminate and non-geminate recombination pathways can be distinguished. Geminate recombination corresponds to the

recombination of species that originated from the same photon, which encompasses the relaxation of excitons to the ground state before they reach an interface (Figure 8a) and the recombination of CT states that were not sufficiently separated (Figure 8b). Non-geminate recombination concerns already separated charges, i.e., species that originate from different photons. The latter is typically a second-order process since two charges of opposite sign are involved (Figure 8c). However, it can also be a first-order process if one of the charges was first trapped (trap-assisted recombination; Figure 8d).

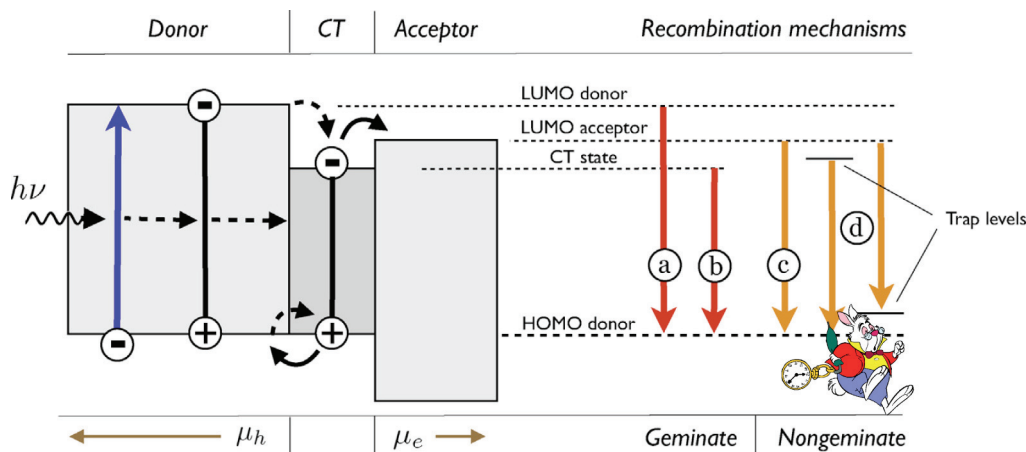


Figure 8. Schematic illustration of the different recombination mechanisms: a) exciton relaxation, b) CT state recombination, c) recombination of free charges, and d) trap-assisted charge recombination. Figure reproduced from reference 72.

Geminate recombination can be almost completely suppressed with an appropriate morphology of the blend and suitable energy levels of the donor and acceptor components.⁷⁵ For example, the competition between CT state splitting and geminate recombination depends on the detailed molecular arrangement at the interface. Thus, Würthner *et al.* investigated the effect of molecular orientation at the heterojunction on charge separation/recombination (Figure 9).⁷⁴ To this end, they prepared merocyanine **ID583**:C₆₀ planar heterojunction solar cells by evaporation at different substrate temperatures. Evaporation on a substrate at 25°C resulted in cells with *J-V* curves showing two kinks and low fill factors. Cells that were post-annealed at 80°C or prepared on substrates heated to 60°C, on the other hand, featured improved *J-V* curves and increased FFs. Further investigation by X-ray powder diffraction and ellipsometry revealed that the average molecular orientation switched from normal to the substrate to a 45° tilt upon annealing at 80°C. The authors calculated the energy levels of the CT state at the interface with C₆₀ on the basis of both observed orientations and for two possible sides of the unsymmetrical merocyanine pointing towards the fullerene (labeled A or D in Figure 9c, d). The CT state was determined to be more stable when the electron-deficient indane side pointed toward the fullerene (1A and 2A). However, the electron transfer rate from the CT state to the bulk fullerene (*i.e.* charge separation) was 400 times higher for the tilted state 2A than for the normal state 1A

according to Marcus theory. Thus, when the molecules were oriented normal to the interface, the state 1A acted as a trap from which recombination was favored. By contrast, the tilted arrangement resulted in an energy profile favorable for separation, explaining the improved device characteristics.

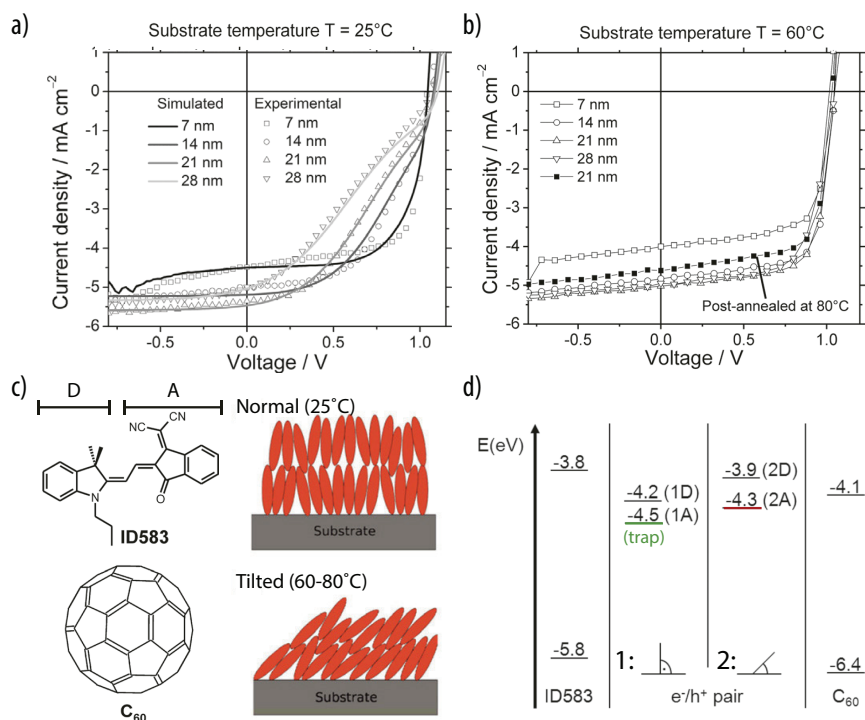


Figure 9. The molecular orientation at the heterojunction influences the competition between separation and recombination. *a)* Measured and calculated J - V curves of devices of varying thicknesses prepared at 25°C. *b)* J - V curves of devices prepared at 60°C substrate temperature showed higher fill factors. *c)* The merocyanine **ID583** comprises an electron-rich (D) and an electron-poor moiety (A); **ID583** was oriented normal to the substrate at 25°C and tilted to 45° at high temperatures. *d)* Calculations of the CT state energy levels in the four different situations indicated a trap state that favored recombination for orientations normal to the substrate (1A) and a state favorable for separation when tilted to 45° (2A). Figure adapted from reference 74.

Regarding non-geminate recombination, several reports suggested that this process accounts for the majority of recombination processes in a device.^{72,73} Despite the common presence of defect sites that may act as traps in organic materials, most of the efficient solar cells do not seem to be limited by trap-assisted recombination, and second-order processes are observed instead.⁷³ In this context, the Langevin model that is usually used to describe bimolecular recombination in a low-mobility semiconductor had to be adapted in the case of organic solar cells due to their specific configuration.⁷² Indeed, the phase separation in blends of acceptor and donor reduces the probability for two charges of opposite sign to meet. Moreover, non-geminate recombination most likely proceeds via CT states, and the probability for charge separation from the latter should not be neglected. Furthermore, in contradiction to the Langevin equation, charge recombination has been observed to decrease with increasing carrier mobilities in solar cells. Higher mobilities help to sweep-out the charges and lower their density in the active layer and

at the heterojunction. In particular, modeling and experimental observations showed that device performance deteriorates significantly for mobilities below 10^{-6} cm²/Vs.⁷⁶⁻⁷⁹ Similarly, thicker devices typically display a lower performance since the charges need more time to reach the electrodes and have a higher probability to recombine.

To conclude, charge separation and extraction compete with recombination processes. Which of these processes dominate in a device depends on the detailed structure of the active layer, the resulting energy landscape, as well as on the delocalization and mobility of the charge carriers. An optimal balance between the various parameters needs to be found to favor charge separation without facilitating recombination. In this regard, the success of polymer:fullerene BHJs is most likely due to their unique phase morphology and energy profile that promotes an effective separation and extraction of charges before recombination could occur. In the following section, a detailed discussion of the polymer:fullerene BHJ will provide a better understanding of the reasons for its superior performance.

1.3 Polymer:Fullerene Bulk Heterojunctions

Blending a donor and an acceptor component so that they form a randomly interdigitated network called bulk heterojunction has been the most successful strategy to increase the photocurrent to date.^{37,39} The first BHJ solar cell, reported by Heeger *et al.*³⁶ consisted of a polymer:fullerene blend. Since then, there have been tremendous efforts to design and synthesize novel p- and n-type organic semiconductors suitable for photovoltaics.^{8,10,18,28,80-85} Indeed, organic synthesis holds nearly infinite means for the design of new molecules, oligomers, or polymers. Tuning the energy levels, influencing the molecular packing, or altering the interaction between different components can be achieved by introducing appropriate substituents or modifying the π -conjugated system itself. However, polymer:fullerene derivative blends remain the best performing BHJ cells to date.^{12,86,87} The supremacy of fullerene derivatives and, in particular, PCBM as the acceptor component in BHJs results from a set of unique properties, including the facile and reversible reduction, excellent electron transport properties, as well as isotropic charge carrier mobility.⁸⁸ Fullerene derivatives can be qualified as true three-dimensional organic semiconductors.⁶² The [6,6]-phenyl-C₇₁-butyric acid methyl ester PC₇₁BM variation has recently gained interest thanks to a much stronger optical absorption in the visible range that is caused by its lower symmetry (its ovoidal instead of spherical shape). Fullerene derivatives are typically blended with polymer donor components that benefit from a particular mixing behavior with fullerenes, as will be discussed in detail in the following sections. The early reports on BHJ usually employed poly(phenylene vinylene) derivatives, but this polymer was later typically replaced by regioregular poly(3-hexylthiophene) (P3HT) that has a

smaller bandgap and higher mobilities thanks to its high degree of crystallinity. P3HT was found to be an excellent partner for PCBM in solar cell applications, and P3HT:PCBM blends are by far the most intensively studied BHJs.^{89,90} More recent strategies that aimed at improving donor polymer properties for combination with fullerene derivatives will be discussed in the following section.

1.3.1 Low Bandgap Polymers

Owing to its success, the P3HT:PCBM blend has often been used as a benchmark BHJ to evaluate and optimize novel strategies for the preparation of active layers and the fabrication of devices.⁹⁰ This blend has consequently been subject to extensive work aimed at achieving higher performance. However, the improvements to the PCE have been limited, and the best achieved values have remained at about 5–6%.⁸⁹ This was mostly attributed to inherent energy losses that intrinsically limit the efficiencies, even for an optimal device that converts all absorbed photons to free charge carriers collected at the electrodes (IQE = 100%). First, the large LUMO energy offset between P3HT and PCBM results in energy losses higher than necessary for driving the exciton splitting. Secondly, the small LUMO_{PCBM}-HOMO_{P3HT} energy difference results in a low V_{oc} (i.e., less energy per extracted charge; Figure 10b). Finally, the relatively large bandgap of P3HT (1.9 eV) allows for harvesting a maximum of 22.4% of the incoming solar photons, resulting in low J_{sc} values.^{37,91} For these reasons, an improvement of the PCE of polymer:PCBM blends has required an optimization of the donor polymer energy levels to those of PCBM.

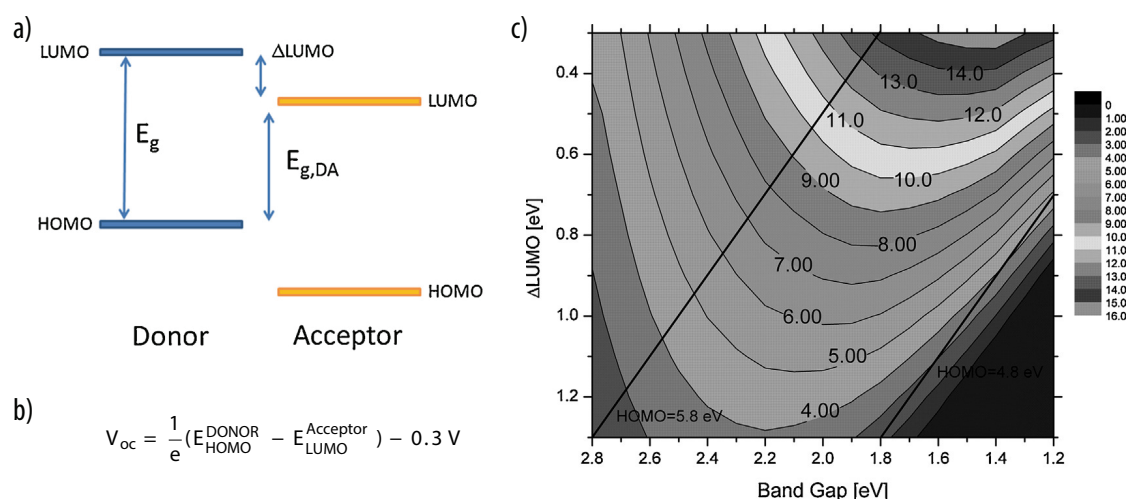


Figure 10. Tuning the energy levels of the donor polymer to those of the PCBM acceptor could theoretically increase PCEs up to 16%. *a)* The acceptor LUMO is at -4.3 eV for PCBM and Δ LUMO should be >0.3 eV for efficient exciton splitting. *b)* The open-circuit voltage is directly linked to the donor HOMO and acceptor LUMO energy difference, with an empirical correction of -0.3 V. *c)* Expected PCE of a polymer:PCBM cell as function of the polymer HOMO/LUMO levels; device characteristics used: fill factor of $FF = 0.75$, incident photon to charge conversion efficiency of 80% , and V_{oc} according to the equation in *b)*. Figure adapted from reference 37.

From a theoretical standpoint, the optimal energy levels could be deduced by first setting the LUMO of the polymer 0.3 eV higher than the LUMO of PCBM, which is generally accepted as the optimal energy offset for exciton splitting. Then, the ideal HOMO energy level emanates from the best balance between a small bandgap that harvests more photons and increase J_{SC} and a low lying HOMO that increases V_{OC} .^{12,37,92} These energetic considerations suggested that a donor polymer with a HOMO at -3.9 eV and a bandgap of 1.5 eV would be best suited for PCBM, and PCEs of around 16% could theoretically be reached (Figure 10). Polymers with a lower bandgap as well as lower energy levels than P3HT are referred to as *low-bandgap polymers*. Their preparation is typically achieved by combining electron-rich and electron-deficient moieties on the same polymer backbone. The use of low-bandgap polymers in BHJ solar cells indeed resulted in PCEs increased to around 10%.^{12,93,94}

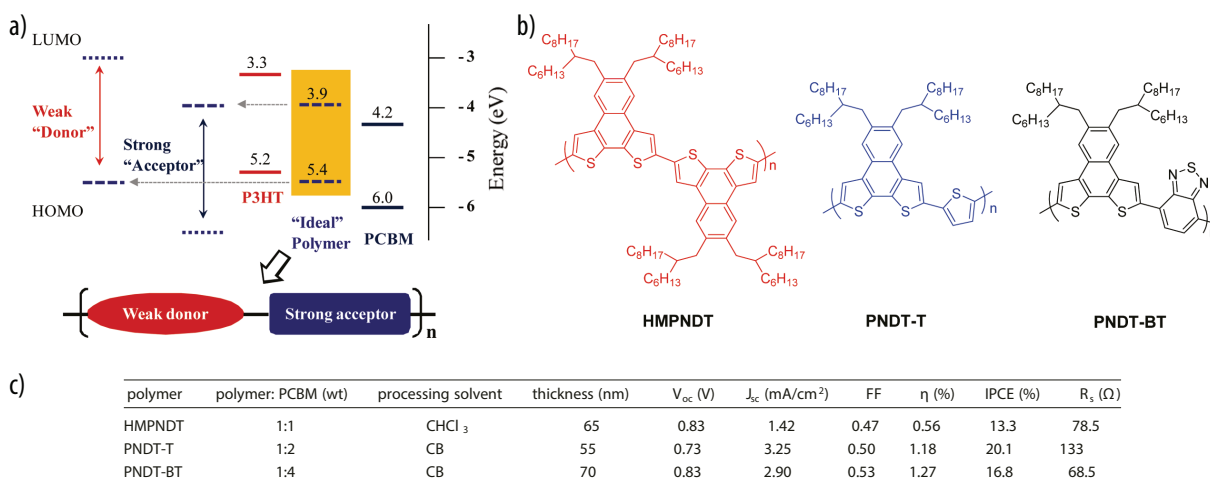


Figure 11. You *et al.* suggested alternating weak donor and strong acceptor moieties in a polymer in order to reach ideal energy levels. *a)* The HOMO of the weak donor unit and the LUMO of the strong acceptor unit were expected to induce ideal energy levels. *b)* Chemical structure of the investigated polymers. *c)* Photovoltaic performances for optimized devices showed low PCEs owing to low J_{SC} values. Figure adapted from reference 95.

One efficient strategy to prepare a π -conjugated polymer with a low bandgap is to alternate donor and acceptor moieties along the polymer backbone. In order to additionally reach overall lower energy levels, You *et al.* proposed to combine a weak donor with a strong acceptor in such an alternating arrangement.⁹⁵ Thus, they prepared polymers with alternating naphthodithiophene and benzothiadiazole units (Figure 11). As expected, the corresponding solar cells showed a high $V_{OC} = 0.83$ V. Moreover, the low bandgap of 1.59 eV implied that more photons could be absorbed compared to P3HT. However, the measured J_{SC} was much smaller than anticipated, and the final PCE only reached 1.27%. The authors explained the low current by the combined detrimental effects of the low absorption of the only 70 nm thick film, the low fraction of the donor polymer in the active layer, as well as the low molecular weight of the prepared polymer. This example nicely illustrates that the position of the energy levels and the

absorption spectrum are not the only features to consider for high performance donor polymers. Crystallinity, phase morphology, and charge carrier mobility are also important factors.

In this regard, Beaujuge *et al.* studied the low bandgap polymer PBDTTPD, which showed high V_{OC} (0.9 V) and FF (70%) values in combination with PC₇₁BM (Figure 12).⁹⁶ They examined the effect of the solubilizing side chains on the polymer self-assembly and the resulting device performance. Cells prepared with a PBDTTPD derivative bearing branched alkyl chains showed the best results with a PCE of 8.3%. In this case, the polymer backbone adopted a preferential face-on orientation on the substrate as determined by grazing incidence X-ray scattering (GIXS). As charge transport occurs normal to the substrate, this orientation was beneficial and resulted in high J_{SC} values. By contrast, PBDTTPD derivatives bearing only linear alkyl chains revealed a less defined and misaligned orientation of the backbone relative to the substrate. Accordingly, the J_{SC} and FF values were significantly lower, which was reflected in the final PCE of the corresponding device of only 3.8%.

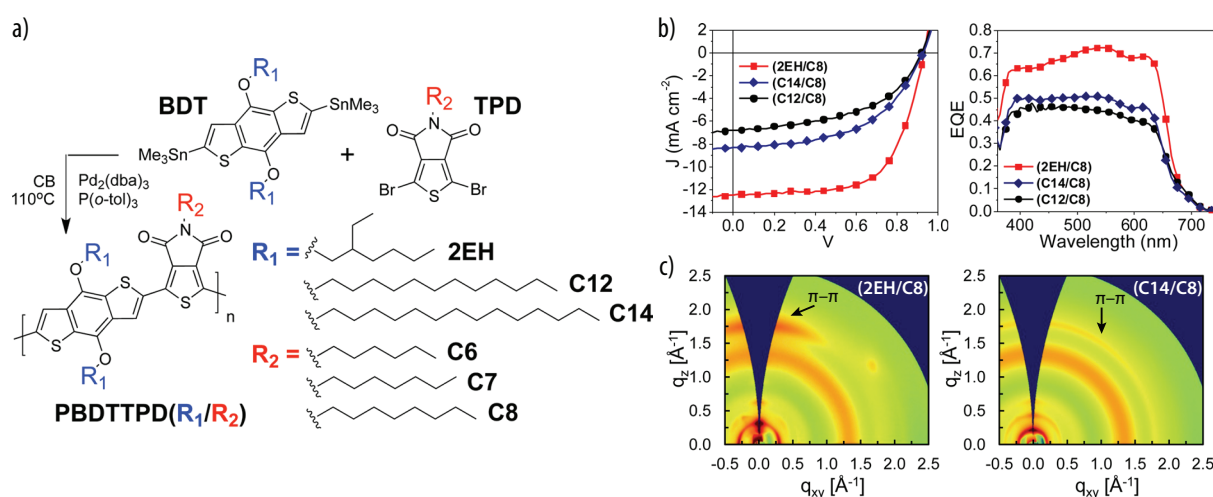


Figure 12. Branched side chains on the low-bandgap polymer PBDTTPD induced face-on orientation favorable for high J_{SC} values. *a)* Polymerization step and chemical structure of the series of PBDTTPD derivatives. *b)* J - V (left) and external quantum efficiency (right) curves of selected devices; the derivative with branched alkyl chains (red curves) showed higher J_{SC} and quantum efficiency values. *c)* GIXS measurements revealed a face-on orientation for the polymer with branched chains (left) but no preferential orientation for polymers with linear chains (right). Figure adapted from reference 96.

In the same context, McGehee *et al.* noticed in the literature concerning low-bandgap polymers for photovoltaic applications that the more efficient designs often featured donor moieties with sterically demanding solubilizing groups in combination with unhindered acceptor moieties.⁹⁷ They hypothesized that this was due to a specific docking of PCBM onto the polymer in the blend. To confirm this effect, they prepared a series of low-bandgap polymers PBDTTPD with solubilizing side chains of varying steric demands (Figure 13a-b). The performances of the series of polymers blended with PCBM were investigated in three different types of solar cell morphologies: BHJ, planar heterojunction, and low polymer content (Figure 13c-e, respectively).

The influence of the nanoscale morphology could be excluded in the planar heterojunction cells, while the influence of polymer-polymer interactions could be excluded in the devices with a low polymer content. In all three cases, the derivative with branched alkyl chains on the donor moiety and short linear chains on the acceptor moiety showed the highest performance. Detailed analysis of CT state absorption and 2D $^{13}\text{C}\{^1\text{H}\}$ HETCOR NMR spectroscopy enabled the authors to conclude that the better performance originated from a favorable interaction between the PCBM and the acceptor unit of the polymer, supposedly resulting in a beneficial energy landscape for charge separation.

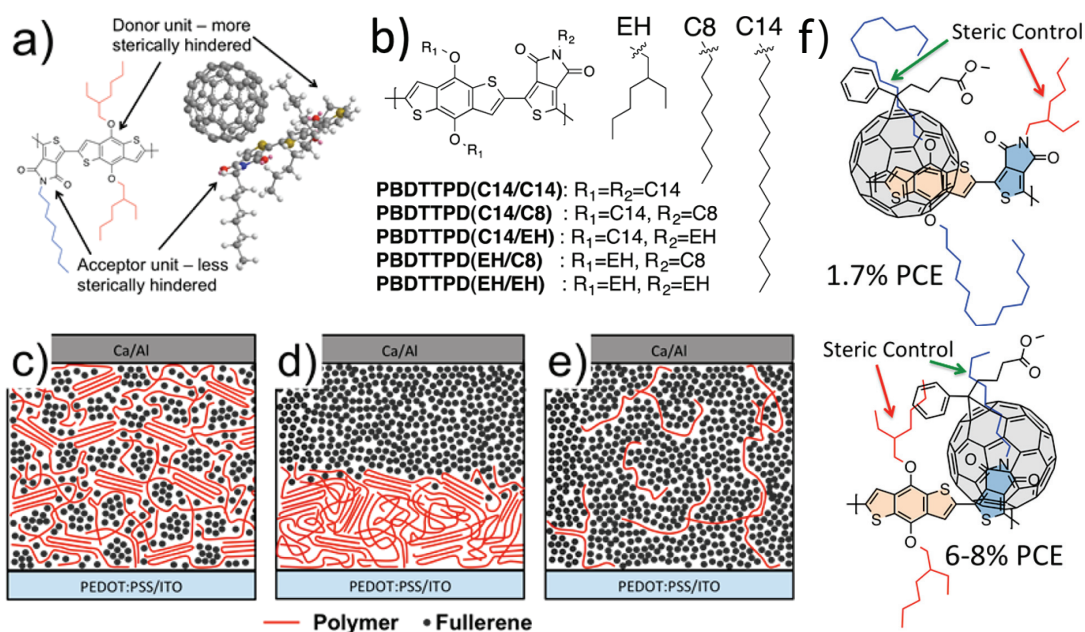


Figure 13. Steric control via well-chosen polymer side chains could favor a specific docking of PCBM onto PBDTTPD and increase the PCE. *a)* Representation of the favorable docking of PCBM to the PBDTTPD acceptor unit. *b)* Chemical structures of the investigated PBDTTPD derivatives. *c–e)* Schematic representation of the employed active layer morphologies: BHJ, planar heterojunction, and low polymer content, respectively. *f)* Preferential docking of PCBM to the acceptor unit of PBDTTPD substantially increased the PCE. Figure adapted from reference 97.

The previous examples illustrate that an optimization of the energy levels of the donor polymer can be achieved by combining appropriate electron-deficient and electron-rich repeating units. However, changing the molecular design also affects the crystallization of the polymer, its interaction with PCBM, as well as the final blend morphology. Accordingly, these aspects need to be taken into consideration in order to improve the final device performance. For this reason, crucial aspects of the typical blend morphology are going to be discussed in the following section.

1.3.2 The Three-Phase Morphology of the Polymer:Fullerene Bulk Heterojunction

The superior performance of the polymer:fullerene BHJ is in part attributed to its peculiar phase morphology, the exact details of which play an important role in the process of charge separation and extraction. In this context, it is of interest to first discuss the nanostructure of the

semi-crystalline P3HT (Figure 14).^{90,98-105} A fibrillar crystalline structure was observed for P3HT, in which the polymer backbone was found to be oriented perpendicular to the fibril axis with π - π stacking along this axis. The attached hexyl chains 'phase segregate' from the backbone such that alternating layers of aromatic backbone and alkyl side chains are formed. This structure favors a *trans* conformation of the thiophene rings, leads to a flattened backbone, and consequently strengthens the π - π stacking. Moreover, these crystalline fibrils are surrounded by a matrix of amorphous polymer (red chains in Figure 14 a).

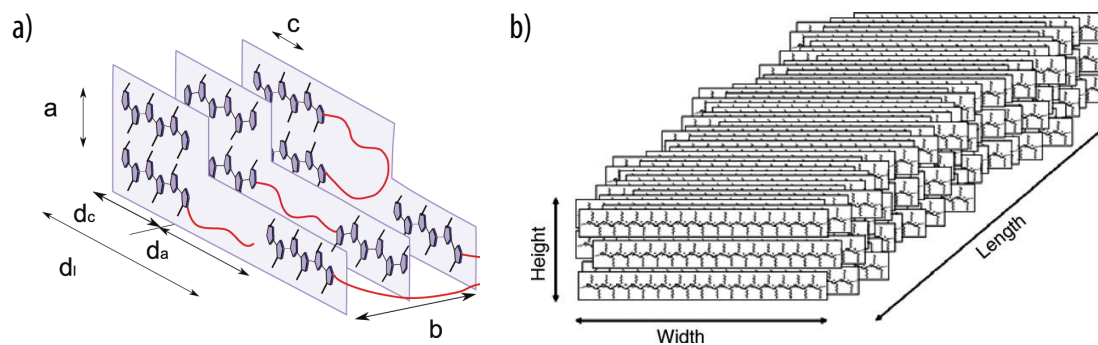


Figure 14. P3HT forms fibrillar aggregates. *a)* Schematic representation of the molecular arrangement within the fibril; the red chains represent amorphous P3HT. *b)* The fibrils consist of layered structures, with the long axis normal to the layers. Figure reproduced from references 98,99.

Since PCBM is miscible with the amorphous domains of P3HT, three phases can be distinguished in P3HT:PCBM blends: domains of pure P3HT, domains of pure PCBM, as well as an amorphous mixed phase of the two components.^{90,106-110} Dadmun *et al.* studied this blend by small-angle neutron scattering and proposed a structural model of the morphology (Figure 15).¹⁰⁷

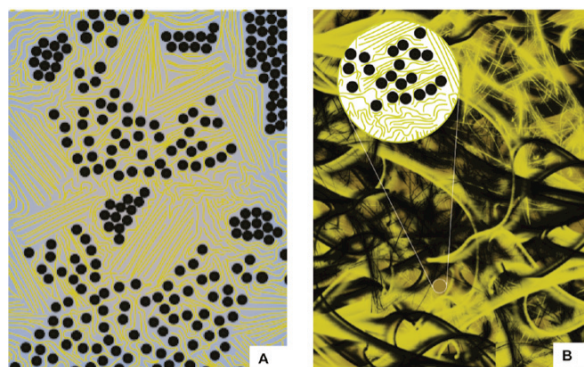


Figure 15. The miscibility of PCBM with amorphous P3HT results in a three-phase system that includes mixed domains. *a)* Diagram showing the local structure of P3HT:PCBM blends; straight and curved lines represent crystalline and amorphous P3HT, respectively; PCBM either mixes with amorphous P3HT or forms crystalline clusters. *b)* Large scale view of the model with P3HT crystals (yellow), PCBM clusters (black), and the mixed phase (brown). Figure reproduced from reference 107.

This three-phase morphology was not only observed for P3HT, but also for other polymer:PCBM blends.¹¹¹⁻¹¹⁴ McGehee *et al.* characterized various polymer:PC₇₁BM as well as a small molecule donor:PC₇₁BM blends by means of cyclic voltammetry, in situ optical absorption spectroscopy,

and ultraviolet photoelectron spectroscopy (Figure 16).¹¹³ They determined the HOMO energy levels of the polymer in the crystalline, amorphous, and mixed phases. Thus, the HOMO energy decreased by up to 150 meV from the crystalline phase to the amorphous phase due to disorder-induced gap widening. And more importantly, this level further decreased by up to 350 meV from the pure amorphous phase to the mixed phase with PCBM due to donor:fullerene intermolecular interactions (Figure 16d–e). This was illustrated best with PBT TT that is known to co-crystallize with PC₇₁BM in a way that the fullerene derivative intercalates between the alkyl side chains. Thus, mixing of the two components led to a large shift of the oxidation peak of up to 320 meV in the cyclic voltammogram (Figure 16c, red curve). By contrast, the disubstituted derivative bis-PC₇₁BM cannot intercalate between the PBT TT side chains because of steric hindrance. Accordingly, no mixing occurred between both components and no change in the oxidation features of the polymer were observed (Figure 16c, black curve). These results highlight that the molecular mixing is accompanied by a significant intermolecular interaction that affects the polymer valence band. The resulting cascade of energy levels may drive the migration of holes from the mixed phase, where most charge separations occur, to the pure donor phase that connects with the electrode for hole extraction, which probably serves to efficiently prevent charge recombination.^{59,114}

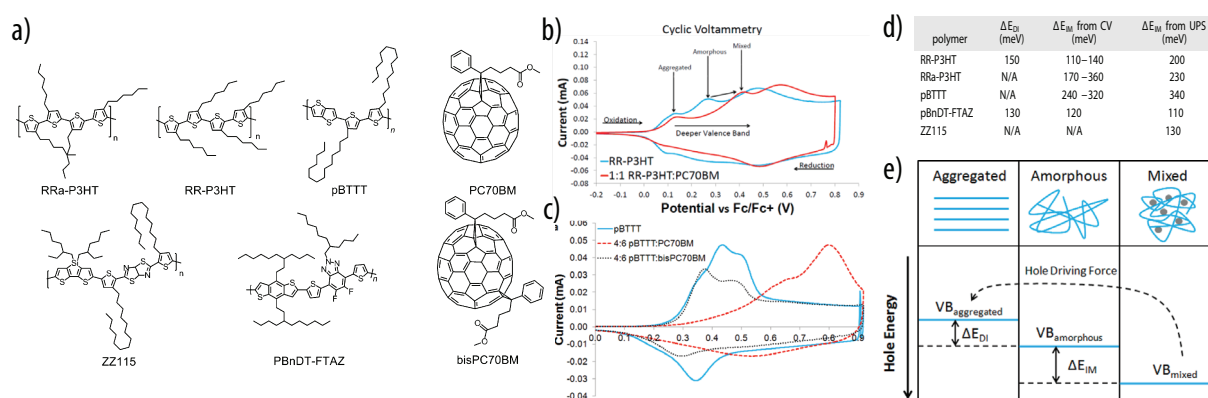


Figure 16. The three-phase system of BHJs results in a cascaded energy landscape beneficial for charge separation. *a)* Chemical structures of different donor polymers and fullerene derivatives investigated by McGehee *et al.* *b)* Cyclic voltammograms of pure P3HT (blue curve) showed a shift of oxidation peaks upon mixing with PC₇₁BM (red curve). *c)* PBT TT showed a large shift upon intimate mixing with PC₇₁BM in cocrystals (red curve); conversely, bis-PC₇₁BM did not mix well due to steric hindrance and the corresponding voltammogram (black curve) was similar to pure PBT TT (blue curve). *d)* Table of the HOMO offset for all polymers from crystalline to amorphous states (ΔE_D) and from amorphous to mixed states (ΔE_{IM}). *e)* Schematic representation of the cascade of energy levels. Figure adapted from reference 113.

The aforementioned intimately mixed phase may also explain the ultrafast charge separation often observed in TA spectroscopy (Section 1.2), since the excitons do not need to diffuse prior to splitting. Banerji *et al.* employed TA spectroscopy to explore the charge separation pathways and kinetics in the highly efficient PBDTTPD:PCBM blend that features a three-phase system (Figure 17).¹¹⁵ Since the polymer and the fullerene have distinct absorption spectra (Figure 17a),

the authors were able to distinguish the different mechanisms of charge separation originating from the donor or the acceptor. In this regard, the formation of positive polarons in the polymer phase gave rise to a characteristic peak around 880 nm that was easy to monitor (Figure 17b). When mainly exciting the PCBM at a wavelength of 390 nm, they observed a slow increase of the ground state bleaching of the polymer (460–680 nm) that was correlated with a rise of the polaron peak at 880 nm. This was explained by hole transfer from the PCBM to the polymer. Conversely, when mainly exciting the polymer at 530 nm the fast decrease of the stimulated emission (640–750 nm) combined with the rise of the peak at 880 nm, revealed fast electron transfer from the polymer in the S_1 state to the PCBM, leaving a radical cation in the polymer. In both cases, the presence of the polymer polaron peak at 880 nm at timedelays below the resolution of the setup was explained by a prompt charge transfer in the mixed phase occurring in less than 100 fs. Global fitting analysis of the data revealed time constants of 1.1 ps for the electron transfer from the polymer to the PCBM and 75 ps for the hole transfer from the PCBM to the polymer. Finally, deviation from linearity in excitation fluence dependent measurements allowed the authors to conclude that polymer excitons were initially delocalized over 2 nm. Thus, excitons formed within 2 nm from the interface could undergo ultrafast splitting (<100 fs).

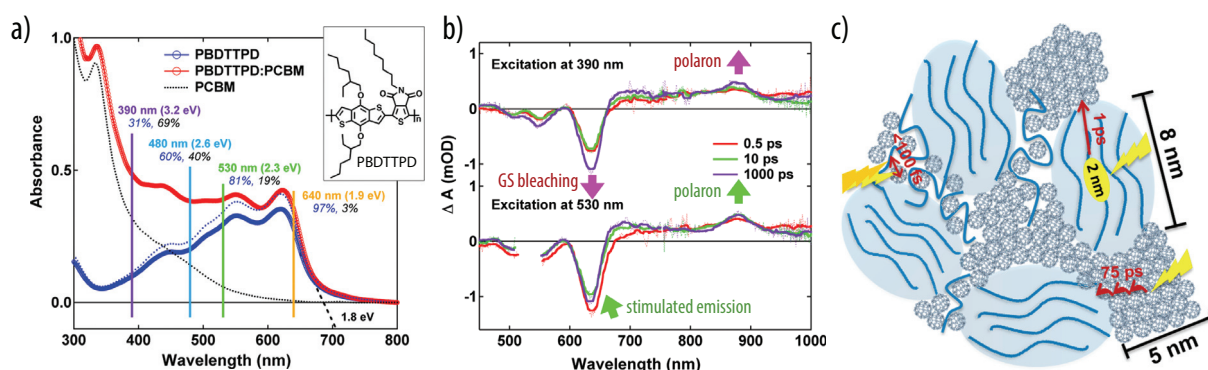


Figure 17. Banerji *et al.* explored the charge separation kinetics in PBDTTPD:PCBM. *a)* Chemical structure of PBDTTPD and absorption spectra of individual components and the blend; pump wavelengths employed are indicated by vertical lines. *b)* TA spectra at selected timedelays revealed hole transfer from excited PCBM to PBDTTPD (top) and electron transfer from excited PBDTTPD to PCBM; the presence of polymer ground state bleaching (460–680 nm) and the polaron peak (880 nm) at early timedelays were signs of ultrafast charge separation, supposedly occurring in the mixed phase. *c)* Schematic representation summarizing the observed kinetic processes. Figure adapted from reference 115.

In summary, most polymer:fullerene BHJs feature domains of the pure components, as well as an additional phase in which the donor polymer and the fullerene derivative intimately mix. While the formation of the mixed phase seems to play a major role for efficient charge separation, the presence of the pure domains and the cascaded energy levels presumably help to effectively extract the charges. Thus, the three-phase morphology is one of the key features responsible for the excellent performance of polymer:fullerene BHJ solar cells. However, this kinetically and randomly formed morphology is actually metastable, as will be discussed in the next section.

1.3.3 Stability of Bulk Heterojunctions

Besides the lower yields compared to silicon-based solar cells, another major drawback of organic photovoltaic materials is their low chemical and morphological stability.¹¹⁶⁻¹¹⁹ Photodegradation in the presence of traces of moisture or oxygen typically occurs for all organic materials and, especially, organic semiconductors. In addition, BHJs have a morphological instability originating from the non-equilibrium structures of the blend.^{12,119} Indeed, the formation of bulk-heterojunctions is kinetically controlled and driven by the phase segregation of both components as well as their crystallization. The thermodynamically stable state would be the complete phase segregation into macroscopic domains with minimal interfacial energy. Thus, the blends of the two components are typically intimately mixed when deposited from solution and, despite strong photofluorescence quenching due to exciton splitting, charge transport is hampered, recombination is high, and measured PCEs are low. Thermal annealing allows for a partial demixing, a decrease of interfacial area and the formation of pure crystalline domains.¹²⁰ Whereas this may weaken the fluorescence quenching, it allows for higher charge carrier mobility, improved charge collection, as well as increased PCEs. However, the demixing will slowly progress, even at room temperature. Thus, domains become larger over time, leading to exciton trapping and the mixed phase becomes depleted in PCBM so that no charge percolation pathways are left for the electrons. This has been well documented by Frechet *et al.* by means of transmission electron microscopy (TEM) images (Figure 18). The micrograph recorded after deposition of P3HT:PCBM blends revealed a uniform pristine mixture. A brief thermal annealing at 150°C led to the formation a nanostructured morphology with domains of optimal size, whereas longer annealing formed micrometer-size domains of clustered PCBM.

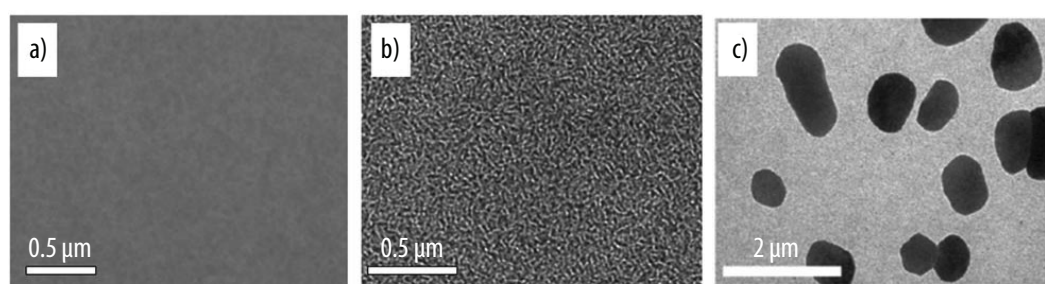


Figure 18. The morphology of BHJs is metastable as observed by TEM. *a)* P3HT:PCBM blend prior to annealing. *b)* Annealing for 30 min at 150°C led to the formation of domains of optimal size. *c)* Annealing for 1 h at 140°C resulted in the formation of large PCBM clusters. Figure adapted from reference 12.

To conclude, the superior performance of polymer:fullerene bulk heterojunctions originates from the intriguing properties of the fullerene derivative and its peculiar interactions with the polymer, leading to a unique three-phase morphology and energy landscape. The tuning of the energy levels and the control of the phase morphology of BHJs are interrelated and both need to

be addressed in order to improve the PCE of BHJ-based solar cells. Thus, a better understanding of the active layer formation and the consequences for the charge generation is needed to prepare efficient solar cells by a rational rather than a trial-and-error approach. Finally, the stability of the BHJ is limited and, most importantly, the metastability of the active layer morphology needs to be taken into account. An efficient strategy to address this issue will be discussed in the next section.

1.4 Ordered Heterojunctions

Solar cells based on BHJs have clearly displayed the best performance so far. However, their morphology is not ideal and difficult to control.¹²¹⁻¹²⁴ The average domain size can be optimized by appropriate preparation protocols, but larger domains that trap excitons and isolated domains that trap free charges cannot be excluded. Moreover, charge percolation pathways to the electrodes are not direct,^{125,126} which favors non-geminate recombination. Additionally, BHJs have metastable morphologies and tend to evolve toward macroscopic demixing. One way to address the stability issue and, at the same time, control the formation of a well-ordered morphology is to covalently link the donor and acceptor components. This prevents macrophase separation and results in the formation of domains with sizes commensurate with the length of the constituting components, i.e., typically on the order of a few to dozens of nanometers. With the macrophase separation suppressed, such materials are self-structuring through microphase segregation. The thermodynamically stable morphology is periodically nanostructured, and its pattern can be controlled by choosing an appropriate molecular design. Since only one molecule comprising both donor and acceptor groups is used instead of a blend of two components, the resulting solar cells are often referred to as single-component organic solar cells.^{127,128}

1.4.1 Block Copolymer Single Component Organic Solar Cells

Block copolymers (BCPs) are well known for their ability to form periodic structures on the nanometer scale via microphase segregation,¹²⁹ and their application in organic photovoltaics has been widely reviewed.^{91,130-133} It is noteworthy that donor-acceptor block copolymers are different from donor-acceptor alternating copolymers that were introduced in Section 1.3 as low-bandgap polymers. The former are simply the result of covalently linking a donor and an acceptor polymer, and π -conjugation is not necessarily continuous. By contrast, the latter are π -conjugated through all donor and acceptor units of the backbone, and the donor and acceptor components are too small to undergo phase segregation. Moreover, these polymers typically retain their donor character, and are therefore used in combination with additional acceptor components.

The first donor-acceptor block copolymer designed for photovoltaic applications was prepared by Hadziioannou and coworkers.¹³⁴⁻¹³⁶ This rod-coil BCP consisted of a poly(phenylene vinylene) as the donor segment and a poly(styrene) segment containing pendant fullerenes as the acceptor block (Figure 19). AFM imaging on thin films cast from dichlorobenzene revealed nanostructured and elongated domains with widths of about 15 nm. Although no conversion efficiency was determined, the comparison between solar cells made from this block copolymer and a reference blend containing the two parent homopolymers as the active layer clearly showed the advantage of covalently binding donor and acceptor, as the J_{SC} of the copolymer was increased by a factor of 40.

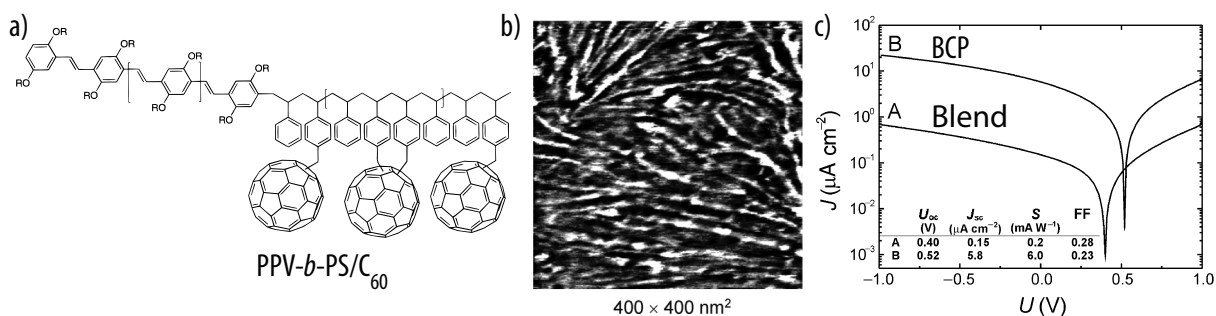


Figure 19. The first donor acceptor BCP designed for photovoltaics showed better performance than a blend of the parent homopolymers. *a)* Chemical structure of the BCP. *b)* Tapping-mode AFM imaging revealed a nanomorphology with domains of about 15 nm width. *c)* J - V curves and performance of solar cells made from either the BCP as a single component or a blend of the corresponding homopolymers; the cell made from the BCP had a largely increase J_{sc} . Figure adapted from references 134,136.

Hashimoto *et al.* prepared a donor-acceptor rod-rod block copolymer based on the successful P3HT/PCBM combination (Figure 20).¹³⁷ They synthesized a P3HT block by quasi-living polymerization and further polymerized a bromoalkyl-substituted thiophene. The bromide was converted to an azide onto which they could subsequently attach a fullerene derivative by ‘click chemistry’. Single component solar cells made from this block copolymer showed a significantly improved PCE of 1.7%, compared to the PCE of 0.48% for the related random copolymer (Figure 20c). This was explained by the formation of domains of about 20 nm in size that were observed by AFM and presumably provided charge percolation pathways to the electrodes (Figure 20b). No such domains were observed in the case of the corresponding random copolymer. In addition, the authors studied the stability of their single component cell compared to a regular P3HT:PCBM BHJ that was prepared under similar conditions. The photovoltaic performance of the BCP solar cell was stable over 80h at 130°C, while the performance of the P3HT:PCBM blend degraded by a factor of three after annealing for 10 min at the same temperature (Figure 20d). The rapid deterioration was explained by the formation of large domains of dozens of micrometers in size, as observed by optical microscopy (Figure 20e).

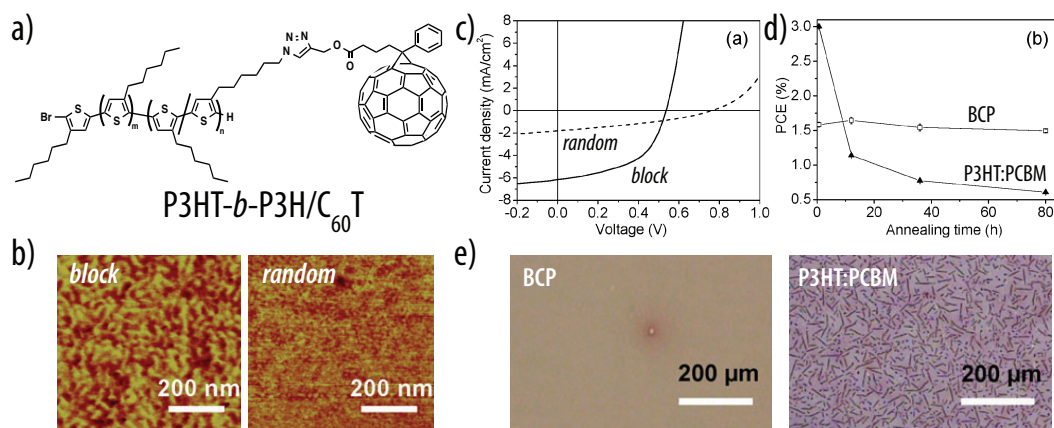


Figure 20. Block copolymer single component solar cells are typically more stable than BHJ cells. *a)* Chemical structure of the investigated BCP. *b)* AFM phase image of the BCP (left) showed elongated domains about 20 nm in width that were absent in the case of the corresponding random copolymer (right). *c)* Accordingly, solar cell performance of the BCP surpassed that of the random copolymer. *d)* Cells made from the BCP were more stable than P3HT:PCBM BHJ cells. *e)* Optical microscopy revealed that the BCP (left) remained unaltered during annealing, while the P3HT:PCBM blend formed micrometer long aggregates. Figure adapted from reference 137.

Before pursuing the discussion, a second digression is made here for the purpose of filling space and improving the overall layout. On this occasion, I would like to briefly introduce the novel written by Lewis Carroll in 1865 and entitled *Alice in Wonderland*, or more accurately, *Alice's Adventures in Wonderland*. It tells of a girl named Alice falling through a rabbit hole into a fantasy world populated by peculiar, anthropomorphic creatures. Its narrative course and structure, characters and imagery have been enormously influential in both popular culture and literature, especially in the fantasy genre. The tale plays with logic, giving the story lasting popularity with adults as well as with children. It is considered to be one of the best examples of the literary nonsense genre, which is a broad categorization of literature that uses sensical and nonsensical elements to defy language conventions or logical reasoning. The 1951 film version of *Alice in Wonderland* in traditional animation from Walt Disney Animation Studios is probably the most well known of the Alice film adaptations, and certainly one of Disney's greatest classics. Interestingly, this 13th in the Walt Disney Animated Classics series contained several additional elements from *Through the Looking-Glass*, in which Lewis Carroll told more adventures of Alice climbing through a mirror into the world that she can see beyond it.

More recently, Gomez and Verduzco *et al.* synthesized a rod-rod donor-acceptor P3HT-*b*-PFTBT copolymer that resulted in a cell reaching a PCE of 3.1%, one of the highest reported PCEs among single component solar cells (Figure 21).¹³⁸ The energy difference between the HOMO level of P3HT and the LUMO level of PFTBT allowed for a high V_{oc} of more than 1 V. The reference cell made from a P3HT:PFTBT blend exhibited a lower initial PCE that decreased further upon annealing at 165°C. By contrast, a single component cell made from P3HT-*b*-PFTBT had a higher initial PCE that further improved after the same annealing procedure. Resonant soft

X-ray scattering and GIXS of films of the P3HT-*b*-PFTBT polymer revealed a lamellar nanostructure with a periodicity of about 16–18 nm in which the PFTBT blocks were amorphous and the P3HT blocks were crystalline with a face-on orientation beneficial for hole conduction to the electrode.

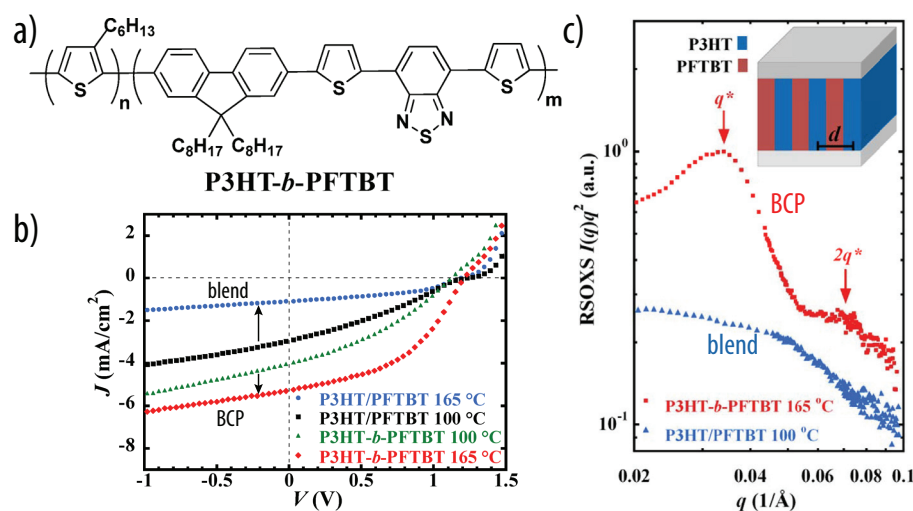


Figure 21. Covalently binding donor and acceptor blocks improved the molecular orientation, the phase morphology, and the stability. *a)* Molecular structure of P3HT-*b*-PFTBT. *b)* Before annealing, the block copolymer (BCP) had better solar cell performance than a blend of the parent homopolymers; upon annealing, the blend's performance worsened and that of the BCP improved. *c)* Resonant soft X-ray scattering revealed lamellar structures with a periodicity of 16–18 nm ($q^* = 0.035 \text{ \AA}^{-1}$) that were not observed for the blend. Figure adapted from reference 138.

According to the selected examples, covalently binding donor and acceptor polymers is an efficient strategy for obtaining an active layer with a stable internal structure. Moreover, this approach allowed for a controlled formation of domains with sizes that are commensurate with the exciton diffusion length. Block copolymer single component solar cells did not have PCEs surpassing those of polymer:fullerene BHJs so far, likely suffering from the absence of any fullerene derivative. However, among all-polymer solar cells, block copolymers clearly exhibited an improved performance compared to cells fabricated from blends.

1.4.2 Small-Molecule Single-Component Solar Cells

The small molecule counterparts of BCPs, i.e. donor-acceptor multiads have been investigated with the purpose of preparing “ideally ordered” heterojunctions. In this case, covalently linking donor and acceptor groups results in a complete molecular mixing of both components, similar to the intermixed phase of bulk heterojunctions. Whereas the domain sizes were on the order of dozens of nanometers for the BCPs described in the previous section, these features were reduced to a few nanometers for small-molecule dyads or triads. As a consequence, excitons are inherently formed in close proximity to a p-n interface and the diffusion step is suppressed, like in the mixed phase of BHJs. Although such narrow domains might disfavor charge separation vs.

In 2011, Geng *et al.* employed a liquid-crystalline oligo(flucorene-*alt*-bithiophene)-perylene dyad and obtained the record PCE of 1.75% for single component solar cell at that time (Figure 23).¹⁴⁰⁻¹⁴² They proved the formation of lamellar structures by TEM imaging, electron, and X-ray diffraction (XRD), and reached the highest PCE after solvent vapor annealing. Upon excitation of the donor at 400 nm, TA spectroscopy confirmed the formation of a new species that was attributed to the CT state, which subsequently recombined. In thin-films, the CT state formation was faster and the recombination was slower since the charges could delocalize within the aggregates. More recently, Geng's group modified the original dyad by adding a spacer between the donor and acceptor units so as to accommodate for differences in packing constraints. Moreover, incorporating a benzothiadiazole unit within the donor lowered the bandgap and extended the solar spectrum coverage.¹⁴³ This led to a PCE of 2.7%, proving that careful molecular design is the key to better efficiencies.

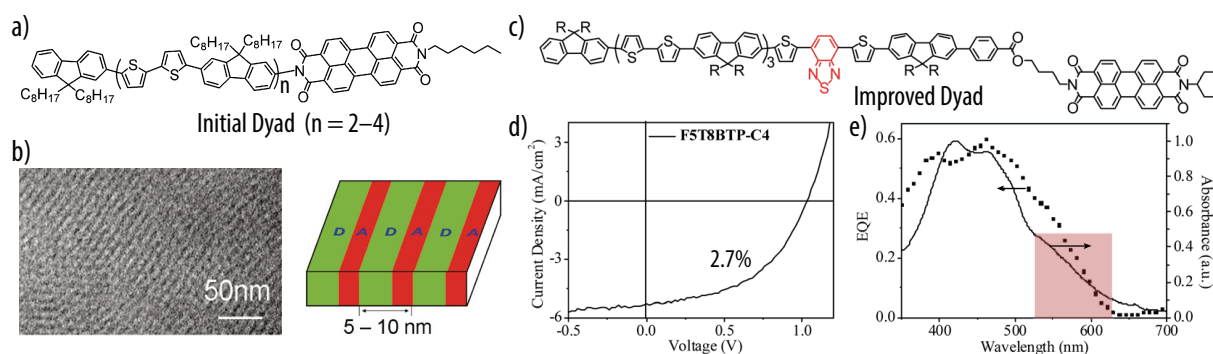


Figure 23. Geng and coworkers prepared a dyad that showed one of the best PCEs reported for small molecule single component solar cells. *a)* Chemical structure of the initial series of dyads. *b)* Selected TEM image and schematic representation of the obtained lamellar phase. *c)* The initial molecular design was improved by adding a butyl spacer and a benzothiadiazole moiety. *d)* *J-V* curve of the improved solar cell. *e)* External quantum efficiency and absorption spectra of the improved dyad; region of increased absorption highlighted in color. Figure adapted from references 142,143.

Inspired by this success, Méry *et al.* presented an extensive XRD and TEM study on the thin film morphology and molecular packing of a series of dyads and triads based on perylene bisimide and donor groups similar to those used by Geng (Figure 24).¹⁴⁴ In particular, they showed that placing the perylene bisimide unit at the end of the molecule in the dyads **AD_n** and triad **ADA** allowed for the compensation of a large difference in cross-sectional area between the donor and acceptor moieties as interdigitated stacks of perylene bisimides could be formed (Figure 24c, left & middle). On the contrary, if the perylene moiety was in the center of the triads **D_nAD_n**, the larger cross-section of the end block disturbed the stacking and decreased the long-range order in the lamellae (Figure 24c, right). These findings highlighted the importance of molecular geometry considerations for the packing of the molecule and the influence on the electronic properties of the resulting materials.

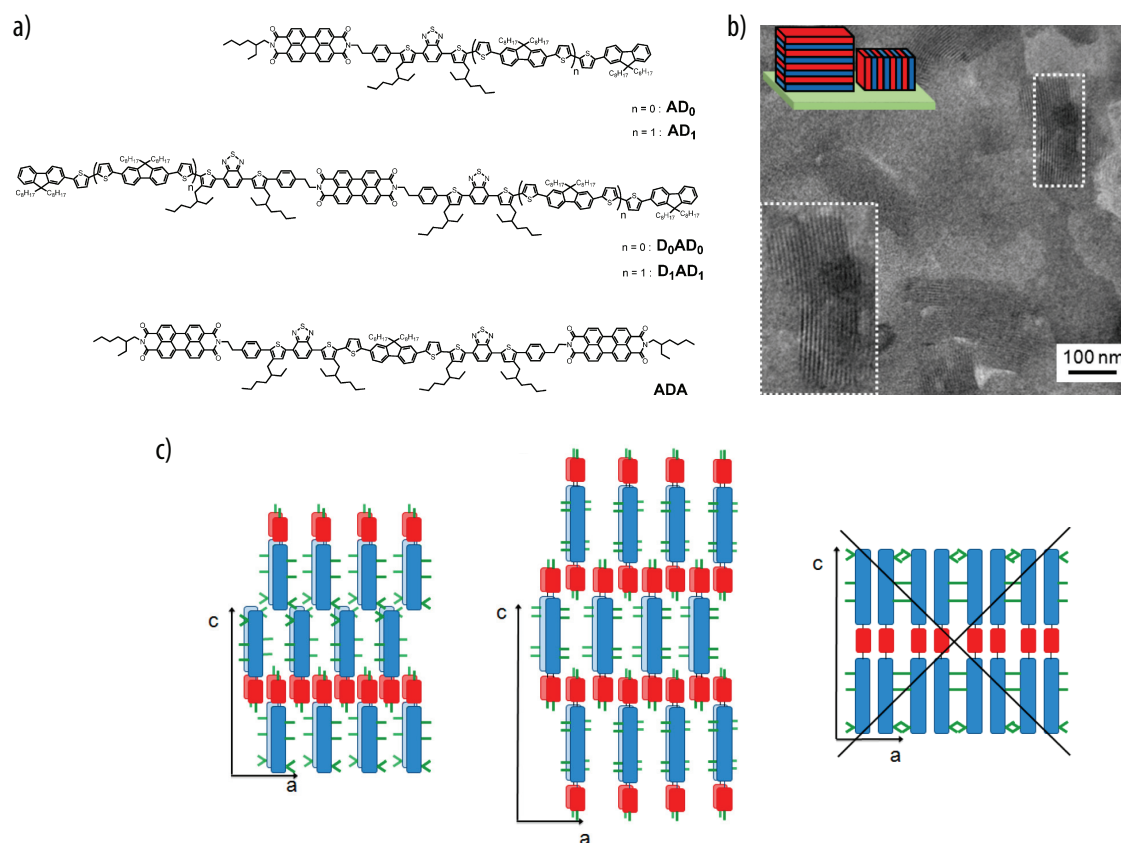


Figure 24. Méry *et al.* investigated the molecular arrangement of a series of dyads and triads towards photovoltaics. *a)* Chemical structure of the investigated AD_n , D_nAD_n , and ADA multiads. *b)* Selected TEM image of an AD_0 thin film showing the lamellar phase oriented face-on and edge-on. *c)* Schematic representation of possible molecular arrangements of the dyads (left) and the ADA triad (middle) showing interdigitated stacks of perylene acceptors, which was not possible for the DAD triads (right). Figure adapted from reference 144.

In conclusion, covalently binding donor and acceptor moieties in small-molecule multiads is the key to the formation of a well-ordered heterojunction with an ideal morphology that maximizes the donor/acceptor interface and provides direct charge percolation pathways for the charges to the electrodes. The covalent bond inherently improves charge separation, but, at the same time, inevitably promotes unfavorable recombination processes. This is particularly true when a large number of defects are present that can immediately trap the formed charges. These issues may explain the lingering PCEs of single component solar cells with a highest reported value of around 3%, compared to the PCEs of BHJ solar cells of above 10%.

1.5 One-Dimensional Nanowires in Organic Photovoltaics

Most approaches that utilized covalently linked donor and acceptor groups aimed at 2D lamellar structures to achieve ordered heterojunctions. On the other hand, nanowires are examples of 1D nanostructures that provide an increased interface per volume, can insure charge percolation pathways, and may exhibit additional properties due to quantum effects arising from the nanoscopic confinement.¹⁴⁵⁻¹⁴⁷

Reports where nanowires are employed in organic solar cells remain scarce. However, the well-known P3HT:PCBM bulk-heterojunction described in Section 1.3 relies in fact on the formation of 1D fibrillar P3HT crystallites. Guillerez *et al.* tried to exploit this particular feature by preparing P3HT fibers via simple thermal annealing in *p*-xylene solution and removal of the non-crystallized polymer by centrifugation and filtration (Figure 25).¹⁴⁸ Scanning electron microscopy (SEM), AFM, and XRD confirmed the presence of fibrils with lengths of 0.5–5 μm and uniform widths of 30–50 nm. Absorption spectra of blends of the fibrils with PCBM showed the characteristic fine structure of nanostructured P3HT, proving that PCBM did not disturb the crystalline arrangement. A series of solar cells were prepared from mixtures of nanostructured and amorphous P3HT that were blended with PCBM. The cell performance increased with an increasing ratio of nanostructured vs. amorphous P3HT up to a ratio of 3:1. More specifically, the J_{SC} increased, most probably due to a better hole transport through the network of nanofibers. These findings demonstrated the significance of the 1D aggregates. However, the PCE of the investigated cells decreased upon further increasing the amount of 1D-nanostructured P3HT to almost 100%. Hence, the presence of amorphous P3HT is essential, as it presumably serves to interconnect the fibers and allows for a mixing with the PCBM, in analogy to the three-phase systems in BHJs presented in Section 1.3.2.

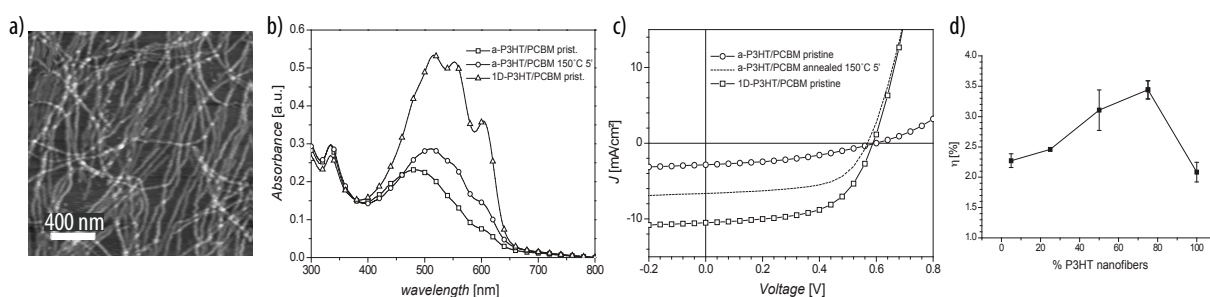


Figure 25. One-dimensional nanofibrils formed from P3HT played a crucial role for the photovoltaic performance. *a)* AFM height image showing micrometer long fibrils with widths of 30–50 nm. *b)* Absorption spectra of a pristine amorphous P3HT:PCBM blend, the same blend annealed 5 min at 150°C, as well as a pristine nanostructured P3HT:PCBM blend; nanostructured P3HT showed a characteristic fine structure in the absorption spectra. *c)* J - V curves of the solar cells corresponding to the blends described in *b)*; the highest performance was obtained with 1D nanostructured P3HT. *d)* PCEs of P3HT:PCBM solar cells with varying amount of 1D nanostructured crystallites within the P3HT phase. Figure adapted from reference 148.

Very similar investigations with poly(3-butylthiophene) (P3BT) were carried out by Jenekhe and coworkers.¹⁴⁹ Although P3BT has a chemical structure very similar to P3HT, its poor solubility and low crystallinity is thought to be the reason for the significantly lower PCE values typically obtained with comparable cells. However, P3BT nanowires prepared by a protocol similar to Guillerez's showed a two orders of magnitude increase in the field effect mobilities when compared to amorphous P3BT. The utilization of these nanowires resulted in solar cells with PCEs of 3%, as high as for a P3HT:PCBM BHJ reference cell. These results show that P3BT

can perform as well as P3HT and serve to demonstrate the importance of a suitable nanostructure.

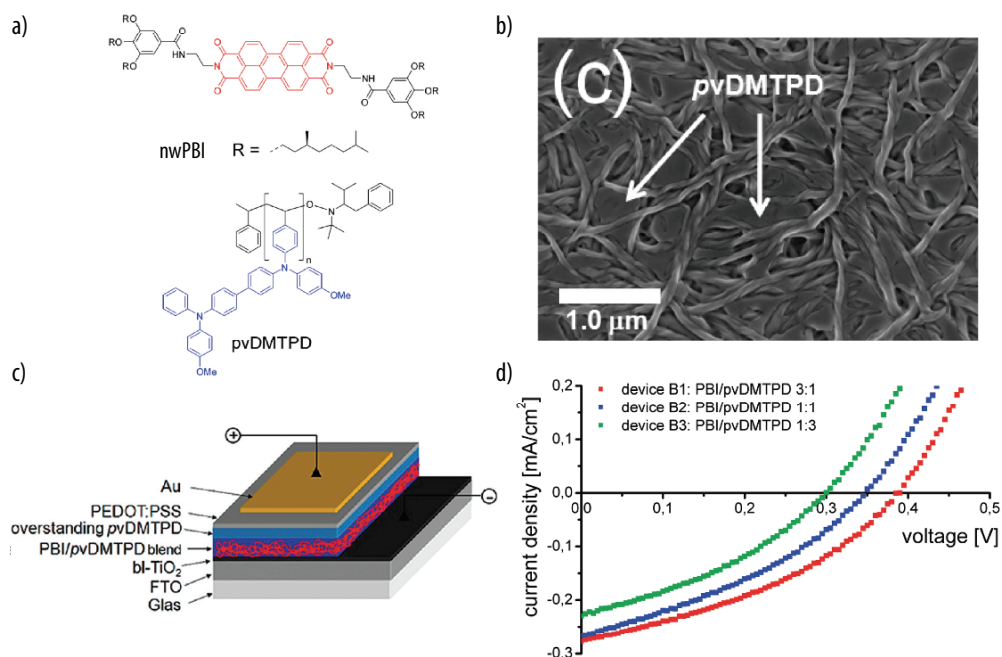


Figure 26. Nanowires consisting of a single-stack of perylene bisimides in a matrix of an amorphous donor polymer were employed in solar cells. *a)* Chemical structures of the nanowire forming perylene bisimide (top) and the donor polymer (bottom). *b)* SEM image of a blend showing the acceptor nanowires and the donor matrix. *c)* Employed device architecture. *d)* *J-V* curves of solar cells with various blend ratios. Figure adapted from reference 150.

Another example for the use of 1D nanostructures was reported by Würthner, Thelakkat, and coworkers.¹⁵⁰ They synthesized a perylene bisimide derivative with hydrogen-bond forming substituents that was designed to self-assemble into well-defined nanowires comprising a single-stack of the chromophore (Figure 26). The formation of long nanowires in solution lead to organogels that were mixed with an amorphous triarylamine based hole-transporting polymer to form bulk heterojunctions by deposition through doctor blading. The best PCE of 0.04% was obtained with an acceptor/donor ratio of 3:1.

Unlike molecules with extended aromatic systems such as perylenes, hexabenzocoronenes, or porphyrins that readily form 1D aggregates by face-to-face stacking, calamitic (linear rod-like) aromatic systems such as acenes, oligophenylenes, or oligothiophenes tend to form 2D aggregates with a herringbone arrangement of the chromophores. However, Frauenrath *et al.* developed a method to prepare nanowires comprising cofacially stacked linear aromatic cores by functionalization of both ends with polymer-oligo(L-alanine) conjugates.^{151,152} Indeed, short oligopeptide segments are known to aggregate by hydrogen-bonding and form 1D extended β -sheets, which guided the aggregation of the central core into 1D fibrils. The terminal polymer chains served to solubilize the aggregates in organic solvents with a low polarity, in which the hydrogen-bond strength was increased.

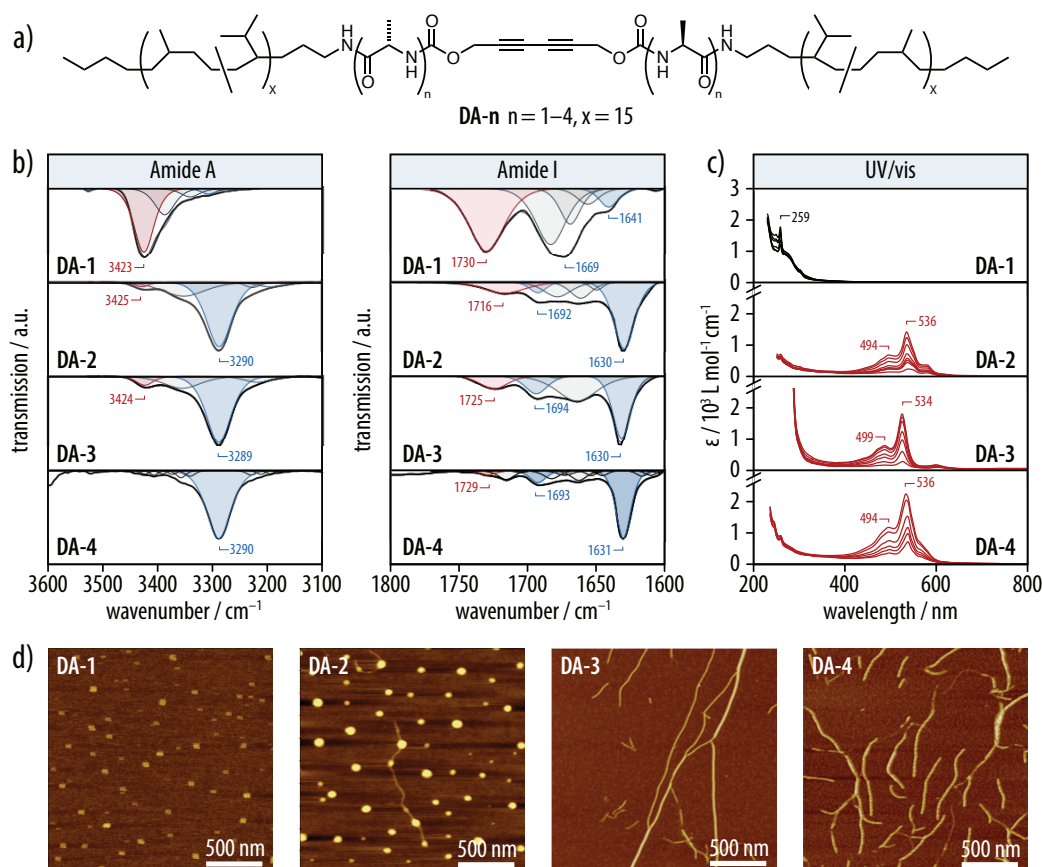


Figure 27. Polymer-oligopeptide conjugates allowed for the formation of 1D nanowires by solution-phase self-assembly. *a)* Chemical structure of the series of nanowire-forming diacetylene derivatives **DA-n**. *b)* From the peaks at 3290 and 1630 cm⁻¹, solution phase IR spectroscopy confirmed the formation of parallel β -sheets for derivatives bearing sequences of two or more alanines. *c)* Accordingly, UV/vis spectra of **DA-2** to **DA-4** showed a diacetylene polymerization in TCE solutions ($c = 1$ mg/mL) upon UV irradiation for up to 150 min, while **DA-1** did not polymerize. *c)* AFM height images of samples prepared by spin coating TCE solutions onto SiO₂ substrate ($c = 10^{-5}$ mol/L); **DA-3** and **DA-4** formed several micrometers long nanowires, while **DA-1** did not; nanowires from **DA-2** were likely degraded in the course of sample preparation. Figure adapted from reference 151.

The initially investigated derivatives contained a central diacetylene unit that served as a probe for the formation of well-ordered aggregates. Thus, topochemical polymerization of the diacetylene core into poly(diacetylene) was only possible when precise packing requirements were met (Figure 27).¹⁵¹ In order to determine these parameters, a series of nanowire-forming diacetylene derivatives with varying polymer and oligo(L-alanine) lengths was studied by solution phase IR spectroscopy, diacetylene polymerization under UV illumination, and AFM imaging. For sufficiently long oligopeptide segments, IR spectroscopy indicated the formation of parallel β -sheet aggregates with two characteristic peaks at 3290 and 1630 cm⁻¹ (Figure 27b). Accordingly, irradiation with UV-light induced the polymerization of the diacetylene core that was observed by absorption spectroscopy (Figure 27c). Hence, nanowires with a high degree of internal order were present in solution even before polymerization as evidenced by AFM imaging except for nanowires from the dialanine derivative that supposedly disassembled on the SiO₂ substrate during sample preparation (Figure 27d). Variation of the polymer length

revealed that a maximum degree of polymerization of 20 was needed to induce aggregation into nanowires with a high degree of internal order.

This method for the formation of nanowires was universal regarding the nature of the π -conjugated chromophore, and the replacement of the diacetylene core by a quaterthiophene or a perylene bisimide also resulted in the formation of well-defined nanowires. Their structure was studied in detail by spectroscopy, AFM, XRD, and computational modeling (Figure 28). The oligo(L-alanine) segments were shown to adopt a right-handed helical conformation, which in turn induced a left-handed helix sense in the resulting β -sheet. The supramolecular helicity of the nanowire together with the peripherally attached polymer segments was responsible for the prevention of lateral interactions of the stacked cores. By injecting a solution of nanowires into a non-solvent, the authors obtained microfibers consisting of aligned arrays of the nanowires. XRD served to elucidate the arrangement of each segment within the fibrils. Hence, in order to accommodate the π - π stacking distance of about 3.4 Å and the hydrogen-bonding distance of about 4.6 Å, the chromophore and the oligopeptide segments were oriented at angles of about 48° and 90° with respect to the nanowire axis, respectively (Figure 28b). This was only possible thanks to the short alkyl spacer between the two segments. Consequently, the synergistic π - π stacking and hydrogen-bonding tightened the packing as evidenced by XRD.

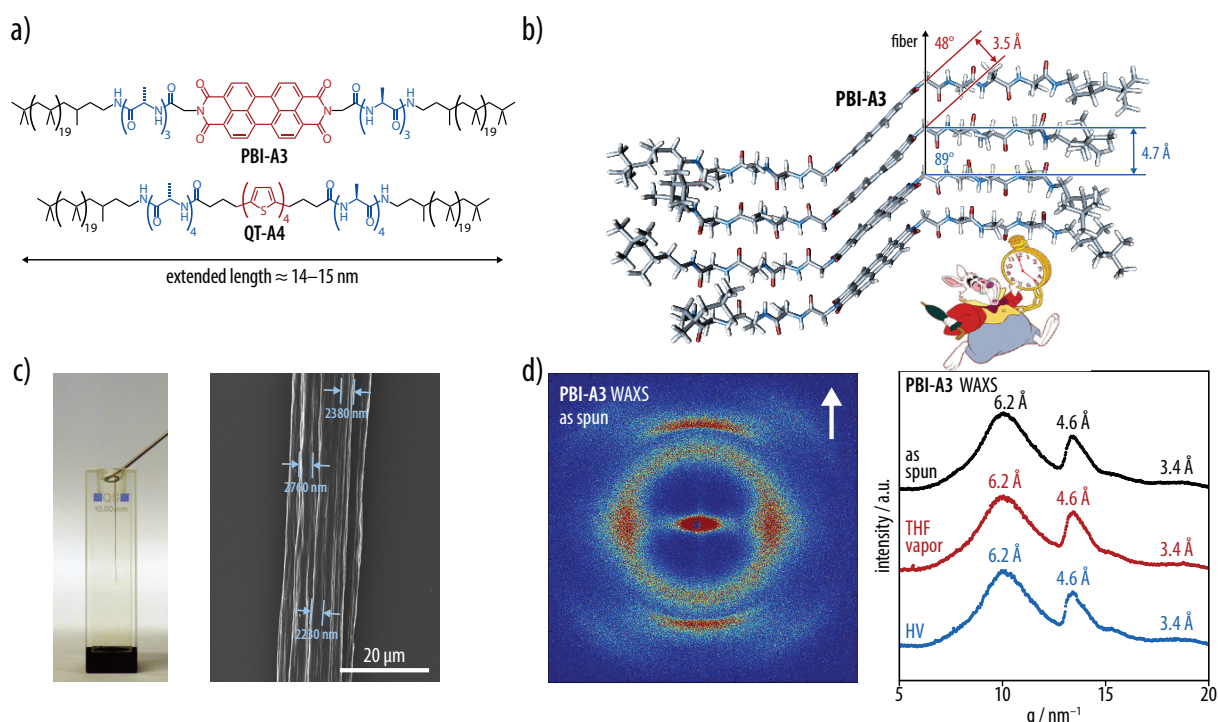


Figure 28. Replacement of the central core allowed for a universal nanowire formation with various chromophores. *a)* Chemical structures of nanowire-forming perylene bisimide **PBI-A3** and quaterthiophene **QT-A4**. *b)* Molecular packing deduced from XRD and computational modeling. *c)* Preparation of the microfibers (left) comprising arrays of aligned nanowires as shown on an SEM image (right). *d)* X-ray diffractogram of **PBI-A3** (left) and corresponding integrated radial profile (right) showing a polymer distance of 6.2 Å, hydrogen bonding distance of 4.6 Å, and π - π stacking distance of 3.4 Å. Figure adapted from reference 152.

Such well-defined nanowires that comprise a single stack of chromophores at their core without lateral interactions provide an excellent subject for the study of charge generation and transport under nanoscopic confinement. Thus, nanowires based on the electron-rich quaterthiophene exhibited a spontaneous formation of polaron-like radical cations with impressively high charge carrier densities of up to 10^6 cm^{-1} and lifetimes of several days (Figure 29).¹⁵³ The quaterthiophene core absorbed in the UV/vis region and, following Kasha's exciton coupling model, showed a blue shift of the absorption maxima to 370 nm upon aggregation. Since the chromophores stacked in a helical fashion, CD-spectroscopy showed a typical bisignate signal with a zero-crossing at the maximum absorption wavelength. Moreover, two additional absorption peaks were observed in the NIR region at about 750 nm and 1200 nm with intensities of around 1% of the main peak. Those features were attributed to delocalized quaterthiophene polarons, as was confirmed by ESR spectroscopy. Finally, charge transport was measured in a two-point device and extraordinarily high current densities of up to 10^4 A/cm^2 were estimated from the number of nanowires spanning the channel as determined by AFM. The current decreased drastically for channel lengths above $5 \mu\text{m}$, suggesting that charge transport between nanowires was limited.

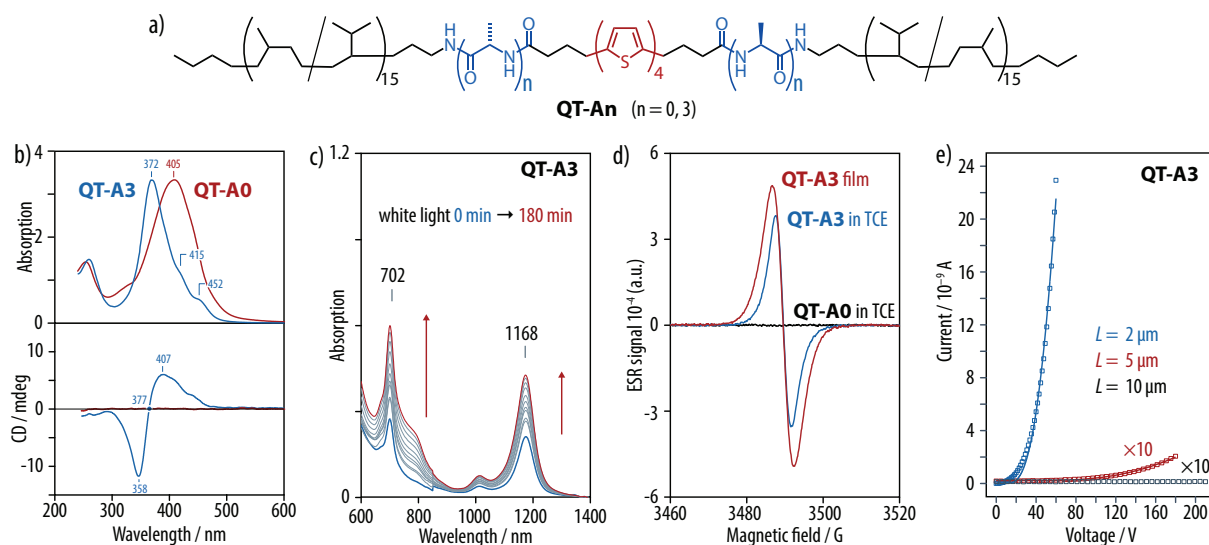


Figure 29. Nanowires made from a p-type quaterthiophene showed spontaneous formation of polarons.¹⁵³ *a*) Chemical structure the nanowire-forming quaterthiophene **QT-A3** and the non-aggregating reference **QT-A0**. *b*) Formation of H-aggregates was associated to a blue shift of the maximum absorption peak (top); the helical aggregates showed a strong bisignate signal in CD-spectroscopy (bottom). *c*) Peaks at 700 and 1200 nm in the NIR were attributed to the formation of quaterthiophene polarons, which could be induced by white light irradiation. *d*) ESR spectroscopy confirmed the presence of quaterthiophene polarons with a g -factor of 2.0024 for the aggregating **QT-A3**; no signal was observed for **QT-A0**. *e*) Two-point devices exhibited high current densities of up to 10^4 A/cm^2 for a channel length of $2 \mu\text{m}$; the much lower current for longer channel length suggested that transport between nanowires was limited.

In conclusion, different from 2D lamellar structures of ordered heterojunctions, a network of 1D nanowires in a matrix seemed to be a viable alternative as active layer for photovoltaics. Indeed, charge percolation pathways to the electrodes, although not direct, are ensured along the

nanowires or through the continuous matrix of the counter component. While nanowires obtained from anisotropic polymer crystallization in solution have been successfully used in solar cells, single-stack nanowires from perylene or quaterthiophene derivatives recently made in our research group appears to be excellent candidates for more fundamental studies on charge generation under nanoscopic confinement.

1.6 Scope and Outline of this Thesis

The promises of organic photovoltaics have stimulated intense and fruitful research efforts over the past years. From the selected examples presented above, it becomes clear that charge generation in organic solar cells is not only governed by the molecular properties and the morphology of the heterojunction. It is also the result of the intricate combination of the detailed energy landscape and the exact molecular arrangement at the interface and in the pure domains. In this regard, the formation of a complex three-phase system in the most prevalent bulk heterojunctions is beneficial for efficient charge generation and extraction, but the kinetic instability of bulk heterojunctions and their optimization based on trial-and-error approaches render more rational approaches desirable. Nevertheless, approaches towards well-ordered heterojunctions that are expected to improve charge generation and collection have so far seen limited success. Apparently, a better understanding of how the different aspects of charge generation and transport are related to structural features on the supramolecular and nanoscopic level is still required.

In the present thesis, we therefore aim to investigate charge generation upon illumination in 1D and 2D organic semiconductor nanostructures. To this end, two different architectures will be investigated: 1D nanowires that consist of single stacks of helically arranged oligothiophenes, as well as a 2D lamellar phase formed by a perylene bisimide/quaterthiophene n-p-n triad. For this purpose, the following research issues need to be addressed:

- The synthesis of highly soluble oligothiophene precursors will allow for the divergent preparation of a library of ter-, quater-, quinque-, sexi-, hepta-, and octathiophenes functionalized with poly(isobutene)-oligopeptide conjugates. These compounds are designed to self-assemble into single-stack nanowires owing to the synergistic π - π stacking and hydrogen-bond interactions in hydrophobic media.
- The nanostructure of the 1D nanowires formed upon self-assembly in organic solvents will be investigated by solution-phase IR, UV-vis, and CD spectroscopy, as well as AFM imaging and X-ray scattering. Moreover, the formation of polaron-like radical cations upon light absorption in solution will be monitored by NIR spectroscopy in order to gain insight into their formation.

-
- The 2D lamellar nanomorphology of the triad will be investigated for oriented thin films by using TEM and electron diffraction. Finally, TA spectroscopy will allow us to elucidate the charge generation upon light absorption and the process of charge recombination in solution and in thin films.

Facile Access to Oligothiophenes via Chlorendic Protecting Groups



2 Facile Access to Oligothiophenes via Chlorendic Protecting Groups

2.1 Introduction

Organic electronic materials from π -conjugated molecules or polymers have become highly relevant for applications in organic field-effect transistors,^{3,4} photovoltaics,^{8,28} light-emitting diodes,⁶ as well as chemical sensors⁷ and other building blocks of nanoelectronic devices.⁵ Materials from oligothiophene derivatives, for example, are among the best-studied p-type organic semiconductors.^{3,154} While the performance of these materials relies on efficient π - π stacking of the constituting molecules in the solid state, these interactions at the same time hamper the synthesis due to the low solubility of the products and intermediates.¹⁵⁵ Therefore, the introduction of flexible, sterically demanding substituents at the π -conjugated core, such as (branched) alkyl chains, dendrons, and polymers is often used to induce entropy-driven solubility.¹⁸ While this facilitates the synthesis and characterization of precursors and products as well as their processing from solution, the presence of bulky or branched substituents may have undesirable effects on the supramolecular arrangement and thus on the desired electric properties of the final materials.^{154,156} Therefore, the preparation of solely end-functionalized oligothiophenes would be desirable, but remains a synthetic challenge.¹⁵⁵ To this end, intriguing synthetic pathways have been developed in recent years, including functionalized molecular precursors of organic electronic materials.^{18,156-165} However, most of the employed syntheses are convergent and, hence, tedious as well as limited in versatility and reaction scale when the preparation of a larger number of similar derivatives is desired.¹⁵⁵

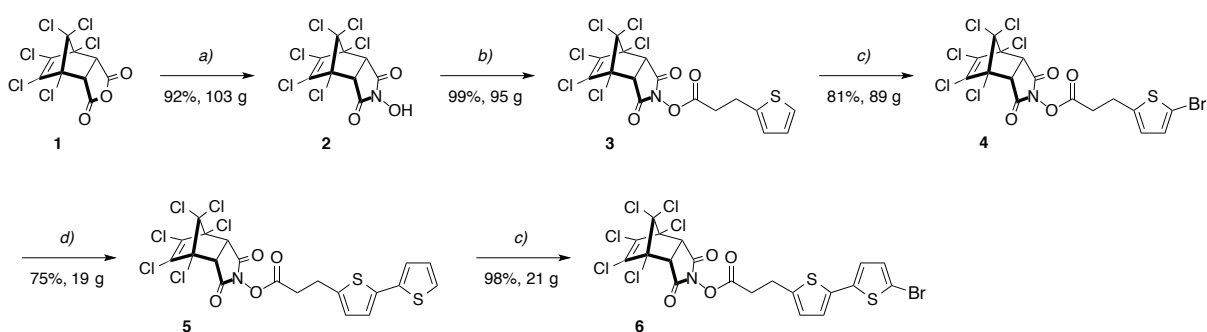
Here, we report a versatile synthetic approach to the divergent synthesis of end-functionalized oligothiophenes on large scales.¹⁵⁵ The developed synthetic pathway relies on the use of chlorendylimidyl esters as novel temporary protecting groups for carboxylic acids. Chlorendic acid derivatives are inexpensive and readily available since they have been widely used as insecticides and fire-retardant additives for polymers.^{166,167} To the best of our knowledge, however, their application in protecting group chemistry has never been investigated. As will be discussed in detail in the following sections, all chlorendylimidyl-protected intermediates and products exhibited a significantly enhanced solubility in organic solvents, as compared to the parent compounds or even some of their alkyl-substituted derivatives. At the same time, the chlorendylimidyl moiety rendered most compounds excellently crystallizable, which allowed us to perform all synthetic steps on the multi-gram scale and purify most products by recrystallization or precipitation, avoiding column chromatography. Single-crystal X-ray structures of various molecules revealed common packing features that might be attributed to

the dominant role of the chlorendylimidyl residue for the crystallization.

We were thus able to prepare chlorendylimidyl-substituted oligothiophenes up to the octamers via straightforward solution-phase synthesis on reaction scales of up to 40 g isolated yields. The protected oligothiophene dicarboxylic acids represent versatile building blocks that can be reacted with a variety of nucleophiles. For the purpose of the present thesis, we readily employed these compounds in the synthesis of amide-substituted terthiophenes, quaterthiophenes, quinquethiophenes, sexithiophenes, heptathiophenes, and octathiophenes that are of interest as materials for organic nanowires.^{151,152,168-170}

2.2 Synthesis of the Oligothiophene Building Blocks

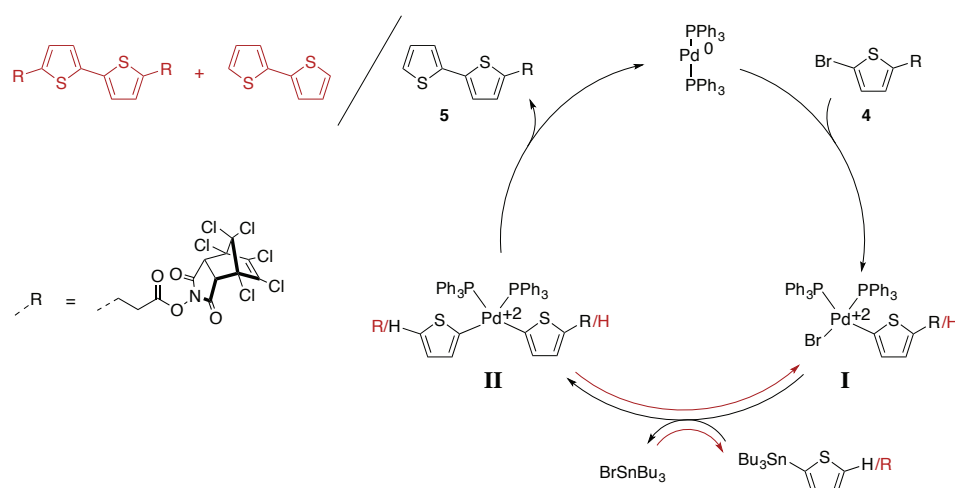
The synthesis of the desired ter-, quarter-, quinque-, sexi-, hepta-, and octathiophene derivatives with chlorendylimidyl active esters as temporary protecting groups started from the inexpensive chlorendic acid anhydride **1** and comprised typical bromination and Stille coupling sequences that served to extend the oligothiophene moiety (Scheme 1).



Scheme 1. Synthesis of the brominated mono- and bithiophene intermediates **4** and **6**. *Reagents and conditions:* a) $\text{H}_2\text{NOH}\cdot\text{HCl}$, K_2CO_3 , water, reflux; b) thiophene-2-propionic acid, EDCI, DPTS, DCM; c) NBS, DMF, r.t.; d) 2-tributyltin-thiophene, $\text{Pd}(\text{PPh}_3)_2\text{Cl}_2$, MeCN, 80°C .

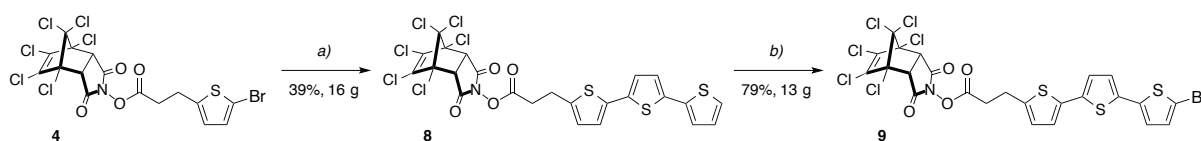
Thus, reaction of chlorendic anhydride **1** with hydroxylamine hydrochloride under basic conditions afforded 103 g (92%) of chlorendyl hydroxylimide **2**. Subsequent esterification of 3-(2-thienyl)propionic acid with **2** promoted by 1-ethyl-3-(3-dimethylaminopropyl)carbodiimide (EDCI) and 4-(dimethylamino)-pyridinium *p*-toluenesulfonate (DPTS)¹⁷¹ resulted in ester **3** in quantitative yield. A bromination/Stille coupling sequence led to the bromothiophene active ester **4** (89 g, 81%) that was converted to the bithiophene active ester **5** (19 g, 75%). During this step, formation of the symmetric bithiophene diester side product was observed (8%), supposedly along with equivalent amount of bithiophene that was removed during solvent evaporation. This formation could be explained by the reversibility of each catalytic step and, more particularly, the transmetallation (Scheme 2). The reverse transmetallation would then be a source of ligand scrambling, so that the subsequent forward reaction would result in the

homocoupling product. In our hands, the diester side product could not be removed by simple recrystallization, and its formation could not be avoided even when changing the catalyst or the reaction conditions. As a consequence, the product was purified by filtration over silica gel, paying attention not to leave the product in contact with the silica for too long and keeping only the first fraction of filtrate. Compound **5** was then brominated to furnish the corresponding bromobithiophene active ester **6** (21 g, 98%).



Scheme 2. Partial formation of homocoupled side products during Stille coupling was rationalized by the reversibility of the transmetalation step (red arrows). During reverse transmetalation, there was no selectivity between both thiophene moieties of complex **II**. The stannyl and Pd catalyst groups were consequently scrambled between both thiophene derivatives. Upon a subsequent forward reaction from complex **I**, the scrambled substituents were transferred on complex **II** and finally formed the homocoupled side product upon reductive elimination.

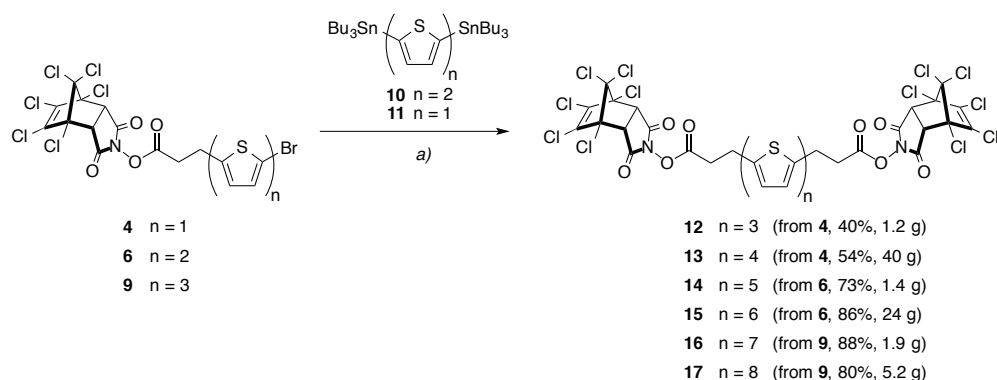
Likewise, Stille coupling of **4** with 5-tri-*n*-butylstannyl-2,2'-bithiophene **7** yielded the terthiophene active ester **8** (16 g, 39%) after filtration over silica gel to remove the quaterthiophene and diester side products (Scheme 3). The terthiophene **8** was then brominated to obtain the bromoterthiophene active ester **9** (13 g, 79%).



Scheme 3. Preparation of the bromoterthiophene intermediate **9**. *Reagents and conditions:* a) 5-tributyltin-2,2'-bithiophene **7**, Pd(PPh₃)₂Cl₂, DMF 100°C; b) NBS, DMF, r.t.

The final oligothiophene active esters **12–17** were prepared by a two-fold Stille coupling of the brominated intermediates **4**, **6**, and **9** to 5,5'-bis(tri-*n*-butylstannyl)-2,2'-bithiophene **10** or to 2,5-bis(tri-*n*-butylstannyl)thiophene **11** for the derivatives with even or odd numbers of thiophene rings, respectively (Scheme 4). Thus, the quaterthiophene active ester **13** was obtained from bromothiophene **4** as a microcrystalline yellow powder in 54% yield on a 40 g scale after precipitation of the crude product from a slurry in diisopropylether/THF/toluene

(3:1:1) and washing with diisopropylether and then pentane. Similarly, Stille coupling to the bromobithiophene **6** furnished the sexithiophene active ester **15** as a microcrystalline orange powder in 86% yield on a 24 g scale after re-suspension in the same solvent mixture and filtration. Then, Stille coupling of the stannylated bithiophene **10** to bromoterthiophene **9** resulted in the octathiophene active ester **17** that was isolated as a red powder in 80% yield on a 5 g scale, after resuspension in toluene and filtration. Next, Stille coupling between the bromoterthiophene **9** and the stannylated monothiophene **11** resulted in the heptathiophene **16**, as a microcrystalline orange-red powder in 88% yield on a 2 g scale after resuspension in toluene and filtration. Last, in order to complete the series, the ter- and quinquethiophene derivatives were prepared in collaboration with Regina Hafner in our group. In this way, the terthiophene active ester **12** was obtained by coupling bromothiophene **4** to **11**. Purification consisted in two precipitations from DCM into heptane and filtration over silica gel to yield the isolated product as a microcrystalline yellow powder in 40% yield on a 1 g scale. Finally, coupling of **6** to **11** afforded the quinquethiophene **14** as a microcrystalline yellow-orange powder in 73% yield on a 1 g scale, after precipitation from THF into diisopropyl ether.



Scheme 4. Synthesis of the oligothiophene active ester precursors **12–17** was facilitated by the chlorendylimidyl protecting group. *Reagents and conditions:* a) Pd(PPh₃)₄, DMF, 80°C.

The use of the chlorendylimide moiety has, hence, enabled us to obtain a range of protected acid-functionalized oligothiophene building blocks on the multi-gram scale (Figure 30).

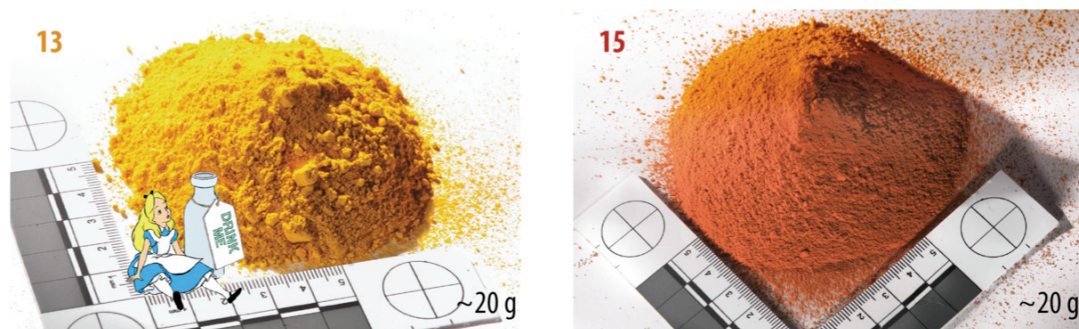


Figure 30. Soluble oligothiophene precursors were prepared on large scales. Photographs of about 20 g of **13** (left) and about 20 g of **15** (right).

Notably, all intermediates and products displayed good to excellent solubility in various organic solvents (Table 1), quite in contrast to other oligothiophene derivatives that typically have solubilities of less than 3–4 g/L (for α -quaterthiophene in CHCl_3).^{172,173} The quaterthiophene **13**, for instance, was soluble in THF or DMSO up to concentrations of $c = 350$ g/L, while up to 1 g/L of the sexithiophene active ester **15** could be dissolved in THF. Even the hepta- and octathiophene active esters **16** and **17** remained sufficiently soluble in several solvents to allow for successful follow-up reactions (see below). Moreover, only two chromatographic purification steps had to be performed since all compounds could be readily precipitated or recrystallized. In this way, we obtained X-ray quality single crystals of intermediates **2–6**, while **8–17** were furnished as microcrystalline powders.

Table 1. The chlorendylimide protecting group resulted in high solubilities of the oligothiophenes (in g/L).

Solvent	heptane	toluene	Et ₂ O	CH ₂ Cl ₂	THF	DMSO
13	0	34	1.3	186	230	350
15	0	0.3	<0.1	0.4	1	0.9
17	0	<0.1	<0.1	<0.1	<0.1	<0.1

2.3 Crystal Structures of the Chlorendylimidyl Esters

The combined high solubility and good crystallizability of the chlorendylimidyl-substituted oligothiophenes allowed for the growth of single crystals of the intermediates **2–6** for structure determination by X-ray diffraction. Recrystallization was carried out from polar mixtures of THF/MeOH 1:10 (**2**) or DCM/MeOH 1:5 (**3–6**). Intermediates **3–6** were also recrystallized from apolar mixtures based on DCM and heptane or diisopropyl ether; the obtained crystal structures were the same, except for compound **4**. As will be described in more detail below, the molecular packing of all analyzed structures revealed the formation of segregated chlorine-rich and thiophene-rich layers, highlighting the role of the chlorendic group in the crystallization process.

The chlorendic hydroxylimide **2** differs from the other intermediates by its strongly polar, hydrogen-bond forming hydroxylimide group, so that cocrystals with two equivalents of water molecules were formed (Figure 31). A layered structure was observed with a hydrophilic, hydrated hydroxylimide layer flanked by two layers of chlorine-rich chlorendic groups. The chlorendic hydroxylimide **2** crystallized in the monoclinic unit cell $P 2_1/c$ with the lattice parameters $a = 15.04$ Å, $b = 8.26$ Å, $c = 12.56$ Å, and $\alpha = \gamma = 90^\circ$, $\beta = 108.9^\circ$.

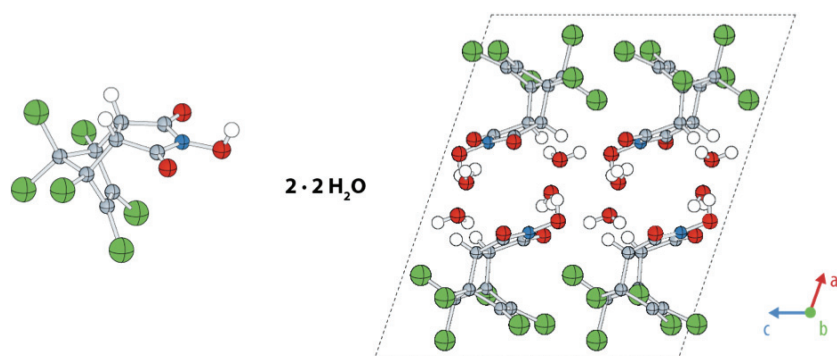


Figure 31. Ball-and-stick representation of the crystal structure of **2**. Detailed view of the 3D molecular structure (left), as well as a view along the *b*-axis displaying the hydrated hydroxylimide and chlorendic layers (right).

With the attachment of the thiophene propionic acid, the monothiophene intermediate **3** showed a less pronounced segregation between the imidyl and the chlorendic moieties, but the chlorine-rich layers were still present (Figure 32). The electron-rich carbons of the thiophene rings interacted with the electron-poor carbons of the imide groups, with C···C short contacts of 3.43 Å, thus forming layers of mingled thiophene and imide groups. The monothiophene-chlorendic conjugate **3** crystallized in the monoclinic unit cell $P 2_1/c$ with the lattice parameters $a = 9.86$ Å, $b = 14.59$ Å, $c = 14.40$ Å, and $\alpha = \gamma = 90^\circ$, $\beta = 96.5^\circ$.

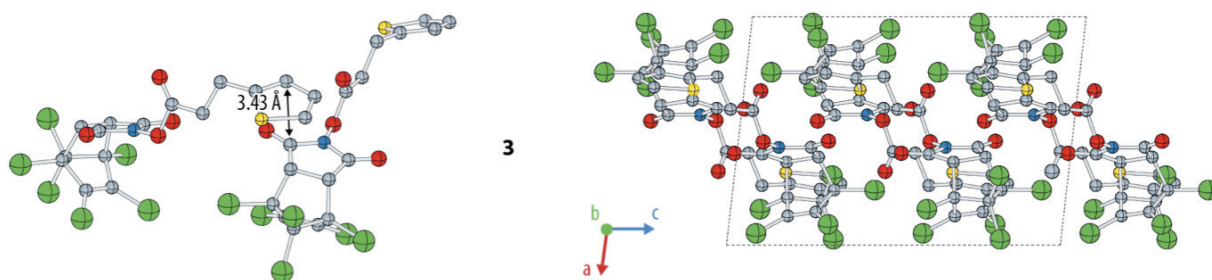


Figure 32. Ball-and-stick representation of the crystal structure of **3**. Detailed view of the imide-thiophene interaction (left), as well as a view along the *b*-axis displaying the chlorine-rich layers (right).

The thiophene bromide **4** crystallized slightly differently from the two solvent mixtures (Figure 33). From the more polar DCM/MeOH 1:5 mixture, it crystallized in the monoclinic unit cell $P 2_1/c$ with the lattice parameters $a = 13.65$ Å, $b = 12.38$ Å, $c = 12.86$ Å, and $\alpha = \gamma = 90^\circ$, $\beta = 95.3^\circ$. The bromines interacted with the imide oxygens with Br···O short contacts of 3.07 Å separating the thiophene ring from the imide moiety such that a thiophene rich layer could be distinguished between chlorendylimide layers, in which the bromine participated. From the rather apolar DCM/heptane 1:10 mixture, compound **4** crystallized in the monoclinic unit cell $P 2_1/n$ with the lattice parameters $a = 9.14$ Å, $b = 14.01$ Å, $c = 17.01$ Å, and $\alpha = \gamma = 90^\circ$, $\beta = 103^\circ$. Similar bromine-imide interactions as before were observed, with Br···O short contacts of 3.33 Å, and thiophene-imide interactions were present with C···N short contacts of 3.22 Å. As a result, chlorine-rich and mingled thiophene-imide-bromine layers were formed.

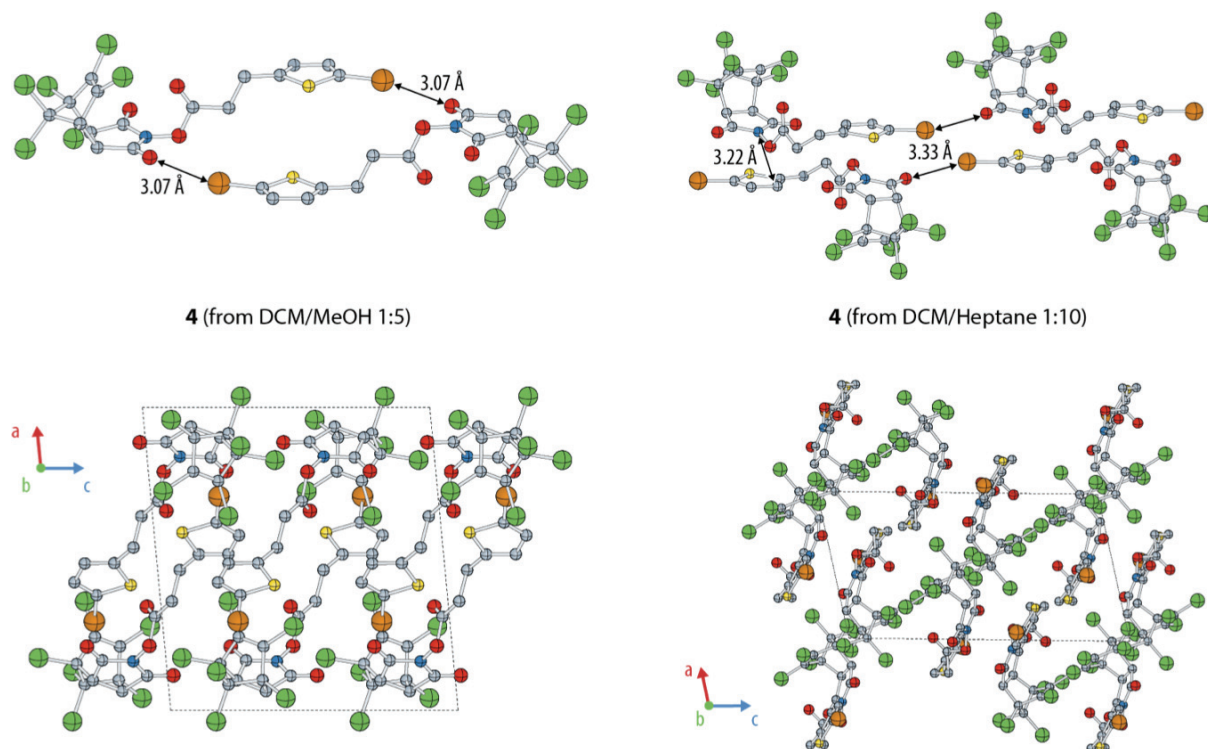


Figure 33. Ball-and-stick representation of the crystal structures of **4**, obtained from polar (left) or apolar (right) solvent mixtures. Detailed view of the bromine-imide and thiophene-imide interactions (top), as well as view along the *b*-axis displaying the halogen-rich layers (bottom).

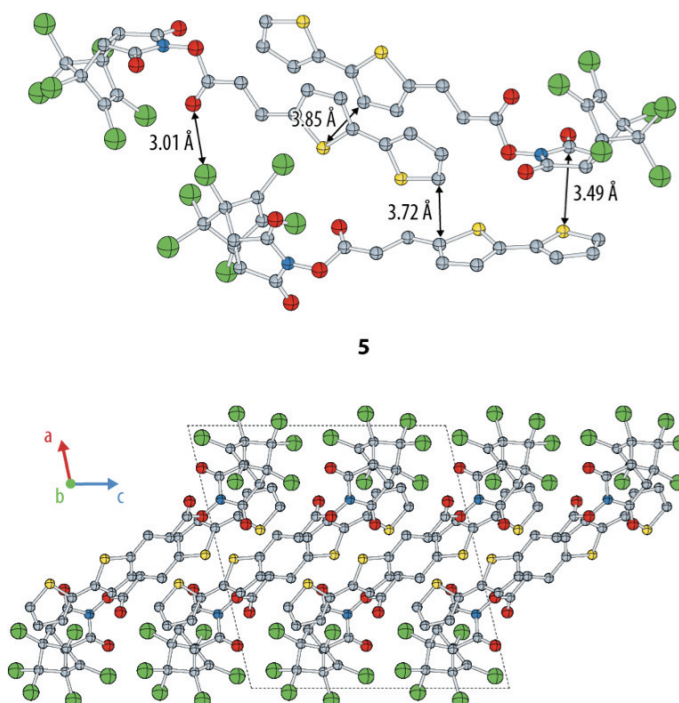


Figure 34. Ball-and-stick representation of the crystal structure of **5**. Detailed view of the thiophene-thiophene and thiophene-imide interactions (top), as well as view along the *b*-axis displaying the chlorine-rich and thiophene-rich layers (bottom).

In the case of the bithiophene derivatives, a clearer segregation was observed between the chlorendic and the thiophene groups, supposedly due to the higher volume fraction of the latter (Figure 34). The bithiophene **5** crystallized in the monoclinic unit cell $P 2_1/c$ with the lattice parameters $a = 14.74 \text{ \AA}$, $b = 11.56 \text{ \AA}$, $c = 14.03 \text{ \AA}$, and $\alpha = \gamma = 90^\circ$, $\beta = 103.6^\circ$. It formed dimers with an interdigitated molecular arrangement and parallel-displaced orientation of the bithiophene moieties with $C\cdots S$ short contacts of 3.85 \AA . The dimers were then arranged in a herringbone fashion with edge-to-face contact of 3.72 \AA . Additionally, thiophene-imide $S\cdots C$ short contacts of 3.49 \AA were observed.

The bromobithiophene **6** crystallized in the monoclinic unit cell $P 2_1/c$ with the lattice parameters $a = 14.52 \text{ \AA}$, $b = 11.64 \text{ \AA}$, $c = 14.88 \text{ \AA}$, and $\alpha = \gamma = 90^\circ$, $\beta = 101.6^\circ$. In this case, the bromine disturbed the arrangement, and $Br\cdots O$ short contacts of 3.08 \AA were formed within the chlorendylimide layers (Figure 35). This resulted in slightly tighter thiophene-thiophene packing as well as thiophene-imide interactions with distances of around 3.5 \AA and 3.29 \AA , respectively.

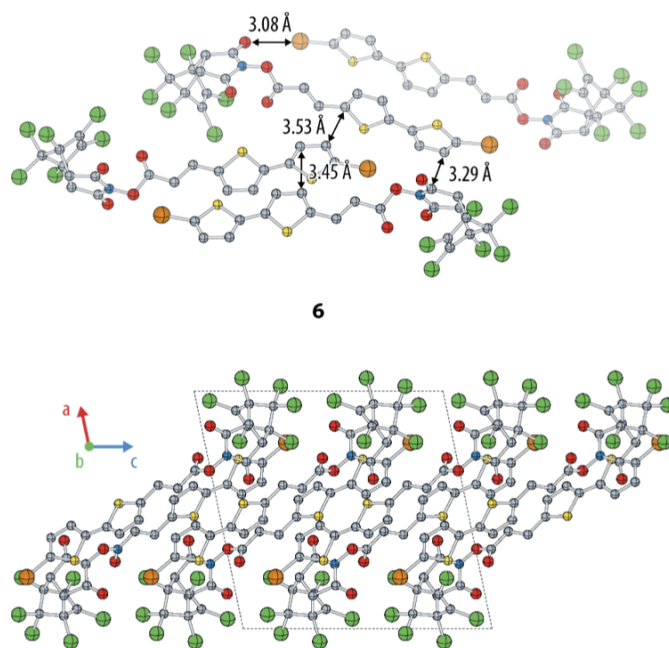


Figure 35. Ball-and-stick representation of the crystal structure of **6**. Detailed view of the thiophene-thiophene, thiophene-imide, and bromine-imide interactions (top), as well as a view along the b -axis displaying the halogen-rich and thiophene-rich layers of the crystal structure (bottom).

The described features allowed us to elucidate the role of the rigid sterically demanding chlorendic group in the crystallization. Most noticeably, the N -chlorendylimide and oligothiophene fragments were always separated into different crystallographic layers. Both bithiophenes adopted a packing reminiscent of a herringbone pattern within their layer, with both edge-to-face and parallel-displaced arrangements resulting in several $C\cdots C$ short contacts of $3.4\text{--}3.6 \text{ \AA}$. More prominently, a face-to-face stacking of one of the electron-rich thiophene

rings with the electron-poor succinyl imide fragment of the *N*-chlorendylimide moiety was encountered in several examples, with a typical C \cdots S short contact of 3.3–3.4 Å between the thiophene sulfur atom and one of the carbonyl carbons of the imide. The close packing of the unsymmetrically substituted oligothiophenes within their layers was achieved by interdigitation, thus accommodating the steric demand of the attached *N*-chlorendylimides with their van der Waals radius of roughly 8 Å. As a result, each oligothiophene layer was flanked by two *N*-chlorendylimide layers and multiple Cl \cdots Cl short contacts of 3.3–3.5 Å, Cl \cdots O short contacts of 2.8–3.1 Å with the imide carbonyl oxygens, as well as O \cdots C short contacts of the latter with the carbonyl carbons of a neighboring chlorendylimide were observed. In the case of the bromothiophene derivatives **4** and **6**, the interdigitation of the oligothiophenes was organized such that the bromine atoms appeared to ‘participate’ in the halogen-rich *N*-chlorendylimide layers, with several Br \cdots Cl short contacts of 3.4–3.6 Å. Moreover, Br \cdots O short contacts of 2.9–3.3 Å were observed with the imide carbonyl oxygens.

In conclusion, the crystal structures corroborated that the sterically demanding chlorendic group was successful in limiting interactions between the oligothiophene segments. At the same time, it apparently facilitated crystallization by introducing numerous chlorine-chlorine interactions that ordered the structures into segregated layers. Compared to typical π - π interactions, the chlorine-chlorine interactions are more easily disrupted by mildly polar solvents, resulting in the observed increase in solubility when compared to unsubstituted thiophene derivatives with comparable core lengths.

2.4 Spectroscopic Properties in Solutions and Thin Films

Since the aggregation of chromophores typically alters the corresponding absorption and emission spectra, UV/vis and fluorescence spectroscopy can provide useful information about the arrangement of chromophores in the solid state. Normalized UV/vis spectra of the oligothiophene active esters **5**, **8**, **13**, **15**, and **16** in THF solutions at concentrations of up to $c = 0.5$ mmol/L showed absorption maxima at 309, 360, 401, 440, and 453 nm respectively (Figure 36). This was in excellent agreement with the absorption spectra expected for molecularly disperse bi-, ter-, quarter-, sexi-, and heptathiophenes.^{165,174} The corresponding fluorescence emission spectra in solution exhibited well-defined bands with Stokes shifts on the order of 60–75 nm and maxima at 370, 435, 460, 511, and 527 nm. All these values were similar to those previously reported for molecularly disperse solutions of such compounds.¹⁷⁴ Moreover, the emission spectra did not change in shape for different excitation wavelengths, proving that these absorption peaks originated from a single species in each case.

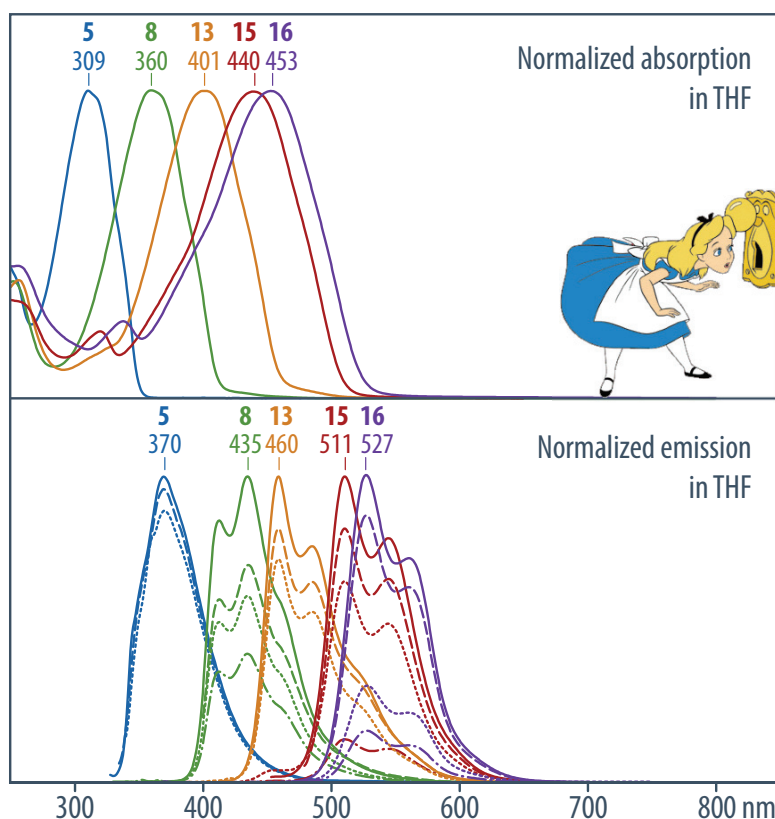


Figure 36. Absorption (top) and fluorescence (bottom) spectroscopy confirmed the presence of molecularly disperse solutions of bi-, ter-, quarter-, sexi-, and heptathiophene **5**, **8**, **13**, **15**, and **16** in THF. The fluorescence emission spectra did not change with excitation wavelength proving they originated from single species. The emission spectra were measured at the following excitation wavelengths (in the order of decreasing emission intensity): **5** (313, 300, 325 nm), **8** (360, 390, 330, 320 nm), **13** (400, 425, 375 nm), **15** (439, 465, 410, 320 nm), **16** (452, 490, 390, 335 nm).

Additionally, measurements of the UV/vis absorption spectra of **13**, **15**, and **16** for a broad range of concentrations did not show any appearance of new bands or a shift of the absorption bands (Figure 37a–c). The band intensities followed Lambert-Beer’s law up to concentrations of at least 6 mmol/L for compound **13**, 0.7 mmol/L for compound **15**, and 0.1 mmol/L for compound **16**. This corroborated that the molecules did not aggregate in the investigated concentration ranges. UV/vis and fluorescence spectroscopy were also carried out with thin films that were cast from organic solvents onto fused silica substrates (Figure 37d–f). The spectra clearly showed that the active esters **13**, **15**, and **16** gave rise to spectroscopic aggregates in the solid state. For instance, the absorption maxima were significantly blue-shifted in the solid state, the sexithiophene **15** as well as the heptathiophene **16** exhibited a vibronic fine structure, and all fluorescence emission spectra experienced a drastic red-shift of up to 130 nm compared to the solution-phase spectra. Nevertheless, all compounds retained some fluorescence in the solid state.

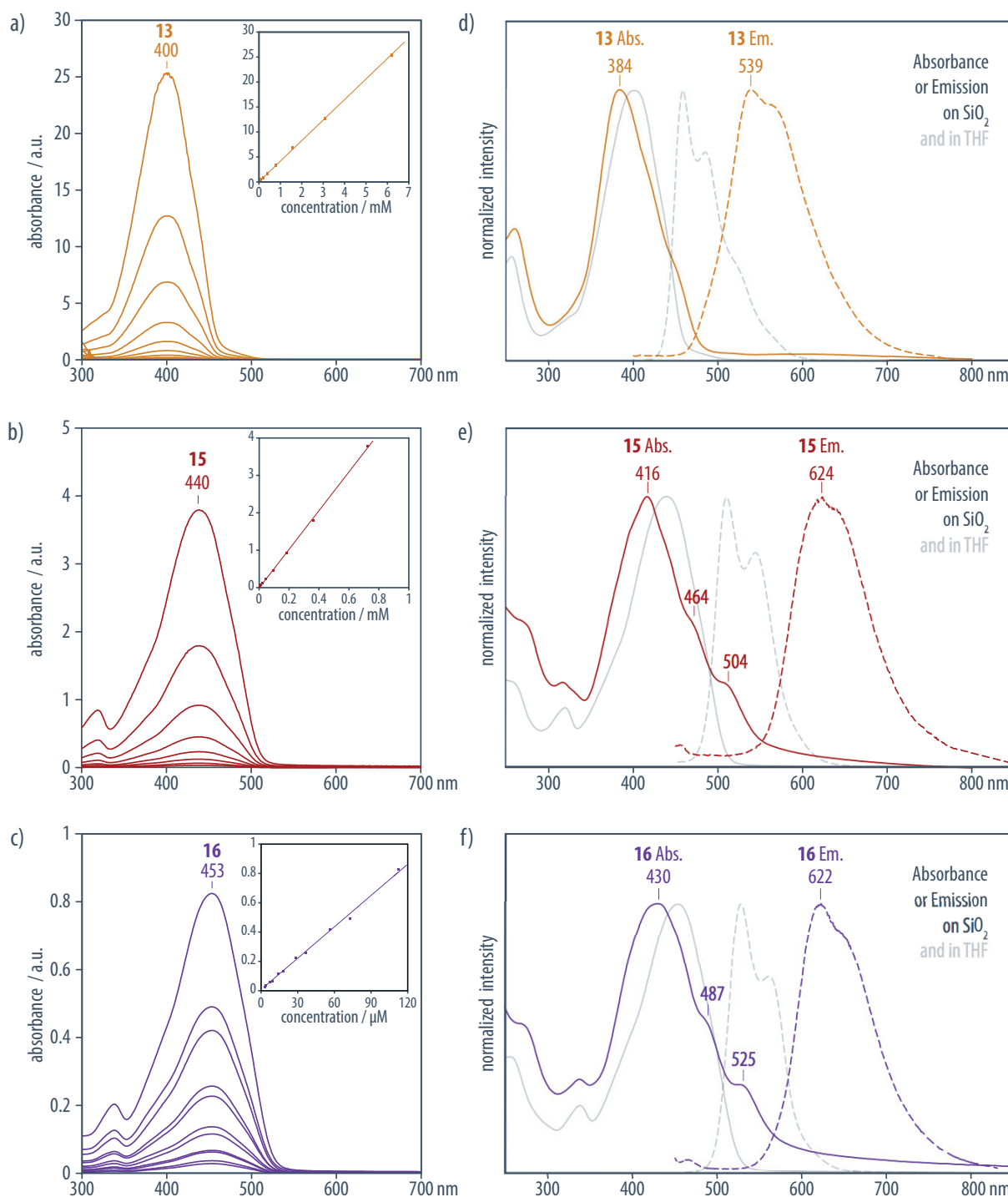


Figure 37. Solutions of quarter-, sexi-, and heptathiophene **13**, **15**, and **16** remained molecularly disperse up to relatively high concentrations and only showed signs of aggregations in the solid state. *a-c*) The absorption spectra of THF solutions of **13**, **15**, and **16** followed Lambert-Beer's law up to concentrations of 6 mmol/L (**13**), 0.7 mmol/L (**15**), and 0.1 mmol/L (**16**). *d-f*) Absorption and emission spectra of **13**, **15**, and **16**, respectively, casted on fused silica; emission spectra were recorded at excitation wavelengths of 384 nm (**13**), 413 nm (**15**), and 430 nm (**16**).

Only the octathiophene active ester **17** showed the presence of spectroscopic aggregates even in dilute THF solution ($c = 2 \mu\text{mol/L}$). This was indicated by a broadened UV/vis absorption band with features reminiscent of a vibronic fine structure, as well as emission spectra that were dependent on the excitation wavelength (Figure 38). In a thin film cast on fused silica the

absorption maxima was drastically blue-shifted by 60 nm and the emission spectrum showed both a band red-shifted by 100 nm along with a secondary band blue-shifted by 50 nm.

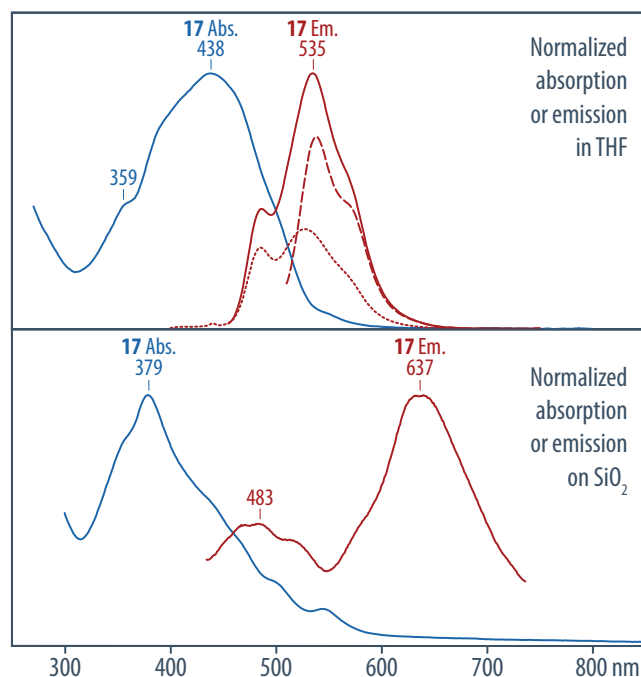


Figure 38. Only the octathiophene **17** exhibited spectroscopic aggregates in dilute THF solution ($c = 2 \mu\text{mol/L}$). In solution (top) the absorption spectrum showed features reminiscent of vibronic fine structure and the emission spectra changed shape with the excitation wavelength. In the solid state (bottom), the bands were drastically shifted and a distinct vibronic fine structure appeared in the absorption spectrum. The emission spectra were measured in solution at 445, 500, and 390 nm excitation wavelengths (in the order of decreasing emission intensity), and in the solid state at 380 nm.

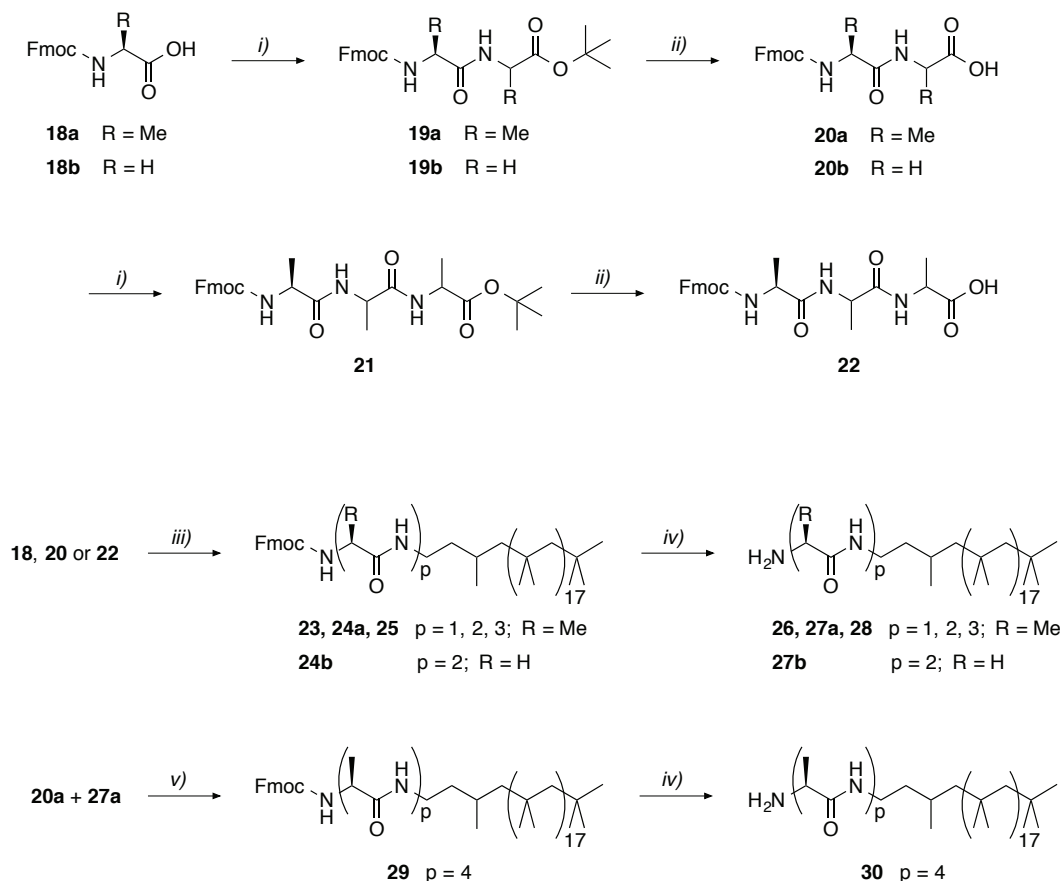
Our findings hence suggest that the chlorendylimidyl-protected oligothiophene derivatives displayed a low tendency for aggregation in organic solution (with the exception of octathiophene **17**). Electronic interactions between the chromophores were observed only in the solid state. Thus, these derivatives could be straightforwardly handled in solution up to relatively high concentrations. Even the octathiophene was still sufficiently soluble for further chemical reactions, as will be described hereafter.

2.5 Divergent Synthesis of Nanowire-Forming Oligothiophene Derivatives

The oligothiophene active esters **12–17** were very convenient precursors because the chlorendylimidyl esters served as temporary protecting groups that were sufficiently stable throughout the synthesis, but could be converted into the corresponding amide-functionalized derivatives in a single step. Thus, simple addition of the desired amine without any base or coupling reagent sufficed to form the amide. This was even true for the octathiophene active ester **17**, despite its lower solubility. Hence, we had a series of chemically functionalized oligothiophene building blocks at hand that could be further used in divergent syntheses. For

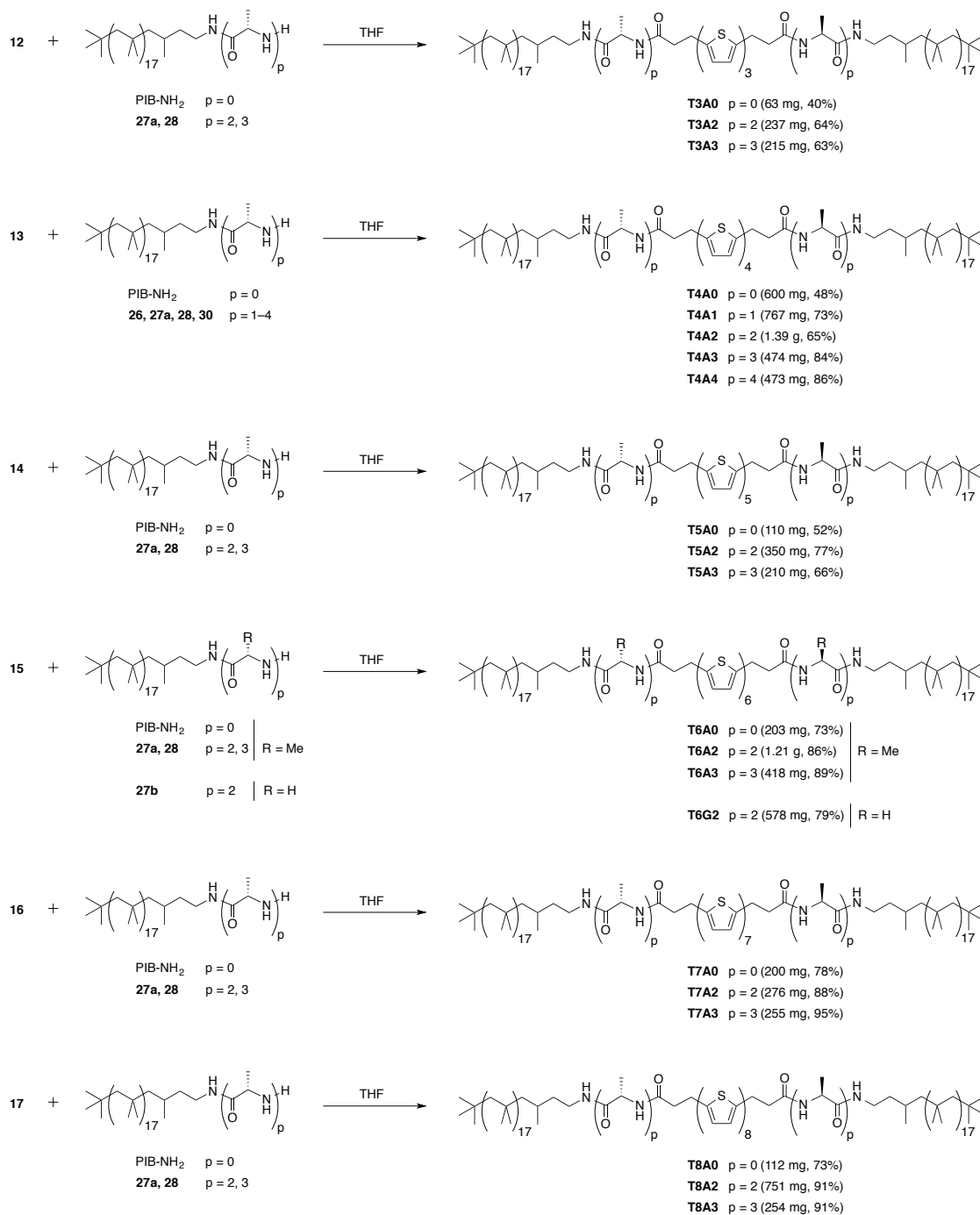
the purpose of the present thesis, the active esters proved to be ideal synthetic precursors for the preparation of a library of nanowire-forming oligothiophenes carrying oligopeptide-polymer substituents.

The required oligopeptide-functionalized polymers were prepared by standard solution-phase peptide coupling and deprotection protocols (Scheme 5). The poly(isobutylene) amine (PIB-NH₂) with an average degree of polymerization $P_n = 17$, was easily obtained on the multigram scale by column chromatography of commercially available Kerocom™ PIBA to remove unfunctionalized PIB, as well as other side products, such as PIB-OH and mineral oil. For the preparation of the oligopeptide, orthogonal protection was achieved with fluorenylmethyloxycarbonyl (Fmoc) group for the amine moiety and *tert*-butyl group for the carboxylic acid functionality. These groups could be cleaved under basic and acidic conditions, respectively. The peptide coupling agent (benzotriazol-1-yloxy)tripyrrolidinophosphonium hexafluorophosphate (PyBOP) was used to react Fmoc-L-alanine **18a** with L-alanine *tert*-butyl ester hydrochloride in THF and obtain Fmoc-L-alanyl-L-alanine *tert*-butyl ester **19a** after repeated precipitation into a 1 M aqueous HCl solution. The *tert*-butyl ester was subsequently cleaved with trifluoroacetic acid (TFA) to furnish the Fmoc-L-alanyl-L-alanine **20a**. From the latter, repeating the same PyBOP coupling and TFA deprotection protocols yielded Fmoc-L-alanyl-L-alanyl-L-alanine *tert*-butyl ester **21** and Fmoc-L-alanyl-L-alanyl-L-alanine **22**. By analogy, peptide coupling of Fmoc-glycine **18b** and glycine *tert*-butyl ester hydrochloride, followed by deprotection yielded the achiral counterparts Fmoc-glycyl-glycine *tert*-butyl ester **19b** and Fmoc-glycyl-glycine **20b**. PyBOP-promoted coupling of PIB-NH₂ to any of the acid-deprotected oligopeptides **18**, **20**, and **22** furnished the Fmoc protected oligopeptide modified polymers **23–25**. Subsequent deprotection with piperidine followed by column chromatography yielded the oligopeptide-functionalized polymers **26–28**. Finally, PyBOP-promoted coupling and Fmoc deprotection of **27a** and dialanine **20a** resulted in the tetra(L-alanine)-modified polymer **30**.



Scheme 5. The required oligopeptide functionalized poly(isobutylene)s **26–28** and **30** were prepared by standard peptide coupling protocols. *Reagents and conditions:* *i*) L-alanine *tert*-butylester hydrochloride (or glycine *tert*-butyl ester hydrochloride for **18b**), PyBOP, DIEA, THF; *ii*) TFA, CHCl₃; *iii*) PIB-NH₂, PyBOP, DIEA, THF; *iv*) piperidine, CHCl₃; *v*) PyBOP, DIEA, THF.

The obtained amine-terminated oligopeptide-modified polymers **26–28**, **30**, as well as PIB-NH₂ were then reacted with the oligothiophene precursors **12–17** in THF. Purification was straightforward and consisted of repeated precipitations into methanol to yield oligopeptide-polymer modified oligothiophene derivatives, with isolated yields ranging between 0.06–1.39 g (40–95%) and an average yield of 74%, including the ter- and quinquethiophene derivatives prepared in collaboration with Regina Hafner. Only **T4A0** and **T3A0** were more tedious to precipitate and consequently purified by gel filtration. The series of compounds **TnAp** will serve to prepare well-defined organic nanowires by solution-phase self-assembly, driven by synergistic π - π stacking and hydrogen bonding.^{151,152,169} The structural characterization and opto-electronic properties of the resulting 1D aggregates will be investigated in the following chapter.



Scheme 6. The developed divergent synthesis allowed for the straightforward preparation of a library of oligothiophenes **TnAp**, as well as **T6G2**.

2.6 Conclusions

In conclusion, the use of chlorendylidyl esters as temporary protecting groups for carboxylic acids represents a versatile tool for the synthesis of terminally functionalized π -conjugated molecules on large reaction scales. In this context, the chlorendylidyl moieties fulfill the double task of enhancing the solubility of all intermediates and products while, at the same time, improving their crystallizability. This unusual behavior is supposedly due to the

chlorendylimides' unique combination of steric demand, rigidity, and polarity, which may also be useful to address other synthetic challenges in organic chemistry. As a result, the synthesis and purification was facilitated at all stages because almost no column chromatography was required and all compounds could be conveniently prepared on reaction scales of up to several tens of grams, including the notoriously difficult to handle end-substituted octathiophene derivative. Moreover, the chlorendylimidyl-protected acids served as useful precursors in subsequent reactions with nucleophiles. This has allowed us to prepare of a variety of end-functionalized π -conjugated compounds in a divergent synthetic approach. For example, reaction with free amines without the use of any additional reactants furnished the corresponding amides. The obtained products do not comprise anymore sterically demanding chlorendic substituents and are therefore suited for use in organic electronics. In this way, we could straightforwardly prepare a library of oligothiophenes with oligopeptide-polymer substituents. These compounds are precursors for the fabrication of organic nanowires showing promising properties in charge generation and stabilization, as will be investigated in the next chapter.

Oligothiophene Nanowires and Polaron Formation



3 Oligothiophene Nanowires and Polaron Formation

3.1 Introduction

One-dimensional nanostructures of organic semiconductors¹⁷⁵⁻¹⁷⁷ are expected to become important components for their use as defined charge percolation paths in future nanoelectronic devices, including electronic,^{3,146,178} photovoltaic,^{149,150} or sensing¹⁷⁹⁻¹⁸¹ devices. They are also excellent model systems for fundamental investigations of charge generation and transport in organic semiconductors under nanoscopic confinement.¹⁸² Organic nanowires of π -conjugated oligomers or polymers have been prepared by different methods, including nanolithography,¹⁸³ templated growth,¹⁸⁴⁻¹⁸⁶ electrospinning,¹⁸⁷⁻¹⁸⁹ anisotropic crystallization,¹⁹⁰⁻¹⁹³ or solution-phase self-assembly.¹⁹⁴⁻¹⁹⁷ Previous works often reported one-dimensional objects of unknown internal order and with no control over lateral dimensions. However, a reliable supramolecular method was developed previously in our laboratory to obtain uniform nanowires that comprise a single stack of chromophores at their core.^{151-153,198} By simple substitution with polymer-functionalized oligopeptides, the chromophores aggregated in a parallel-displaced, helically twisted arrangement. This was still true for calamitic (rod-like) compounds such as quaterthiophenes, known to otherwise preferentially crystallize in a herringbone fashion.¹⁹⁹

A cofacial arrangement of the thiophene units is also observed in poly(3-hexylthiophene) (P3HT), which forms fibrillar crystalline domains with the polymer chains aligned perpendicular to and π - π stacking along the fibril axis.^{98,100,102,103} This layered arrangement promotes a more planar conformation of the poly(thiophene) backbones and enhances the interchain π -interactions, with typical distances of 3.8 Å. Thanks to its outstanding properties, such as its high degree of crystallinity, excellent hole conductivity, and decent spectral coverage, P3HT has found applications in organic electronics and in particular in photovoltaic devices. Both neat P3HT itself and P3HT:PCBM bulk heterojunctions, have meanwhile become archetypal models for mechanistic studies of elementary photon-to-current conversion processes. While photoexcitation of P3HT solutions primarily resulted in the expected formation of intrachain singlet excitons, light absorption in neat P3HT films gave rise to excitons but, notably, also directly produced pairs of free charge carriers of opposite sign.²⁰⁰⁻²⁰² The yields for this direct charge generation have been reported to be as high as 30%, which was attributed to the strong interchain coupling in the crystalline phases.²⁰³ For this reason, the conventional model for the photogeneration of charge carriers in a P3HT:PCBM bulk heterojunction, i.e., the diffusion of the exciton to the interface and splitting into a charge transfer state, had to be revised. It was inferred from transient absorption measurements on neat P3HT and P3HT:PCBM bulk

heterojunctions that, after photoexcitation of the polymer, excitons split at the interface as commonly described while, in a parallel, the negative P3HT polarons of the directly formed charge carrier pairs are transferred to the PCBM.²⁰¹

Furthermore, Frisbie *et al.* investigated hole transport in organic field-effect transistor prepared with P3HT as the active layer and a polymer-electrolyte gate dielectric with a high capacitance.²⁰⁴ The latter allowed for reaching hole densities in the P3HT thin film of 10^{15} cm^{-2} . At such charge densities, P3HT exhibited metallic conductivity with activation energies of 0.7–4 meV, i.e., well below the thermal energy at the operating temperature. A transition to metallic or superconductive behaviour has been reported for example in polyaniline²⁰⁵, graphene,²⁰⁶ or fullerene²⁰⁷ for sheet charge densities around 10^{14} cm^{-2} , i.e., 10^7 cm^{-1} for 1D nanostructures.²⁰⁸

In this context, previous investigations in our group had found that the highly ordered nanowires made from **QT-A3** (Figure 39) comprised a single stack of cofacially aggregated quaterthiophenes and showed the photo-induced formation of unusually long-lived polaron-like charge carriers with densities of close to 10^6 cm^{-1} .¹⁵³ This finding was presumably the consequence of a tight π - π stacking of the electron-rich oligothiophene chromophores in a helical supramolecular arrangement within the nanowires. These nanowires exhibited macroscopic electric conductivity properties that were linked to the spectroscopically characterized charge carriers. It was estimated that current densities reached 10^4 A cm^{-2} within the nanowires, and the charge carrier mobility of $0.12 \text{ cm}^2 \text{ V}^{-1} \text{ s}^{-1}$ was comparable to the best values observed in single crystals.

In the present study, we investigated the nanowire formation and the resulting spectroscopic properties of a library of oligothiophene derivatives from the trimer up to the octamer, substituted with polymer-functionalized oligopeptides of different lengths, in order to get a better insight into the polaron formation under 1D nanoscopic confinement. As will be discussed in this chapter, the shorter spacer between the oligothiophene and oligopeptide segments of **TnAp**, improved the aggregation strength compared to the previous case of **QT-A3**. Consequently, derivatives containing oligopeptide segments of two or more alanines gave rise to uniform nanowires that comprised a single stack of the oligothiophene chromophores at their core (Figure 39). The tight stacking of the oligothiophenes in a helical fashion within the nanowires was accompanied by the facile generation of polaron-like charge carriers with lifetimes of up to several days, while achiral derivatives resulted in substantially shorter nanowires and charge carriers with significantly shorter lifetimes. The comparison of the kinetics for charge generation and decay revealed that the maximum charge concentration increased with the length of the oligopeptide substituents and also reached higher values for derivatives with an even number of thiophene units.

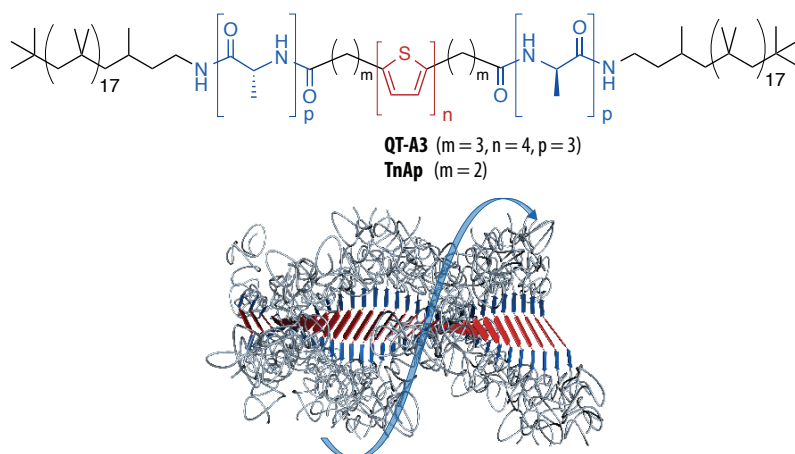


Figure 39. Molecular design of the investigated oligothiophene compounds **TnAp** and schematic representation of a single-stack nanowire formed by supramolecular self-assembly in solution. The quaterthiophene derivative **QT-A3** previously employed in our group comprised a propylene spacer between the oligothiophene and the oligopeptide segments. An ethylene spacer was employed for **TnAp** and resulted in enhanced aggregation strength.

3.2 Structural Investigation of the Nanowires

The nanowire-forming oligothiophene derivatives **TnAp** with n thiophene units and p L-alanine units in the terminally attached oligopeptide segment were prepared as described in the previous chapter. Homogeneous and optically clear solutions of the nanowires were prepared by thermally equilibrating solutions of **TnAp** in 1,1,2,2-tetrachloroethane (TCE; $c = 1$ mmol/L) at appropriate temperatures. A detailed structural analysis of the nanowires was then performed by means of solution-phase IR spectroscopy, AFM imaging, small- and wide-angle X-ray scattering, as well as UV/vis and CD spectroscopy.

As known from our previous investigations,^{151,152} sufficiently long oligo(L-alanine) segments form parallel β -sheets that feature characteristic vibrations at 3290 cm^{-1} in the amide A region and at 1630 cm^{-1} in the amide I region, corresponding to the N–H and C=O bond stretching vibrations, respectively (Figure 40). The series of quaterthiophene compounds **T4Ap** ($p = 0\text{--}4$) is an illustrative example for the effect of an increasing number of alanine units on the aggregation. The compounds **T4A0** and **T4A1** comprising none or one L-alanine did not undergo aggregation and, accordingly, the IR spectra exhibited an amide A band above 3400 cm^{-1} as well as an amide I band at around $1660\text{--}1670\text{ cm}^{-1}$, indicating the presence of non-hydrogen-bonded amides. On the contrary, **T4A2–T4A4** with two or more L-alanines in each terminal substituent showed the formation of parallel β -sheets, resulting in a shift of the two bands to the expected wavenumbers.

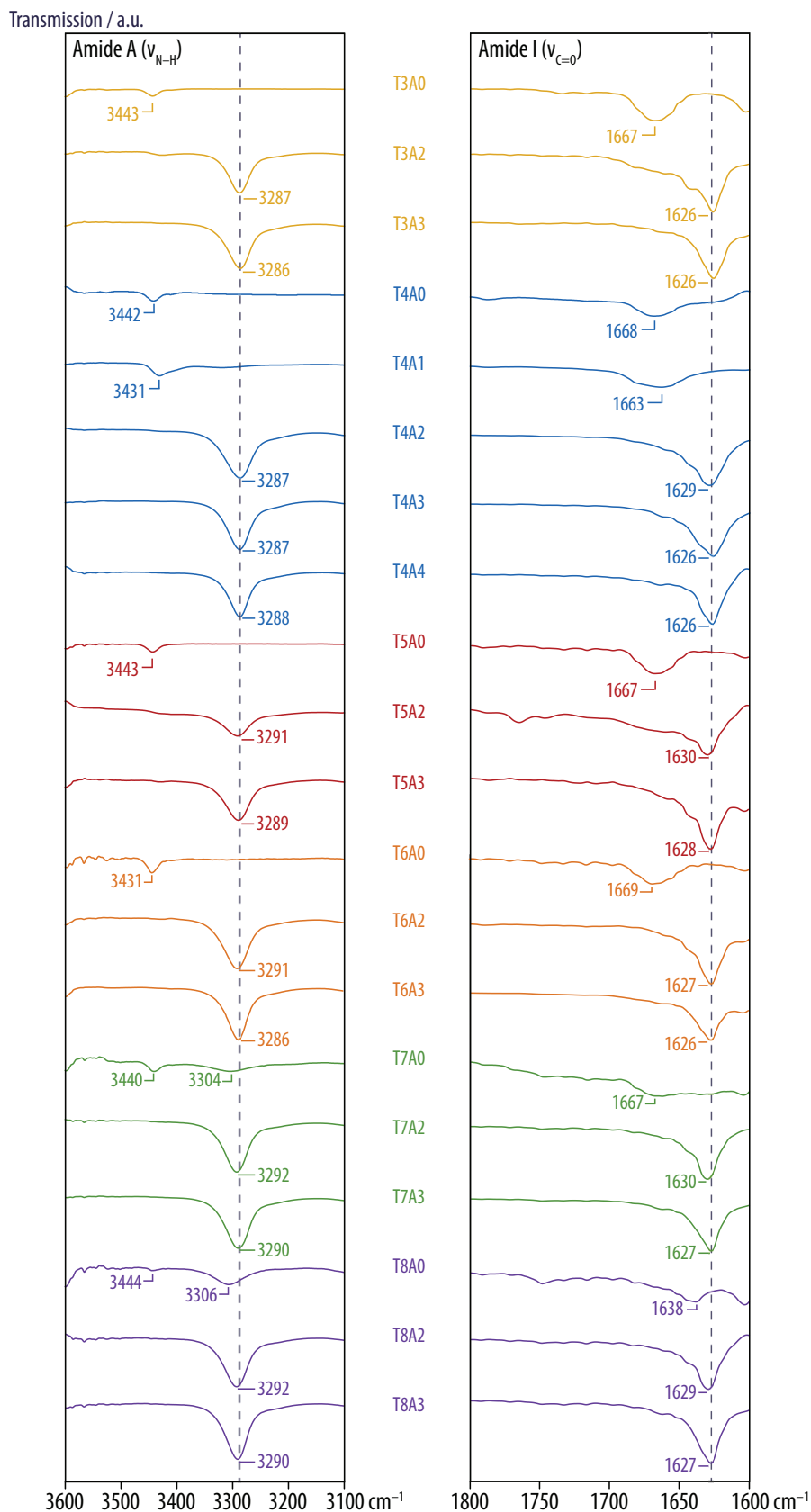


Figure 40. Solution-phase IR spectroscopy was used to probe the aggregation of the oligopeptides into parallel β -sheets in solution. Aggregates exhibited a band at about 3290 cm^{-1} in the amide A region (N-H stretching vibration), as well as a band at around 1630 cm^{-1} in the amide I region (C=O stretching vibration). Non-aggregating derivatives typically showed an amide A band above 3400 cm^{-1} and an amide I band in the 1660–1670 cm^{-1} range.

The same characteristic features were observed in the IR spectra of almost all other oligothiophene derivatives bearing sequences of two or more alanines, while all molecules that did not contain any alanine remained molecularly disperse in solution. Only the longest oligothiophenes **T7A0** and **T8A0** both showed an additional small band at around 3305 cm^{-1} in the amide A region, as well as a band at 1638 cm^{-1} in the amide I region for **T8A0**, which indicated that these molecules, even in the absence of the oligopeptide segments, already started to form weak aggregates via π - π stacking and hydrogen-bonding between the remaining two amide groups.

In order to visualize the nanowires by AFM imaging (Figure 41 & Figure 42), the thermally equilibrated solutions of **TnAp** were diluted to a concentration of $c = 5\text{ }\mu\text{mol/L}$, drop-cast onto mica substrates, and subsequently blow-dried in a gentle stream of argon. In agreement with the IR spectroscopy results, height images of all derivatives containing oligopeptide segments with two or more L-alanines showed the formation of several micrometres long nanowires, while the derivatives bearing none or one L-alanine exhibited featureless deposits or droplet-like conglomerates that presumably formed only upon solvent evaporation during sample preparation. Corroborating the IR spectroscopy results, **T7A0**, and **T8A0** were again exceptions and gave rise to nanowires of a few hundreds of nanometres in length. IR spectroscopy and AFM results were in disagreement only for **T3A2** that did not show any nanowires, although β -sheet formation in solution had been confirmed in IR spectroscopy. The aggregates were presumably too weak in this case and disassembled during sample preparation. A phase image of nanowires from **T6A2** at higher magnification showed that they consisted of a 'harder' core with a width of about 5 nm, corresponding to the single stack of chromophores and oligopeptide substituents, and a 'softer' shell of poly(isobutylene) chains that spread on the mica surface, all of which was consistent with previous investigations in our laboratory.¹⁵² Noteworthy, the annealing temperature had to be increased with an increasing length of oligothiophene or oligopeptide segment. This was necessary to achieve a degree of deaggregation sufficient to support the formation of long 1D aggregates during the slow cooling of the solution. Consistent with this assumption, the nanowires obtained from the most strongly aggregating derivatives **T4A4**, **T7A3**, and **T8A3** were, on average, less than $1\text{ }\mu\text{m}$ long. The aggregation of those derivatives was presumably too strong to allow for sufficient deaggregation and efficient, thermodynamically controlled self-assembly during the annealing process.

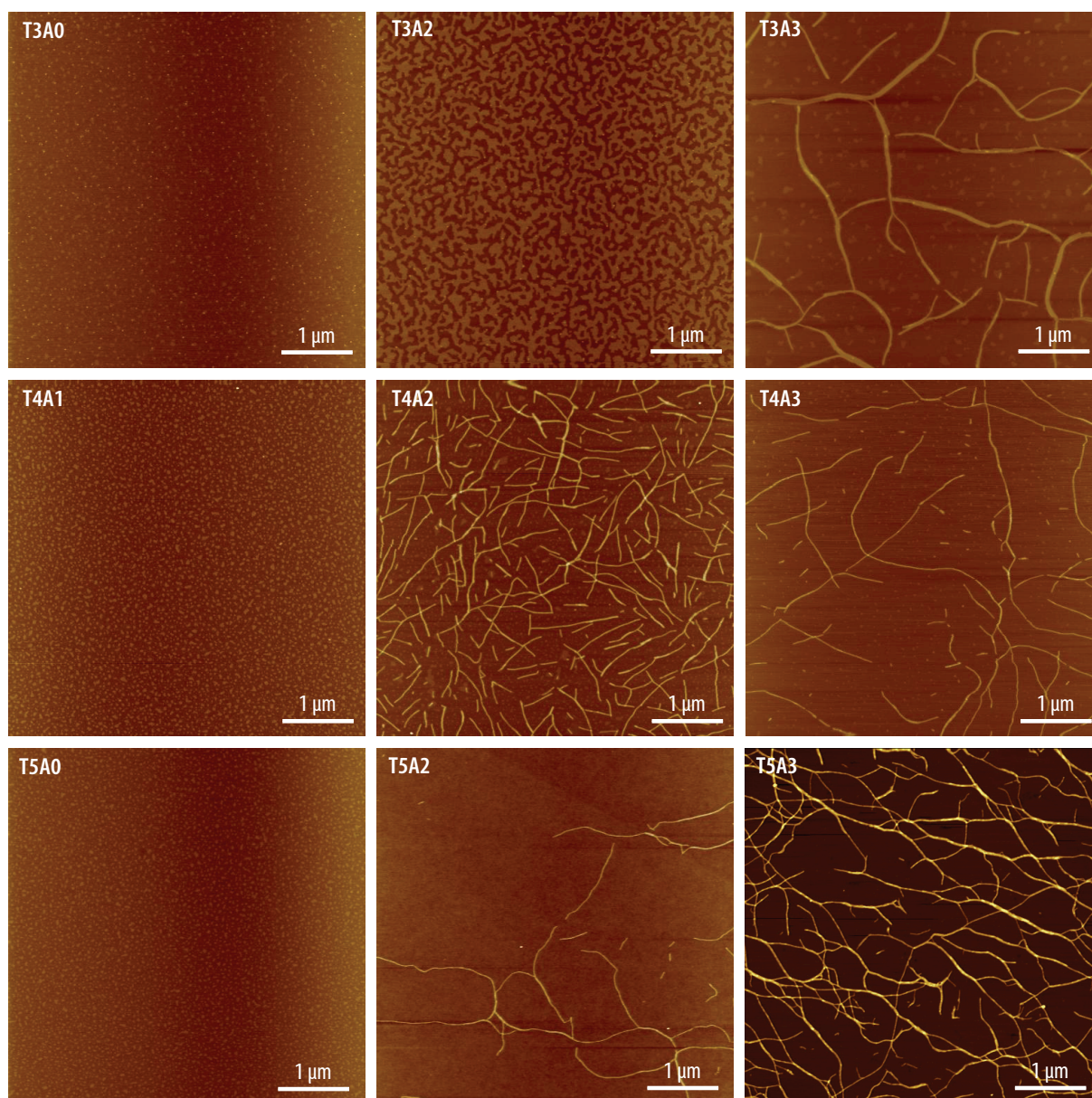


Figure 41. AFM height images of samples of **TnAp** on mica showed the formation of several micrometres long nanowires for derivatives with sufficient aggregation strength, and droplet-like features for the non-aggregating compounds.

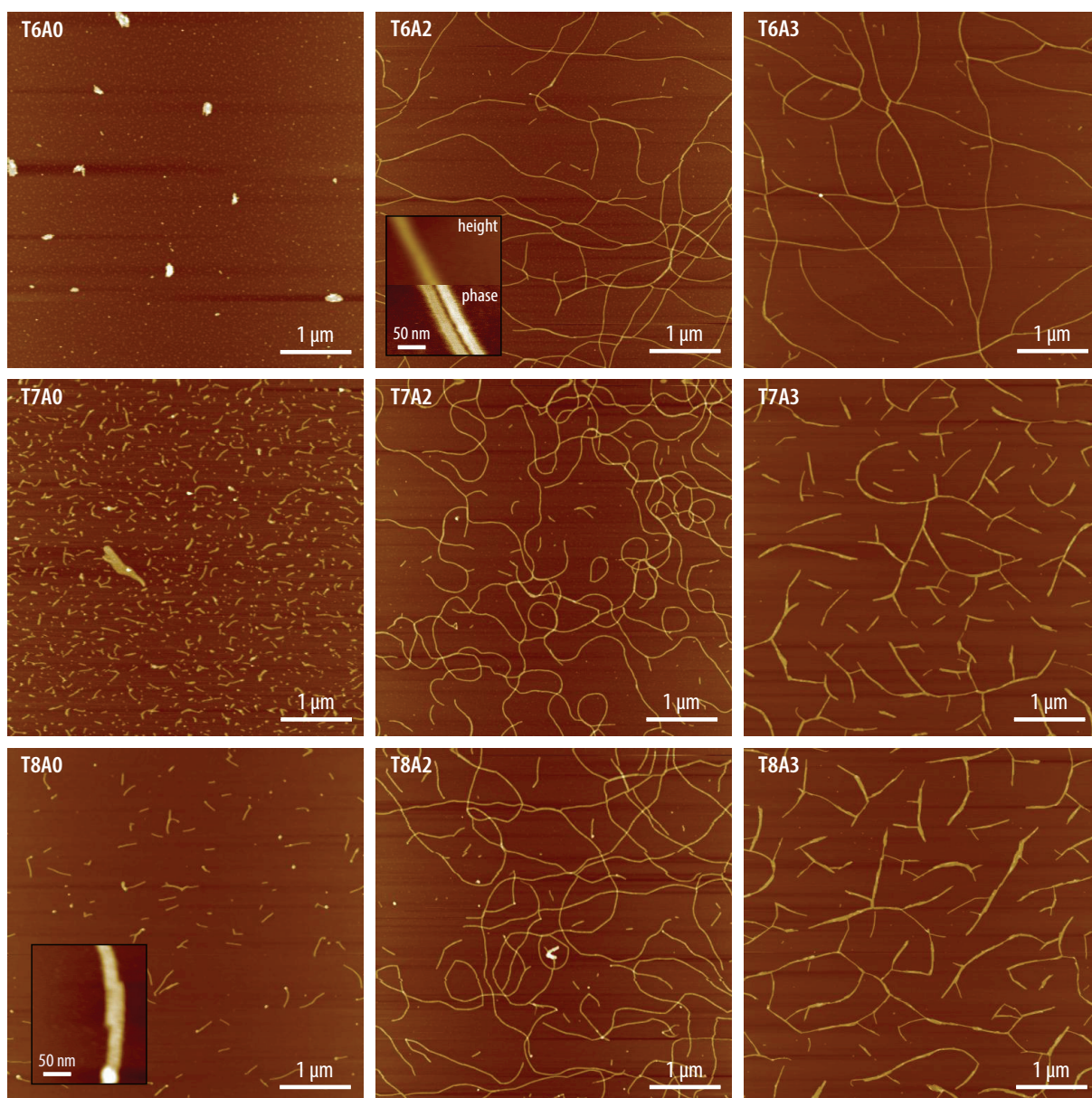


Figure 42. AFM height images of samples of **TnAp** on mica showed the formation of several micrometres long nanowires for derivatives with sufficient aggregation strength, and droplet-like features for the non-aggregating compounds.

Additionally, small- and wide-angle X-ray scattering (SAXS and WAXS) measurements were conducted in collaboration with Dr. Sandor Balog at the Adolphe Merklé Institute, Fribourg on bulk samples that were obtained by the drop-wise precipitation of thermally equilibrated TCE solutions into acetone (Figure 43). Although the exact aggregation pattern in bulk may differ to some extent from the one in solution, those measurements provided useful information on the packing of the molecules within the aggregates. The main reflection in the small-angle region was observed at positions corresponding to characteristic spacings of $d = 5.3\text{--}8.4$ nm that roughly increased with the extended molecular length of the compounds **TnAp** of 13–17 nm. Additional weak reflections were observed in some cases but could not be clearly assigned to higher order reflections. Consistent with our previous results, one can hence assume the

nanowires to give rise to random close-packed cylinders in the bulk, with the terminally attached polymer segments assuming a coiled conformation and filling the grooves of the helically twisted cores.¹⁵² In the wide-angle region, the derivatives showed four reflections at characteristic spacings of $d = 6.1, 4.6, 4.0,$ and 3.2 \AA , of which the latter three became better defined for longer oligothiophene cores. The first reflection can be assigned to the packing of PIB in a short-range 8_3 -helical conformation,²⁰⁹ while the second one represents the intermolecular distance within the nanowires and excellently corresponds to the characteristic spacing observed in β -sheet-like aggregates of the oligopeptides.²¹⁰ The exact assignment of the other two reflections is not yet clear; the reflection at 4.0 \AA may well represent the π - π stacking distance. However, a reflection at the same position is also commonly observed in β -sheet-like oligopeptide aggregates even in the absence of a π -conjugated chromophore, and has never been assigned to a particular structural feature. Moreover, this reflection was still observed for nanowires where the oligothiophene core was replaced by a perylene bisimide moiety.¹⁵² The reflection at 3.2 \AA , on the other hand, would be drastically smaller than the typical distances of $3.6\text{--}3.8 \text{ \AA}$ observed for cofacially stacked oligothiophene aggregates or the polymer backbones in fibrillar crystalline P3HT aggregates, and even smaller than the interlayer distance observed in graphite.^{102,103,211} Further investigations are required to resolve this issue, e.g., the determination of the azimuthal intensity distributions of the two reflections for aligned samples of the nanowires. In any case, the fact that the intermolecular distance of 4.6 \AA is shorter than the 4.8 \AA typically observed in oligopeptide β -sheets, together with the concomitant intensity increase and sharpening of all the $4.6, 4.0,$ and 3.2 \AA with the length of the oligothiophene segments in the series **TnA2** and **TnA3** can be seen as a manifestation of an enhanced degree of order due to synergistic π - π stacking and hydrogen-bonding. The apparent mismatch between the intermolecular distance and the π - π stacking distance of either 4.0 \AA or 3.2 \AA is presumably accommodated by a tilt angle of about 30° or 46° , respectively, of the oligothiophene relative to the oligopeptide long axis, associated with a longitudinal displacement of the oligothiophenes of 2.3 \AA or 3.3 \AA relative to the neighbours. This arrangement was made possible by the incorporation of a flexible ethylene spacer between the oligothiophene and the oligopeptide segments in the molecular design.

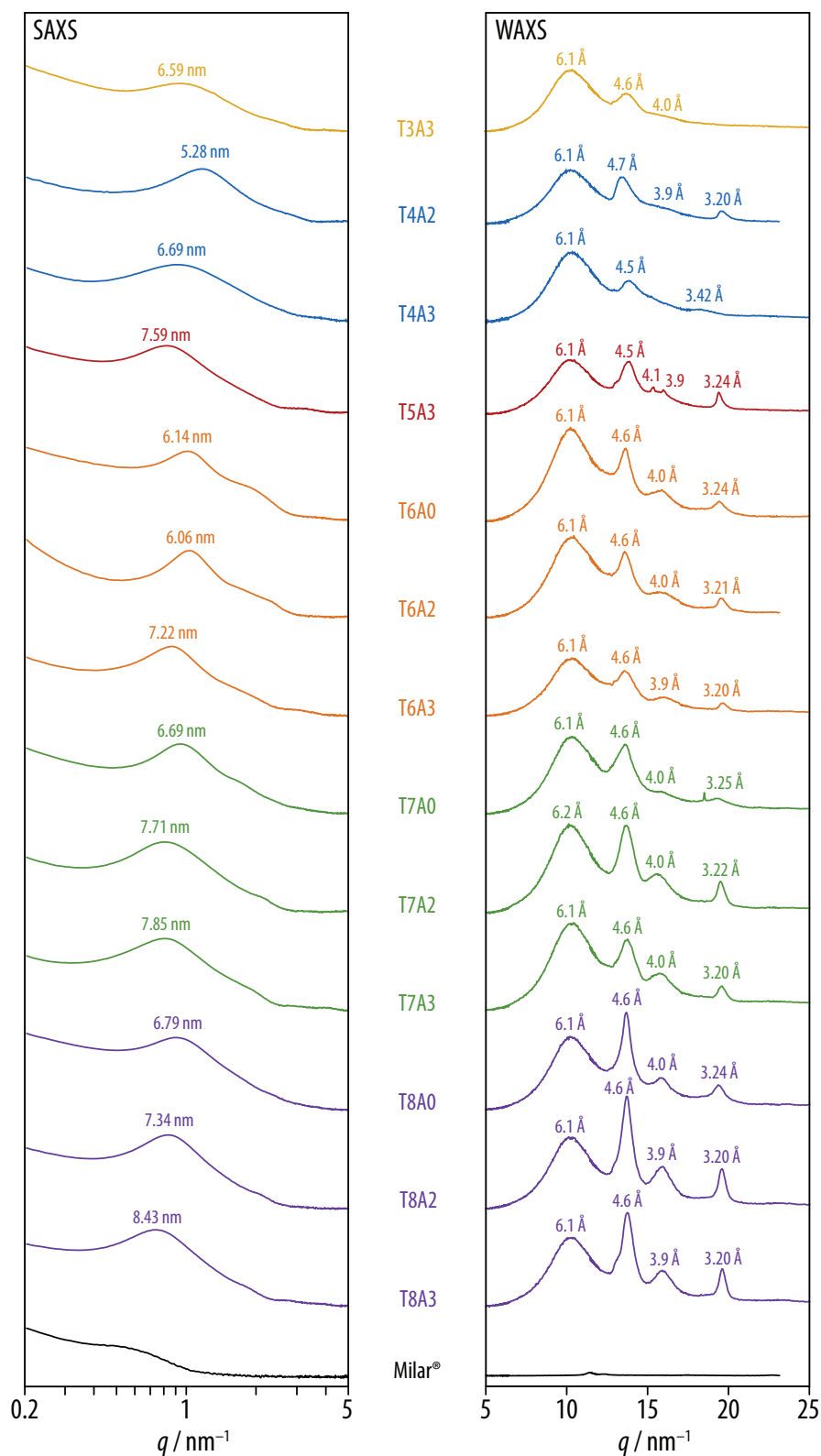


Figure 43. Small-angle X-ray scattering (left, logarithmic scale) revealed nanowire widths of $d = 5.2\text{--}8.4$ nm, substantially smaller than the estimated molecular lengths of 13–17 nm and indicating the terminal polymer chains adopted a random coil conformation and filled the groves of the helically twisted stack of molecules. Wide-angle X-ray scattering (right, linear scale) showed four reflections at characteristic spacings of $d = 6.1, 4.6, 4.0,$ and 3.2 Å; the first two were attributed to the short-range order of the polymers and the hydrogen-bonded oligopeptides, respectively, while the attribution of the latter two to higher order oligopeptide reflections or π - π stacking of the chromophores remained unclear.

The aggregation of the chromophores in the nanowires was monitored by UV/vis absorption spectroscopy. When compared to the spectra of the molecularly disperse derivatives, a blue-shift of the main absorption peak of the 1D aggregates was observed as a consequence of the π - π stacking of the oligothiophene chromophores. Additionally, the blue-shifted peaks had a smaller full width at half-maximum, and a vibronic fine structure in the form of shoulders at longer wavelengths was observed. These findings were in agreement with Kasha's exciton coupling model for H-aggregates of chromophores with juxtaposed transition dipole moments.²¹²

Temperature-dependent UV/vis absorption measurements proved that the nanowires of some derivatives could be reversibly deaggregated and re-assembled by heating and cooling in solution, which allowed us to better investigate the details of the self-assembly process. For instance the UV/vis spectra of **T4A2** (Figure 44) featured an absorption maximum at 372 nm at 20°C. Upon heating to 100°C, the nanowires deaggregated, and the obtained solution showed an absorption maximum at 403 nm, as is typical for molecularly disperse quaterthiophenes. Cooling this solution allowed the molecules to re-aggregate, and the initial absorption spectrum was completely recovered. The presence of two isosbestic points in this temperature series were a strong indication for the presence of only two spectroscopic species, and thus suggested that self-assembly occurred via a nucleation-elongation growth model, as opposed to an isodesmic growth.

Furthermore, helical stacks of chromophores are known to produce a strong bisignate signal in circular dichroism (CD) spectroscopy with a zero-crossing around the maximum absorption.²¹³ In the case of **T4A2**, annealed solutions gave rise to a negative bisignate signal at 20°C, with a zero-crossing at 368 nm (Figure 44), and the CD signal disappeared upon heating and re-appeared upon cooling. To evaluate the reversibility of the process, the ratio of the UV/vis absorptions at 365 and 413 nm, as well as the amplitude of the CD signal were plotted as function of the temperature. Both plots showed that the onset and complete de-aggregation upon heating were at around 45°C and 70°C, respectively. Upon cooling, both the UV/vis absorption and CD activity of the solutions exhibited hysteresis, with onset and complete aggregation temperatures of about 45°C and 20°C. Nevertheless, the initial spectral states were eventually recovered, allowing us to conclude that the reversible, i.e., thermodynamically controlled aggregation into 1D helical nanowires was at the origin of the observed blue-shift of the UV/vis absorption band and the appearance of an associated bisignate CD signal.

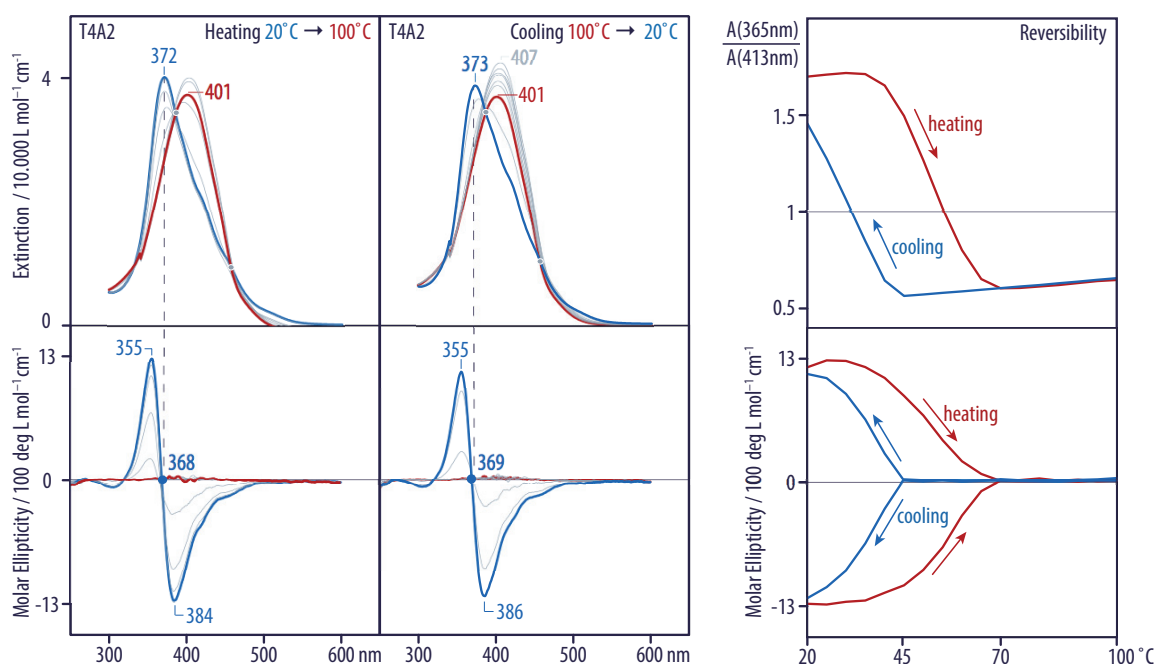


Figure 44. UV/vis (top) and CD (bottom) spectra of **T4A2** as a function of temperature (20–100°C) were correlated, and the presence of isosbestic points indicated a nucleation-elongation growth process. For the UV/vis spectra, the aggregation state was evaluated by the ratio of the absorption intensities at 365 and 413 nm. UV/vis and CD spectroscopy revealed an identical evolution of the aggregation as a function of temperature.

The same temperature-dependent UV/vis and CD spectroscopy measurements were conducted for all derivatives **TnAp** (Figure 45 & Figure 46). In agreement with the IR and AFM results, neither a shift of the maximum absorption, nor a CD signal were observed for the non-aggregating derivatives **T3A0**, **T3A2**, **T4A0**, **T4A1**, **T5A0** and **T6A0**. On the contrary, all derivatives that formed 1D nanowires featured a blue-shifted maximum absorption peak, weak red-shifted bands, and a bisignate CD signal (except for the achiral **T7A0** and **T8A0**). It should be noted, however, that compounds comprising longer oligothiophene or oligopeptide sequences were still at least partially aggregated at 100°C, and their absorption spectra therefore remained almost unchanged within the investigated temperature range.

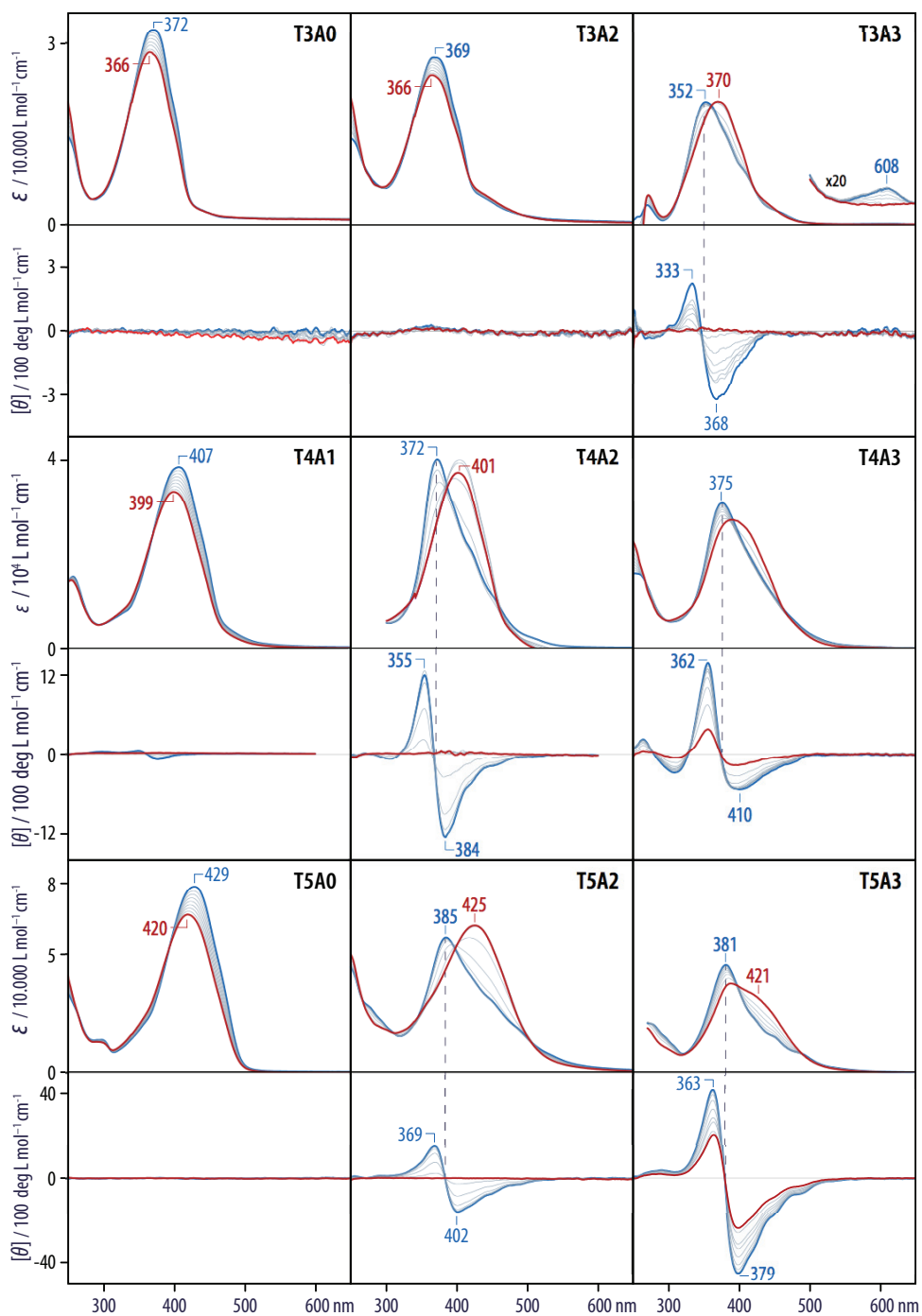


Figure 45. Temperature-dependent UV/vis and CD spectra of annealed solutions (TCE, $c = 0.1\text{--}0.5$ mmol/L) of compounds **TnAp**; from 20°C (blue) to 100°C (red). The observed isosbestic points indicated a nucleation-elongation growth mechanism.

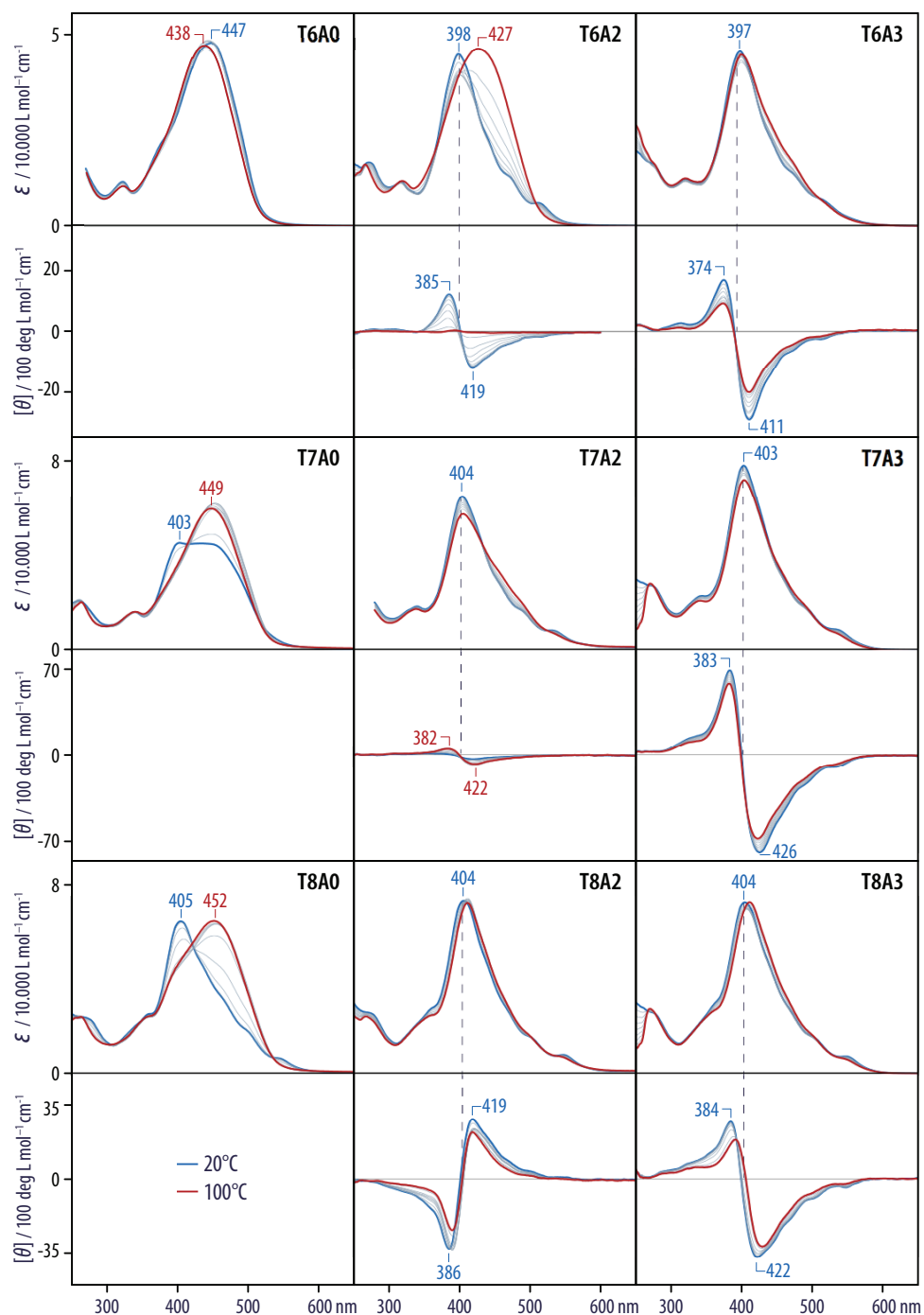


Figure 46. Temperature-dependent UV/vis and CD spectra of annealed solutions (TCE, $c = 0.1\text{--}0.5$ mmol/L) of compounds **TnAp**; from 20°C (blue) to 100°C (red). The observed isosbetic points indicated a nucleation-elongation growth mechanism.

The sign of the bisignate CD signals can be related to the helix sense of a stack of chromophores, whereby a so-called “negative” or “positive” bisignate signal (with a minimum or a maximum at higher wavelengths, respectively) corresponds to a left-handed or right-handed helical stack in the case of oligothiophenes, respectively.^{162,213,214} In our case, all derivatives except **T8A2** exhibited a negative bisignate signal, in agreement with a left-handed helical arrangement induced by the oligo(L-alanine)s. In order to confirm the influence of the oligopeptide chirality

on the helicity, both enantiomers of the derivatives **T4A2**, **T4A3**, and **T6A2** were prepared, i.e., compounds comprising oligopeptide sequences of exclusively either L- or D-alanines. IR and UV/vis spectroscopy, as well as AFM imaging showed the same results for the two enantiomers in all three cases. CD spectroscopy, however, revealed bisignate signals of the same shape but opposite sign (Figure 47), confirming that the supramolecular helicity indeed originated from the molecular chirality of the oligo(alanine) segments. The exceptional helix sense observed for **T8A2** as well as the very small CD intensity of **T7A2** could have their origin in the fact that these samples were not completely deaggregated even at 100°C, and the observed aggregates could therefore represent a kinetically trapped arrangement different from the thermodynamically stable one.

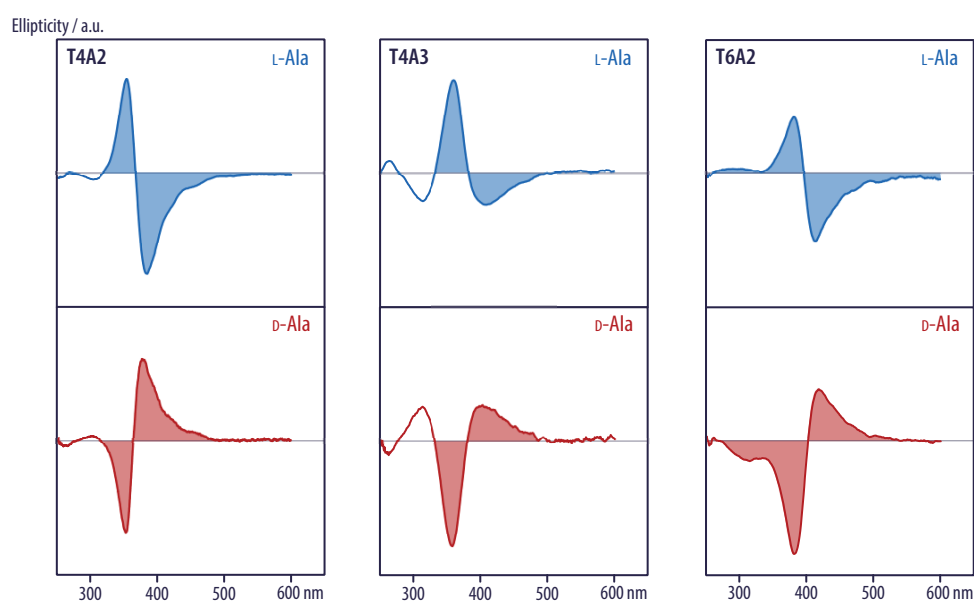


Figure 47. The supramolecular helix sense was controlled by the molecular chirality of the oligopeptides. CD spectra of both levorotatory (blue) and dextrorotatory (red) enantiomers of **T4A2**, **T4A3**, and **T6A2**.

Finally, the derivative **T6G2** comprising diglycyl sequences was prepared as an achiral reference compound that could form the same number of hydrogen bonds and similar π - π interactions as the chiral **T6A2** (Figure 48). In IR spectroscopy, **T6G2** exhibited vibrations at 3310 and 1648 cm^{-1} , slightly different from those observed for **T6A2**. These observed values, however, were in excellent agreement with oligopeptide conformations corresponding to ‘rippled’ instead of ‘pleated’ parallel β -sheets, as is typically observed for oligo(glycine) aggregates or poly(glycine) in the crystalline state.^{215,216} AFM height images of **T6G2** samples prepared from annealed solutions revealed the formation of 1D nanowires of a similar width as those obtained from **T6A2** but only a few hundreds of nanometres in length. Consistently, SAXS measurements on bulk samples of **T6G2** revealed a main reflection corresponding to a nanowire width of about 7.5 nm, and WAXS diffractograms showed four reflections at the same positions as for **T6A2** that

were, however, significantly broader and less intense. The UV/vis spectra of **T6A2** and **T6G2** were similar, except for a stronger blue shift of 46 nm in the case of **T6G2** as compared to 30 nm in the case of **T6A2**, which reflected a different aggregation pattern of the molecules, in agreement with the IR results. However, aggregates of both **T6G2** and **T6A2** seemed to be similarly stable since they showed comparable onset temperatures for the aggregation-deaggregation transition as function of temperature. The fact that the superstructures of **T6A2** and **T6G2** were virtually identical may be seen as a strong indication that, while the details of the internal arrangement may be slightly different, also the achiral **T6G2** actually aggregated into helical structures. The absence of CD activity would then just result from the presence of a racemic mixture of supramolecular helicities. Hence, the absence of a homochiral helix sense along individual nanowires would induce a higher degree of disorder, which could be an explanation for the observed shorter nanowire lengths. Finally, it should be mentioned that similar considerations also apply for aggregates of the achiral derivatives **T7A0** and **T8A0**.

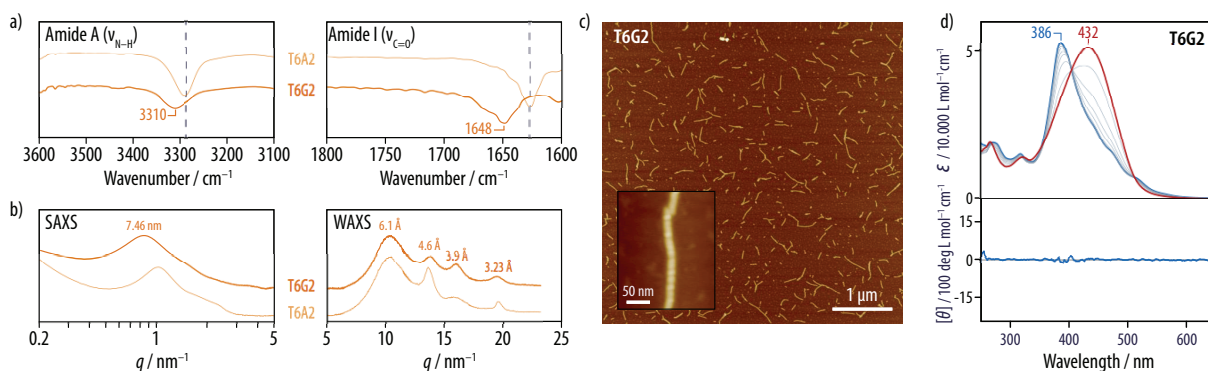


Figure 48. The achiral derivative **T6G2** showed superstructures similar to those of **T6A2**. *a)* The two characteristic bands observed in IR spectroscopy originated from ‘rippled’ parallel β -sheets, as typically observed for achiral glycine sequences. *b)* SAXS revealed a nanowire width in the same range as **T6A2**; WAXS showed four reflections at the same positions as for **T6A2**, but substantially broader and less intense. *c)* AFM height image showing the formation of short nanowires with similar width than **T6A2**. *d)* Temperature-dependent UV/vis spectra exhibited a blue-shift of 46 nm which was higher than for **T6A2**; as expected, no chirality was observed in CD spectroscopy.

In conclusion, the chosen molecular design allowed us to prepare well-defined nanowires of the whole series of oligothiophene derivatives, from the terthiophene to the octathiophene. These nanowires comprised the cofacially aggregated oligothiophenes at their core. The oligothiophenes were arranged in a helically twisted, parallel-displaced fashion that resulted in a tight π - π stacking of the cores. This arrangement of the chromophores was reflected in a blue shift of the absorption maximum in the UV/vis spectra, and the appearance of a strong negative bisignate CD signal in the aggregated state. It is worth noting that achiral derivatives such as **T6G2**, **T7A0**, and **T8A0** still gave rise to aggregates with similar (supposedly helical) superstructures, but the absence of a homochiral helix sense was a source of disorder that apparently limited the length of the aggregates.

3.3 Facile Polaron Formation in the Nanowires

We then investigated solutions of the well-defined nanowires formed from the oligothiophene derivatives **TnAp** as model systems for charge generation under 1D nanoscopic confinement. Absorption spectroscopy in the NIR region of all those derivatives that aggregated into nanowires revealed the presence of two additional peaks with intensities of a few per cent compared to that of the main peak, as shown in the case of **T6A3** as a representative example (Figure 49a). According to the literature²¹⁷⁻²²² and our own previous investigations,¹⁵³ those peaks can be attributed to the formation of polaron-like oligothiophene radical cations. Indeed, the formation of positive polarons results in two additional energy levels within the bandgap and, consequently, two additional sub-bandgap energy transitions P1 and P2 (Figure 49b).^{31,223} For derivatives **T3A3**, **T4A2**, and **T6A2** that could be completely deaggregated upon heating to 100°C, the NIR peaks disappeared at high temperature (cf **T3A3** in Figure 45) and reappeared with substantially smaller intensities upon cooling to room temperature. However, the peak intensities increased again when the solutions were exposed to daylight, and decayed surprisingly slowly over several days in the dark, proving the presence of polarons with very high lifetimes.

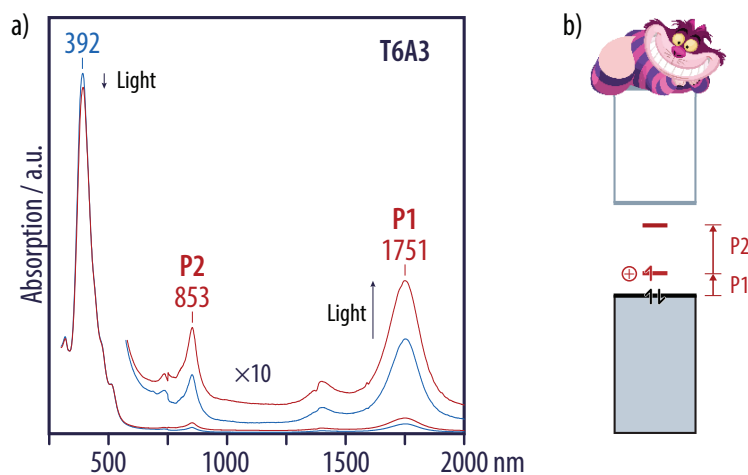


Figure 49. a) Absorption spectroscopy in the NIR region revealed two additional bands; after exposition to daylight, the intensity of those bands increased, while that of the main peak decreased. b) Schematic energy diagram of an oligothiophene nanowire containing positive polarons, giving rise to both transitions observed in the NIR.

We then compared the UV/vis/NIR spectra within the series **TnA3** ($n = 3-8$) with a varying length of the oligothiophene core (Figure 50). The UV/vis/NIR spectra of **TnA0** ($n = 3-6$) at 20°C, as well as **T7A0** and **T8A0** at 100°C were also recorded as reference samples representing molecularly disperse solutions of the same chromophores. Thus, we observed that, with an increasing length of the oligothiophenes, the position of all peaks shifted to longer wavelengths, while both the intensity of the main absorption and its blue shift compared to the molecularly disperse reference solutions became larger.

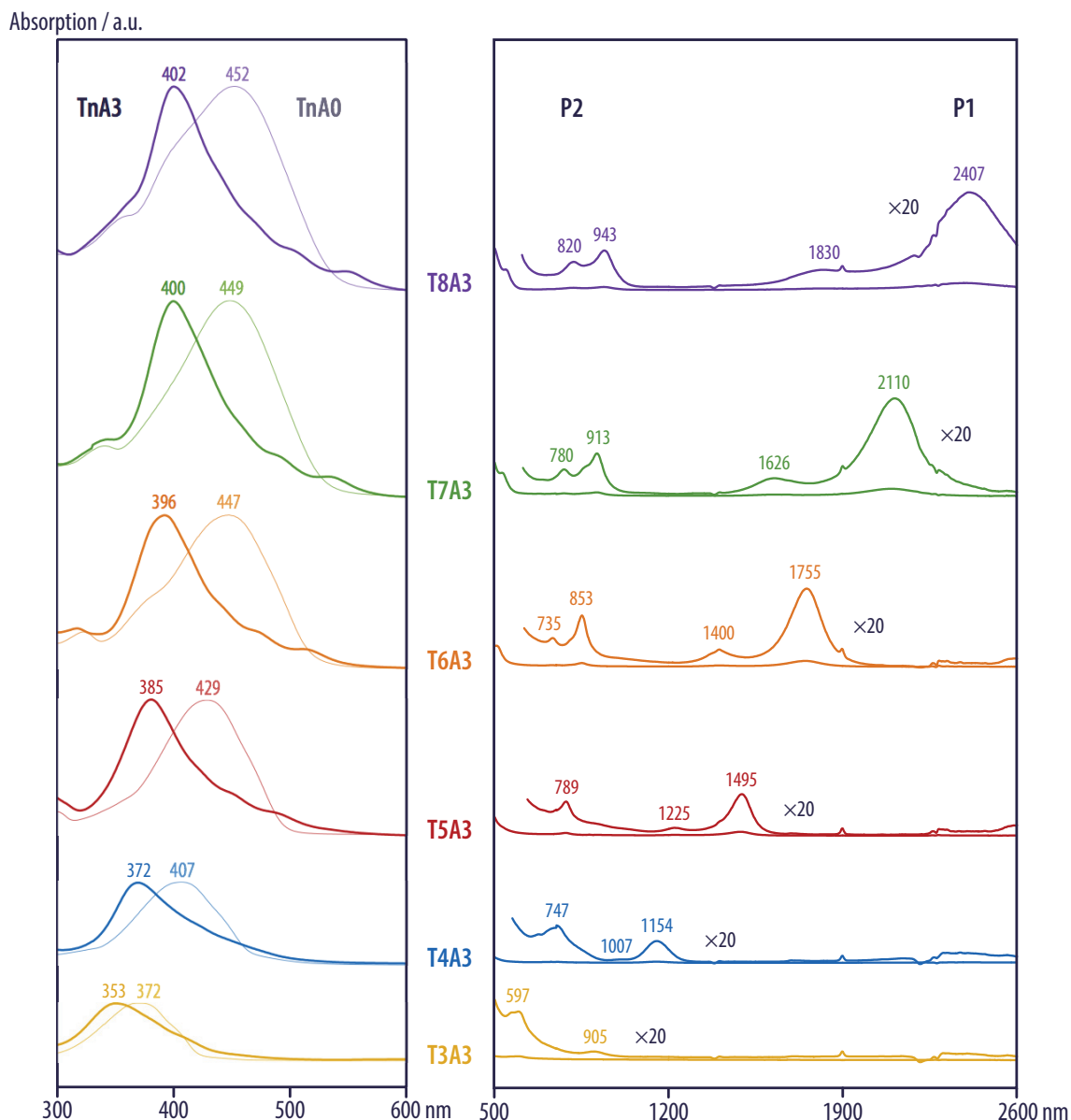


Figure 50. UV/vis spectra (left) of **TnA3** ($n = 3-8$) were shown along with molecularly disperse reference spectra of **TnA0** ($n = 3-6$) at 20°C, as well as **T7A0** and **T8A0** at 100°C, in order to highlight the blue-shift associated to the formation of H-aggregates. In the NIR region (right), both polarons bands were observed in nanowires made from all derivatives **TnA3** ($n = 3-8$), as highlighted in the zoom $\times 20$.

Kuhn plots of the main transition energies for the aggregated and non-aggregated derivatives, as well as the blue-shift of the main transition (i.e., the difference of the transition energies for the aggregated and non-aggregated derivatives) revealed linear trends in all cases (Figure 51). It should be noted that, since the absorption spectra of **T7A0** and **T8A0** were recorded at 100°C instead of 20°C, their absorption maxima were slightly blue-shifted by probably about 10 nm, estimated from the corresponding hypsochromic shift observed for **TnA0** ($n = 3-6$) at the two different temperatures (Figure 45 & Figure 46). This shift translated into small deviations from linearity in the corresponding Kuhn plots, which were hence disregarded. The linear trends over the entire range of oligothiophene lengths indicated that the excitons were intramolecularly

delocalized across the entire chromophores with up to at least eight thiophene units. The increase of the blue-shift upon aggregation with the chromophore length may be due to an improved intermolecular overlap between the increasingly extended chromophores, as well as stronger interactions within the stack. Likewise, the Kuhn plots of both polaron transitions in the NIR showed linear trends, from which one can conclude that also the polarons were intramolecularly delocalized over the entire chromophores of up to eight thiophene units.

The observed transition energies at maximum intensity of the main absorptions in the UV/vis and of both polaron absorptions in the NIR were used to qualitatively deduce schematic energy diagrams of the nanowires. In this regard, it should be mentioned that the optical bandgap as determined from the main transition energy does not actually represent the HOMO-LUMO gap because of the exciton binding energy.³² Nevertheless, the optical bandgap values were used as first approximations in order to illustrate the general trends. For comparison, the diagrams of all compounds **TnA3** ($n = 3-8$) compounds were centered at the middle of their bandgaps. From the schematic energy diagrams, one can infer that the polaron bands moved closer to the HOMO levels with an increasing oligothiophene length, which illustrates the increasing donor character of the chromophores and the successively improved stabilization of positive polarons within the nanowires.

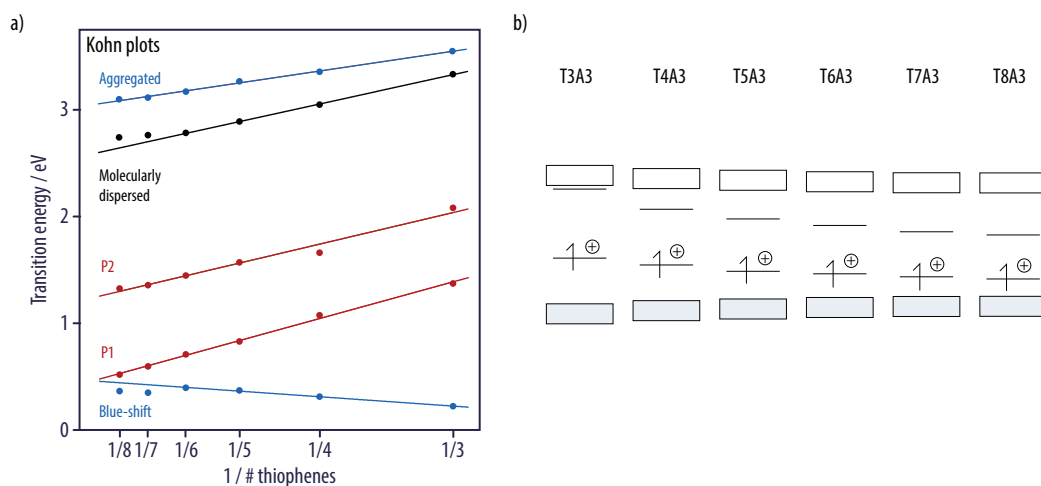


Figure 51. Comparison of the observed transition energies as function of the oligothiophenes length. *a)* Kuhn plot for the main transition of the molecularly dispersed **TnA0**, the main transition of the aggregated **TnA3**, the blue-shift of the latter as compared to the molecularly dispersed reference compounds, as well as the two polaron transitions P1 and P2. *b)* Schematic energy diagrams qualitatively deduced from the optically observed transition energies; the HOMO-LUMO gap is represented by the transition energy of the main transition (i.e., the optical bandgap), without any correction for the exciton binding energy; the diagrams are artificially centred at mid-bandgap.

Finally, the NIR spectra of the P1 transitions as function of transition energy were normalized and their positions were centered relative to one another, in order to compare the evolution of their shape and full width at half-maximum (FWHM) with the elongation of the oligothiophene cores (Figure 52). As the **T3A3** P1 peak was in the flank of the main absorption, its

characterization was rendered more difficult. Except for **T3A3** and **T4A3** that were slightly broader, the FWHM remained similar for **T5A3–T8A3**. For the derivatives **T4A3–T8A3**, weaker secondary transitions P1' and P2' were visible at smaller wavelengths with respect to the respective primary polaron transitions P1 and P2 that successively increased in intensity with an increasing oligothiophenes length, which may be an indication of an increased degree of intermolecular delocalization of polarons between the stacked chromophores within the nanowires.²²³ The P1' transitions appeared to have a similar intensity relative to the P1 transitions, except for **T4A3** that showed a much weaker P1' transition. Moreover, their FWHM remained similar, except for the broader peak in the case of **T8A3**.

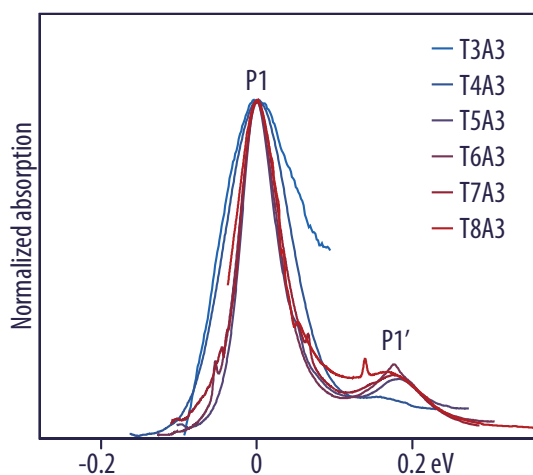


Figure 52. Normalized and centered NIR absorption spectra showed similar P1 polaron band spectra as function of transition energy, featuring constant full width at half maximum (FWHM), as well as secondary P1' bands with similar relative intensity, shift, and FWHM. The exceptions were **T3A3** that did not exhibit a secondary P1' transition, **T4A3** that revealed a weak P1' band, and **T8A3** that show a broader P1' band.

3.4 Polaron Generation under Illumination

In the course of our investigations, we observed that the intensities of the polaron bands strongly increased upon illumination of the samples with white light. This photo-induced charge carrier generation turned out to be surprisingly facile in the sense that, different from previous work in the field, polarons were formed at high densities of several molar percent and with very long lifetimes. As will be discussed in the following, these features allowed us to investigate their generation with steady-state spectroscopy.

The formation of positive polarons in solutions of oligothiophenes in chlorinated organic solvents was previously reported in the literature and rationalized by the role of the chlorinated solvent as an oxidant, resulting in oligothiophene radical cations and chlorine anions.^{221,224} Moreover, it was proposed that oxygen could be involved in the mechanism.²²⁵ Furthermore, Blom *et al.* recently suggested hydrated oxygen complexes as common electron traps in both electron rich and electron poor polymers.²²⁶ While the exact mechanism of the photo-induced

polaron formation is not clear yet in our case, it presumably involved an electron transfer from the excited state to an appropriate electron acceptor, such as a defect in the 1D aggregates, an organic impurity, hydrated oxygen complexes, or the chlorinated solvent (TCE). It must be noted, however, that the photo-induced polaron generation was also observed both in carefully degassed TCE solutions and in toluene solutions, rendering a participation of the chlorinated solvent or oxygen in the process less likely. Nevertheless, traces of chlorinated solvent originating from the synthesis and work-up procedures, oxygen, or other impurities may still be present in sufficient amount to induce polaron formation.

We performed in situ absorption spectroscopy measurements during the irradiation of nanowire solutions with white light from a plasma lamp, using a high pass filter to cut off UV light at wavelengths below 320 nm. The collimated beam of the light was about 4 mm in diameter and had a power of approximately 40 mW. Nanowire solutions of derivatives **TnA3** ($n = 3-8$) were prepared in deuterated TCE that has a lower absorption intensity in the NIR than regular TCE. The samples were thermally equilibrated in the dark to suppress the premature formation of polarons as much as possible, and were then transferred in the dark to a 4×10 mm fluorescence cuvette. The cuvette was placed in a four-way cuvette holder so as to allow for two illumination channels: white light across the long path of the cuvette to irradiate the whole sample and record the UV/vis absorption spectra, and NIR irradiation across the short path to record the NIR absorption spectra.

Allow me to get off subject for the third and last time, so as to fill space. The scientific discussion will continue after this short excerpt from *Alice in Wonderland*. “Who are you?” said the Caterpillar. This was not an encouraging opening for a conversation. Alice replied rather shyly, “I — I hardly know, Sir, just at present — at least I know who I was when I got up this morning, but I think I must have been changed several times since then.” “What do you mean by that?” said the Caterpillar sternly. “Explain yourself!” “I can’t explain myself, I’m afraid, sir,” said Alice, “because I’m not myself, you see.” “I don’t see,” said the Caterpillar. “I’m afraid I can’t put it more clearly,” Alice replied very politely, “for I can’t understand it myself to begin with; and being so many different sizes in a day is very confusing.” “It isn’t,” said the Caterpillar. “Well, perhaps you haven’t found it so yet,” said Alice; “but when you have to turn into a chrysalis — you will some day, you know — and then after that into a butterfly, I should think you’ll feel it a little queer, won’t you?” “Not a bit,” said the Caterpillar. “Well, perhaps your feelings may be different,” said Alice; “all I know is, it would feel very queer to me.” “You!” said the Caterpillar contemptuously. “Who are you?” Which brought them back again to the beginning of the conversation.

As a representative example, the spectra of **T6A3** (Figure 53a) were recorded every 5 s during 3 h of illumination, while a reference sample was kept in the dark during the same time. After

the excitation period, the white light was turned off, and the decay of the polarons was monitored for another 48 h, using only the NIR source. The combination of the two measurements allowed us to monitor the time-evolution of the intensity of the polaron transition P1 during illumination and its subsequent decay in the dark (Figure 53b). Both time-evolutions could be best fitted with double-exponential functions, indicating that both charge generation and decay probably proceeded via two mechanistic pathways. A possible explanation is that the predominant mechanistic pathway may depend on the charge density within the nanowire. During illumination, a slower polaron generation mechanism would dominate above a certain density threshold, while a slower decay mechanism in the dark would be prevalent below a certain threshold.

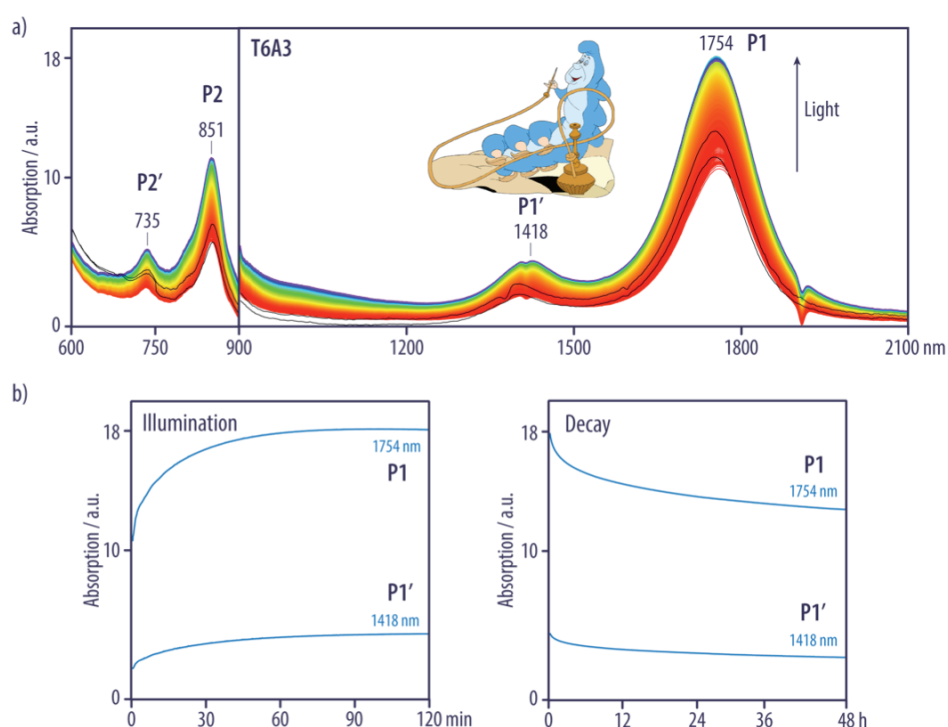


Figure 53. *a)* The formation of polarons in nanowire solutions of **T6A3** ($c = 1\text{ mmol/L}$) under white light illumination was monitored by in situ UV/vis/NIR steady state spectroscopy (rainbow colour-code); a reference sample was kept in dark and measured before and after the experiment (black curves). *b)* The evolution of the P1 and P1' transition intensities was plotted as a function of time during the illumination and the subsequent decay in the dark.

These measurements were executed under the exact same conditions for nanowire solutions of the whole series of compounds **TnA3** ($n = 3\text{--}8$). All derivatives showed double-exponential time-evolutions, from which two time constants for charge generation τ_{1}^{gen} and τ_{2}^{gen} , two decay time constants τ_{1}^{dec} and τ_{2}^{dec} , as well as a saturation absorption $A_{\text{sat}} = A(\text{P1})/A(\lambda_{\text{max}})$ could be extracted (Figure 54). The latter normalization was employed in order to obtain a coarse estimate for the actual number of charges per molecule. For this, the polaron extinction coefficient was assumed to have, in first approximation, a value close to that of the main UV/vis band.^{222,224}

Notably, the rates of polaron generation $k_1^{\text{gen}} = 1/\tau_1^{\text{gen}}$ and $k_2^{\text{gen}} = 1/\tau_2^{\text{gen}}$ decreased for an increasing oligothiophene length. The relative absorbed photon fluxes were estimated for each oligothiophene nanowire solution from their absorption spectra and the emission spectrum of the plasma lamp. As the relative number of absorbed photons increased within the series **T3A3–T8A3**, correcting the measurements for the photon flux would even make this trend more pronounced. A plausible explanation for the observed trend could be the fact that excited states of shorter oligothiophenes typically have higher energy levels, from which the activation energy for a subsequent electron transfer should be reduced.

Remarkably, the saturation absorptions A_{sat} showed a clear odd-even effect with an increasing number of thiophene units, as nanowires obtained from derivatives with an odd number of thiophene units accumulated about 2.5 mol% of charge carriers, while 4 mol% of charge carriers were formed in the case of compounds with an even number of thiophene units. Considering an intermolecular spacing of 4.6 Å along the nanowires, as observed by XRD, a concentration of charge carriers of 4 mol% would translate into a linear charge density of $8.7 \cdot 10^5 \text{ cm}^{-1}$. While this value is still lower than the reported critical charge density of 10^7 cm^{-1} for a transition to metallic conductivity,²⁰⁸ it remains impressively high when taking into account the fact that, in our case, those charge densities were achieved by simple illumination of nanowire solutions without the use of any strong oxidant as a chemical dopant or electrochemical potential.

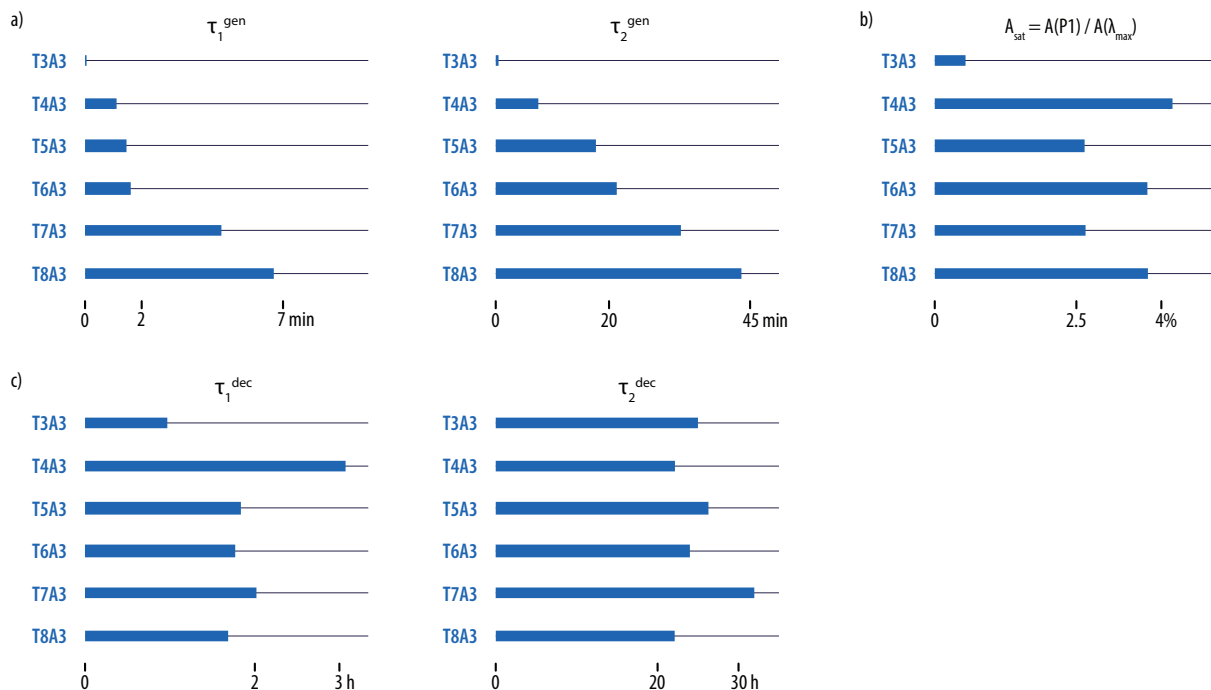


Figure 54. Summary of the dynamics of polaron generation and decay for the derivatives **TnA3** ($n = 3-8$). *a*) Both time constants τ_1^{gen} and τ_2^{gen} for charge generation increased for increasing oligothiophene length. *b*) The maximum proportion of charges formed under illumination A_{sat} exhibited an odd-even effect as a function of the number of thiophenes. *c*) An odd-even effect was also observed for the decay constants, in particular for the τ_2^{dec} (right).

Moreover, the decay time constants τ_1^{dec} and τ_2^{dec} varied from 1 h to more than 30 h. The surprisingly long lifetimes of the polarons may indicate a deep trapping of electrons or a large stabilization of the positive polarons, for example, due to their delocalization along the nanowires. Again, an odd-even effect was observed in the evolution of the decay time constants with an increasing number of thiophene units, as derivatives with an odd number of thiophene units exhibited slightly longer decay times. The presence of odd-even effects with increasing number of thiophene rings probably originated from the difference in the symmetry of the molecule. As an example of a possible explanation, a varying molecular symmetry may result in different compensations of dipoles of the oligopeptide substituents, which may in turn alter the internal supramolecular arrangement within the aggregates (e.g., the helicity) and/or the stability of charged states.

It should further be noted that the evolution of the ratio of the time constants of charge generation and decay with the number of thiophene units could not be correlated with the evolution of the saturation absorptions. This may indicate that the latter were not related to a simple dynamic equilibrium where generation and decay processes compensate each other, but rather to the intrinsic capacity of the nanowires to accept charge carriers. Hence, the decay presumably did not result from the reverse electron transfer mechanism, but was rather due to the reduction from a different species than the electron acceptor of the generation process. Nonetheless, it is not excluded that the reductive species was the product of chemical reactions following the initial electron transfer to the acceptor.

3.5 Influence of Oligopeptide Length

Similar illumination experiments were also conducted in order to compare **T6A2/T6A3**, **T7A2/T7A3**, and **T8A2/T8A3** (except for using a halogen lamp as the light source, resulting in a different illumination spectrum, as well as a lower power of around 4 mW). This allowed us to investigate the effect of the oligopeptide length on the polaron generation and decay (Figure 55). In this case, faster charge generation rates and slower decay rates were observed for the respective derivatives comprising di-L-alanine segments, when compared to the counterparts bearing tri-L-alanines (with the only exception of a faster decay in the case of **T6A2**, compared to **T6A3**). However, the maximum intensity reached under illumination was lower in the case of di-L-alanines. The stronger aggregation of the tri-L-alanine segments may account for the observed differences. Finally, it should be noted that, with an illumination power about an order of magnitude lower as compared to the previous series of experiments, the generation time constants were indeed about one order of magnitude longer, but the saturation absorptions were of a similar magnitude. This corroborates the previous notion that the saturation

absorption did likely not correspond to a dynamic equilibrium between two reverse electron transfer mechanisms.

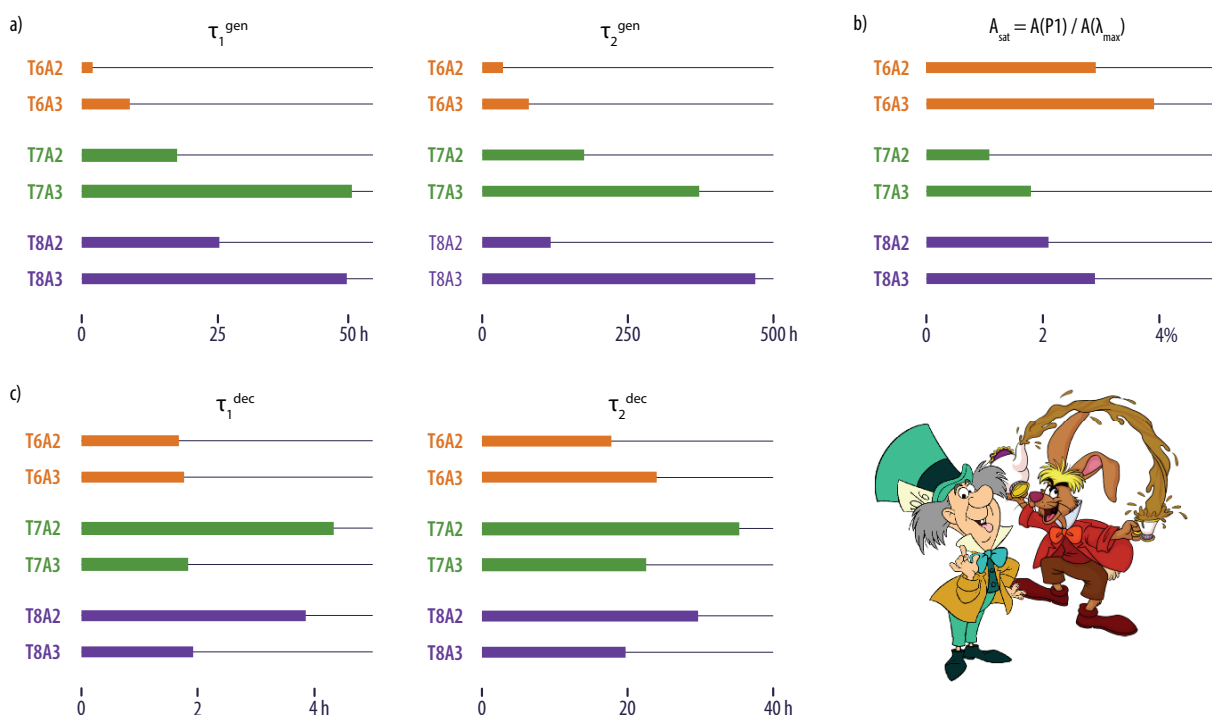


Figure 55. Comparison of the positive polaron generation and decay dynamics between corresponding di- or tri-L-alanine derivatives. *a)* Charge generation was faster for di-L-alanine derivatives. *b)* Higher charge densities could be reached for tri-L-alanine derivatives. *c)* Polaron decay in the dark was slower for di-L-alanine derivatives, except for **T6A2**.

3.6 Polaron Formation in Nanowires from Achiral Compounds

The formation of polaron-like charge carriers was also observed for the aggregating achiral derivatives **T6G2**, **T7A0**, and **T8A0** that presumably formed twisted stacks similar to the corresponding derivatives **T6A2**, **T7A2**, and **T8A2**, but without a homochiral supramolecular helicity. The same illumination experiments were performed and compared to the results obtained from the corresponding chiral compounds (Figure 56). In all cases, both generation and decay were faster, and the saturation absorption was substantially lower for the achiral derivatives. For instance, **T6G2** showed generation rates about three times higher, a saturation of about one quarter in intensity and decay rates four to five times as fast, as compared to **T6A2**. Very similar trends were observed for **T7A0** versus **T7A2** as well as for **T8A0** versus **T8A2**. Hence, the absence of homochiral supramolecular helicity, and the supposedly higher degree of disorder resulted in significantly lower concentrations of charge carriers with significantly shorter lifetimes within the nanowires.

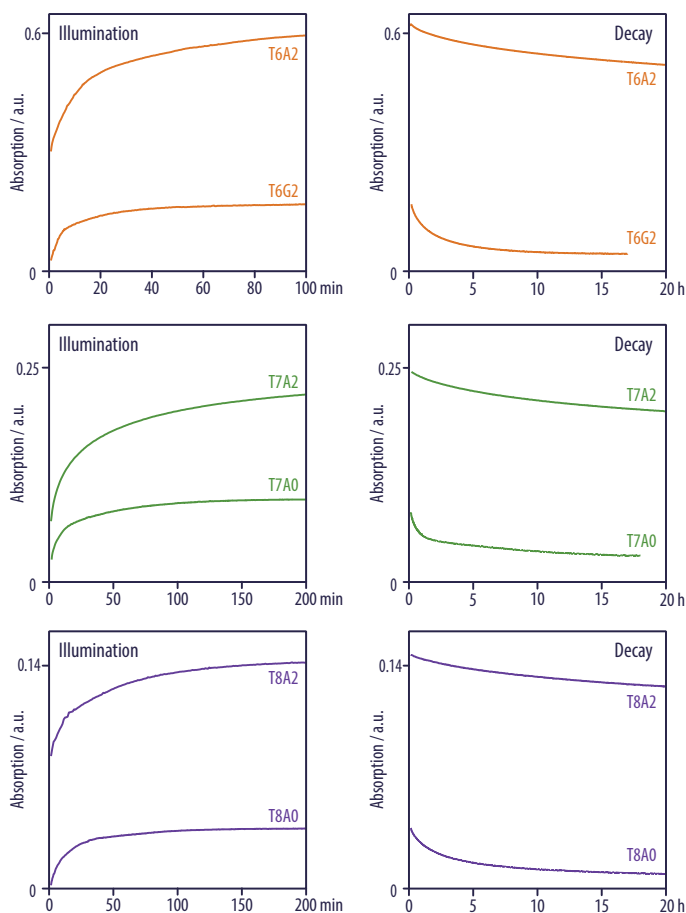


Figure 56. The achiral derivatives showed faster generation and decay of charge carriers and a lower saturation intensity, when compared to corresponding chiral compounds. *a*) Polaron P1 transition intensity (at 1776 nm) for **T6G2** and **T6A2** during illumination (left) and in the dark (right). *b*) Polaron P1 transition intensity (at 2029 nm) for **T7A0** and **T7A2** during illumination (left) and in the dark (right). *c*) Polaron P1 transition intensity (at 2022 nm) for **T8A0** and **T8A2** during illumination (left) and in the dark (right).

3.7 Conclusions

The use of β -sheet forming oligopeptides was shown to be a useful tool to form well defined nanowires consisting of a single stack of molecules and featuring a helically twisted, parallel-displaced arrangement. This supramolecular arrangement of electron-rich chromophores proved in turn to promote a facile photogeneration of polarons at charge densities close to 10^6 cm^{-1} and with unusually long lifetimes of several days. As a result, polaron generation under illumination and decay in the dark could be straightforwardly monitored by steady-state spectroscopy for nanowire solutions of the **TnAp** derivatives. Notably, nanowires from derivatives comprising even numbers of thiophene units accumulated significantly higher concentrations of charges. Moreover, the homochiral helix sense in aggregates comprising oligo(alanine) segments resulted in substantially longer nanowires with a supposedly higher degree of internal order, which was presumably the reason for their higher polaron concentrations under illumination and longer lifetimes in the dark. The saturation absorption under illumination increased even more with the oligopeptide length.



Acceptor-Donor-Acceptor Triad Forming Lamellar Phases

4 Acceptor-Donor-Acceptor Triad Forming Lamellar Phases

4.1 Introduction

Research in photovoltaic devices is one of the corner stones of solving the problems associated with the world's growing energy demand.^{1,2} In this context, the use of organic materials promises a low cost production of large area, flexible, and light devices. In organic photovoltaic materials, charge generation at the interface between an electron donor and an acceptor component as well as charge extraction towards the electrodes are the two crucial steps that determine device performance.^{33,44,45} Therefore, both a large interface and continuous charge percolation pathways are essential for an overall efficient energy conversion. Hence, the active layer morphology is one of the most important parameters determining device performance.⁹⁰ To this end, simply blending the donor and the acceptor components such that they form an interpenetrating network called "bulk heterojunction" (BHJ) has been the most successful strategy to date.^{12,37,39} In BHJ devices based on an electron donor polymer and a fullerene acceptor, for instance, the formation of a three-phase system including an amorphous mixed interphase of the two components plays a major role for their superior efficiency.¹¹²⁻¹¹⁵ However, the exact structure of BHJs is difficult to control, and they will still contain domains that trap excitons or charges. Moreover, their kinetically controlled formation results in metastable morphologies that slowly undergo macrophase segregation, resulting in significantly reduced device performance over time.^{12,119}

Covalently connecting the donor and acceptor components has been explored as an approach to address these issues.^{91,127,128} For example, brush copolymers of acceptor moieties grafted to an electron-rich polymer backbone as the donor component have been referred to as "double-cables" that transport electrons through the pendant groups and holes through the polymer backbone. Similarly, dyads or triads of small molecule donors and acceptors have been designed with the purpose of maximizing the donor/acceptor interface. The intimate mixing of donor and acceptor moieties in such "molecular heterojunctions" is supposedly related to the mixed phase observed in polymer:fullerene BHJs. However, typical power conversion efficiencies of devices using such materials were well below 1%,^{127,128} and in some cases even significantly lower than those of the corresponding blends,²²⁷ presumably due to the better charge extraction through larger domains of the pure components. One may conclude that covalently linking the donor and acceptor components should be complemented with the formation of nanostructures with at least one extended dimension in so-called "ordered heterojunctions". In this context, Hashimoto *et al.* prepared a fullerene-substituted oligothiophene that formed lamellar phases in thin

films.²²⁸ Geng *et al.* prepared a liquid-crystalline dyad comprising a fluorene-*alt*-bithiophene oligomer and a perylene acceptor that, likewise, self-assembled into lamellar phases.^{140,142} Tuning the band gap of the donor part and adding a flexible alkyl spacer between the donor and acceptor to accommodate packing constraints resulted in a power conversion efficiency of 2.7%,¹⁴³ which represents one of the best values reported for a single-component organic solar cell but is still low compared to BHJs. This problem has mostly been attributed to the lack of long-range order; as the lamellar thickness is typically on the order of only a few nanometers, an increasing number of defects will quickly impede charge transport and favor charge recombination.

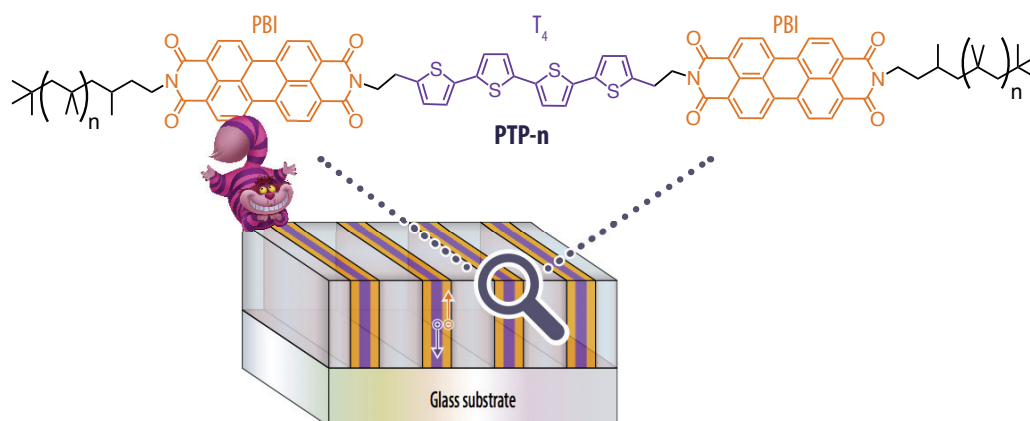


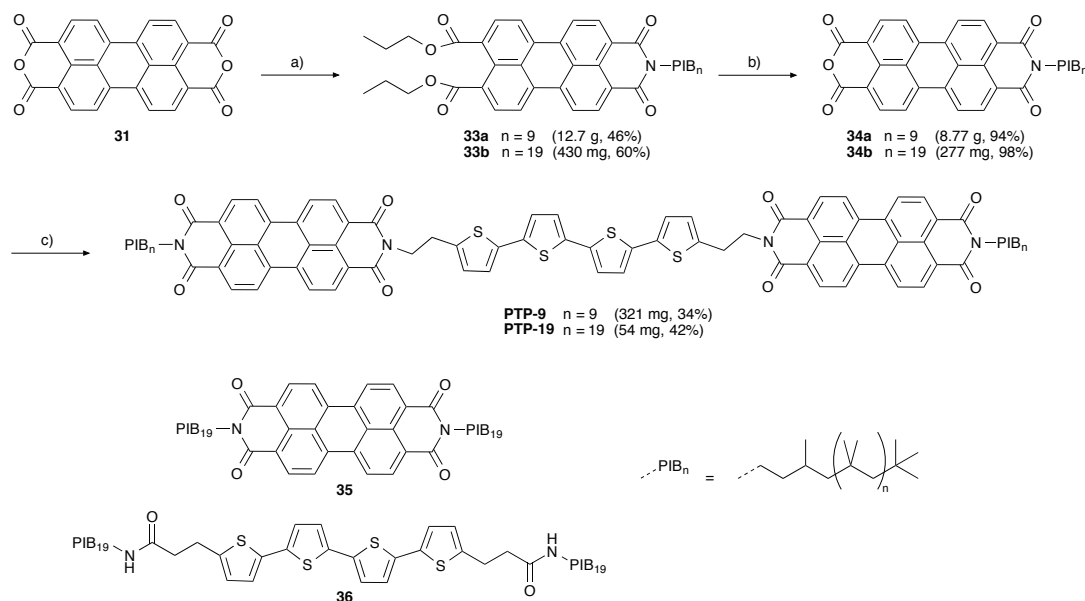
Figure 57. Molecular design and schematic illustration of lamellar phase enhanced by the phase segregation between the rigid core and the flexible polymer side chains.

Here, we show that terminally attaching soft polymer segments to an acceptor-donor-acceptor triad is an excellent way to reliably obtain thin films comprising well-ordered lamellar nanostructures (Figure 57). This “coil-rod-coil” architecture was chosen because it was expected to strongly favor microphase segregation into domains with non-curved interfaces. The resulting confinement of the triad core should consequently promote a packing of the acceptor and donor segments into separate sublayers. As will be discussed in detail in the following sections, we chose to investigate the triad (perylene bisimide)-quaterthiophene-(perylene bisimide) substituted with two differently long poly(isobutylene) (PIB) segments (number-average degrees of polymerization $P_n = 9$ and 19) that will be named **PTP-9** and **PTP-19**, respectively. The triads were shown to form lamellar phases, with an “edge-on” orientation of the layers relative to the substrate. Rubbing and annealing served to achieve a macroscopic alignment of the lamellar phases. In this context, the longer polymer segments of **PTP-19** helped to improve the degree of long-range order and, moreover, prevented the lamellae to attain a face-on orientation that was observed in the case of **PTP-9** after rubbing and annealing. Transient absorption studies confirmed that light absorption was followed by charge separation.

The charges lifetimes were increased in thin films in comparison to solution-phase samples, and were even higher in the case of **PTP-19** than observed for **PTP-9**. While the present study represents a first step in studying the effect of introducing phase segregating side chains on the resulting phase morphology, the ultimate goal is to develop efficient strategies to rationally strengthen the lamellar phase formation.

4.2 Synthesis and Steady-State Spectroscopy

The synthesis of **PTP-9** and **PTP-19** started from perylene bisanhydride **31** that was first coupled to the poly(isobutylene) amines $\text{PIB}_9\text{-NH}_2$ **32a** and $\text{PIB}_{19}\text{-NH}_2$ **32b**, respectively (Scheme 7). Due to solubility reasons, however, a simple statistical coupling of one equivalent of the poly(isobutylene) amine to perylene bisanhydride yielded exclusively the symmetrically disubstituted product. In order to circumvent this issue, **31** was first reacted with propanol in the presence of a strong base in DMF.^{229,230} The resulting partially esterified intermediate became well soluble in DMF and was then statistically reacted in situ with substoichiometric amounts of poly(isobutylene) amine **32a** or **32b**. Addition of bromopropane finally yielded the unsymmetric perylene diesters **33a** and **33b**, respectively. The latter were subsequently saponified in acidic conditions, and the resulting perylene monoanhydrides **34a** and **34b** were coupled to 2,5'''-bis(2-amino-ethyl)-5,2':5',2'':5'',2'''-quaterthiophene¹⁵⁵ in quinoline at 175°C, yielding the desired triads **PTP-9** and **PTP-19**. Moreover, the poly(isobutylene)-substituted perylene bisimide **35** and the quaterthiophene **36** (**T4A0**) were prepared as reference compounds.^{155,198}



Scheme 7. Synthesis of the poly(isobutylene)-substituted triads **PTP-9** and **PTP-19**. *Reagents and conditions:* a) (i) propanol, DBU, DMF, r.t., 16 h; (ii) PIB-NH_2 , THF, r.t., 3 d; (iii) bromopropane, r.t., 16 h; b) $\text{TsOH} \cdot \text{H}_2\text{O}$, toluene, 95°C, 16 h; c) 2,5'''-bis(2-amino-ethyl)-5,2':5',2'':5'',2'''-quaterthiophene, $\text{Zn}(\text{OAc})_2$, quinoline, 175°C, 16 h.

Molecularly disperse solutions of **PTP-9** and **PTP-19** in *o*-dichlorobenzene ($c = 25 \mu\text{mol/L}$) were obtained at 100°C . The UV/vis absorption spectra of these solutions at 100°C (Figure 58a) resembled a superposition of the absorption spectra of perylene bisimide **35** and quaterthiophene **36**, confirming that no coupling occurred between both chromophores. While the solutions remained optically clear upon cooling, both blue-shifted H-bands and red-shifted J-bands appeared in the absorption spectra, indicating that the triads started to form spectroscopic aggregates. The H-bands of the perylene bisimide chromophores presumably overlapped with the quaterthiophene absorption, so that the contribution of the latter became impossible to distinguish. Thin film samples of **PTP-9** and **PTP-19** were prepared on glass slides by doctor-blading from *o*-dichlorobenzene solutions ($c = 5 \text{ mg/mL}$) at 180°C . As no thermal transitions were observed in differential scanning calorimetry up to temperatures of 380°C except for the poly(isobutylene) glass transition at around -60°C , absorption spectra of the thin films were recorded over a temperatures range of $25\text{--}300^\circ\text{C}$ (Figure 58b). The shape of the spectra persisted up to temperatures of about 175°C , with only a small intensity decrease of the absorption at 467 nm . Above that temperature, the shape of the absorption changed, as the bands at about 460 nm and 610 nm disappeared, and new maxima at 509 as well as 542 nm emerged. For this reason, we chose to subject film samples to further treatments at temperatures above 175°C .

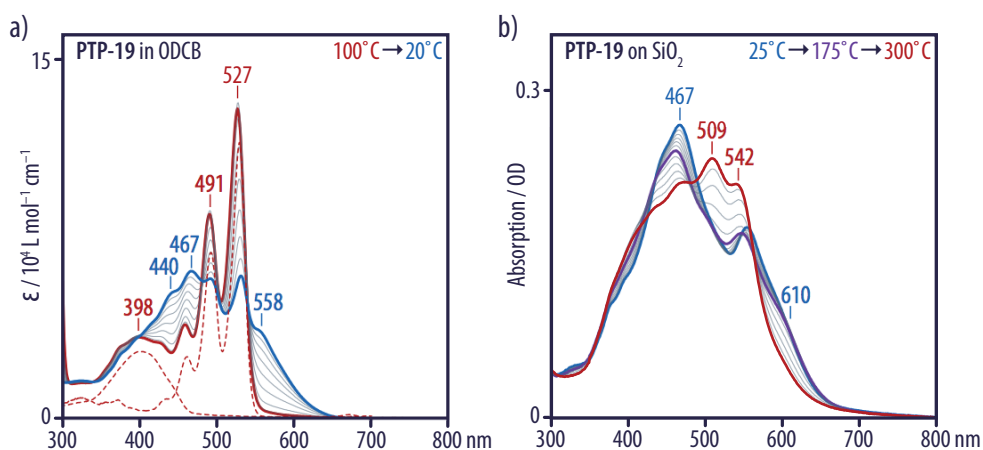


Figure 58. *a)* The UV/vis absorption spectrum of **PTP-19** in *o*-dichlorobenzene ($c = 25 \mu\text{mol/L}$) at 100°C (red) was a superposition of the contributions of perylene bisimide and quaterthiophene chromophores, as seen from a comparison to the UV/vis spectra of molecularly disperse solutions of the reference compounds **35** and **36** (red, dashed). Upon cooling to 20°C (blue), the triad formed spectroscopic aggregates, showing both H- and J-bands of the perylene bisimide. *b)* The shape of the UV/vis absorption spectra of **PTP-19** in thin films remained almost unchanged upon heating from 25°C (blue) to 175°C (purple), but underwent significant changes upon further heating to 300°C (red).

4.3 Alignment and Thin Film Morphology

In order to produce macroscopically aligned samples, the thin film samples were then subjected to mechanical rubbing with a rotating cylinder covered with a cloth at a substrate temperature

of 200°C in an inert atmosphere, followed by thermal annealing at 300°C, in collaboration with Dr. Martin Brinkmann at Charles Sadron Institute, Strasbourg. After the alignment procedure, the thin films were strongly birefringent according to polarized optical microscopy, with a transmission maximum when the crossed polarizers were oriented at 45° relative to the rubbing direction, and a total extinction across the whole sample at 0°/90° orientation (Figure 59a). This finding was an indication for a homogeneous alignment over a length scale of centimeters. Moreover, polarized UV/vis absorption spectroscopy of **PTP-9** revealed a dichroic ratio of 6.4 for the absorption band at 558 nm, with a maximum absorption when the polarizer was oriented parallel to the rubbing direction (Figure 59b). **PTP-19** showed similar absorption spectra under polarized light, but exhibited a lower dichroic ratio of 2.4. A lower ratio could come from a lower degree of orientational order or an increased angle of the chromophores relative to the rubbing direction, in case two equivalent orientations of opposite angle are possible.

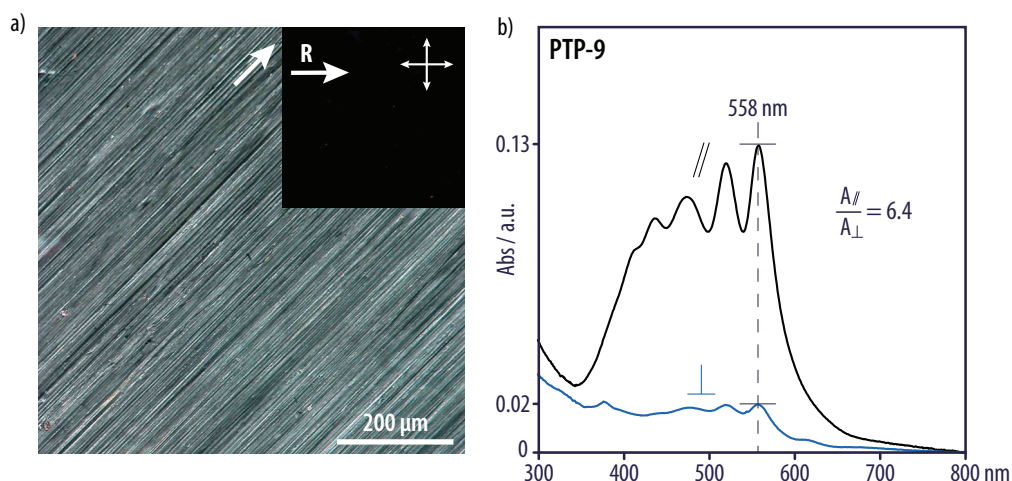


Figure 59. Aligned thin films of **PTP-9** showed birefringence and dichroism. *a)* Polarized optical micrographs showed a strong birefringence when the rubbing direction (white arrows) was oriented at 45° relative to the crossed polarizers, and no transmission the rubbing direction was perpendicular to one of the polarizers (inset). *b)* Polarized UV/vis spectra revealed an absorption maximum at 558 nm with a maximum intensity when the incident light was parallel to the rubbing direction.

We confirmed the presence of lamellar nanostructures in the rubbed thin films with macroscopically aligned lamellae oriented vertical to the substrate by a combination of small-angle X-ray scattering (SAXS), wide-angle X-ray scattering (WAXS), transmission electron microscopy (TEM), and atomic force microscopy (AFM). SAXS measurements on bulk samples of **PTP-9** exhibited series of peaks with a ratio of reciprocal spacings of $q_1:q_2:q_3 = 1:2:3$, as is characteristic for lamellar phases (Figure 60). For **PTP-19**, a ratio of $q_1:q_2:q_3:q_4 = 1:2:3:4$ was observed, with the q_3 reflection hidden in the flank of the next reflection. The main reflections corresponded to lamellar periodicities of 6.40 (**PTP-9**) and 7.47 nm (**PTP-9**), which is smaller than the respective molecular lengths of 10 and 13 nm, considering the poly(isobutylene)

segments assumed its preferred 8_3 helical conformation.²⁰⁹ Since the significantly larger cross-sectional areas of the poly(isobutylene)s (36 \AA^2)²⁰⁹ as compared to the perylene bisimide (28 \AA^2)¹⁴⁴ and quaterthiophene segments (21 \AA^2)¹⁹⁹ render an interdigitation of the former unlikely, this finding would imply that the different segments assume tilt angles relative to the layer normal. WAXS measurements revealed reflections at 3.8 and 7.9 \AA , which were attributed to π - π stacking and a packing distance typically observed for perylenes. A broad reflection was observed with an apparent maximum at 6.7 \AA and comprised at least the polymer reflection centered at around 6 \AA .^{152,231}

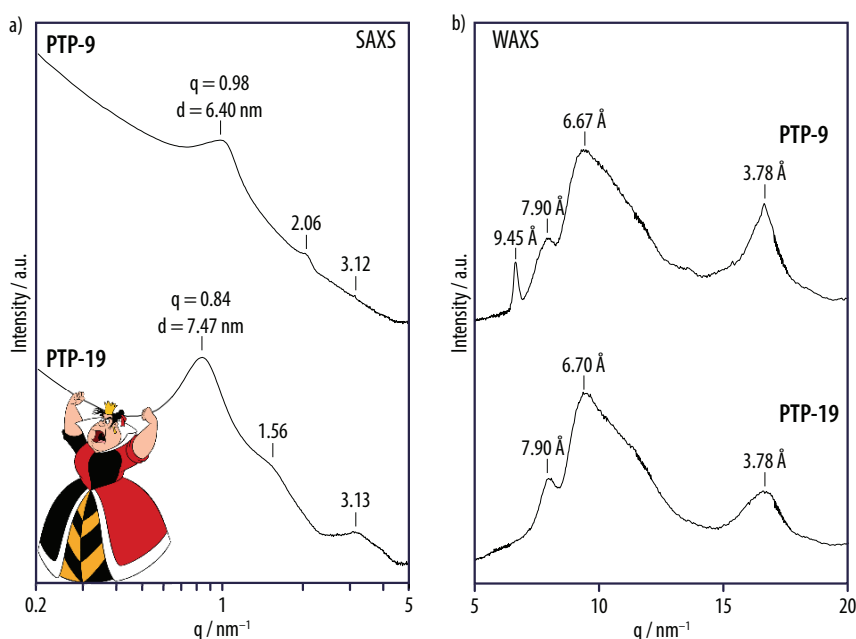


Figure 60. X-ray scattering of the triads **PTP-9** and **PTP-19** revealed lamellar structures in the bulk. *a)* In the small-angle region, lamellar phase resulted in a reciprocal spacing ratio of $q_1:q_2:q_3 = 1:2:3$ and a periodicity of 6.4 nm for **PTP-9**, and $q_1:q_2:q_4 = 1:2:4$ and a periodicity of 7.5 nm for **PTP-19**. *b)* In the wide-angle region, a π - π stacking distance of 3.78 \AA and additional spacings at about 7.9 and 6.7 \AA (that included at least the polymer reflection at about 6 \AA) could be distinguished. The reflection at 9.45 \AA for **PTP-9** probably originates from an impurity.

Further investigation of the thin film nanomorphology by transmission electron microscopy confirmed the formation of lamellar phases. After doctor blading but before annealing, the thin films of both **PTP-9** and **PTP-19** showed stripes with a periodicity of about 7 nm (Figure 61a, b). Since this periodicity was in excellent agreement with the SAXS data, one can unambiguously attribute the observed stripes to lamellae oriented normal to the substrate, with the contrast in the bright-field TEM images originating from domains of the triad cores comprising the sulfur atoms versus the peripheral isobutylene layers. For **PTP-19** with its longer polymer side chains, these stripes appeared to be locally aligned with a longer range order, indicative of aligned smectic lamellar phases. After rubbing and annealing of the samples, the lamellae of **PTP-19** were homogeneously aligned parallel to the rubbing direction over the whole film (Figure 61d), with an azimuthal orientation distribution of about 20°. In the case of **PTP-9**, the lamellar

orientation of the rubbed films changed after annealing at 300°C, from an “edge-on” to a “face-on” orientation. The change in orientation of the lamellae is visible in the bright-field TEM images showing a characteristic terraced morphology (Figure 61c). This reorientation and its dependence on the molecular length is similar to what had been observed for other perylene bisimide co-oligomers.²³²

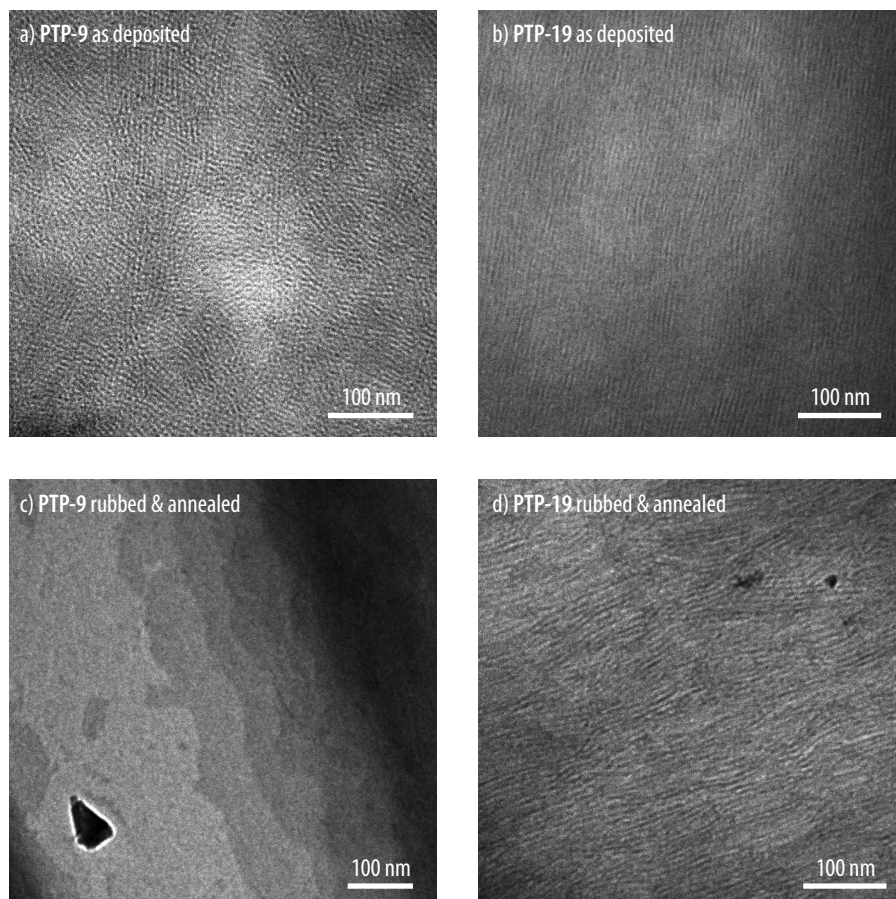


Figure 61. Transmission electron microscopy of the triads **PTP-9** and **PTP-19** revealed stripes or terraces that were attributed to lamellae oriented edge-on or face-on relative to the substrate. *a)* Films of **PTP-9** deposited by doctor-blading revealed stripes with a periodicity of about 7 nm. *b)* doctor-bladed films of **PTP-19** showed a higher degree of long range order. *c)* Upon rubbing and annealing films of **PTP-9**, the lamellae changed their orientation to a face-on orientation, resulting in terraces. *d)* This reorientation did not occur for **PTP-19** with longer side chains, which still showed stripes aligned by the rubbing process.

Atomic force microscopy (AFM) of rubbed films confirmed the TEM observations. AFM phase images of rubbed and annealed samples of **PTP-9** exhibited terraces characteristic of flat-on lamellae, of which the step height could not be determined from the corresponding height images, probably due to the soft nature of the poly(isobutylene) segments (Figure 62a). By contrast, the phase images of **PTP-19** thin films revealed a pattern of darker and lighter stripes with a periodicity of about 7 nm, presumably originating in the phase-segregated “harder” triad cores and the “softer” polymer segments exposed to the surface in the case of vertically oriented lamellae (Figure 62b).

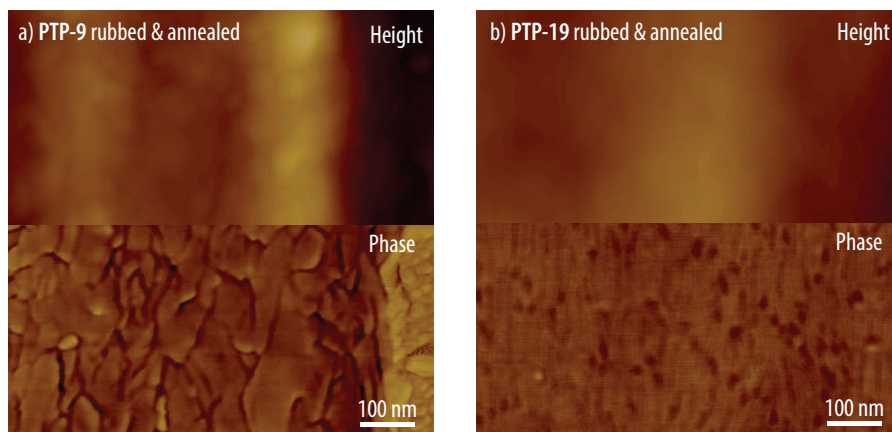


Figure 62. AFM imaging confirmed the lamellae were oriented *a)* face-on for **PTP-9** and *b)* edge-on for **PTP-19**. Rubbing direction is vertical in both cases.

Electron diffraction of the aligned thin films in collaboration with Dr. Martin Brinkmann allowed us to obtain more insight into the molecular arrangement within the layers (Figure 63). In agreement with the distances obtained from XRD, **PTP-19** showed reflections corresponding to distances of $d = 7.93$, 6.68 , and 3.66 Å. The latter was tentatively attributed to the π - π stacking distance of the aromatic core segment and their orientation relative to the rubbing axis suggested that the perylene was aligned along the rubbing axis with an azimuthal orientation distribution of $\pm 15^\circ$. **PTP-9** that formed terraces consisting of lamellae oriented flat-on showed a similar diffraction pattern. However, the reflection at 3.78 Å was less intense and the one at 7.99 was more pronounced. By tilting the same sample by an angle of 23° around the rubbing axis, the diffraction pattern was comparable to that of **PTP-19** and showed a very intense reflection at 3.77 Å. Moreover, the diffraction patterns appeared sharper for **PTP-9** with shorter side chains, which indicated a higher level of crystalline order as compared to **PTP-19** thin films.

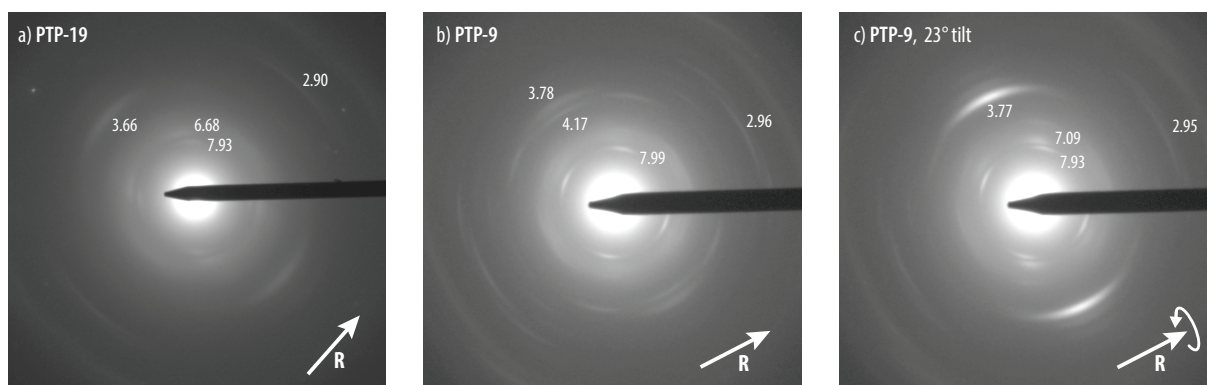


Figure 63. Electron diffraction patterns of aligned films. *a)* **PTP-19** showed reflections at 7.93 , 6.68 , and 3.66 Å corroborating the distances observed in X-ray diffraction. *b)* The diffraction pattern of **PTP-9** appeared sharper; the reflection at 3.78 Å was less intense and the one at 7.99 was more pronounced. *c)* The diffraction pattern obtained by tilting the **PTP-9** sample grid to 23° around the rubbing axis resembled that of *a)*, showing an intense band at 3.77 Å.

To summarize, the polymer-substituted triads **PTP-9** and **PTP-19** formed lamellar phases. Within these lamellae, the π -conjugated cores adopted a parallel-displaced π - π stacked arrangement with a tilt angle relative to the layer normal, serving to achieve a molecularly dense packing and compensate the large difference in the cross-sectional areas of the core and the attached polymer segments.

4.4 Charge Generation under Illumination

Solutions of **PTP-19** in tetracholorethane (TCE; $c = 10 \mu\text{mol/L}$) thermally equilibrated at 100°C for 1 min, as well as solutions of a mixture of the reference compounds **35/36** (2:1) at the same concentration of chromophores remained molecularly disperse for several hours at room temperature, according to UV/vis spectroscopy (Figure 64). However, while the emission spectrum of the mixture at an excitation wavelength of 400 nm was a superposition of the spectra of the two chromophores, the emission spectrum of **PTP-19** resembled the emission of the perylene bisimide alone, but with its intensity quenched by 99%. The absence of any quaterthiophene emission feature in the emission spectrum of **PTP-19** suggested an efficient energy transfer from the quaterthiophene to the perylene moiety, and the fluorescence quenching can be seen as an indication of a subsequent charge separation.

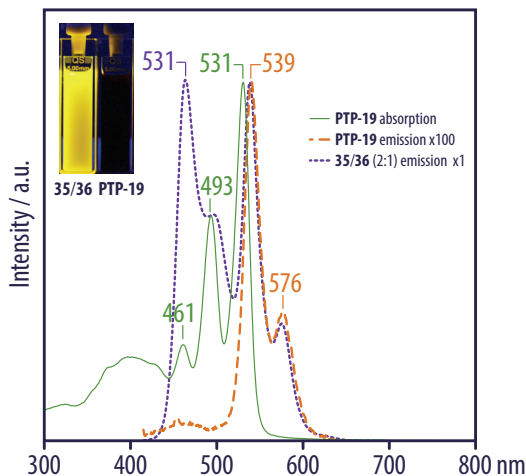


Figure 64. The emission spectrum of the triad **PTP-19** (orange dashed curve) was identical to the emission of the perylene **35**. However, compared to the mixture **35/36** (2:1), with the same composition of the individual chromophores, fluorescence was quenched to more than 99% (inset). In comparison with the mixture, the absence of quaterthiophene emission feature in the emission of the triad **PTP-19** suggested an energy transfer to the perylene moiety.

In order to verify this hypothesis, transient absorption (TA) spectroscopy was performed in collaboration with Dr. Natalie Banerji at EPFL, Lausanne, on the triad **PTP-19**, the individual reference molecules **35** and **36** as well as their mixture **35/36** (2:1), both in molecularly disperse solutions in TCE and in thin films. Since the absorption bands in the solution-phase

spectra were well separated, the perylene bisimide moieties could be exclusively excited at 530 nm, while mostly the quaterthiophene chromophores were excited at 390 nm. Exciting the perylene **35** or the mixture **35/36** (2:1) at 530 nm yielded identical TA spectra that showed the ground state bleaching, the stimulated emission, and the absorption of the excited perylene bisimide in the S_1 state and did not change on the experiment time scale of 1 ns (Figure 65b). Similarly, the TA spectra of the mixture **35/36** (2:1) excited at 390 nm were comparable to those of the pure quaterthiophene **36** as they showed the transition of the excited quaterthiophene from the singlet to the triplet state with a time constant of 400 ps (Figure 65d, e). The mixture exhibited an additional small contribution of the TA spectrum of **35** that also had a UV/vis absorption at 390 nm. Thus, one can conclude that a quaterthiophene and a perylene bisimide chromophore that are not covalently bonded to one another do not exert an influence on their respective transient absorption spectra at the employed concentration ($c = 10 \mu\text{mol/L}$).

By contrast, the initially formed perylene bisimide in the S_1 state was quenched within a few picoseconds in the case of the triad **PTP-19** (Figure 65c). We thus first observed a decrease of the stimulated emission that was associated to the formation of two new bands at 690 and 717 nm that can be attributed to a quaterthiophene radical cation and a perylene radical anion, respectively.^{139,219} Afterwards, the ground state bleaching and both peaks of the charged species decreased to zero. In this process, charge separation by hole transfer from the S_1 state of the perylene bisimide to the quaterthiophene and charge recombination occurred and were correlated to time constants of 5 and 27 ps, respectively, as deduced from multi-exponential global fitting analysis. It should be noted that a small, long-lived photoabsorption at about 710 nm was observed that was tentatively attributed to small amounts of **35** as an impurity in the sample. Upon excitation at 390 nm, the triad **PTP-19** also did not exhibit any feature of quaterthiophene in the singlet or triplet state (Figure 65f). The TA spectra instead revealed the excited perylene bisimide in the S_1 state, from which charge separation and recombination occurred with similar time constants as after excitation at 530 nm. The relative contribution of the excited perylene bisimide was now significantly larger than in the case of the mixture **35/36**. Consequently, this contribution could not be explained in this second case by the absorption of the perylene bisimide at 390 nm alone, and suggested a fast Förster energy transfer from the excited quaterthiophene to the perylene bisimide occurred with a time constant below the resolution of the experimental setup.

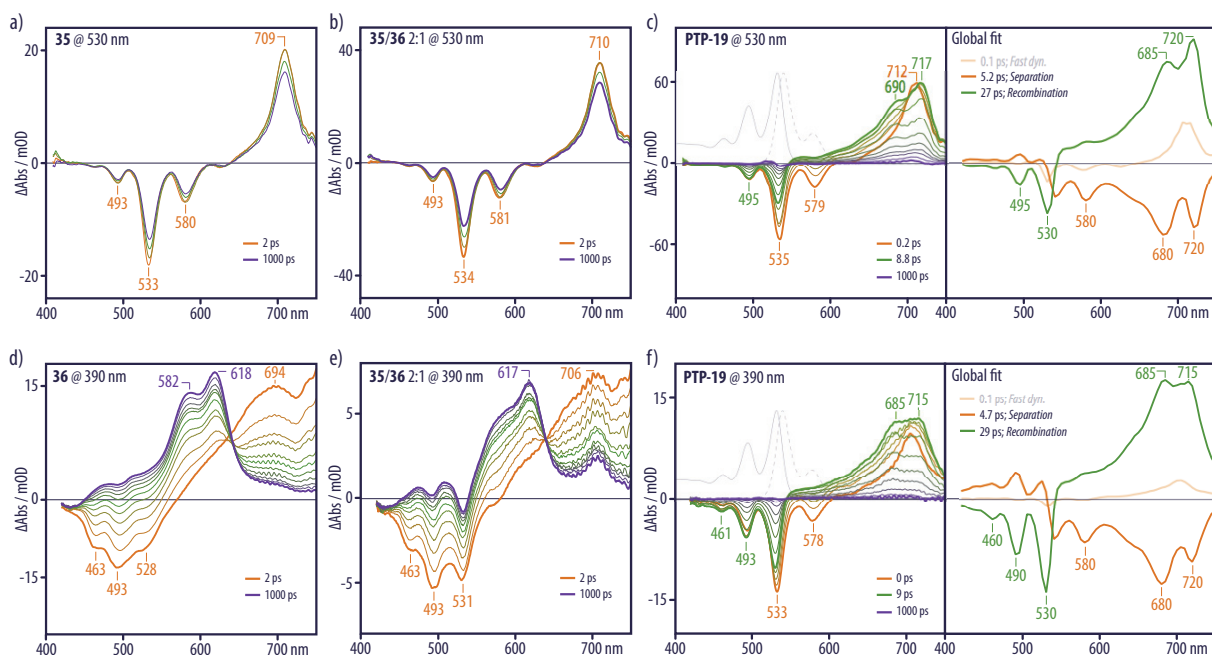


Figure 65. Transient absorption spectroscopy of the triad **PTP-19** in solution revealed charge separation and recombination upon light absorption. *a)* TA spectra of **35** excited at 530 nm showed the typical ground state bleaching, stimulated emission, and photoinduced absorption of the perylene in the S_1 state. *b)* TA spectra of a mixture **35/36** (2:1) excited at 530 nm showed the perylene in the S_1 state without any influence of the quaterthiophene **36**. *c)* TA spectra of **PTP-19** excited at 530 nm (left): from the perylene in the S_1 state (orange curve), charged species formed (green curve), and recombined to the ground state (purple curve); the corresponding global fitting analysis (right) correlated charge separation to a time constant of 5 ps (orange curve) and recombination to a time constant of 27 ps (green curve). *d)* TA spectra of **36** excited at 390 nm showed the quaterthiophene in the S_1 state, which evolved to the triplet state with a time constant of 400 ps. *e)* TA spectra of **35/36** (2:1) excited at 390 nm were similar to *d)*, with an additional contribution from the perylene in the S_1 state since it is absorbing as well at 390 nm; no influence of the perylene on the excited quaterthiophene was observed. *f)* TA spectra (left) and the corresponding global fit (right) of **PTP-19** excited at 390 nm were almost identical to *b)*, showing that an energy transfer from the quaterthiophene to the perylene occurred faster than the resolution of the experimental setup.

Transient absorption measurements were then conducted on thin films obtained by drop-casting from TCE solutions. Upon irradiation at 530 nm, only the perylene moiety was excited. As had been the case for the solution-phase samples, the TA spectra of **35** and the mixture **35/36** (2:1) were identical, showing the ground state bleaching in the 420–570 nm region, the stimulated emission at 560 nm, and a broad photo-induced absorption visible in the region above 600 nm (Figure 66a, b). The decay of these three features was associated to the same time constants and thus correlated. At an excitation wavelength of 390 nm, a more significant amount of the perylene was excited in addition to the quaterthiophene, as compared to the solution-phase samples, since the perylene absorption in the aggregated form significantly extended to the blue. TA spectra of films of the mixture **35/36** (2:1) (Figure 66e) appeared like the superposition of the TA spectra of **35** (Figure 66d) and **36** excited at the same wavelength. The ground state bleaching, stimulated emission, and broad photo-induced absorption of the perylene was superposed with the broad photo-induced absorption of the quaterthiophene that featured a maximum at around 700 nm. On the other hand, the TA spectra of the triad **PTP-19**

excited at either 530 or 390 nm were very similar to one another and showed a different evolution than the reference mixture (Figure 66c, f). The initial excited state featured the ground state bleaching below 560 nm, the stimulated emission at 560 nm, and a broad photo-induced absorption with a peak at around 710 nm. The latter peak was reminiscent of the absorptions of the charged species in solution and thus tentatively attributed to charged species in the solid state. The initial increase of this peak was correlated to a decrease of the stimulated emission, associated to a time constant of 1–2 ps, and attributed to charge separation. It should be noted that the global fitting analysis revealed a simultaneous increase of the ground state bleaching (peaks around 440 and 470 nm) correlated to the same time constant of 1–2 ps (Figure 66c, f; right). A possible explanation of this phenomenon would be the migration of the exciton to regions where the absorption coefficient of the perylene is different due to disorder within the film, which supposedly occurred at a time constant similar to the charge separation. Finally, the decay of the ground state bleaching and the peak at 710 nm was attributed to charge recombination occurring with a time constant of about 150 ps according to the global analysis. Differently from the solution-phase spectra, however, the system did not completely return to the ground state. Instead, a broad absorption peak at 710 nm persisted on the experiment time scale of 1.5 ns, suggesting the formation of long-lived charge carriers in the thin film samples.

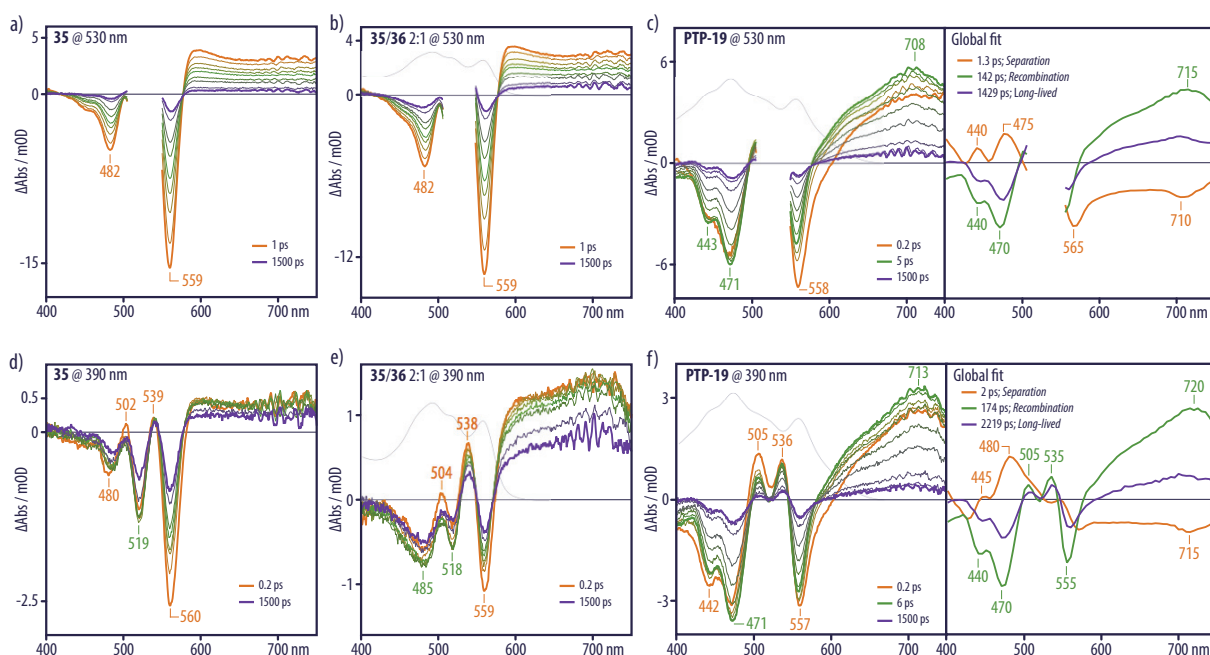


Figure 66. Transient absorption spectroscopy in thin films of **PTP-19** showed a slower charge recombination than in solution and the eventual formation of long-lived charge carriers. *a–b*) TA spectra of the perylene **35** alone and of the mixture **35/36** (2:1) excited at 530 nm were identical. *c*) TA spectra (left) and the corresponding global fitting analysis (right) of **PTP-19** excited at 530 nm showed the formation of charged species with an absorption peak at around 710 nm; charge separation and recombination occurred with time constants of 1 and 140 ps, respectively; long-lived charge carriers were formed. *d*) TA spectra of **35** excited at 390 nm. *e*) TA spectra of **35/36** (2:1) excited at 390 nm looked like a superposition of the spectra of both pure compounds excited at the same wavelength. *f*) TA spectra (left) and the corresponding global fitting analysis (right) of **PTP-19** excited at 390 nm were comparable to *b*).

The TA spectra of thin film samples of **PTP-9** were qualitatively identical to those of **PTP-19**. A detailed comparison of the time evolution of the TA intensity at 710 nm, however, showed that the charge-separated species were slightly more long-lived for **PTP-19** than for **PTP-9** (Figure 67a). While the difference was small, it may still indicate that the higher degree of nanostructural order of **PTP-19** was beneficial for charge delocalization and stabilization. Furthermore, the anisotropy of the charged species at 710 nm was evaluated on films of **PTP-9** that had been excited at 530 nm (Figure 67b). As expected, films before alignment by rubbing showed an anisotropy coefficient lower than 0.4, while aligned films had a coefficient well above. For the non-aligned film, the anisotropy was stable over the timescale of the experiment, which indicated that the charged species did not travel from across domain boundaries and kept their (local) alignment.

In summary, TA spectroscopy confirmed that charge separation occurred in the triads **PTP-9** and **PTP-19** upon light absorption. The initial charge separation process involved the excited state of the perylene bisimide moiety, which could be accessed either by direct excitation or by energy transfer from the excited quaterthiophene moiety. Charge generation was found to be faster and charge recombination slower in thin films as compared to solution-phase samples. The faster charge separation was presumably due to the closer proximity of the chromophores in the solid state, while the slower recombination and especially the formation of long lived charged species was most likely due to the higher stability of charges delocalized in stacks of the triad.

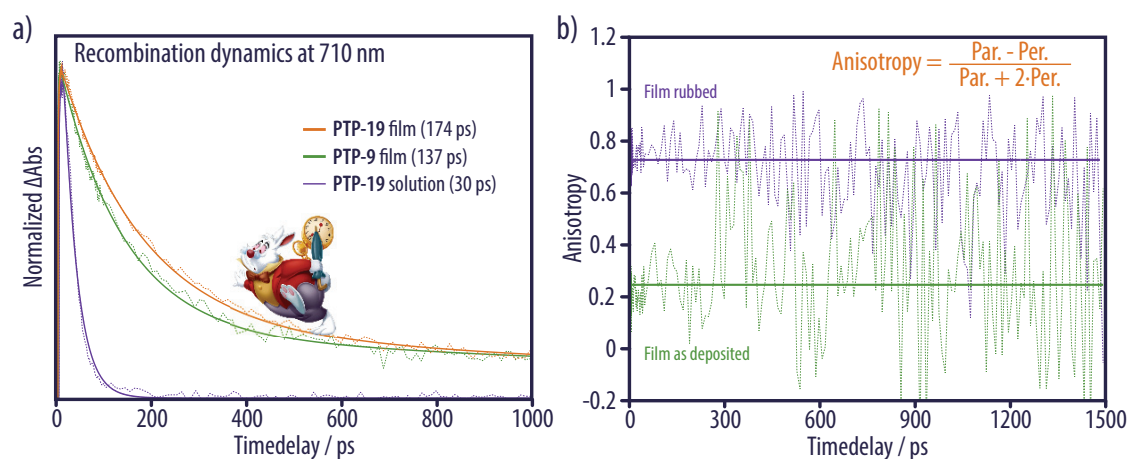


Figure 67. a) Comparison of the dynamics (dashed curves) and the corresponding fit (solid curves) showed that recombination was slower in films compared to solutions, and films made from **PTP-19** showed a slightly slower recombination as compared to **PTP-9**. b) Anisotropy was calculated at 710 nm and after excitation at 530 nm; aligned films showed an anisotropy well above that of non-aligned films; the stability of the anisotropy for non-aligned films suggested that charges did not travel between domains within the 1.5 ns timeframe of the experiment.

4.5 Conclusions

We prepared a perylene-quaterthiophene-perylene triad substituted with poly(isobutene) chains that served to induce the reliable formation of lamellar phases by means of the phase segregation between the rod-like triad core and the attached random coil polymers. In thin films, the triads indeed gave rise to lamellar structures that could then be aligned by rubbing and annealing. The longer side chains of the derivative **PTP-19** helped to increase the long-range order and maintain an “edge-on” orientation of the lamellae relative to the substrate after rubbing and annealing. In solution, the fluorescence of the triad **PTP-19** was quenched to more than 99% compared to the mixture **35/36** (2:1). Transient absorption measurements confirmed that fluorescence quenching was due to charge separation between the perylene and quaterthiophene moieties, followed by recombination. In thin films, this recombination was slower, and long-lived charged species were observed, presumably due to stabilization through delocalization in stacks of the chromophores. The stable anisotropy factor recorded for nonaligned films suggested that charges do not travel across domain boundaries within the 1.5 ns of the experiment. In this way, the higher degree of long-range order in films of **PTP-19** should enhance charge stabilization, and was likely responsible for the even slower charge recombination compared to films of **PTP-9**.

An investigation of photovoltaic devices from these materials was beyond the scope of the present study, in particular, because it would have required using a more promising donor segment than the quaterthiophene. Nevertheless, our investigations demonstrate that the terminal attachment of soft polymer segments to a triad system represents a viable concept to prepare triad-based materials with a phase morphology suited for an ordered heterojunction, and that this morphology was beneficial for the stabilization of charge carriers.

Final Conclusions and Outlook

5 Final Conclusions and Outlook

In present thesis, 1D and 2D organic semiconductor nanostructures were prepared from nanowire-forming oligothiophenes with oligopeptide-polymer substituents and an acceptor-donor-acceptor triad functionalized with flexible polymer chains, respectively. Their structural features and spectroscopic properties were characterized in detail, and their interaction with light was investigated.

To this end, soluble oligothiophene precursors with terminal chlorendylimidyl active esters as temporary protecting groups were prepared with the purpose of developing a straightforward divergent synthesis for functionalized oligothiophenes. The sterically demanding chlorendylimide group increased the solubility of all derivatives and, at the same time, enhanced the crystalizability of all intermediates. The synthetic procedures were consequently greatly simplified. Furthermore, the active ester allowed for a straightforward removal of the solubilizing group by direct coupling to a free amine. We used this approach to prepare a large library of oligothiophenes carrying polymer-oligopeptide substituents.

The obtained oligothiophenes derivatives gave rise to well-defined organic nanowires by solution-phase self-assembly. The molecular chirality of the oligopeptide segments was translated into a supramolecular helicity that, in combination with the peripheral polymer attachment, served to prevent lateral interaction. Consequently, the nanowires comprised a helically twisted stack of cofacial and parallel-displaced oligothiophenes at their core. These features were presumably responsible for the facile photo-generation of delocalized polaron-like charge carriers with lifetimes of several days and up to charge densities of 4 mol%, even in the absence of a strong oxidant as a chemical dopant or an electrochemical potential. This allowed us to monitor the charge generation under white light illumination and the subsequent decay in the dark with simple steady-state spectroscopy. Although the built-up of the charges was slow (minutes to hours), as compared to the transient phenomena observed in P3HT or bulk-heterojunctions, supramolecular helicity may be regarded as a morphological feature to stabilize charge carriers and sustain high charge densities.

In the case of the acceptor-donor-acceptor triad, the terminal polymer attachment served to use coil-rod-coil microphase segregation as a tool to reliably form lamellar phases suitable for photovoltaic applications. We showed that a derivative bearing longer polymer substituents exhibited a higher degree of long-range order, combined with a more robust edge-on orientation of the lamellae and, as a consequence, a slower recombination of the photogenerated charges. The proposed strategy might therefore be useful for other donor-acceptor systems more suited for a use in organic solar cells.

Several interesting aspects need to be addressed in future work:

- An identification of the electron acceptors in the polaron generation mechanism within the nanowires would help to improve our understanding of the exact relation between molecular design, supramolecular morphology, and opto-electronic properties. For this purpose, triplet sensitization experiments could serve to assess the role of the oligothiophene triplet state in the polaron generation. Moreover, the impact of the addition of an electron acceptor with known energy levels, in solution or attached to the oligopeptide substituents, onto the generation and decay kinetics could be investigated.
- Characterization of the transport of the polarons generated within the nanowires is certainly of great significance. In this regard, temperature-dependent ESR measurements are already being carried out in our group. Additionally, field-effect transistor behavior would be of high interest and temperature-dependent macroscopic conductivities should provide precious information on the nature of the hole transport within the nanowires. Furthermore, the high charge densities already observed by simple illumination may be increased even further in field-effect transistors with a high dielectric capacitance. Ultra-high charge densities under strict 1D confinement might result in unexpected features.
- The use of the polymer-substituted triad in an organic photovoltaic device will certainly require the replacement of the quaterthiophene by a better donor segment. It may also be beneficial to employ a donor-acceptor-donor sequence to better balance both components. Furthermore, in order to avoid the use of an inherently inactive material, the flexible aliphatic polymer chains could be replaced by an amorphous donor polymer such as a poly(triarylamine).
- Finally, by analogy to the polymer:fullerene bulk-heterojunctions where charges were shown to be generated in the mixed interphase and extracted via the pure domains, it would probably be beneficial to design a triad where the two functions of charge generation and extraction are fulfilled by different molecular segments. Thus, one can imagine using electron-rich and electron-poor π -conjugated moieties with excellent charge transport properties, separated by a chromophore that exhibit a strong and broad absorption and efficiently splits excitons. For this purpose, a chromophore with a 'donor-acceptor polarity' such as merocyanines could be considered. Indeed, the latter showed outstanding power conversion efficiencies in single-junction solar cells, presumably due to their still good ability to split excitons, even in the absence of a donor-acceptor interface.^{233,234}

Experimental Part



6 Experimental Part

6.1 Instrumentation and Methods

Atomic Force Microscopy. Thermally annealed solutions of **TnAp** in TCE ($c = 1$ mmol/L) were diluted to a concentration of $5 \mu\text{mol/L}$, then drop-cast onto a mica substrate, and gently dried in an argon flow. Thin films of the triads **PTP-9** and **PTP-19** obtained in the course of the TEM investigations were measured directly. The samples were analyzed in tapping mode using a Nanoscope IIIa (Veeco Instruments Inc., Santa Barbara, USA) instrument at room temperature in air. Cantilevers with a resonance frequency on average of $f_0 = 325$ kHz and $k = 40$ N/m were used. Scan rates between 0.5 and 2 Hz were applied, the image resolution was 512×512 pixels.

In Situ UV/vis/NIR Absorption Spectroscopy. A solution of **TnAp** in deuterated tetrachloroethane (TCE- d_2 , $c = 1$ mmol/L) was degassed by three freeze-pump-thaw cycles, shielded from light with aluminium foil, and annealed following the corresponding protocol described in Section 6.2. A volume of $400 \mu\text{L}$ was subsequently transferred into a 4×10 mm quartz fluorescence cuvette (Hellma). In order to avoid light exposure during sample handling, sample transfer was carried out under low intensity red light, and all sample containers were wrapped in aluminium foil. The cuvette was subsequently placed in a four-way cuvette holder (Ocean optics, cuv-all-uv) to allow for two illumination channels, white light and NIR. As a fiber-coupled white-light source, either a plasma lamp (Energetiq, LDLS EQ-99-FC) or a custom-built set-up with a 100 W halogen lamp (Osram) were used, resulting in light powers of 40 or 4 mW, respectively, along the long path of the cuvette with a collimated beam diameter of 4 mm in both cases. The strong UV light of the plasma lamp was blocked with a 320 nm longpass Schott glass filter. A HL200-FHSA halogen lamp from Ocean Optics with a 1000 nm longpass colored glass filter was employed as a separate NIR source to measure absorption spectra across the short path of the cuvette. Spectra in the UV/vis (Ocean Optics, QE-65000) and NIR (Ocean Optics, NIR-Quest) regions were recorded every 5 s for 3 h in the case of the plasma lamp, and every 15–60 s for 15 h in the case of the halogen lamp. To monitor the decay in the dark, the white light source was turned off, and NIR spectra were recorded every 1–2 min for 48 h.

IR, UV/vis/NIR, and CD Spectroscopy. Solution-phase IR spectra ($c = 1$ mmol/L in TCE) were recorded on a Jasco FTIR 6300 spectrometer using a solution-phase cell with KBr windows and a path length of $500 \mu\text{m}$. Solution-phase UV/vis/NIR spectra ($c = 0.1$ or 0.5 mmol/L in TCE) were recorded on a Jasco V-670 spectrometer using a Hellma quartz cuvette with 1 mm path length. Solution-phase CD spectra ($c = 0.1$ mmol/L in TCE) were recorded on a Jasco J-815 spectrometer using a Hellma quartz cuvette with 1 mm path length. Both the UV/vis and the CD spectrometers

were equipped with a Jasco ETCR-762 temperature controller connected to a Jasco MCB-100 mini circulation bath. The resolution was set to 1 nm for both UV/vis and CD spectroscopy. Spectroscopy-grade solvents were used for all spectroscopic investigations. UV/vis spectra of thin films of the triads **PTP-9** and **PTP-19** obtained in the course of the TEM investigations, on glass or fused silica substrates, were measured directly.

Mass Spectrometry. Mass Spectra were recorded at the Mass Spectrometry Service of EPFL on either a Waters Q-TOF Ultima for ESI-TOF, a Shimadzu Biotech AXIMA Performance for MALDI-TOF, or on a Thermo Scientific LTQ FT-ICR MS for APPI.

NMR Spectroscopy. ^1H and ^{13}C NMR spectroscopy was carried out on Bruker Avance 400 or 600 spectrometers operating at frequencies of 400.13 MHz or 600.13 MHz for ^1H nuclei, and 100.62 MHz or 150.91 MHz for ^{13}C nuclei, respectively. Deuterated solvents were purchased from Cambridge Isotope Laboratories, Inc. The spectra were calibrated to the respective residual proton peaks of the deuterated solvents (^1H NMR: 7.26 ppm CDCl_3 , 2.50 ppm DMSO-d_6 , and 6.00 ppm for TCE-d_2 ; ^{13}C NMR: 77.00 ppm for CDCl_3 , and 40.45 ppm for DMSO-d_6). Data are reported as follows: s = singlet, d = doublet, t = triplet, q = quartet, m = multiplet). Coupling constants J are reported in Hz. The coupling patterns and coupling constants were evaluated with Mestrenova NMR data processing.

SAXS and WAXS. Measurements were performed in collaboration with Dr. Sandor Balog at the Adolphe Merklé Institute, Fribourg with a NanoMax-IQ camera (Rigaku Innovative Technologies, Auburn Hills, USA). The samples were kept in vacuum at room temperature during the measurements. The scattering data were presented as a function of the scattering vector modulus $q = 4\pi/\lambda \sin(\theta/2)$, where θ is the scattering angle and λ is the photon wavelength.

Thin Film Rubbing, Transmission Electron Microscopy, and Electron Diffraction. Those thin film rubbing, transmission electron microscopy (TEM), and electron diffraction (ED) experiments were performed in collaboration with Dr. Martin Brinkmann at the Institut Charles Sadron, Université de Strasbourg. Thin film samples were prepared by doctor-blading from sample solutions in *ortho*-dichlorobenzene ($c = 5 \text{ mg/mL}$) on a clean glass substrate maintained at 170°C . The thin films were subsequently rubbed with a microfiber fabric in an inert atmosphere. The rubbing apparatus consisted of a rotating cylinder (4 cm diameter) covered by a microfiber cloth. The rubbing was performed in a glove box by applying the rotating cylinder with a 2 bar pressure on the translating sample holder (1 cm/s) such that it took accordingly 5 s to align a 5 cm long film. The sample holder was heated to 200°C during the rubbing process and the temperature was allowed to equilibrate for 1–2 min before rubbing. One rubbing cycle corresponded to a rubbing length (i.e. the length of the rubbing tissue applied at a given point of the sample) of 50 cm. The films were finally annealed in a nitrogen flow by

heating the sample to 300°C for 5 min and cooling to room temperature at a rate of 10°C/min. Areas for TEM analysis were identified by optical microscopy (Leica DMR-X microscope). The thin film samples for TEM imaging were coated with a thin amorphous carbon film and removed from the glass substrate by floating on a diluted aqueous HF solution (10 wt %) and subsequent recovery on TEM copper grids. TEM imaging was performed in bright field, high resolution and diffraction modes using a CM12 Philips microscope equipped with a MVIII (Soft Imaging System) charge coupled device camera.

Transient Absorption Spectroscopy. Transient absorption (TA) spectroscopy was carried out in collaboration with Dr. Natalie Banerji at EPFL, Lausanne. Transient absorption spectra were recorded using femtosecond pulsed laser pump-probe spectroscopy. The sample solutions were placed into a 1 mm cell and constantly bubbled with argon gas to provide stirring and prevent degradation by oxygen. For the thin film measurements, the samples were mounted in a custom-built sample chamber filled with argon to avoid sample degradation. The probe beam consisted of a white light continuum (350 nm- 950 nm), generated by passing a part of the 780 nm amplified 1 kHz Ti:sapphire output (Clark-MXR, CPA-2001) through a 5 mm CaF₂ plate. The remaining intensity of the fundamental was removed by a 750 nm low pass filter. Excitation pulses at 390 nm were generated by frequency doubling of the fundamental of the laser. Excitation pulses at 540 nm were generated in a custom-built NOPA. The probe intensity was always less than the pump intensity, and the probe spot size was chosen to be much smaller than the pump spot size to allow for a homogeneous excitation over the probed area. The pump pulses were delayed with respect to the probe pulses using a computerized translation stage. The probe pulses were split before the sample by means of a beamsplitter into a signal (transmitted through the sample) and a reference beam. The probe signal and reference beams were detected separately using a pair of 163 mm spectrographs (Andor Technology, SR163) equipped with 512 x 58 pixel back-thinned CCDs (Hamamatsu S07030-0906) and assembled by Entwicklungsbüro Stresing, Berlin. The pump beam was chopped at half the amplifier frequency to improve the sensitivity of the set-up. The transmitted intensity of the probe beam was recorded shot by shot and corrected for laser intensity fluctuations using the reference beam. The transient spectra were averaged at each delay until the desired signal-to-noise ratio was achieved (3000 times). To avoid polarization effects, the relative polarization of the probe and pump pulses was set to the magic angle. All spectra were corrected for the chirp of the white-light probe.

6.2 Synthesis Procedures and Analytical Data for Compounds

Materials. 5,5''-Bis(2-amino-ethyl)-2,2':5',2'':5'',2'''-quaterthiophene dihydrochloride and PIB-

PBI-PIB **35** were synthesized as published previously.^{155,198} Poly(isobutylene) amine (PIB-NH₂) with an average degree of polymerization $P_n = 17$ was obtained from BASF (KeroCom™ PIBA) and separated from side products (~50 wt%) by column chromatography. All other reagents, including chlorendic anhydride **1**, 2,5-bis(tributylstannyl)-thiophene **11**, and perylene bishanydride **31** were purchased as reagent grade from commercial sources and used without further purification. THF, chloroform, dichloromethane, and methanol were purchased as technical grade and distilled once prior to use. Thin layer chromatography (TLC) analyses were performed on TLC plates from Merck; UV-light (254 or 366 nm) or standard coloring reagents were used for detection. Column chromatography was conducted on Geduran® Silica gel Si 60 from Merck (40–60 μm). Spectroscopy-grade solvents were used for all spectroscopic investigations.

Chlorendic hydroxylimide 2. Hydroxylamine hydrochloride (18.7 g, 269 mmol) was added to a solution of potassium carbonate (18.6 g, 134 mmol) in water (800 mL). After stirring for 5 min, chlorendic anhydride **1** (100 g, 269 mmol) was added. The resulting mixture was heated to reflux (130°C) for 24 h and then cooled to 0°C. The obtained precipitate was filtered off, washed with water, dried in an air flow and then *in vacuo* to afford **2** as a grey powder (96.0 g, 92%) that can directly be used for subsequent reactions, or further be purified by fractionated recrystallization from MeOH to obtain a white solid (73 g, 70%). Crystals of **2** suitable for single crystal X-ray analysis were obtained by slow recrystallization from THF solutions after the addition of MeOH (THF/MeOH 1:10) over a few hours.

¹H NMR (400.13 MHz, DMSO-d₆): δ = 4.07 (s, 2H, 2 CH), 11.50 (s, 1H, OH). ¹³C NMR (151 MHz, DMSO-d₆): δ = 49.1, 78.7, 103.7, 130.5, 166.2. HRMS (ESI): calcd C₉H₂Cl₆N₃- ([M-H]-) 383.8141; found 383.8143. EA: calcd for C₉H₃Cl₆N₃ C 28.09%, H 0.78%, N 3.63%; found C 27.86%, H 0.96%, N 3.43%. m.p.: 252–254°C. R_f (DCM/MeOH 10:1): 0.32.

Chlorendylimidyl 3-(thien-2-yl)propanoate 3. 3-(Thien-2-yl)propionic acid (28.5 g, 182 mmol), **2** (70.6 g, 182 mmol), and DPTS (53.8 g, 182 mmol) were dissolved in DCM (1 L), and EDCI (45.6 g, 237 mmol) was added. The reaction mixture was stirred for 4 h, washed with water (4 times), and finally with a saturated aqueous solution of NaCl. The organic phase was dried over MgSO₄, and the solvent was removed to yield the product (95.3 g, 99%) as a brownish solid. Crystals suitable for single crystal X-ray analysis of thiophene active ester **3** were obtained by slow recrystallization from DCM solutions after the addition of MeOH (DCM/MeOH 1:5) over a few hours.

¹H NMR (400.13 MHz, CDCl₃): δ = 2.95 (t, $J = 7.6$ Hz, 2H, CH₂C(O)), 3.26 (t, $J = 7.6$ Hz, 2H, CH₂-Ar), 3.96 (s, 2H, 2 CH), 6.86 (d, $J = 2.0$ Hz, 1H, Ar-H), 6.90–6.95 (m, 1H, Ar-H), 7.16 (dd, $J = 1.2, 5.2$ Hz,

¹H, Ar-*H*). ¹³C NMR (151 MHz, CDCl₃, 50°C): δ = 24.9, 33.0, 50.0, 79.3, 104.1, 124.2, 125.4, 127.2, 131.6, 141.3, 162.9, 166.6. HRMS (APPI): calcd C₁₆H₉Cl₆NO₄S ([M]⁺) 520.8378; found 520.8381. EA: calcd for C₁₆H₉Cl₆NO₄S C 36.67%, H 1.73%, N 2.67%; found C 36.61%, H 1.58%, N 2.54%; m.p.: 146–148°C. UV/vis (THF): λ_{max} (ε) = 233 nm (10.5); R_f (DCM): 0.60.

Chlorendylimidyl 3-(2-bromothien-5-yl)propanoate 4. Chlorendylimidyl 3-(thien-2-yl)propanoate **3** (95.1 g, 181 mmol) was dissolved in DMF (500 mL) and cooled to 0°C before adding NBS (32.9 g, 185 mmol). The reaction flask was shielded from light with aluminum foil, and the reaction mixture was stirred overnight. Diisopropyl ether (500 mL) was added, and the mixture was cooled to 0°C. Then, water was added, and the aqueous phase was extracted twice with diisopropyl ether (200 mL). The combined organic phases were washed three times with water. Brown crystals of **4** (76.5 g, 70%) formed from the organic phase overnight. By repeating the previous purification/crystallization procedure with the supernatant, a second fraction of **11** (12.7 g) was collected. Thus, a total of 89.1 g (81 %) of pure **4** were obtained. Crystals of **4** suitable for single crystal X-ray analysis were obtained by slow recrystallization from DCM solutions after the addition of MeOH (DCM/MeOH 1:5) over a few hours.

¹H NMR (400.13 MHz, CDCl₃): δ = 2.91 (t, *J* = 7.6 Hz, 2H, CH₂C(O)), 3.17 (t, *J* = 7.6 Hz, 2H, CH₂-Ar), 3.96 (s, 2H, 2 CH) 6.62 (d, *J* = 3.6 Hz, 1H, Ar-*H*), 6.87 (d, *J* = 3.6 Hz, 1H, Ar-*H*). ¹³C NMR (151 MHz, CDCl₃, 50°C): δ = 25.2, 32.7, 50.0, 79.3, 104.1, 110.5, 126.0, 130.1, 131.6, 142.9, 162.8, 166.4. HRMS (APPI): calcd C₁₆H₉BrCl₆NO₄S ([M]⁺) 598.7483; found 598.7496. EA: calcd for C₁₆H₈BrCl₆NO₄S C 31.87%, H 1.34%, N 2.32%; found C 31.91%, H 1.26%, N 2.25%. m.p.: 115–117°C. UV/vis (THF): λ_{max} (ε) = 237 nm (10.2); R_f (DCM): 0.65.

Chlorendylimidyl 3-(2,2'-bithien-5-yl)propanoate 5. A 500 mL Schlenk flask was charged with 2-(tributylstannyl)thiophene (14.6 mL, 45.8 mmol), chlorendylimidyl 3-(2-bromothien-5-yl)propanoate **4** (25.1 g, 41.6 mmol), and acetonitrile (100 mL). Bis(triphenylphosphine)palladium(II) chloride (584 mg, 2 mol%, 0.92 mmol) was added. The reaction mixture was stirred overnight at 80°C and then extracted five times with heptane. A careful filtration over silica gel (DCM) afforded the product as a light yellow solid (19.0 g, 75%). Crystals of **5** suitable for single crystal X-ray analysis were obtained by slow recrystallization from DCM solutions after the addition of MeOH (DCM/MeOH 1:5) over a few hours.

¹H NMR (400.13 MHz, CDCl₃): δ = 2.96 (t, *J* = 7.6 Hz, 2H, CH₂C(O)), 3.23 (t, *J* = 7.6 Hz, 2H, CH₂-Ar), 3.96 (s, 2H, 2 CH), 6.73–6.80 (m, 1H, Ar-*H*), 6.95–7.04 (m, 2H, 2 Ar-*H*), 7.11 (dd, *J* = 1.2 Hz, 3.6 Hz, 1H, Ar-*H*), 7.18 (dd, *J* = 3.6, 5.2 Hz, 1H, Ar-*H*). ¹³C NMR (151 MHz, CDCl₃, 50°C): δ = 25.1, 32.9, 50.0, 79.3, 104.1, 123.8, 123.9, 124.4, 126.2, 127.9, 131.6, 136.4, 137.6, 140.5, 162.8, 166.5. HRMS (APPI): calcd C₂₀H₁₁Cl₆NO₄S₂ ([M]⁺) 602.8255; found 602.8262. EA: calcd for C₂₀H₁₁Cl₆NO₄S₂ C 39.63%, H 1.83%, N 2.31%; found C 39.75%, H 1.79%, N 2.24%; m.p.: 162–

164°C; UV/vis (THF): λ_{\max} (ϵ) = 309 nm (13.9); R_f (DCM): 0.65.

Chlorendylimidyl 3-(5-bromo-2,2'-bithien-5'-yl)-propanoate 6. A solution of chlorendylimidyl 3-(2,2'-bithien-5-yl)propanoate **5** (18.9 g, 31.2 mmol) in DMF (200 mL) was cooled to 0°C before adding NBS (5.68 g, 31.89 mmol). The flask was shielded from light with aluminum foil, and the reaction mixture was stirred overnight at room temperature. Then it was poured into water, and the resulting slurry was stirred overnight. The precipitate was filtered off, washed with deionized water, taken up in THF, and reprecipitated into water. After stirring overnight, the precipitate was filtered off, washed with water, redissolved in DCM, and dried over Mg₂SO₄. Solvent removal afforded the product as a light yellow solid (21.0 g, 98%). Crystals of **6** suitable for single crystal X-ray analysis were obtained by slow recrystallization from DCM solutions after the addition of MeOH (DCM/MeOH 1:5) over a few hours.

¹H NMR (400.13 MHz, CDCl₃): δ = 2.95 (t, J = 7.6 Hz, 2H, CH₂C(O)), 3.21 (t, J = 7.6 Hz, 2H, CH₂-Ar), 3.96 (s, 2H, 2 CH), 6.75 (d, J = 3.6 Hz, 1H, Ar-H), 6.84 (d, J = 3.6 Hz, 1H, Ar-H), 6.92 (d, J = 3.6 Hz, 1H, Ar-H), 6.94 (d, J = 3.6 Hz, 1H, Ar-H). ¹³C NMR (151 MHz, CDCl₃, 50°C): δ = 25.1, 32.8, 50.0, 79.3, 104.1, 111.1, 123.9, 124.2, 126.3, 130.8, 131.6, 135.4, 139.1, 141.0, 162.8, 166.5. HRMS (APPI): calcd C₂₀H₁₀BrCl₆NO₄S₂ ([M]⁺) 680.7360; found 680.7373. EA: calcd for C₂₀H₁₀BrCl₆NO₄S₂ C 35.07%, H 1.47%, N 2.04%; found C 35.14%, H 1.41%, N 1.95%. m.p.: 116–118°C; UV/vis (THF): λ_{\max} (ϵ) = 319 nm (17.9); R_f (DCM): 0.65.

5-Tributylstannyl-2,2'-bithiophene 7. Bithiophene (13.5 g, 81.4 mmol) and tetramethylethylenediamine (TMEDA, 12.3 mL, 81.4 mmol) were dissolved in dry THF (600 mL) in 1 L pre-dried Schlenk flask. The mixture was cooled to -78°C before slowly adding *n*-BuLi (34.2 mL, 85.5 mmol). The mixture was then stirred for 30 min at a temperature of -78°C, and for 45 min at room temperature. The dark green slurry was cooled again to -78°C, and Bu₃SnCl (24.3 mL, 89.6 mmol) was added slowly. The clear orange solution was stirred over 3 d at room temperature, and solvents were removed *in vacuo* afterwards. The black oil was finally purified by distillation (10⁻³ mbar, side product <150°C, product >170°C) to afford the product **7** as a clear slightly yellowish oil (28.1 g, 76 %).

¹H NMR (400 MHz, CDCl₃): δ = 0.91 (t, J = 7.2 Hz, 9H, CH₃), 1.02-1.21 (m, 6H, CH₂), 1.29-1.41 (m, 6H, CH₂), 1.47-1.69 (m, 6H, CH₂), 6.98-7.11 (m, 2H, ArH), 7.15-7.25 (m, 2H, ArH), 7.30 (d, J = 3.2 Hz, 1H, ArH). ¹³C NMR (100.62 MHz, CDCl₃): δ = 11.1, 13.8, 27.4, 29.1, 123.6, 124.1, 125.1, 127.9, 136.2.

Chlorendylimidyl 3-(2,2':5',2''-terthiophen-5''-yl)propanoate 8. A dried 500 mL Schlenk flask was charged with 5-(tributylstannyl)2,2'-bithiophene **7** (28.1 g, 61.7 mmol) in dry and degassed DMF (150 mL), and **4** (35.4 g, 58.7 mmol). Bis(triphenylphosphine)palladium(II)

chloride (824 mg, 2 mol%, 1.2 mmol) was added. The reaction mixture was stirred overnight at 80°C and then extracted five times with heptane (500 mL). It was subsequently poured into water, and the resulting slurry was stirred overnight at room temperature. The precipitate was filtered off, washed with deionized water, taken up in THF, and reprecipitated into water. After stirring overnight, the precipitate was filtered off, washed with water, redissolved in chloroform and dried over Mg₂SO₄. Purification by a short column chromatography (2 L SiO₂, DCM) afforded terthiophene **8** as a light yellow solid (15.8 g, 39 %).

¹H NMR (400.13 MHz, CDCl₃): δ = 2.96 (t, *J* = 7.6 Hz, 2H, CH₂C(O)), 3.23 (t, *J* = 7.6 Hz, 2H, CH₂-Ar), 3.96 (s, 2H, 2 CH), 6.77 (d, *J* = 3.6 Hz, 1H, Ar-*H*), 6.96—7.09 (m, 4H, Ar-*H*), 7.16 (dd, *J* = 1.2, 4.0 Hz, 1H, Ar-*H*), 7.22 (dd, *J* = 1.2, 5.2 Hz, 1H, Ar-*H*). ¹³C NMR (151 MHz, CDCl₃, 50°C): δ = 25.1, 32.8, 50.0, 79.2, 104.1, 123.8, 123.9, 124.3, 124.5, 124.6, 126.3, 128.0, 131.6, 136.1, 136.4, 136.4, 137.3, 140.6, 162.8, 166.4. HRMS (APPI): calcd C₂₄H₁₃Cl₆NO₄S₃ ([M+H]⁺) 685.8211; found 685.8236. EA: calcd for C₂₄H₁₂Cl₆NO₄S₃ C 41.88%, H 1.90%, N 2.04%; found C 41.96%, H 1.92%, N 2.15%; m.p.: 170-172°C; UV/vis (THF): λ_{max} (ε) = 360 nm (24.5); R_f (DCM): 0.60.

Chlorendylimidyl 3-(5-bromo-2,2':5',2''-terthiophen-5''-yl)propanoate 9. A solution of chlorendylimidyl 3-(2,2':5',2''-terthiophen-5''-yl)propanoate **8** (15.0 g, 21.7 mmol) in DMF (150 mL) was cooled to 0°C before adding NBS (3.95 g, 22.2 mmol). The reaction flask was shielded from light with aluminum foil, and the reaction mixture was stirred overnight at room temperature. Then it was poured into water, and the resulting suspension was stirred overnight. The precipitate was filtered off, washed with deionized water, taken up in THF, and reprecipitated into water. After stirring overnight, the precipitate was filtered off, washed with water, dissolved in DCM, and dried over MgSO₄. Filtration over silica gel (DCM) afforded bromoterthiophene **9** as a light yellow solid (13.1 g, 79 %).

¹H NMR (400.13 MHz, CDCl₃): δ = 2.96 (t, *J* = 7.6 Hz, 2H, CH₂C(O)), 3.23 (t, *J* = 7.6 Hz, 2H, CH₂-Ar), 3.97 (s, 2H, 2 CH), 6.77 (d, *J* = 3.6 Hz, 1H, Ar-*H*), 6.90 (d, *J* = 4.0 Hz, 1H, Ar-*H*), 6.94—7.02 (m, 4H, Ar-*H*). ¹³C NMR (151 MHz, CDCl₃, 50°C): δ = 25.1, 32.8, 49.9, 79.2, 104.1, 111.2, 123.9, 124.0, 124.3, 124.8, 126.4, 130.9, 131.6, 135.2, 135.8, 136.9, 138.8, 140.9, 162.8, 166.5. HRMS (APPI): calcd C₂₄H₁₃BrCl₆NO₄S₃ ([M+H]⁺) 763.7316; found 763.7351. EA: calcd for C₂₄H₁₂BrCl₆NO₄S₃ C 37.58%, H 1.58%, N 1.83%; found C 37.78%, H 1.52%, N 1.87%; m.p.: 176-178°C; UV/vis (THF): λ_{max} (ε) = 366 nm (24.5); R_f (DCM): 0.60.

5,5'-Bis(tributylstannyl)-2,2'-bithiophene 10. Bithiophene (16.0 g, 96.2 mmol) and tetramethylethylenediamine (TMEDA, 29.1 mL, 192 mmol) were dissolved in dry THF (600 mL) in 1 L dried Schlenk flask. The mixture was cooled to -78°C before slowly adding *n*-BuLi (78.9 mL, 197 mmol). The mixture was then stirred for 30 min at a temperature of -78°C, and for 1.5 h at room temperature. The white slurry was cooled again to -78°C, and Bu₃SnCl

(54.8 mL, 202 mmol) was added slowly. The clear brown solution was stirred over 4 d at room temperature. Then, heptane was added, and the solution was washed three times with aqueous 5 wt% Na₂CO₃ solution, once with water, and finally with a saturated aqueous NaCl solution. The organic phase was dried over MgSO₄, filtered, and the solvents were removed *in vacuo* to yield the product as a brown oil (74.3 g). The product was pure enough to be used in the following reactions without further purification. It was synthesized fresh for all following reactions.

¹H NMR (400 MHz, CDCl₃): δ = 0.91 (t, *J* = 7.2 Hz, 18H, CH₃), 1.03-1.21 (m, 12H, CH₂), 1.29-1.41 (m, 12H, CH₂), 1.45-1.70 (m, 12H, CH₂), 7.06 (d, *J* = 3.2 Hz, 2H, ArH), 7.30 (d, *J* = 3.2 Hz, 2H, ArH). ¹³C NMR (400 MHz, CDCl₃): δ = 11.0, 13.8, 27.4, 29.1, 124.8, 136.2, 136.2, 143.16. HRMS (APCI): calcd C₃₂H₅₈S₂Sn₂ ([M]⁺) 746.2018; found 746.2098.

2,2':5',2''-terthiophene-5,5''-di(propan-3-oic acid) di(chlorendylimidyl ester) 12. A dried 30 mL Schlenk flask was charged with 2,5-bis(tributylstannyl)thiophene **11** (1.80 g, 1.72 mmol), chlorendylimidyl 3-(2-bromothien-5-yl)-propanoate **4** (3.30 g, 5.47 mmol), and dry and degassed DMF (30 mL). Tetrakis(triphenyl-phosphine)palladium(0) (162 mg, 0.16 mmol, 5 mol%) was added, and the reaction mixture was stirred overnight at 85°C. The solvent was removed *in vacuo* while avoiding contact with air, and the resulting solid was two times redispersed in DCM (15 ml) and precipitated into heptane. After a short column with DCM, the pure terthiophene **12** was obtained as yellow powder (1.22 g, 40%).

¹H NMR (400.13 MHz, CDCl₃): δ = 2.97 (t, *J* = 7.6 Hz, 4H, CH₂C(O)), 3.23 (t, *J* = 7.6 Hz, 4H, CH₂-Ar), 3.97 (s, 4H, 2 CH), 6.77 (d, *J* = 3.6 Hz, 2H, Ar-H), 6.98 (d, *J* = 3.6 Hz, 2H, Ar-H), 6.99 (s, 2H, Ar-H), 7.04 (d, *J* = 3.6 Hz, 1H, Ar-H).

2,2':5',2''':5''',2''''-quaterthiophene-5,5''''-di(propan-3-oic acid) di(chlorendylimidyl ester) 13. Degassed dry DMF (500 mL), degassed 5,5'-bis(tributylstannyl)-2,2'-bithiophene **10** (45.5 g, 61.1 mmol; see below), and chlorendylimidyl 3-(2-bromothien-5-yl)-propanoate **4** (75.6 g, 125 mmol) were placed in a dried 1 L Schlenk flask. Tetrakis(triphenylphosphine)palladium(0) (353 mg, 0.5 mol%, 0.3 mmol) was added, and the reaction mixture was stirred overnight at 80°C. DMF was evaporated *in vacuo*, paying careful attention to keeping the mixture in an inert atmosphere. The residue was subsequently suspended at 60°C in a mixture of diisopropyl ether (300 mL), toluene (100 mL) and THF (100 mL), and the resulting slurry was stirred overnight. The yellow precipitate was filtered off and washed with diisopropyl ether (100 mL) and pentane (100 mL). The filtrate was concentrated and diluted with dry diisopropyl ether (100 mL) and dry toluene (25 mL) at 60°C. The yellow precipitate that slowly formed upon stirring was filtered off and washed with diisopropyl ether and pentane. Both fractions were combined to afford quaterthiophene **13** as a yellow microcrystalline solid (40.2 g, 54%).

^1H NMR (400.13 MHz, CDCl_3): δ = 2.97 (t, J = 7.6 Hz, 4H, $\text{CH}_2\text{C}(\text{O})$), 3.23 (t, J = 7.6 Hz, 4H, $\text{CH}_2\text{-Ar}$), 3.97 (s, 2H, 4 CH), 6.77 (d, J = 3.6 Hz, 2H, Ar- H), 6.98 (d, J = 3.6 Hz, 2H, Ar- H), 7.01 (d, J = 3.6 Hz, 2H, Ar- H), 7.04 (d, J = 3.6 Hz, 2H, Ar- H). ^{13}C NMR (151 MHz, CDCl_3 , 50°C): δ = 25.2, 32.8, 50.0, 79.3, 104.1, 123.9, 124.4, 124.5, 126.4, 131.6, 136.1, 136.1, 136.5, 140.7, 162.8, 166.5. HRMS (APPI): calcd $\text{C}_{40}\text{H}_{20}\text{Cl}_{12}\text{N}_2\text{O}_8\text{S}_4$ ($[\text{M}]^+$) 1203.6359; found 1203.6361. EA: calcd for $\text{C}_{40}\text{H}_{20}\text{Cl}_{12}\text{N}_2\text{O}_8\text{S}_4$ C 39.70%, H 1.67%, N 2.31%; found C 39.59%, H 1.69%, N 2.11%. m.p.: 134–136°C; UV/vis (THF): λ_{max} (ϵ) = 401 nm (38.5); R_f (DCM): 0.38.

2,2':5',2'':5'',2''':5''',2''''-pentathiophene-5,5''''-di(propan-3-oic acid) di(chlorendylimidyl ester) 14. A dried 50 mL Schlenk flask was charged with 2,5-bis(tributylstannyl)thiophene **11** (1.00 g, 1.51 mmol), chlorendylimidyl 3-(5-bromo-2,2'-bithien-5'-yl)-propanoate **6** (2.30 g, 3.35 mmol), and dry and degassed DMF (20 mL). Tetrakis(triphenyl-phosphine)palladium(0) (166 mg, 0.15 mmol, 10 mol%) was added, and the reaction mixture was stirred overnight at 80°C. The solvent was removed *in vacuo*, avoiding contact with air, and the resulting solid was redispersed in THF (20 mL) and precipitated into DIPE. After filtration and washing with DIPE, the pentathiophene **14** was obtained as orange powder (1.43 g, 73%).

^1H NMR (400.13 MHz, CDCl_3): δ = 2.97 (m, 4H, $\text{CH}_2\text{C}(\text{O})$), 3.24 (m, 4H, $\text{CH}_2\text{-Ar}$), 3.97 (s, 4H, 4 CH), 6.78 (m, 2H, Ar- H), 6.8–7.2 (m, 8H, Ar- H).

2,2':5',2'':5'',2''':5''',2''''-sexithiophene-5,5''''-di(propan-3-oic acid) di(chlorendylimidyl ester) 15. 5,5'-bis(tributylstannyl)-2,2'-bithiophene **10** (15.3 g, 20.6 mmol) and chlorendylimidyl 3-(5-bromo-2,2'-bithien-5'-yl)-propanoate **6** (28.8 g, 42.1 mmol) were dissolved in dry and degassed DMF (200 mL) in a dried 500 mL Schlenk flask. Tetrakis(triphenylphosphine)palladium(0) (477 mg, 2 mol%, 0.41 mmol) was added, and the mixture was stirred overnight at 80°C. DMF was subsequently removed *in vacuo*, and the orange residue was dispersed in a mixture of diisopropyl ether (100 mL), toluene (30 mL) and dry THF (30 mL). The mixture was gently refluxed (85°C) for about 15 min. The precipitate was filtered off and washed with three times with diisopropyl ether to afford pure sexithiophene **15** as an orange microcrystalline powder (24.4 g, 86%).

^1H NMR (400.13 MHz, TCE- d_2 , 80°C): δ = 3.01 (t, J = 7.6 Hz, 4H, $\text{CH}_2\text{C}(\text{O})$), 3.29 (t, J = 7.6 Hz, 4H, $\text{CH}_2\text{-Ar}$), 4.00 (s, 4H, 2 CH), 6.84 (d, J = 3.6 Hz, 2H, Ar- H), 7.02–7.17 (m, 10H, Ar- H). ^{13}C NMR (151 MHz, TCE- d_2 , 60°C): δ = 24.6, 32.2, 49.3, 78.6, 123.5, 123.9, 124.1, 124.2, 125.9, 131.0, 135.2, 135.2, 135.5, 135.7, 136.1, 140.3, 162.3. HRMS (APPI): calcd $\text{C}_{48}\text{H}_{24}\text{Cl}_{12}\text{N}_2\text{O}_8\text{S}_6$ ($[\text{M}]^+$) 1367.6114; found 1367.6103. EA: calcd for $\text{C}_{48}\text{H}_{24}\text{Cl}_{12}\text{N}_2\text{O}_8\text{S}_6$ C 41.94%, H 1.76%, N 2.04%; found C 40.73%, H 1.71%, N 1.79%. m.p.: 260°C. UV/vis (THF): λ_{max} (ϵ) = 440 nm (51.8). R_f (DCM): 0.36.

2,2':5',2'':5'',2''':5''',2''''-heptathiophene-5,5''''-di(propan-3-oic acid) di(chlorendylimidyl ester) 16.

di(chlorendylimidyl ester) 16. A dried 250 mL Schlenk flask was charged with 5,5'-bis(tributylstannyl)-thiophene (993 mg, 1.50 mmol), chlorendylimidyl 3-(5-bromo-2,2':5',2''-terthiophen-5''-yl)propanoate **9** (2.32 g, 3.03 mmol), and degassed dry DMF (50 mL) in an argon atmosphere. Tetrakis(triphenyl-phosphine)palladium(0) (55 mg, 45 μ mol) was added, and the reaction mixture was stirred overnight at 80°C. The solvent was removed and the residue was redispersed in dry toluene and heated to 100 °C for 1h. The precipitate was filtered off, washed with diethyl ether (60 mL) and pentane (40 mL) to yield 1.91 g (88 %) of the pure heptathiophene ester **16** as an orange-red microcrystalline powder.

^1H NMR (400.13 MHz, CDCl_3): δ = 3.07 (t, J = 7.6 Hz, 4H, 2 $\text{CH}_2\text{C}(\text{O})$), 3.37 (t, J = 7.6 Hz, 4H, 2 $\text{CH}_2\text{-Ar}$), 4.04 (s, 4H, 4 CH), 6.90 (m, 2H, Ar- H), 7.12 (m, 2H, Ar- H), 7.15 (m, 2H, Ar- H), 7.17-7.22 (m, 8H, Ar- H). HRMS (MALDI): calcd $\text{C}_{52}\text{H}_{26}\text{Cl}_{12}\text{N}_2\text{O}_8\text{S}_7$ ($[\text{M}]^+$) 1455.5902; found 1455.5851. EA: calcd for $\text{C}_{52}\text{H}_{26}\text{Cl}_{12}\text{N}_2\text{O}_8\text{S}_7$ C 42.88%, H 1.80%, N 1.92%; found C 43.07%, H 1.76%, N 1.90%. UV/vis (THF): λ_{max} (ϵ) = 453 nm (70.8).

2,2':5',2'':5''',2''':5''''',2''''':5''''''',2''''''':5''''''''',2''''''''':5'''''''''''-octathiophene-5,5''''''''''-di(propan-3-oic acid) di(chlorendylimidyl ester) 17. A dried 250 mL Schlenk flask was charged with 5,5'-bis(tributylstannyl)2,2'-bithiophene **10** (3.15 g, 4.23 mmol), chlorendylimidyl 3-(5-bromo-2,2':5',2''-terthiophen-5''-yl)propanoate **9** (6.48 g, 8.45 mmol), and dry and degassed DMF (110 mL) in an argon atmosphere. Tetrakis(triphenyl-phosphine)palladium(0) (244 mg, 0.21 mmol, 5 mol%) was added, and the reaction mixture was stirred overnight at 80°C. The solvent was removed *in vacuo* while avoiding contact with air. The residual solid was redispersed in dry toluene (100 L). The resulting suspension was stirred 20 min at 100°C and then cooled to room temperature. After filtration and washing with toluene, the pure octathiophene **17** was obtained as a red microcrystalline powder (5.21 g, 80 %).

^1H NMR (400.13 MHz, TCE- d_2 , 120°C): δ = 3.03 (t, J = 7.6 Hz, 4H, 2 $\text{CH}_2\text{C}(\text{O})$), 3.33 (t, J = 7.6 Hz, 4H, 2 $\text{CH}_2\text{-Ar}$), 4.00 (s, 4H, 4 CH), 6.86 (m, 2H, Ar- H), 7.03—7.20 (m, 14H, Ar- H). HRMS (APPI): calcd $\text{C}_{58}\text{H}_{29}\text{Cl}_{12}\text{N}_2\text{O}_8\text{S}_8$ ($[\text{M}+\text{H}]^+$) 1538.5870; found 1538.5870. EA: calcd for $\text{C}_{58}\text{H}_{28}\text{Cl}_{12}\text{N}_2\text{O}_8\text{S}_8$ C 43.71%, H 1.83%, N 1.82%; found C 43.70%, H 2.05%, N 1.93%; m.p.: >400°C; UV/vis (THF): λ_{max} (ϵ) = 438 nm (42.5).

***N*-(9-Fluorenylmethyloxycarbonyl)-L-alanyl-L-alanine tert-butyl ester 19a.** *N*-(9-Fluorenylmethyloxycarbonyl)-L-alanine **18a** (49.7 g, 160 mmol, 1 equiv.) and L-alanine *tert*-butylester hydrochloride (29.0 g, 160 mmol, 1 equiv.) were dissolved in THF (750 mL). DIEA (82 mL, 479 mmol, 3 equiv.) and PyBOP (99.7 g, 192 mmol, 1.2 equiv.) were added. After 2 h, most of the THF was removed *in vacuo*, and the crude product was precipitated by slowly pouring the residual THF solution into a 1 M aqueous HCl solution. The precipitate was again dissolved in THF and precipitated into a 1 M aqueous HCl solution. This precipitation was

repeated one more time. The obtained material was dissolved in DCM, and most of the remaining water was removed with a separatory funnel. The organic phase was dried over MgSO_4 and evaporated to obtain compound **19a** as a colorless solid (66.9 g, 152 mmol, 96%).

^1H NMR (400 MHz, CDCl_3) δ = 7.75 (d, J = 7.5 Hz, 2H, aromatic H), 7.65–7.54 (m, 2H, aromatic H), 7.39 (t, J = 7.5 Hz, 2H, aromatic H), 7.34–7.27 (m, 2H, aromatic H), 6.61 (m, 1H, NH), 5.55 (m, 1H, NH), 4.44 (p, J = 7.2 Hz, 1H, CHCH_3), 4.38 (d, J = 7.0 Hz, 2H, $\text{CO}_2\text{CH}_2\text{-Fmoc}$), 4.31 (p, J = 6.8 Hz, 1H, CHCH_3), 4.21 (t, J = 7.1 Hz, 1H, fluorenyl CH), 1.45 (s, 9H, $\text{C}(\text{CH}_3)_3$), 1.41 (d, J = 6.8 Hz, 3H, CHCH_3), 1.37 (d, J = 7.1 Hz, 3H, CHCH_3). ^{13}C NMR (101 MHz, CDCl_3) δ = 172.19, 172.13, 156.18, 144.02, 141.48, 127.91, 127.29, 125.35, 120.17, 82.15, 67.31, 50.58, 48.94, 47.30, 28.16, 19.38, 18.54. Anal. calcd. for $\text{C}_{25}\text{H}_{30}\text{N}_2\text{O}_5$: C, 68.47%; H, 6.90%; N, 6.39%; found: C, 68.09%; H, 6.67%; N, 6.62%. HRMS (ESI): calcd. for $\text{C}_{25}\text{H}_{30}\text{N}_2\text{O}_5\text{Na}$: $[\text{M}+\text{Na}]^+$ 461.2047; found: 461.2055. R_f : 0.6 (DCM/MeOH 10:1).

***N*-(9-Fluorenylmethyloxycarbonyl)-L-glycyl-L-glycine tert-butyl ester 19b.** *N*-(9-Fluorenylmethyloxycarbonyl)-L-glycine **18b** (5.0 g, 16.8 mmol, 1 equiv.) and L-glycine *tert*-butylester hydrochloride (2.82 g, 16.8 mmol, 1 equiv.) were dissolved in THF (100 mL). DIEA (8.8 mL, 50.5 mmol, 3 equiv.) and PyBOP (9.63 g, 18.5 mmol, 1.1 equiv.) were added. After 3 h, the crude product was precipitated by slowly pouring the reaction mixture into a 1 M aqueous HCl solution. The precipitate was again dissolved in THF and precipitated into a 1 M aqueous HCl solution. This precipitation was repeated one more time. The obtained material was dissolved in CHCl_3 ; the resulting solution was dried over MgSO_4 and evaporated to obtain compound **19b** as a colorless solid (5.31 g, 12.9 mmol, 77%).

^1H NMR (400 MHz, CDCl_3) δ = 7.76 (d, J = 7.6 Hz, 2H, aromatic H), 7.62–7.52 (m, 2H, aromatic H), 7.40 (t, J = 7.4 Hz, 2H, aromatic H), 7.34–7.27 (m, 2H, aromatic H), 6.46 (m, 1H, NH), 5.52 (m, 1H, NH), 4.44 (d, J = 7.2 Hz, 2H, CH_2CH), 4.23 (t, J = 6.8 Hz, 1H, CH), 4.05–3.85 (m, 4H, $(\text{CO})\text{CH}_2\text{NH}$), 1.47 (s, 9H, $\text{C}(\text{CH}_3)_3$).

***N*-(9-Fluorenylmethyloxycarbonyl)-L-alanyl-L-alanine 20a.** *N*-(9-Fluorenylmethyloxycarbonyl)-L-alanyl-L-alanine *tert*-butyl ester **19a** (18.0 g, 41 mmol, 1 equiv.) was suspended in CHCl_3 (50 mL). TFA (92 mL, 1230 mmol, 30 equiv.) was added, and the reaction mixture was stirred for 7 h. The volatiles were removed by distillation and repeated addition of CHCl_3 followed by evaporation *in vacuo*. The crude product was washed three times with DCM to obtain **20a** as a slightly grey solid (14.9 g, 39 mmol, 95%).

^1H NMR (400 MHz, DMSO) δ = 8.13 (d, J = 7.3 Hz, 1H, NH), 7.89 (d, J = 7.5 Hz, 2H, aromatic H), 7.73 (m, 2H, aromatic H), 7.50 (d, J = 7.9 Hz, 1H, NH), 7.42 (t, J = 7.1 Hz, 2H, aromatic H), 7.33 (t, J = 6.9 Hz, 2H, aromatic H), 4.27–4.18 (m, 4H, 2 CHCH_3 ; $\text{Fmoc-CO}_2\text{CH}_2$), 4.08 (t, J = 7.2 Hz, 1H,

fluorenyl CH), 1.27 (d, $J = 7.3$ Hz, 3H, CHCH₃), 1.22 (d, $J = 7.1$ Hz, 3H, CHCH₃). ¹³C NMR (101 MHz, DMSO) $\delta = 175.04, 173.32, 156.62, 144.76, 141.68, 128.60, 128.04, 126.27, 121.06, 66.57, 50.65, 48.39, 47.62, 19.15, 18.13$. Anal. calcd. for C₂₁H₂₂N₂O₅: C, 65.96%; H, 5.80%; N, 7.33%; found: C, 65.98%; H, 6.02%; N, 7.45%. HRMS (ESI): calcd. for C₂₁H₂₃N₂O₅: ([M+H]⁺) 383.1602; found: 383.1607. *R*_f: 0.1 (DCM/MeOH 10:1).

***N*-(9-Fluorenylmethyloxycarbonyl)-L-glycyl-L-glycine** **20b**. *N*-(9-Fluorenylmethyloxycarbonyl)-L-glycyl-L-glycine *tert*-butyl ester **19b** (5.29 g, 13 mmol, 1 equiv.) was suspended in CHCl₃ (60 mL). TFA (30 mL, 386 mmol, 30 equiv.) was added, and the reaction mixture was stirred for 16 h. The volatiles were removed by distillation and repeated addition of CHCl₃ followed by evaporation *in vacuo*. The residue was recrystallized from hot acetone to give the pure product **20b** as a white solid.

¹H NMR (400 MHz, DMSO) $\delta = 12.57$ (s, 1H, COOH), 8.14 (t, $J = 5.6$ Hz, 1H, NH), 7.89 (d, $J = 7.5$ Hz, 2H, aromatic *H*), 7.72 (d, $J = 7.5$ Hz, 2H, aromatic *H*), 7.58 (t, $J = 5.6$ Hz, 1H, NH), 7.42 (t, $J = 7.1$ Hz, 2H, aromatic *H*), 7.33 (t, $J = 6.9$ Hz, 2H, aromatic *H*), 4.35–4.28 (m, 3H, CHCH₂), 3.77 (d, $J = 5.6$ Hz, 2H, (CO)CH₂NH), 3.65 (d, $J = 5.6$ Hz, 2H, (CO)CH₂NH).

***N*-(9-Fluorenylmethyloxycarbonyl)-L-alanyl-L-alanyl-L-alanine *tert*-butyl ester** **21**. *N*-(9-Fluorenylmethyloxycarbonyl)-L-alanyl-L-alanine **20a** (12.0 g, 31 mmol, 1 equiv.) and L-alanine *tert*-butylester hydrochloride (5.7 g, 31 mmol, 1 equiv.) were dissolved in THF (300 mL). DIEA (17 mL, 94 mmol, 3 equiv.) and PyBOP (20.0 g, 38 mmol, 1.2 equiv.) were added. After 3 h, most of the THF was removed *in vacuo*, and the crude product was precipitated by slowly pouring the residual THF solution into a 1 M aqueous HCl solution. The precipitate was again dissolved in THF and precipitated into a 1 M aqueous HCl solution. This precipitation was repeated one more time. The obtained material was dissolved in DCM, and most of the remaining water was removed with a separatory funnel. The organic phase was dried over MgSO₄ and evaporated to obtain compound **21** as a colorless solid (11.7 g, 22.9 mmol, 73%).

¹H NMR (400 MHz, CDCl₃) $\delta = 7.76$ (d, $J = 7.5$ Hz, 2H, aromatic *H*), 7.58 (d, $J = 7.4$ Hz, 2H, aromatic *H*), 7.39 (t, $J = 7.5$ Hz, 2H, aromatic *H*), 7.30 (t, $J = 7.5$ Hz, 2H, aromatic *H*), 6.80 (d, $J = 6.6$ Hz, 1H, NH), 6.74 (d, $J = 6.6$ Hz, 1H, NH), 5.59 (d, $J = 7.0$ Hz, 1H, NH), 4.71–4.50 (m, 1H, CHCH₃), 4.50–4.35 (m, 3H, CHCH₃, Fmoc-CO₂CH₂), 4.35–4.25 (m, 1H, CHCH₃), 4.21 (t, $J = 7.0$ Hz, 1H, fluorenyl CH), 1.45 (s, 9H, C(CH₃)₃), 1.40 (d, $J = 7.0$ Hz, 6H, 2 CHCH₃), 1.35 (d, $J = 7.0$ Hz, 6H, CHCH₃). ¹³C NMR (101 MHz, CDCl₃) $\delta = 172.54, 171.98, 171.80, 156.14, 143.94, 141.32, 127.75, 127.12, 125.24, 120.01, 81.97, 67.21, 50.48, 48.93, 48.78, 47.14, 27.99, 19.46, 19.09, 18.47$. Anal. calcd. for C₂₈H₃₅N₃O₆: C, 65.99%; H, 6.92%; N, 8.25%; O, 18.84%; found: C, 65.90%; H, 6.97%; N, 8.21%; O, 18.86%. HRMS (ESI): calcd. for C₂₈H₃₆N₃O₆: ([M+H]⁺) 510.2599; found 510.2598. *R*_f: 0.7 (DCM/MeOH 10:1).

***N*-(9-Fluorenylmethyloxycarbonyl)-L-alanyl-L-alanyl-L-alanine** **22.** *N*-(9-Fluorenylmethyloxycarbonyl)-L-alanyl-L-alanyl-L-alanine *tert*-butyl ester **21** (11.7 g, 23 mmol, 1 equiv.) was suspended in CHCl₃ (50 mL). TFA (52 mL, 686 mmol, 30 equiv.) was added, and the reaction mixture was stirred for 16 h. The volatiles were removed by distillation and repeated addition of CHCl₃ followed by evaporation *in vacuo*. The crude product was washed three times with DCM to give **22** as a slightly grey solid (9.52 g, 21 mmol, 92%).

¹H NMR (400 MHz, DMSO) δ = 8.13 (d, *J* = 7.1 Hz, 1H, NH), 7.98 (d, *J* = 7.5 Hz, 1H, NH), 7.93 (d, *J* = 7.5 Hz, 2H, aromatic *H*), 7.76 (t, *J* = 6.7 Hz, 2H, aromatic *H*), 7.56 (d, *J* = 7.5 Hz, 1H, NH), 7.46 (t, *J* = 7.4 Hz, 2H, aromatic *H*), 7.37 (t, *J* = 7.2 Hz, 2H, aromatic *H*), 4.41 – 4.17 (m, 5H, 3 CHCH₃, Fmoc-CO₂CH₂), 4.12 – 4.08 (m, 1H, fluorenyl CH), 1.30 (d, *J* = 7.2 Hz, 3H, CHCH₃), 1.25 (d, *J* = 7.0 Hz, 6H, 2 CHCH₃). ¹³C NMR (101 MHz, DMSO) δ = ¹³C NMR (101 MHz, DMSO) δ 174.92, 173.06, 172.84, 156.66, 144.84, 144.75, 141.67, 128.59, 128.05, 126.24, 121.06, 66.56, 50.89, 48.68, 48.36, 47.61, 19.20, 19.12, 18.09. HRMS (ESI): calcd. for C₂₄H₂₈N₃O₆ ([M+H]⁺) 454.1973; found 454.1972. *R*_f: 0.1 (DCM/MeOH 10:1).

PIB-L-Ala-Fmoc 23. PIB-NH₂ (11.6 g, 9.6 mmol, 1 equiv.) and fluorenylmethyloxycarbonyl)-L-alanine **18a** (3.0 g, 9.6 mmol, 1 equiv.) were dissolved in THF (250 mL). DIEA (5.1 mL, 28.9 mmol, 3 equiv.) and PyBOP (6.0 g, 11.6 mmol, 1.2 equiv.) were added. After 4 h, most of the THF was removed *in vacuo*, and the crude product was precipitated by slowly pouring the residual THF solution into a 1 M aqueous HCl solution. The precipitate was again dissolved in THF and precipitated into a 1 M aqueous HCl solution. This precipitation was repeated one more time. The obtained material was dissolved in DCM, and most of the remaining water was removed with a separatory funnel. The organic phase was dried over MgSO₄ and evaporated. The residue was purified by column chromatography (SiO₂; DCM/MeOH 20:1) to obtain pure **23** as a slightly yellow oil (13.2 g, 8.8 mmol, 91 %).

¹H NMR (400 MHz, CDCl₃) δ = 7.77 (d, *J* = 7.5 Hz, 2H, aromatic *H*), 7.58 (d, *J* = 7.4 Hz, 2H, aromatic *H*), 7.40 (t, *J* = 7.4 Hz, 2H, aromatic *H*), 7.32 (td, *J* = 7.4, 1.0 Hz, 2H, aromatic *H*), 5.89 (m, 1H, NH), 5.35 (m, 1H, NH), 4.40 (d, *J* = 6.9 Hz, 2H, CO₂CH₂-Fmoc), 4.21 (m, 2H, CHCH₃, fluorenyl CH), 3.35–3.19 (m, 2H, PIB-CH₂NHCO), 1.57–0.86 (m, 220H, polymer *H*, CH₃). HRMS (MALDI): calcd. for C₆₃H₁₀₈N₂O₃Na: (*n* = 9 [M+Na]⁺) 964.5324; found: 964.7109. *R*_f: 0.8 (DCM/MeOH 10:1).

PIB-L-Ala₂-Fmoc 24a. PIB-NH₂ (9.6 g, 7.8 mmol, 1 equiv.) and *N*-(9-fluorenylmethyloxycarbonyl)-L-alanyl-L-alanine **20a** (3.0 g, 7.8 mmol, 1 equiv.) were dissolved in THF (250 mL). DIEA (4.1 mL, 23.5 mmol, 3 equiv.) and PyBOP (4.9 g, 9.4 mmol, 1.2 equiv.) were added. After 6 h, most of the THF was removed *in vacuo*, and the crude product was precipitated by slowly pouring the residual THF solution into a 1 M aqueous HCl solution. The precipitate was again dissolved in THF and precipitated into a 1 M aqueous HCl solution. This

precipitation was repeated one more time. The obtained material was dissolved in DCM, and most of the remaining water was removed with a separatory funnel. The organic phase was dried over MgSO_4 and evaporated. The residue was purified by column chromatography (SiO_2 ; DCM/MeOH 20:1) to obtain **24a** as slightly yellow oil (11.9 g, 7.6 mmol, 96%).

^1H NMR (400 MHz, CDCl_3) δ = 7.77 (d, J = 7.5 Hz, 2H, aromatic H), 7.58 (d, J = 7.5 Hz, 2H, aromatic H), 7.40 (t, J = 7.4 Hz, 2H, aromatic H), 7.31 (m, 2H, aromatic H), 6.59 (d, J = 7.2 Hz, 1H, NH), 6.10 (s, 1H, NH), 5.34 (d, J = 5.5 Hz, 1H, NH), 4.42 (m 3H, Fmoc- CO_2CH_2 , CHCH_3), 4.21 (m, 2H, CHCH_3 , fluorenyl CH), 3.24 (m, 2H, PIB- CH_2NHCO), 1.69–0.70 (m, 187H, polymer H , 2 CH_3). HRMS (MALDI): calcd. for $\text{C}_{50}\text{H}_{81}\text{N}_3\text{O}_4\text{Na}$: ($n = 5$ [$\text{M}+\text{Na}$] $^+$) 811.1851; found: 811.3933. R_f : 0.6 (DCM/MeOH 10:1).

PIB-Gly₂-Fmoc 24b. PIB-NH₂ (1.54 g, 1.4 mmol, 1 equiv.) and *N*-(9-fluorenylmethyloxycarbonyl)-L-glycyl-L-glycine **20b** (497 mg, 1.4 mmol, 1 equiv.) were dissolved in THF. DIEA (0.75 mL, 4.2 mmol, 3 equiv.) and PyBOP (950 mg, 1.8 mmol, 1.3 equiv.) were added. After 6 h, the crude product was precipitated by slowly pouring the reaction mixture into a 1 M aqueous HCl solution. The precipitate was again dissolved in THF and precipitated into a 1 M aqueous HCl solution. This precipitation was repeated one more time. The obtained material was dissolved in DCM. The resulting solution was dried over MgSO_4 and evaporated to obtain **24b** as slightly yellow oil.

^1H NMR (400 MHz, CDCl_3) δ = 7.76 (d, J = 7.5 Hz, 2H, aromatic H), 7.58 (d, J = 7.5 Hz, 2H, aromatic H), 7.40 (t, J = 7.4 Hz, 2H, aromatic H), 7.31 (m, 2H, aromatic H), 6.82 (s, 1H, NH), 6.13 (s, 1H, NH), 5.564 (d, 1H, NH), 4.45 (d, J = 6.8 Hz, 2H, CHCH_2OCO), 4.21 (t, 1H, fluorenyl CH), 3.90 (m, 4H, $(\text{CO})\text{CH}_2\text{NH}$), 3.23 (m, 2H, PIB- CH_2NHCO), 1.80–0.65 (m, 176H, polymer H).

PIB-L-Ala₃-Fmoc 25. PIB-NH₂ (30.9 g, 25.4 mmol, 1 equiv.) and *N*-(9-fluorenylmethyloxycarbonyl)-L-alanyl-L-alanyl-L-alanine **22** (11.5 g, 25.4 mmol, 1 equiv.) were dissolved in THF (300 mL). DIEA (13 mL, 76.1 mmol, 3 equiv.) and PyBOP (15.9 g, 30.4 mmol, 1.2 equiv.) were added. After 19 h, most of the THF was removed *in vacuo*, and the crude product was precipitated by slowly pouring the residual THF solution into a 1 M aqueous HCl solution. The precipitate was again dissolved in THF and precipitated into a 1 M aqueous HCl solution. This precipitation was repeated one more time. The obtained material was dissolved in DCM, and most of the remaining water was removed with a separatory funnel. The organic phase was dried over MgSO_4 and evaporated. The residue was purified by column chromatography (SiO_2 ; DCM/MeOH 20:1) to obtain pure **25** as a slightly yellow solid (30.8 g, 18.7 mmol, 74%).

^1H NMR (400 MHz, CDCl_3) δ = 7.75 (d, J = 7.5 Hz, 2H, aromatic H), 7.57 (d, J = 7.5 Hz, 2H, aromatic

H), 7.50 (1H, *NH*), 7.39 (t, *J* = 7.4 Hz, 2H, aromatic *H*), 7.29 (t, *J* = 7.4 Hz, 2H, aromatic *H*), 7.13 (m, 1H, *NH*), 6.76 (m, 1H, *NH*), 5.84 (m, 1H, *NH*), 4.63–4.33 (m, 5H, Fmoc-CO₂CH₂, 3 CHCH₃), 4.20 (t, *J* = 7.0 Hz, 1H, fluorenyl *CH*), 3.25–3.12 (m, 2H, PIB-CH₂NHCO), 1.69–0.60 (m, 202H, polymer *H*, 3 CH₃). HRMS (MALDI): calcd. for C₅₇H₉₄N₄O₅Na: (n = 6 [M+Na]⁺) 937.7116.; found: 937.6147. *R*_f: 0.4 (DCM/MeOH 10:1).

PIB-L-Ala-H 26. PIB-L-Ala-Fmoc **23** (15.6 g, 10.4 mmol, 1 equiv.) was dissolved in CHCl₃ (250 mL), and piperidine (31 mL, 311 mmol, 30 equiv.) was added. The reaction mixture was stirred for 24 h, and the volatiles were removed by evaporation *in vacuo*. The residue was purified by column chromatography (SiO₂; DCM/MeOH 10:1) to obtain pure **26** as a slightly yellow oil (9.1 g, 7.1 mmol, 68 %).

¹H NMR (400 MHz, CDCl₃) δ = 7.22 (s, 1H, *NH*), 3.49 (m, 1H, CHCH₃), 3.34–3.18 (m, 2H, PIB-CH₂NHCO), 1.85–0.69 (m, 248H, polymer *H*, CH₃). HRMS (MALDI): calcd. for C₅₆H₁₁₅N₂O: (n = 11 [M+H]⁺) 831.9001; found: 831.8402. *R*_f: 0.4 (DCM/MeOH 10:1).

PIB-L-Ala₂-H 27a. PIB-L-Ala₂-Fmoc **24a** (10.9 g, 6.9 mmol, 1 equiv.) was dissolved in CHCl₃ (250 mL), and piperidine (20 mL, 208 mmol, 30 equiv.) was added. The reaction mixture was stirred for 17 h, and the volatiles were removed by evaporation *in vacuo*. The residue was purified by column chromatography (SiO₂; DCM/MeOH 10:1) to obtain pure **27a** as a slightly yellow oil (6.9 g, 5.1 mmol, 74 %).

¹H NMR (400 MHz, CDCl₃) δ = 7.73 (d, *J* = 7.6 Hz, 1H, *NH*), 6.38–6.26 (m, 1H, *NH*), 4.39 (m, 1H, CHCH₃), 3.49 (m, 1H, CHCH₃), 3.24 (m, 2H, PIB-CH₂NHCO), 1.45–0.98 (m, 176H, polymer *H*, 2 CH₃). HRMS (MALDI): calcd. for C₃₉H₇₉N₃O₂Na: (n = 6 [M+Na]⁺) 644.6064; found: 644.4175. *R*_f: 0.2 (DCM/MeOH 10:1).

PIB-Gly₂-H 27b. PIB-Gly₂-Fmoc **24b** (1.83 g, 1.2 mmol, 1 equiv.) was dissolved in CHCl₃, and piperidine (1.2 mL, 11.8 mmol, 30 equiv.) was added. The reaction mixture was stirred for 16 h, and the volatiles were removed by evaporation *in vacuo*. The residue was purified by column chromatography (SiO₂; DCM/MeOH 50:1, then 20:1) to obtain pure **27b** as a slightly yellow oil (680 mg, 514 μmol, 43 %).

¹H NMR (400 MHz, CDCl₃) δ = 7.86 (m, 1H, *NH*), 6.08 (m, 1H, *NH*), 3.92 (d, *J* = 5.6 Hz, 2H, (CO)CH₂NH), 3.41 (m, 2H, (CO)CH₂NH), 3.25 (m, 2H, PIB-CH₂NHCO), 2.00–0.70 (m, 163H, polymer *H*).

PIB-L-Ala₃-H 28. PIB-L-Ala₃-Fmoc **25** (26.8 g, 16.3 mmol, 1 equiv.) was dissolved in CHCl₃ (450 mL), and piperidine (48 mL, 489 mmol, 30 equiv.) was added. The reaction mixture was stirred for 17 h, and the volatiles were removed by evaporation *in vacuo*. The residue was purified by column chromatography (SiO₂; DCM/MeOH 10:1) to obtain pure **28** as slightly yellow solid

(17.4 g, 12.3 mmol, 75 %).

^1H NMR (400 MHz, CDCl_3) δ = 7.74 (d, J = 7.3 Hz, 1H, NH), 6.76 (d, J = 7.2 Hz, 1H, NH), 6.15 (s, 1H, NH), 4.51–4.30 (m, 2H, 2 CHCH_3), 3.52 (q, J = 7.0 Hz, 1H, CHCH_3), 3.32–3.13 (m, 2H, $\text{PIB-CH}_2\text{NHCO}$), 1.66–0.72 (m, 213H, polymer H , 3 CH_3). HRMS (MALDI): calcd. for $\text{C}_{46}\text{H}_{92}\text{N}_4\text{O}_3\text{Na}$: ($n = 7$ [$\text{M}+\text{Na}$] $^+$) 771.7062.; found: 771.9130. R_f : 0.1 (DCM/MeOH 10:1).

PIB-L-Ala₄-Fmoc 29. PIB-L-Ala₂-H **27a** (4.0 g, 3.0 mmol, 1 equiv.) and *N*-(9-Fluorenylmethyloxycarbonyl)-L-alanyl-L-alanine **20a** (1.3 g, 3.3 mmol, 1.1 equiv.) were dissolved in THF (300 mL). DIEA (1.5 mL, 8.9 mmol, 3 equiv.) and PyBOP (1.9 g, 3.6 mmol, 1.2 equiv.) were added. After 3 h, most of the THF was removed *in vacuo*, and the crude product was precipitated by slowly pouring the residual THF solution into a 1 M aqueous HCl solution. The precipitate was again dissolved in THF and precipitated into a 1 M aqueous HCl solution. This precipitation was repeated one more time. The obtained material was dissolved in DCM, and most of the remaining water was removed with a separatory funnel. The organic phase was dried over MgSO_4 and evaporated. The residue was purified by column chromatography (SiO_2 ; DCM/MeOH 20:1) to obtain pure **29** as a slightly yellow solid (4.74 g, 2.8 mmol, 93 %).

^1H NMR (400 MHz, $\text{C}_2\text{D}_2\text{Cl}_4$) δ = 7.82 (d, J = 7.5 Hz, 2H, aromatic H), 7.62 (d, J = 6.9 Hz, 2H, aromatic H), 7.46 (t, J = 7.4 Hz, 2H, aromatic H), 7.37 (t, J = 7.3 Hz, 2H, aromatic H), 6.62 (m, 2H, 2 NH), 6.35 (d, J = 6.4 Hz, 1H, NH), 6.03 (s, 1H, NH), 5.16 (d, J = 5.8 Hz, 1H, NH), 4.54 (d, J = 6.4 Hz, 2H, Fmoc- CO_2CH_2), 4.39 (m, 3H, 3 CHCH_3), 4.28 (m, 1H, CHCH_3), 4.21–4.15 (m, 1H, fluorenyl CH), 3.38–3.22 (m, 2H, $\text{PIB-CH}_2\text{NHCO}$), 1.84–0.86 (m, 224H, polymer H , 4 CH_3). HRMS (MALDI): calcd. for $\text{C}_{56}\text{H}_{91}\text{N}_5\text{O}_6\text{Na}$: ($n = 5$ [$\text{M}+\text{Na}$] $^+$) 952.6862.; found: 952.7375. R_f : 0.4 (DCM/MeOH 10:1).

PIB-L-Ala₄-H 30. PIB-L-Ala₄-Fmoc **29** (4.5 g, 2.6 mmol, 1 equiv.) was dissolved in CHCl_3 (200 mL), and piperidine (8 mL, 78 mmol, 30 equiv.) was added. The reaction mixture was stirred for 6 h, and the volatiles were removed by evaporation *in vacuo*. The residue was purified by column chromatography (SiO_2 ; DCM/MeOH 10:1) to obtain pure **30** as a colorless solid (3.45 g, 2.3 mmol, 89 %).

^1H NMR (400 MHz, $\text{C}_2\text{D}_2\text{Cl}_4$) δ = 7.50 (m, 1H, NH), 6.63 (m, 2H, 2 NH), 5.96 (m, 1H, NH), 4.40 (m, 3H, 3 CHCH_3), 3.60 (m, 1H, CHCH_3), 3.30 (m, 2H, $\text{PIB-CH}_2\text{NHCO}$), 2.07 (m, 2H, CH_2NH_2), 1.60–0.84 (m, 228H, polymer H , 4 CH_3). HRMS (MALDI): calcd. for $\text{C}_{65}\text{H}_{129}\text{N}_5\text{O}_4\text{Na}$: ($n = 11$ [$\text{M}+\text{Na}$] $^+$) 1066.9937; found: 1066.8450. R_f : 0.1 (DCM/MeOH 10:1).

PIB-T₃-PIB T3A0. PIB-NH₂ (0.14 g, 0.125 mmol) was dissolved in THF (50 mL), and **12** (73 mg, 0.63 mmol) was added. The reaction mixture was stirred overnight at room temperature. After reducing the volume of the solution *in vacuo* to about 20 mL, the crude product was precipitated with methanol (100 mL) and stirring of the resulting slurry for an hour. The precipitate was

collected by filtration. After a short column (20:1 DCM:MeOH), the **T3A0** was obtained as an yellow sticky solid (0.063 g, 40%). TCE solutions ($c = 1$ mmol/L) of **T3A0** were annealed at 120°C overnight under stirring and then slowly allowed to cool to room temperature in the oil bath without any stirring.

^1H NMR (400.13 MHz, CDCl_3): $\delta = 0.65\text{--}1.60$ (m, 248H, aliphatic H), 2.51 (t, $J = 7.4$ Hz, 4H, $\text{CH}_2\text{C}(\text{O})$), 3.16 (t, $J = 7.2$ Hz, 4H, $\text{CH}_2\text{-Ar}$), 3.20–3.30 (m, 4H, $\text{CH}_2\text{-NHC}(\text{O})$), 5.32 (m, 2H, NH), 6.72 (d, $J = 3.6$ Hz, 2H, Ar- H), 6.94 (d, $J = 3.5$ Hz, 2H, Ar- H), 6.96 (s, 2H, Ar- H).

PIB-Ala₂-T₃-Ala₂-PIB T3A2. PIB-Ala₂-NH₂ **27a** (0.33 g, 0.28 mmol) was dissolved in THF (100 mL), and 2,2':5',2''-terthiophene-5,5''-di(propan-3-oic acid) di(chlorendylimidyl ester) **12** (150 mg, 0.13 mmol) was added. The reaction mixture was stirred overnight at room temperature. After reducing the volume of the solution *in vacuo* to about 30 mL, the crude product was precipitated with methanol (200 mL), and the resulting slurry was stirred for 1 h. The precipitate was filtered off, taken up in DCM (30 mL), and reprecipitated into methanol (200 mL). This precipitation procedure was repeated one more time to afford **T3A2** as an yellow-green sticky solid (0.237 g, 64%). TCE solutions ($c = 1$ mmol/L) of **T3A2** were annealed at 120°C overnight under stirring and then slowly allowed to cool to room temperature in the oil bath without any stirring.

^1H NMR (400.13 MHz, TCE- d_2 , 100°C): $\delta = 0.75\text{--}1.72$ (m, 400H, aliphatic H), 2.64 (t, $J = 7.2$ Hz, 4H, $\text{CH}_2\text{C}(\text{O})$), 3.22 (t, $J = 7.2$ Hz, 4H, $\text{CH}_2\text{-Ar}$), 3.25–3.40 (m, 4H, $\text{CH}_2\text{-NHC}(\text{O})$), 4.33–4.50 (m, 4H, C* H), 5.76–5.90 (m, 4H, NH), 6.39 (m, 2H, NH), 6.79 (d, $J = 3.6$ Hz, 2H, Ar- H), 7.03 (d, $J = 3.5$ Hz, 2H, Ar- H), 7.04 (s, 2H, Ar- H).

PIB-Ala₃-T₃-Ala₃-PIB T3A3. PIB-Ala₃-NH₂ **28** (0.10 g, 0.084 mmol) was dissolved in THF (50 mL), and 2,2':5',2''-terthiophene-5,5''-di(propan-3-oic acid) di(chlorendylimidyl ester) **12** (314 mg, 0.18 mmol) was added. The reaction mixture was stirred overnight at room temperature. After reducing the volume of the solution *in vacuo* to about 20 mL, the crude product was precipitated with methanol (100 mL) and the resulting slurry was stirred for 1 h. The precipitate was filtered off, taken up in THF (20 mL), and reprecipitated into methanol (100 mL). This precipitation procedure was repeated one more time to afford **T3A3** as an yellow-green sticky solid (0.215 g, 63%). TCE solutions ($c = 1$ mmol/L) of **T3A3** were annealed at 120°C overnight under stirring and then slowly allowed to cool to room temperature in the oil bath without any stirring.

^1H NMR (400.13 MHz, TCE- d_2 , 100°C): $\delta = 0.78\text{--}1.77$ (m, 381H, aliphatic H), 2.65 (t, $J = 7.2$ Hz, 4H, $\text{CH}_2\text{C}(\text{O})$), 3.20–3.40 (m, 8H, 2 $\text{CH}_2\text{-Ar}$ & 2 $\text{CH}_2\text{-NHC}(\text{O})$), 4.41 (m, 6H, C* H), 5.80–5.95 (m, 4H, NH), 6.41 (m, 2H, NH), 6.57 (m, 2H, NH), 6.80 (m, 2H, Ar- H), 7.03 (m, 4H, Ar- H).

PIB-T₄-PIB T4A0. PIB-NH₂ (1.11 g, 0.92 mmol) was dissolved in THF (100 mL), and **13** (530 mg, 0.44 mmol) was added. The reaction mixture was stirred for 3h at room temperature, solvent was removed *in vacuo* and the residue was dissolved in DCM. Filtration over a short SiO₂ plug afforded pure **T4A0** as a yellow-brown sticky solid (600 mg, 48%).

¹H NMR (400.13 MHz, CDCl₃): δ = 0.75–1.65 (m, 429H, aliphatic *H*), 2.51 (t, *J* = 7.4 Hz, 4H, CH₂C(O)), 3.16 (t, *J* = 7.2 Hz, 4H, CH₂-Ar), 3.20–3.30 (m, 4H, CH₂-NHC(O)), 5.32 (m, 2H, NH), 6.73 (d, *J* = 3.6 Hz, 2H, Ar-*H*), 6.97 (d, *J* = 3.6 Hz, 2H, Ar-*H*), 6.98 (d, *J* = 4.0 Hz, 2H, Ar-*H*), 7.02 (d, *J* = 3.6 Hz, 2H, Ar-*H*). MS (MALDI): calcd C₁₅₂H₂₈₀N₂O₂S₄ ([M]⁺) 2296.0814; found 2296.4393.

PIB-Ala-T₄-Ala-PIB T4A1. PIB-Ala-NH₂ **26** (921 mg, 0.69 mmol) was dissolved in THF (250 mL), and 2,2':5',2'':5'',2''':5''',2''''-quaterthiophene-5,5''''-di(propan-3-oic acid) di(chlorendylimidyl ester) **13** (407 mg, 0.34 mmol) was added. The reaction mixture was stirred overnight at room temperature. After reducing the volume of the solution *in vacuo* to about 100 mL, the crude product was precipitated by dropwise addition of the solution into methanol (1 L) and stirring of the resulting slurry overnight. The precipitate was collected by filtration, taken up in chloroform (35 mL), and reprecipitated into methanol (0.4 L) to afford **T4A1** as a yellow-brown sticky solid (767 mg, 73%). TCE solutions (*c* = 1 mmol/L) of **T4A2** were annealed at 120°C for 2 h without any stirring, then at 100°C for 2 h, and finally allowed to slowly cool to room temperature in the oil bath.

¹H NMR (400.13 MHz, CDCl₃): δ = 0.70–1.62 (m, 371H, aliphatic *H*), 2.56 (t, *J* = 7.6 Hz, 4H, CH₂C(O)), 3.15 (t, *J* = 7.4 Hz, 4H, CH₂-Ar), 3.17–3.32p (m, 4H, CH₂-NHC(O)), 4.43 (m, 2H, C**H*), 5.97 (m, 2H, NH), 6.17 (d, *J* = 7.6 Hz, 2H, C*NH), 6.71 (d, *J* = 3.6 Hz, 2H, Ar-*H*), 6.92–7.02 (m, 6H, Ar-*H*). MS (MALDI): calcd C₁₃₈H₂₅₀N₄O₄S₄ (*n* = 11/12 [M]⁺) 2155.8359; found 2155.9396.

PIB-Ala₂-T₄-Ala₂-PIB T4A2. PIB-Ala₂-NH₂ **27a** (1.88 g, 1.29 mmol) was dissolved in THF (500 mL), and 2,2':5',2'':5'',2''':5''',2''''-quaterthiophene-5,5''''-di(propan-3-oic acid) di(chlorendylimidyl ester) **13** (770 mg, 0.64 mmol) was added. The reaction mixture was stirred overnight at room temperature. After reducing the volume of the solution *in vacuo* to about 250 mL, the crude product was precipitated by the drop-wise addition of the solution to methanol (3 L). The resulting slurry was stirred overnight. This precipitation procedure was repeated two times using MeOH as the non-solvent, once more using deionized water, and finally acetone to afford **T4A2** as a yellow-brown sticky solid (1.39 g, 65%). TCE solutions (*c* = 1 mmol/L) of **T4A2** were annealed at 120°C for 2 h without any stirring, then at 100°C for 2 h, and finally allowed to slowly cool to room temperature in the oil bath.

¹H NMR (400.13 MHz, TCE-d₂, 100°C): δ = 0.78–1.72 (m, 468H, aliphatic *H*), 2.64 (t, *J* = 7.2 Hz, 4H, CH₂C(O)), 3.22 (t, *J* = 7.2 Hz, 4H, CH₂-Ar), 3.25–3.40 (m, 4H, CH₂-NHC(O)), 4.33–4.50 (m, 4H, C**H*),

5.76–5.90 (m, 4H, NH), 6.33–6.41 (m, 2H, NH), 6.80 (d, $J = 3.2$ Hz, 2H, Ar- H), 7.02–7.11 (m, 6H, Ar- H). MS (MALDI): calcd $C_{132}H_{236}N_6O_6S_4$ ($n = 10$ [M]⁺) 2131.7291; found 2131.1796.

PIB-Ala₃-T₄-Ala₃-PIB T4A3. PIB-Ala₃-NH₂ **28** (507 mg, 0.33 mmol) was dissolved in THF (250 mL), and 2,2':5',2'':5'',2''':5''',2''''-quaterthiophene-5,5''''-di(propan-3-oic acid) di(chlorendylimidyl ester) **13** (197 mg, 0.16 mmol) was added. The reaction mixture was stirred overnight at room temperature. After reducing the volume of the solution *in vacuo* to about 90 mL, the crude product was precipitated by the drop-wise addition of the solution to methanol (1 L). The resulting slurry was stirred for 30 min. This precipitation procedure was repeated two times to afford **T4A3** as a yellow-brown sticky solid (489 mg, 86%). TCE solutions ($c = 1$ mmol/L) of **T4A3** were degassed by three freeze-pump-thaw cycles, annealed at 160°C under stirring for 30 min, at 120°C for 5 h without stirring, and finally slowly cooled to room temperature in the oil bath.

¹H NMR (400.13 MHz, TCE-d₂, 100°C): $\delta = 0.78$ –1.72 (m, 468H, aliphatic H), 2.65 (t, $J = 7.2$ Hz, 4H, CH₂C(O)), 3.22 (t, $J = 7.2$ Hz, 4H, CH₂-Ar), 3.25–3.40 (m, 4H, CH₂-NHC(O)), 4.33–4.50 (m, 6H, C* H), 5.80–5.95 (m, 4H, NH), 6.33–6.41 (m, 2H, NH), 6.47–6.57 (m, 2H, NH), 6.80 (d, $J = 3.2$ Hz, 2H, Ar- H), 7.02–7.12 (m, 6H, Ar- H). MS (MALDI): calcd $C_{138}H_{246}N_8O_8S_4$ ($n = 10$ [M]⁺) 2272.8005; found 2272.7102.

PIB-Ala₄-T₄-Ala₄-PIB T4A4. PIB-Ala₄-NH₂ **30** (501 mg, 0.28 mmol) was dissolved in THF (250 mL), and 2,2':5',2'':5'',2''':5''',2''''-quaterthiophene-5,5''''-di(propan-3-oic acid) di(chlorendylimidyl ester) **13** (163 mg, 0.13 mmol) was added. The reaction mixture was stirred overnight at room temperature. After reducing the volume of the solution *in vacuo* to about 110 mL, the crude product was precipitated by the drop-wise addition of the solution to methanol (1.5 L). The resulting slurry was stirred overnight. This precipitation was repeated two times to afford **T4A4** as a yellow-brown sticky solid (478 mg, 87%). TCE solutions ($c = 1$ mmol/L) of **T4A4** were degassed by three freeze-pump-thaw cycles, annealed at 140°C for 2 h, at 100°C for 2 h, and finally slowly cooled to room temperature in the oil bath.

¹H NMR (400.13 MHz, TCE-d₂, 120°C): $\delta = 0.75$ –1.80 (m, aliphatic H), 2.67 (m, 4H, CH₂C(O)), 3.18–3.38 (m, 8H, CH₂-Ar & CH₂-NHC(O)), 4.28–4.48 (m, 8H, C* H), 5.85–5.90 (m, 2H, NH), 6.35–6.40 (m, 2H, NH), 6.55–6.70 (m, 6H, NH), 6.81 (m, 2H, Ar- H), 7.02–7.17 (m, 6H, Ar- H).

PIB-T₅-PIB T5A0. PIB-NH₂ (0.20 g, 0.182 mmol) was dissolved in THF (100 mL), and 2,2':5',2'':5'',2''':5''',2''''-pentathiophene-5,5''''-di(propan-3-oic acid) di(chlorendylimidyl ester) **14** (100 mg, 0.077 mmol) was added. The reaction mixture was stirred overnight at room temperature. After reducing the volume of the solution *in vacuo* to about 50 mL, the crude product was precipitated by the addition of methanol (200 mL), and the resulting slurry was

stirred for 1 h. The precipitate was filtered off, taken up in DCM (20 mL), and reprecipitated into methanol (100 mL). This precipitation procedure was repeated one more time to afford **T5A0** as a yellow-brown sticky solid (0.110 g, 52%). TCE solutions ($c = 1$ mmol/L) of **T5A0** were annealed at 120°C overnight under stirring and then slowly allowed to cool to room temperature in the oil bath without any stirring.

^1H NMR (400.13 MHz, CDCl_3): $\delta = 0.70\text{--}1.75$ (m, 201H, aliphatic H), 2.52 (t, 4H, $\text{CH}_2\text{C}(\text{O})$), 3.17 (m, 4H, $\text{CH}_2\text{-Ar}$), 3.26 (m, 4H, $\text{CH}_2\text{-NHC}(\text{O})$), 5.35 (m, 2H, NH), 6.74 (m, 2H, Ar-H), 6.8–7.2 (m, 8H, Ar-H).

PIB-Ala₂-T₅-Ala₂-PIB T5A2. PIB-Ala₂-NH₂ **27a** (0.539 g, 0.32 mmol) was dissolved in THF (250 mL), and 2,2':5',2'':5'',2''':5''',2''''-pentathiophene-5,5''''-di(propan-3-oic acid) di(chlorendylimidyl ester) **14** (200 mg, 0.15 mmol) was added. The reaction mixture was stirred overnight at room temperature. After reducing the volume of the solution *in vacuo* to about 120 mL, the crude product was precipitated by the addition of methanol (2 L). The resulting slurry was stirred for a few hours. The precipitate was collected by filtration, taken up in THF (100 mL), and reprecipitated into methanol (2 L) to afford **T5A2** as a yellow-brown sticky solid (0.35 g, 77%). TCE solutions ($c = 1$ mmol/L) of **T5A2** were annealed at 120°C overnight under stirring and then slowly allowed to cool to room temperature in the oil bath without any stirring.

^1H NMR (400.13 MHz, TCE- d_2 , 120°C): $\delta = 0.80\text{--}1.70$ (m, 422H, aliphatic H), 2.63 (m, 4H, $\text{CH}_2\text{C}(\text{O})$), 3.21 (m, 4H, $\text{CH}_2\text{-Ar}$), 3.29 (m, 4H, $\text{CH}_2\text{-NHC}(\text{O})$), 4.30–4.52 (m, 4H, C^*H), 5.72–5.87 (m, 4H, NH), 6.33–6.41 (m, 2H, NH), 6.79 (m, $J = 3.2$ Hz, 2H, Ar-H), 7.00–7.20 (m, 8H, Ar-H).

PIB-Ala₃-T₅-Ala₃-PIB T5A3. PIB-Ala₃-NH₂ **28** (0.289 g, 0.16 mmol) was dissolved in THF (100 mL), and 2,2':5',2'':5'',2''':5''',2''''-pentathiophene-5,5''''-di(propan-3-oic acid) di(chlorendylimidyl ester) **14** (100 mg, 0.77 mmol) was added. The reaction mixture was stirred overnight at room temperature. After reducing the volume of the solution *in vacuo* to about 50 mL, the crude product was precipitated by the addition of methanol (300 L). The resulting slurry was stirred for a few hours. The precipitate was collected by filtration, taken up in THF (40 mL), and reprecipitated by the addition of methanol to afford **T5A3** as an orange-brown sticky solid (0.21 g, 66%). TCE solutions ($c = 1$ mmol/L) of **T5A3** were annealed at 120°C overnight under stirring and then slowly allowed to cool to room temperature in the oil bath without any stirring.

^1H NMR (400.13 MHz, TCE- d_2 , 120°C): $\delta = 0.75\text{--}2.00$ (m, 618H, aliphatic H), 2.66 (t, $J = 7.2$ Hz, 4H, $\text{CH}_2\text{C}(\text{O})$), 3.23 (t, $J = 7.2$ Hz, 4H, $\text{CH}_2\text{-Ar}$), 3.33 (m, 4H, $\text{CH}_2\text{-NHC}(\text{O})$), 4.40 (m, 6H, C^*H), 5.86 (m, 4H, NH), 6.35 (m, 2H, NH), 6.49 (m, 2H, NH), 6.81 (m, 2H, Ar-H), 7.05–7.19 (m, 8H, Ar-H).

PIB-T₆-PIB T6A0. PIB-NH₂ (224 mg, 0.20 mmol) was dissolved in THF (30 mL), and

2,2':5',2'':5'',2''':5''',2''''':5''''',2''''':5'''''-Sexithiophene-5,5'''''-di(propan-3-oic acid) di(chlorendylimidyl ester) **15** (137 mg, 0.10 mmol) was added. The reaction mixture was stirred overnight at room temperature. After reducing the volume of the solution *in vacuo* to about 8 mL, the crude product was precipitated by the drop-wise addition of the solution into acetone (100 mL). The resulting slurry was stirred for 1 h. The precipitate was collected by filtration, taken up in THF and reprecipitated into acetone to afford **T6A0** as an orange-brown sticky solid (203 mg, 73%).

^1H NMR (400.13 MHz, CDCl_3 , 50°C): δ = 0.70–1.75 (m, 360H, aliphatic *H*), 2.51 (t, J = 7.4 Hz, 4H, $\text{CH}_2\text{C}(\text{O})$), 3.17 (t, J = 7.2 Hz, 4H, $\text{CH}_2\text{-Ar}$), 3.21–3.32 (m, 4H, $\text{CH}_2\text{-NHC}(\text{O})$), 5.26 (m, 2H, NH), 6.74 (d, J = 3.6 Hz, 2H, Ar-*H*), 6.98 (d, J = 3.6 Hz, 2H, Ar-*H*), 7.00 (d, J = 4.0 Hz, 2H, Ar-*H*), 7.03–7.10 (m, 6H, Ar-*H*). MS (MALDI): calcd $\text{C}_{92}\text{H}_{149}\text{N}_2\text{O}_2\text{S}_6$ ($n = 5/6$ [M+H]⁺) 1505.9938; found 1505.5914.

PIB-Ala₂-T₆-Ala₂-PIB T6A2. PIB-Ala₂-NH₂ **27a** (1.23 g, 0.84 mmol) was dissolved in THF (600 mL), and 2,2':5',2'':5'',2''':5''',2''''':5''''',2''''':5'''''-Sexithiophene-5,5'''''-di(propan-3-oic acid) di(chlorendylimidyl ester) **15** (550 mg, 0.40 mmol) was added. The reaction mixture was stirred overnight at room temperature. After reducing the volume of the solution *in vacuo* to about 300 mL, the crude product was precipitated by the drop-wise addition of the solution into methanol (3.2 L). The resulting slurry was stirred overnight. The precipitate was collected by filtration, taken up in THF (200 mL), and reprecipitated into methanol (3 L) to afford **T6A2** as an orange-brown sticky solid (1.2 g, 86%). TCE solutions ($c = 1$ mmol/L) of **T6A2** were degassed by three freeze-pump-thaw cycles, annealed at 120°C under stirring for 5 h, and finally slowly cooled to room temperature in the oil bath without stirring.

^1H NMR (400.13 MHz, TCE- d_2 , 120°C): δ = 0.75–1.75 (m, 449H, aliphatic *H*), 2.65 (t, J = 7.2 Hz, 4H, $\text{CH}_2\text{C}(\text{O})$), 3.23 (t, J = 7.2 Hz, 4H, $\text{CH}_2\text{-Ar}$), 3.27–3.40 (m, 4H, $\text{CH}_2\text{-NHC}(\text{O})$), 4.34–4.52 (m, 4H, C**H*), 5.72–5.87 (m, 4H, NH), 6.33–6.41 (m, 2H, NH), 6.81 (d, J = 3.2 Hz, 2H, Ar-*H*), 7.04–7.20 (m, 10H, Ar-*H*). MS (MALDI): calcd $\text{C}_{228}\text{H}_{416}\text{N}_6\text{O}_6\text{S}_6$ ([M]⁺) 3527.0756; found 3531.3691.

PIB-Ala₃-T₆-Ala₃-PIB T6A3. PIB-Ala₃-NH₂ **28** (410 mg, 0.27 mmol) was dissolved in THF (200 mL), and 2,2':5',2'':5'',2''':5''',2''''':5''''',2''''':5'''''-Sexithiophene-5,5'''''-di(propan-3-oic acid) di(chlorendylimidyl ester) **15** (175 mg, 0.13 mmol) was added. The reaction mixture was stirred overnight at room temperature. After reducing the volume of the solution *in vacuo* to about 100 mL, the crude product was precipitated by the drop-wise addition of the solution into methanol (1.3 L). The resulting slurry was stirred for 1 h. The precipitate was collected by filtration, taken up in THF, and reprecipitated into methanol to afford **T6A3** as an orange-brown sticky solid (418 mg, 89%). TCE solutions ($c = 1$ mmol/L) of **T6A3** were degassed by three freeze-pump-thaw cycles, annealed at 180°C for 30 min under stirring, 120°C for 5 h without stirring, and finally slowly allowed to cool to room temperature in the oil bath.

PIB-Ala₂-T₇-Ala₂-PIB T7A2. PIB-Ala₂-NH₂ **27a** (268 mg, 0.18 mmol) was dissolved in THF (120 mL), and 2,2':5',2'':5'',2''':5''',2''''':5''''',2''''':5''''',2''''':5''''',2''''':5'''''-Heptathiophene-5,5''''''-di(propan-3-oic acid) di(chlorendylimidyl ester) **16** (122 mg, 0.08 mmol) was added. The red suspension was sonicated for 5 min and stirred overnight at room temperature. After reducing the volume of the resulting solution *in vacuo* to about 50 mL, the crude product was precipitated by the drop-wise addition of the solution into methanol (0.5 L). The resulting slurry was stirred for 2 h. The precipitate was collected by filtration, taken up in THF (50 mL), and reprecipitated into methanol (0.5 L) to afford **T7A2** as a sticky red-brown solid (276 mg, 88%). TCE solutions (*c* = 1 mmol/L) of **T7A2** were degassed by three freeze-pump-thaw cycles, annealed at 180°C for 30 min under stirring, at 120°C for 5 h without stirring, and finally slowly cooled to room temperature in the oil bath.

¹H NMR (400.13 MHz, TCE-d₂, 130°C): δ = 0.88–1.82 (m, 385H, aliphatic *H*), 2.69 (m, 4H, CH₂C(O)), 3.28 (t, 4H, CH₂-Ar), 3.37 (m, 4H, CH₂-NHC(O)), 4.30–4.60 (m, 4H, C**H*), 5.75–5.90 (m, 4H, NH), 6.31–6.39 (m, 2H, NH), 6.86 (m, 2H, Ar-*H*), 7.07–7.27 (m, 12H, Ar-*H*). MS (MALDI): calcd C₁₇₂H₂₉₈N₆O₆S₇K (n = 13/14 [M+K]⁺) 2807.0874; found 2806.5602.

PIB-Ala₃-T₇-Ala₃-PIB T7A3. PIB-Ala₃-NH₂ **28** (230 mg, 0.15 mmol) was dissolved in THF (130 mL), and 2,2':5',2'':5'',2''':5''',2''''':5''''',2''''':5''''',2''''':5''''',2''''':5'''''-Heptathiophene-5,5''''''-di(propan-3-oic acid) di(chlorendylimidyl ester) **16** (104 mg, 0.07 mmol) was added. The red suspension was sonicated for 5 min and stirred overnight at room temperature. After reducing the volume of the resulting solution *in vacuo* to about 50 mL, the crude product was precipitated by the drop-wise addition of the solution into methanol (600 mL). The resulting slurry was stirred for 2 h. The precipitate was collected by filtration, taken up in THF (50 mL), and reprecipitated into methanol (600 mL) to afford **T7A3** as a sticky red-brown solid (255 mg, 95%). TCE solutions (*c* = 1 mmol/L) of **T7A3** were degassed by three freeze-pump-thaw cycles, annealed at 180°C for 30 min under stirring, at 120°C for 5 h without stirring, and finally slowly cooled to room temperature in the oil bath.

¹H NMR (400.13 MHz, TCE-d₂, 130°C): δ = 0.80–1.80 (m, 610H, aliphatic *H*), 2.67 (t, *J* = 6.8 Hz, 4H, CH₂C(O)), 3.25 (t, *J* = 6.8 Hz, 4H, CH₂-Ar), 3.28–3.41 (m, 4H, CH₂-NHC(O)), 4.42 (m, 6H, C**H*), 5.79–5.87 (m, 4H, NH), 6.28–6.49 (m, 4H, NH), 6.82 (m, 2H, Ar-*H*), 7.05–7.21 (m, 12H, Ar-*H*). MS (MALDI): calcd C₁₅₀H₂₅₂N₈O₈S₇ (n = 10 [M]⁺) 2518.7631; found 2518.7564.

PIB-T₈-PIB T8A0. PIB-NH₂ (122 mg, 0.11 mmol) was dissolved in THF (50 mL), and 2,2':5',2'':5'',2''':5''',2''''':5''''',2''''':5''''',2''''':5''''',2''''':5'''''-octathiophene-5,5''''''-di(propan-3-oic acid) di(chlorendylimidyl ester) **17** (80 mg, 0.05 mmol) was added. The red suspension was sonicated for 5 min and stirred for 45 h at room temperature. After reducing the volume of the resulting solution *in vacuo* to about 15 mL, the crude product was precipitated by the drop-wise addition

(m, 4H, CH_2 -Ar), 3.32 (m, 4H, CH_2 -NHC(O)), 4.41 (m, 6H, C^*H), 5.82 (m, 4H, NH), 6.33 (m, 2H, NH), 6.45 (m, 2H, NH), 6.82 (m, 2H, Ar-H), 7.04–7.22 (m, 14H, Ar-H).

N-poly(isobutene)-yl perylene-9,10-di(propylcarboxylate)-3,4-dicarboximide 33. A slurry of perylene-3,4:9,10-tetracarboxylic dianhydride **31** (7.16 g, 18.3 mmol), 1-propanol (11 mL, 146 mmol), and DBU (11 mL, 73.1 mmol) in dry DMF (150 mL) was stirred for 16 h at room temperature in an inert atmosphere. The slurry became a clear solution after 1 h. Dry THF (130 mL), and then a solution of PIB-NH₂ **32** (11.0 g, 9.13 mmol) in dry THF (30 mL) were added slowly to the reaction mixture. The solution was stirred vigorously for 3 d, treated with 1-bromopropane (13 mL, 146 mmol), stirred for another 16 h, and finally poured into a 1M aqueous HCl solution. The slurry was extracted three times with DCM. The combined organic phases were washed with a 1M aqueous HCl solution, two times with a saturated aqueous NaCl solution, and finally dried over Mg₂SO₄. The solvent was removed *in vacuo*, and the residue (about 23 g) was purified by column chromatography (3.5 L SiO₂, DCM) to afford pure **33** as a red sticky solid (7.6 g, 49%).

¹H NMR (400.13 MHz, CDCl₃): δ = 0.65–1.80 (m, 154H, aliphatic *H*), 1.85 (sex, 2H, COOCH₂CH₂CH₃) 4.13–4.26 (m, 2H, CH_2 -N), 4.32 (t, 4H, COOCH₂), 8.58–8.72 (m, 8H, ArH).

N-poly(isobutene)-yl perylene-9,10-di(carboxylic anhydride)-3,4-dicarboximide 34. N-poly(isobutene)-yl perylene-9,10-di(propylcarboxylate)-3,4-dicarboximide **33** (6.97 g, 4.13 mmol) and *p*-toluenesulfonic acid monohydrate (7.86 g, 41.4 mmol) were dissolved in toluene (200 mL), and the resulting solution was stirred for 16 h at 95°C. After cooling to room temperature, the reaction mixture was poured into MeOH (2.5 L), and the resulting slurry was stirred for 1.5 h. The red precipitate was filtered off, washed with MeOH, taken up in THF (150 mL), and reprecipitated into MeOH (1.5 L) to afford pure **34** as a red sticky solid (6.33 g, 97%).

¹H NMR (400.13 MHz, CDCl₃, 120°C): δ = 0.65–1.85 (m, 152H, aliphatic *H*), 4.17–4.29 (m, 2H, CH_2 -N), 8.58–8.72 (m, 8H, ArH).

PIB₁₉-PBI-T₄-PBI-PIB₁₉ PTP-19. 5-5'''-Bis(2-amino-ethyl)-2,2':5',2'':5'',2'''-quaterthiophene dihydrochloride (15 mg, 36 μmol), perylene-9,10-dicarboxylic anhydride-3,4-dicarboximide-N-(polyisobutyl) **34** (120 mg, 76 μmol), and Zn(OAc)₂ (13 mg, 72 μmol) were dissolved in quinoline (20 mL). The resulting solution was stirred for 16 h at 175°C. The reaction mixture was subsequently cooled to room temperature and then poured into MeOH (150 mL). After stirring for 4 h, the dark red precipitate was filtered off, redissolved in THF (20 mL), and reprecipitated into MeOH (150 mL). The obtained residue was then redissolved in THF containing SiO₂ (10 mL), and the slurry was evaporated to obtain the crude product dry-loaded

on SiO₂ for the subsequent column chromatography (50 mL SiO₂, DCM/MeOH 10:1, then pure THF). A final precipitation from THF to MeOH afforded pure **PTP-19** as a red sticky solid (54 mg, 42%).

¹H NMR (400.13 MHz, TCE-d₂, 120°C): δ = 0.75–1.95 (m, 358H, aliphatic *H*), 3.35–3.42 (m, 4H, CH₂-N), 4.26–4.35 (m, 4H, quaterthiophene-CH₂CH₂-N), 4.56–4.65 (m, 4H, quaterthiophene-CH₂CH₂-N), 8.65–8.80 (m, 16H, perylene Ar*H*).

References



7 References

- (1) Armaroli, N.; Balzani, V. The future of energy supply: challenges and opportunities. *Angew. Chem. Int. Ed.* **2007**, *46*, 52–66.
- (2) Morton, O. Solar energy: a new day dawning? Silicon Valley sunrise. *Nature* **2006**, *443*, 19–22.
- (3) Wang, C.; Dong, H.; Hu, W.; Liu, Y.; Zhu, D. Semiconducting π -conjugated systems in field-effect transistors: a material odyssey of organic electronics. *Chem. Rev.* **2012**, *112*, 2208–2267.
- (4) Braga, D.; Horowitz, G. High-performance organic field-effect transistors. *Adv. Mater.* **2009**, *21*, 1473–1486.
- (5) Guo, Y.; Yu, G.; Liu, Y. Functional organic field-effect transistors. *Adv. Mater.* **2010**, *22*, 4427–4447.
- (6) Gather, M. C.; Köhnen, A.; Meerholz, K. White organic light-emitting diodes. *Adv. Mater.* **2010**, *23*, 233–248.
- (7) Lin, P.; Yan, F. Organic thin-film transistors for chemical and biological sensing. *Adv. Mater.* **2012**, *24*, 34–51.
- (8) Facchetti, A. π -Conjugated polymers for organic electronics and photovoltaic cell applications. *Chem. Mater.* **2011**, *23*, 733–758.
- (9) Torsi, L.; Magliulo, M.; Manoli, K.; Palazzo, G. Organic field-effect transistor sensors: a tutorial review. *Chem. Soc. Rev.* **2013**, *42*, 8612.
- (10) Delgado, J. L.; Bouit, P.-A.; Filippone, S.; Herranz, M. A.; Martin, N. Organic photovoltaics: a chemical approach. *Chem. Commun.* **2010**, *46*, 4853–4865.
- (11) Joshi, D.; Shivanna, R.; Narayan, K. S. Organic photovoltaics: key photophysical, device and design aspects. *Journal of Modern Optics* **2014**, 1–11.
- (12) Thompson, B. C.; Fréchet, J. M. J. Polymer–fullerene composite solar cells. *Angew. Chem. Int. Ed.* **2008**, *47*, 58–77.
- (13) Kippelen, B.; Brédas, J.-L. Organic photovoltaics. *Energy Environ. Sci.* **2009**, *2*, 251.
- (14) Service, R. F. Solar energy. Outlook brightens for plastic solar cells. *Science*, 2011, *332*, 293.
- (15) Guo, X.; Baumgarten, M.; Müllen, K. Designing π -conjugated polymers for organic electronics. *Progress in Polymer Science* **2013**, *38*, 1832–1908.
- (16) Mei, J.; Diao, Y.; Appleton, A. L.; Fang, L.; Bao, Z. Integrated materials design of organic semiconductors for field-effect transistors. *J. Am. Chem. Soc.* **2013**, *135*, 6724–6746.
- (17) Holliday, S.; Donaghey, J. E.; McCulloch, I. Advances in charge carrier mobilities of

- semiconducting polymers used in organic transistors. *Chem. Mater.* **2014**, *26*, 647–663.
- (18) Mishra, A.; Ma, C.-Q.; Bäuerle, P. Functional oligothiophenes: molecular design for multidimensional nanoarchitectures and their applications. *Chem. Rev.* **2009**, *109*, 1141–1276.
- (19) Virkar, A. A.; Mannsfeld, S.; Bao, Z.; Stingelin, N. Organic semiconductor growth and morphology considerations for organic thin-film transistors. *Adv. Mater.* **2010**, *22*, 3857–3875.
- (20) Tsao, H. N.; Müllen, K. Improving polymer transistor performance via morphology control. *Chem. Soc. Rev.* **2010**, *39*, 2372.
- (21) Rivnay, J.; Mannsfeld, S. C. B.; Miller, C. E.; Salleo, A.; Toney, M. F. Quantitative determination of organic semiconductor microstructure from the molecular to device scale. *Chem. Rev.* **2012**, *112*, 5488–5519.
- (22) Lehn, J.-M. Toward self-organization and complex matter. *Science* **2002**, *295*, 2400–2403.
- (23) Stupp, S. I.; Palmer, L. C. Supramolecular chemistry and self-assembly in organic materials design. *Chem. Mater.* **2014**, *26*, 507–518.
- (24) Tambara, K.; Pantoş, G. D. Supramolecular chemistry of donor–acceptor interactions. *Annu. Rep. Prog. Chem., Sect. B: Org. Chem.* **2012**, *108*, 186.
- (25) Palmer, L. C.; Velichko, Y. S.; la Cruz, de, M. O.; Stupp, S. I. Supramolecular self-assembly codes for functional structures. *Phil. Trans. R. Soc. A* **2007**, *365*, 1417–1433.
- (26) Banerji, N. Sub-picosecond delocalization in the excited state of conjugated homopolymers and donor–acceptor copolymers. *J. Mater. Chem. C* **2013**, *1*, 3052.
- (27) Qi, B.; Wang, J. Fill factor in organic solar cells. *Phys. Chem. Chem. Phys.* **2013**, *15*, 8972.
- (28) Mishra, A.; Bäuerle, P. Small molecule organic semiconductors on the move: promises for future solar energy technology. *Angew. Chem. Int. Ed.* **2012**, *51*, 2020–2067.
- (29) Gregg, B. A.; Hanna, M. C. Comparing organic to inorganic photovoltaic cells: Theory, experiment, and simulation. *J. Appl. Phys.* **2003**, *93*, 3605.
- (30) Brédas, J.-L.; Beljonne, D.; Coropceanu, V.; Cornil, J. Charge-transfer and energy-transfer processes in π -conjugated oligomers and polymers: A molecular picture. *Chem. Rev.* **2004**, *104*, 4971–5004.
- (31) Brédas, J.-L.; Street, G. B. Polarons, bipolarons, and solitons in conducting polymers. *Acc. Chem. Res.* **1985**, *18*, 309–315.
- (32) Brédas, J.-L. Mind the gap! *Mater. Horiz.* **2013**, *1*, 17.
- (33) Brédas, J.-L.; Norton, J. E.; Cornil, J.; Coropceanu, V. Molecular understanding of organic

- solar cells: the challenges. *Acc. Chem. Res.* **2009**, *42*, 1691–1699.
- (34) Spanggaard, H.; Krebs, F. C. A brief history of the development of organic and polymeric photovoltaics. *Sol. Energ. Mat. Sol. C.* **2004**, *83*, 125–146.
- (35) Tang, C. W. Two-layer organic photovoltaic cell. *Appl. Phys. Lett.* **1986**, *48*, 183–185.
- (36) Yu, G.; Gao, J.; Hummelen, J. C.; Wudl, F.; Heeger, A. J. Polymer photovoltaic cells: enhanced efficiencies via a network of internal donor-acceptor heterojunctions. *Science* **1995**, *270*, 1789–1791.
- (37) Scharber, M. C.; Sariciftci, N. S. Efficiency of bulk-heterojunction organic solar cells. *Progress in Polymer Science* **2013**, *38*, 1929–1940.
- (38) Kim, J.; Kim, K.; Ko, S. H.; Kim, W. Optimum design of ordered bulk heterojunction organic photovoltaics. *Sol. Energ. Mat. Sol. C.* **2011**, *95*, 3021–3024.
- (39) Heeger, A. J. 25th Anniversary article: bulk heterojunction solar cells: understanding the mechanism of operation. *Adv. Mater.* **2013**, *26*, 10–28.
- (40) Huang, Y.; Kramer, E. J.; Heeger, A. J.; Bazan, G. C. Bulk heterojunction solar cells: morphology and performance relationships. *Chem. Rev.* **2014**, *114*, 7006–7043.
- (41) Chart, N. S. C. E. <http://www.nrel.gov/ncpv/> (accessed Jan 12, 2015).
- (42) Green, M. A.; Emery, K.; Hishikawa, Y.; Warta, W.; Dunlop, E. D. Solar cell efficiency tables (Version 45). *Prog. Photovolt: Res. Appl.* **2014**, *23*, 1–9.
- (43) Shockley, W.; Queisser, H. J. Detailed balance limit of efficiency of p-n junction solar cells. *J. Appl. Phys.* **1961**, *32*, 510.
- (44) Clarke, T. M.; Durrant, J. R. Charge photogeneration in organic solar cells. *Chem. Rev.* **2010**, *110*, 6736–6767.
- (45) Gao, F.; Inganäs, O. Charge generation in polymer–fullerene bulk-heterojunction solar cells. *Phys. Chem. Chem. Phys.* **2014**, *16*, 20291–20304.
- (46) Few, S.; Frost, J. M.; Nelson, J. Models of charge pair generation in organic solar cells. *Phys. Chem. Chem. Phys.* **2014**, 1–15.
- (47) Brabec, C. J.; Zerza, G.; Cerullo, G.; De Silvestri, S.; Luzzati, S.; Hummelen, J. C.; Sariciftci, S. Tracing photoinduced electron transfer process in conjugated polymer/fullerene bulk heterojunctions in real time. *Chem Phys Lett* **2001**, *340*, 232–236.
- (48) De, S.; Pascher, T.; Maiti, M.; Jespersen, K. G.; Kesti, T.; Zhang, F.; Inganäs, O.; Yartsev, A.; Sundström, V. Geminate charge recombination in alternating polyfluorene copolymer/fullerene blends. *J. Am. Chem. Soc.* **2007**, *129*, 8466–8472.
- (49) Hwang, I. W.; Soci, C.; Moses, D.; Zhu, Z.; Waller, D.; Gaudiana, R.; Brabec, C. J.; Heeger, A. J. Ultrafast electron transfer and decay dynamics in a small band gap bulk heterojunction material. *Adv. Mater.* **2007**, *19*, 2307–2312.

- (50) Grancini, G.; Maiuri, M.; Fazzi, D.; Petrozza, A.; Egelhaaf, H.-J.; Brida, D.; Cerullo, G.; Lanzani, G. Hot exciton dissociation in polymer solar cells. *Nature Materials* **2013**, *12*, 29–33.
- (51) Hwang, I.-W.; Moses, D.; Heeger, A. J. Photoinduced carrier generation in P3HT/PCBM bulk heterojunction materials. *J. Phys. Chem. C* **2008**, *112*, 4350–4354.
- (52) Ohkita, H.; Cook, S.; Astuti, Y.; Duffy, W.; Tierney, S.; Zhang, W.; Heeney, M.; McCulloch, I.; Nelson, J.; Bradley, D. D. C.; et al. Charge carrier formation in polythiophene/fullerene blend films studied by transient absorption spectroscopy. *J. Am. Chem. Soc.* **2008**, *130*, 3030–3042.
- (53) Armin, A.; Zhang, Y.; Burn, P. L.; Meredith, P.; Pivrikas, A. Measuring internal quantum efficiency to demonstrate hot exciton dissociation. *Nat. Mater.* **2013**, *12*, 593–593.
- (54) Scharber, M. Measuring internal quantum efficiency to demonstrate hot exciton dissociation. *Nat. Mater.* **2013**, *12*, 594–594.
- (55) Pettersson, L. A.; Roman, L. S.; Inganäs, O. Modeling photocurrent action spectra of photovoltaic devices based on organic thin films. *J. Appl. Phys.* **1999**, *86*, 487–496.
- (56) Grancini, G.; Binda, M.; Criante, L.; Perissinotto, S.; Maiuri, M.; Fazzi, D.; Petrozza, A.; Egelhaaf, H.-J.; Brida, D.; Cerullo, G.; et al. Measuring internal quantum efficiency to demonstrate hot exciton dissociation. *Nat. Mater.* **2013**, *12*, 594–595.
- (57) Vandewal, K.; Albrecht, S.; Hoke, E. T.; Graham, K. R.; Widmer, J.; Douglas, J. D.; Schubert, M.; Mateker, W. R.; Bloking, J. T.; Burkhard, G. F.; et al. Efficient charge generation by relaxed charge-transfer states at organic interfaces. *Nature Materials* **2013**, *13*, 63–68.
- (58) Albrecht, S.; Vandewal, K.; Tumbleston, J. R.; Fischer, F. S. U.; Douglas, J. D.; Fréchet, J. M. J.; Ludwigs, S.; Ade, H.; Salleo, A.; Neher, D. On the efficiency of charge transfer state splitting in polymer:fullerene solar cells. *Adv. Mater.* **2014**, *26*, 2533–2539.
- (59) Burke, T. M.; McGehee, M. D. How high local charge carrier mobility and an energy cascade in a three-phase bulk heterojunction enable >90% quantum efficiency. *Adv. Mater.* **2014**, *26*, 1923–1928.
- (60) Albrecht, U.; Bässler, H. Yield of geminate pair dissociation in an energetically random hopping system. *Chem Phys Lett* **1995**, *235*, 389–393.
- (61) Fu, Y.-T.; Risko, C.; Brédas, J.-L. Intermixing at the pentacene-fullerene bilayer interface: a molecular dynamics study. *Adv. Mater.* **2013**, *25*, 878–882.
- (62) Gregg, B. A. Entropy of charge separation in organic photovoltaic cells: the benefit of higher dimensionality. *J. Phys. Chem. Lett.* **2011**, *2*, 3013–3015.
- (63) Dibb, G. F. A.; Jamieson, F. C.; Maurano, A.; Nelson, J.; Durrant, J. R. Limits on the fill factor in organic photovoltaics: distinguishing nongeminate and geminate recombination mechanisms. *J. Phys. Chem. Lett.* **2013**, *4*, 803–808.

- (64) Holdcroft, S. A photochemical study of poly(3-hexylthiophene). *Macromolecules* **1991**, *24*, 4834–4838.
- (65) Shimoi, Y.; Abe, S.; Kuroda, S. I.; Murata, K. Polarons and their endor spectra in poly(p-phenylene vinylene). *Solid State Commun.* **1995**, *95*, 137–141.
- (66) Bernardo, B.; Cheyns, D.; Verreet, B.; Schaller, R. D.; Rand, B. P.; Giebink, N. C. Delocalization and dielectric screening of charge transfer states in organic photovoltaic cells. *Nature Communications* **2014**, *5*, 1–7.
- (67) Savoie, B. M.; Rao, A.; Bakulin, A. A.; Gelinas, S.; Movaghar, B.; Friend, R. H.; Marks, T. J.; Ratner, M. A. Unequal partnership: asymmetric roles of polymeric donor and fullerene acceptor in generating free charge. *J. Am. Chem. Soc.* **2014**, *136*, 2876–2884.
- (68) Deibel, C.; Strobel, T.; Dyakonov, V. Origin of the efficient polaron-pair dissociation in polymer-fullerene blends. *Phys. Rev. Lett.* **2009**, *103*, 036402.
- (69) Bakulin, A. A.; Rao, A.; Pavelyev, V. G.; van Loosdrecht, P. H. M.; Pshenichnikov, M. S.; Niedzialek, D.; Cornil, J.; Beljonne, D.; Friend, R. H. The role of driving energy and delocalized states for charge separation in organic semiconductors. *Science* **2012**, *335*, 1340–1344.
- (70) Gelinas, S.; Rao, A.; Kumar, A.; Smith, S. L.; Chin, A. W.; Clark, J.; van der Poll, T. S.; Bazan, G. C.; Friend, R. H. Ultrafast long-range charge separation in organic semiconductor photovoltaic diodes. *Science* **2014**, *343*, 512–516.
- (71) Kaake, L. G.; Moses, D.; Heeger, A. J. Coherence and uncertainty in nanostructured organic photovoltaics. *J. Phys. Chem. Lett.* **2013**, *4*, 2264–2268.
- (72) Proctor, C. M.; Kuik, M.; Nguyen, T.-Q. Charge carrier recombination in organic solar cells. *Progress in Polymer Science* **2013**, *38*, 1941–1960.
- (73) Cowan, S. R.; Banerji, N.; Leong, W. L.; Heeger, A. J. Charge formation, recombination, and sweep-out dynamics in organic solar cells. *Adv. Funct. Mater.* **2012**, *22*, 1116–1128.
- (74) Ojala, A.; Petersen, A.; Fuchs, A.; Lovrincic, R.; Poelking, C.; Trollmann, J.; Hwang, J.; Lennartz, C.; Reichelt, H.; Hoeffken, H. W.; et al. Merocyanine/C60 planar heterojunction solar cells: effect of dye orientation on exciton dissociation and solar cell performance. *Adv. Funct. Mater.* **2012**, *22*, 86–96.
- (75) Park, S. H.; Roy, A.; Beaupré, S.; Cho, S.; Coates, N.; Moon, J. S.; Moses, D.; Leclerc, M.; Lee, K.; Heeger, A. J. Bulk heterojunction solar cells with internal quantum efficiency approaching 100%. *Nature Photon* **2009**, *3*, 297–302.
- (76) Wagenpfahl, A.; Deibel, C.; Dyakonov, V. Organic solar cell efficiencies under the aspect of reduced surface recombination velocities. *IEEE J. Select. Topics Quantum Electron.* **2010**, *16*, 1759–1763.

- (77) Deibel, C.; Wagenpfahl, A.; Dyakonov, V. Influence of charge carrier mobility on the performance of organic solar cells. *Phys. Stat. Sol. (RRL)* **2008**, *2*, 175–177.
- (78) Baumann, A.; Lorrmann, J.; Rauh, D.; Deibel, C.; Dyakonov, V. A new approach for probing the mobility and lifetime of photogenerated charge carriers in organic solar cells under real operating conditions. *Adv. Mater.* **2012**, *24*, 4381–4386.
- (79) Tessler, N.; Rappaport, N. Loss of photocurrent efficiency in low mobility semiconductors: Analytic approach to space charge effects. *Appl. Phys. Lett.* **2006**, *89*, 013504.
- (80) Umeyama, T.; Imahori, H. Design and control of organic semiconductors and their nanostructures for polymer–fullerene-based photovoltaic devices. *J. Mater. Chem. A* **2014**, *2*, 11545.
- (81) Facchetti, A. Polymer donor–polymer acceptor (all-polymer) solar cells. *Mater. Today* **2013**, *16*, 123–132.
- (82) Li, C.; Wonneberger, H. Perylene imides for organic photovoltaics: yesterday, today, and tomorrow. *Adv. Mater.* **2012**, *24*, 613–636.
- (83) Li, C.; Liu, M.; Pschirer, N. G.; Baumgarten, M.; Müllen, K. Polyphenylene-based materials for organic photovoltaics. *Chem. Rev.* **2010**, *110*, 6817–6855.
- (84) Lin, Y.; Zhan, X. Materials Horizons. *Mater. Horiz.* **2014**, *1*, 470–488.
- (85) Anthony, J. E. Small-molecule, nonfullerene acceptors for polymer bulk heterojunction organic photovoltaics. *Chem. Mater.* **2011**, *23*, 583–590.
- (86) Nelson, J. Polymer:fullerene bulk heterojunction solar cells. *Mater. Today* **2011**, *14*, 462–470.
- (87) Brabec, C. J.; Gowrisanker, S.; Halls, J. J. M.; Laird, D.; Jia, S.; Williams, S. P. Polymer-fullerene bulk-heterojunction solar cells. *Adv. Mater.* **2010**, *22*, 3839–3856.
- (88) He, Y.; Li, Y. Fullerene derivative acceptors for high performance polymer solar cells. *Phys. Chem. Chem. Phys.* **2011**, *13*, 1970.
- (89) Dang, M. T.; Hirsch, L.; Wantz, G. P3HT:PCBM, best seller in polymer photovoltaic research. *Adv. Mater.* **2011**, *23*, 3597–3602.
- (90) Dang, M. T.; Hirsch, L.; Wantz, G.; Wuest, J. D. Controlling the morphology and performance of bulk heterojunctions in solar cells. lessons learned from the benchmark poly(3-hexylthiophene):[6,6]-phenyl-C61-butyric acid methyl ester system. *Chem. Rev.* **2013**, *113*, 3734–3765.
- (91) Yassar, A.; Miozzo, L.; Gironda, R.; Horowitz, G. Rod–coil and all-conjugated block copolymers for photovoltaic applications. *Progress in Polymer Science* **2013**, *38*, 791–844.
- (92) Scharber, M. C.; Mühlbacher, D.; Koppe, M.; Denk, P.; Waldauf, C.; Heeger, A. J.; Brabec,

- C. J. Design rules for donors in bulk-heterojunction solar cells—towards 10 % energy-conversion efficiency. *Adv. Mater.* **2006**, *18*, 789–794.
- (93) Bian, L.; Zhu, E.; Tang, J.; Tang, W.; Zhang, F. Recent progress in the design of narrow bandgap conjugated polymers for high-efficiency organic solar cells. *Progress in Polymer Science* **2012**, *37*, 1292–1331.
- (94) Xu, T.; Yu, L. How to design low bandgap polymers for highly efficient organic solar cells. *Mater. Today* **2014**, *17*, 11–15.
- (95) Zhou, H.; Yang, L.; Stoneking, S.; You, W. A weak donor–strong acceptor strategy to design ideal polymers for organic solar cells. *ACS Appl. Mater. Interfaces* **2010**, *2*, 1377–1383.
- (96) Cabanetos, C.; Labban, El, A.; Bartelt, J. A.; Douglas, J. D.; Mateker, W. R.; Fréchet, J. M. J.; McGehee, M. D.; Beaujuge, P. M. Linear side chains in benzo[1,2-b:4,5-b']dithiophene–thieno[3,4-c]pyrrole-4,6-dione polymers direct self-assembly and solar cell performance. *J. Am. Chem. Soc.* **2013**, *135*, 4656–4659.
- (97) Graham, K. R.; Cabanetos, C.; Jahnke, J. P.; Idso, M. N.; Labban, El, A.; Ngongang Ndjawa, G. O.; Heumueller, T.; Vandewal, K.; Salleo, A.; Chmelka, B. F.; et al. Importance of the donor:fullerene intermolecular arrangement for high-efficiency organic photovoltaics. *J. Am. Chem. Soc.* **2014**, *136*, 9608–9618.
- (98) Wu, Z.; Petzold, A.; Henze, T.; Thurn-Albrecht, T.; Lohwasser, R. H.; Sommer, M.; Thelakkat, M. Temperature and molecular weight dependent hierarchical equilibrium structures in semiconducting poly(3-hexylthiophene). *Macromolecules* **2010**, *43*, 4646–4653.
- (99) Verilhac, J.-M.; LeBlevenec, G.; Djurado, D.; Rieutord, F.; Chouiki, M.; Travers, J.-P.; Pron, A. Effect of macromolecular parameters and processing conditions on supramolecular organisation, morphology and electrical transport properties in thin layers of regioregular poly(3-hexylthiophene). *Synthetic Met.* **2006**, *156*, 815–823.
- (100) Prosa, T. J.; Winokur, M. J.; Moulton, J.; Smith, P.; Heeger, A. J. X-ray structural studies of poly(3-alkylthiophenes) - an example of an inverse comb. *Macromolecules* **1992**, *25*, 4364–4372.
- (101) Sirringhaus, H.; Brown, P. J.; Friend, R. H.; Nielsen, M. M.; Bechgaard, K.; Langeveld-Voss, B.; Spiering, A.; Janssen, R.; Meijer, E. W.; Herwig, P.; et al. Two-dimensional charge transport in self-organized, high-mobility conjugated polymers. *Nature* **1999**, *401*, 685–688.
- (102) Kayunkid, N.; Uttiya, S.; Brinkmann, M. Structural model of regioregular poly(3-hexylthiophene) obtained by electron diffraction analysis. *Macromolecules* **2010**, *43*, 4961–4967.
- (103) Brinkmann, M. Structure and morphology control in thin films of regioregular poly(3-hexylthiophene). *J. Polym. Sci. B Polym. Phys.* **2011**, *49*, 1218–1233.

- (104) Salammal, S. T.; Mikayelyan, E.; Grigorian, S.; Pietsch, U.; Koenen, N.; Scherf, U.; Kayunkid, N.; Brinkmann, M. Impact of thermal annealing on the semicrystalline nanomorphology of spin-coated thin films of regioregular poly(3-alkylthiophene)s as observed by high-resolution transmission electron microscopy and grazing incidence X-ray diffraction. *Macromolecules* **2012**, *45*, 5575–5585.
- (105) Merlo, J. A.; Frisbie, C. D. Field effect transport and trapping in regioregular polythiophene nanofibers. *J. Phys. Chem. B* **2004**, *108*, 19169–19179.
- (106) Ro, H. W.; Akgun, B.; O'Connor, B. T.; Hammond, M.; Kline, R. J.; Snyder, C. R.; Satija, S. K.; Ayzner, A. L.; Toney, M. F.; Soles, C. L.; et al. Poly(3-hexylthiophene) and [6,6]-phenyl-C61-butyric acid methyl ester mixing in organic solar cells. *Macromolecules* **2012**, *45*, 6587–6599.
- (107) Yin, W.; Dadmun, M. A new model for the morphology of P3HT/PCBM organic photovoltaics from small-angle neutron scattering: rivers and streams. *ACS Nano* **2011**, *5*, 4756–4768.
- (108) Pfannmöller, M.; Flügge, H.; Benner, G.; Wacker, I.; Sommer, C.; Hanselmann, M.; Schmale, S.; Schmidt, H.; Hamprecht, F. A.; Rabe, T.; et al. Visualizing a homogeneous blend in bulk heterojunction polymer solar cells by analytical electron microscopy. *Nano Lett.* **2011**, *11*, 3099–3107.
- (109) Collins, B. A.; Gann, E.; Guignard, L.; He, X.; McNeill, C. R.; Ade, H. Molecular miscibility of polymer–fullerene blends. *J. Phys. Chem. Lett.* **2010**, *1*, 3160–3166.
- (110) Treat, N. D.; Brady, M. A.; Smith, G.; Toney, M. F.; Kramer, E. J.; Hawker, C. J.; Chabinc, M. L. Interdiffusion of PCBM and P3HT reveals miscibility in a photovoltaically active blend. *Adv. Energy Mater.* **2011**, *1*, 82–89.
- (111) Bartelt, J. A.; Beiley, Z. M.; Hoke, E. T.; Mateker, W. R.; Douglas, J. D.; Collins, B. A.; Tumbleston, J. R.; Graham, K. R.; Amassian, A.; Ade, H.; et al. The importance of fullerene percolation in the mixed regions of polymer–fullerene bulk heterojunction solar cells. *Adv. Energy Mater.* **2012**, *3*, 364–374.
- (112) Westacott, P.; Tumbleston, J. R.; Shoaee, S.; Fearn, S.; Bannock, J. H.; Gilchrist, J. B.; Heutz, S.; deMello, J.; Heeney, M.; Ade, H.; et al. On the role of intermixed phases in organic photovoltaic blends. *Energy Environ. Sci.* **2013**, *6*, 2756.
- (113) Sweetnam, S.; Graham, K. R.; Ngongang Ndjawa, G. O.; Heumüller, T.; Bartelt, J. A.; Burke, T. M.; Li, W.; You, W.; Amassian, A.; McGehee, M. D. Characterization of the polymer energy landscape in polymer:fullerene bulk heterojunctions with pure and mixed phases. *J. Am. Chem. Soc.* **2014**, *136*, 14078–14088.
- (114) Groves, C. Suppression of geminate charge recombination in organic photovoltaic devices with a cascaded energy heterojunction. *Energy Environ. Sci.* **2013**, *6*, 1546.
- (115) Paraecattil, A. A.; Banerji, N. Charge separation pathways in a highly efficient polymer: fullerene solar cell material. *J. Am. Chem. Soc.* **2014**, *136*, 1472–1482.

- (116) Grossiord, N.; Kroon, J. M.; Andriessen, R.; Blom, P. W. M. Degradation mechanisms in organic photovoltaic devices. *Org. Electron.* **2012**, *13*, 432–456.
- (117) Cao, H.; He, W.; Mao, Y.; Lin, X.; Ishikawa, K.; Dickerson, J. H.; Hess, W. P. Recent progress in degradation and stabilization of organic solar cells. *Journal of Power Sources* **2014**, *264*, 168–183.
- (118) Jørgensen, M.; Norrman, K.; Gevorgyan, S. A.; Tromholt, T.; Andreasen, B.; Krebs, F. C. Stability of polymer solar cells. *Adv. Mater.* **2011**, *24*, 580–612.
- (119) Gholamkhash, B.; Holdcroft, S. Toward stabilization of domains in polymer bulk heterojunction films. *Chem. Mater.* **2010**, *22*, 5371–5376.
- (120) Yang, X.; Uddin, A. Effect of thermal annealing on P3HT:PCBM bulk-heterojunction organic solar cells: A critical review. *Renewable and Sustainable Energy Reviews* **2014**, *30*, 324–336.
- (121) Ruderer, M. A.; Müller-Buschbaum, P. Morphology of polymer-based bulk heterojunction films for organic photovoltaics. *Soft Matter* **2011**, *7*, 5482.
- (122) Hamed, W.; Yahya, R.; Bola, A.; Mahmud, H. Recent approaches to controlling the nanoscale morphology of polymer-based bulk-heterojunction solar cells. *Energies* **2013**, *6*, 5847–5868.
- (123) Pivrikas, A.; Neugebauer, H.; Sariciftci, N. S. Influence of processing additives to nanomorphology and efficiency of bulk-heterojunction solar cells: A comparative review. *Solar Energy* **2011**, *85*, 1226–1237.
- (124) Chen, W.; Nikiforov, M. P.; Darling, S. B. Morphology characterization in organic and hybrid solar cells. *Energy Environ. Sci.* **2012**, *5*, 8045.
- (125) Moon, J. S.; Lee, J. K.; Cho, S.; Byun, J.; Heeger, A. J. “Columnlike” structure of the cross-sectional morphology of bulk heterojunction materials. *Nano Lett.* **2009**, *9*, 230–234.
- (126) Ma, W.; Gopinathan, A.; Heeger, A. J. Nanostructure of the interpenetrating networks in poly(3-hexylthiophene)/fullerene bulk heterojunction materials: implications for charge transport. *Adv. Mater.* **2007**, *19*, 3656–3659.
- (127) Roncali, J. Single material solar cells: the next frontier for organic photovoltaics? *Adv. Energy Mater.* **2011**, *1*, 147–160.
- (128) Dong, L.; Li, W.; Li, W.-S. Construction of a long range p/n heterojunction with a pair of nanometre-wide continuous D/A phases. *Nanoscale* **2011**, *3*, 3447.
- (129) Bates, F. S.; Fredrickson, G. H. Block copolymers—designer soft materials. *Phys. Today* **1999**, *52*, 32.
- (130) Topham, P. D.; Parnell, A. J.; Hiorns, R. C. Block copolymer strategies for solar cell technology. *J. Polym. Sci. B Polym. Phys.* **2011**, *49*, 1131–1156.

- (131) He, M.; Qiu, F.; Lin, Z. Conjugated rod-coil and rod-rod block copolymers for photovoltaic applications. *J. Mater. Chem.* **2011**, *21*, 17039.
- (132) Botiz, I.; Darling, S. B. Optoelectronics using block copolymers. *Mater. Today* **2010**, *13*, 42–51.
- (133) Darling, S. B. Block copolymers for photovoltaics. *Energy Environ. Sci.* **2009**, *2*, 1266.
- (134) Hadziioannou, G. Semiconducting block copolymers for self-assembled photovoltaic devices. *Mrs Bulletin* **2002**, *27*, 456–460.
- (135) Stalmach, U.; de Boer, B.; Vidélot, C.; van Hutten, P. F.; Hadziioannou, G. Semiconducting diblock copolymers synthesized by means of controlled radical polymerization techniques. *J. Am. Chem. Soc.* **2000**, *122*, 5464–5472.
- (136) de Boer, B.; Stalmach, U.; van Hutten, P. F.; Melzer, C.; Krasnikov, V. V.; Hadziioannou, G. Supramolecular self-assembly and opto-electronic properties of semiconducting block copolymers. *Polymer* **2001**, *42*, 9097–9109.
- (137) Miyanishi, S.; Zhang, Y.; Tajima, K.; Hashimoto, K. Fullerene attached all-semiconducting diblock copolymers for stable single-component polymer solar cells. *Chem. Commun.* **2010**, *46*, 6723.
- (138) Guo, C.; Lin, Y.-H.; Witman, M. D.; Smith, K. A.; Wang, C.; Hexemer, A.; Strzalka, J.; Gomez, E. D.; Verduzco, R. Conjugated block copolymer photovoltaics with near 3% efficiency through microphase separation. *Nano Lett.* **2013**, *13*, 2957–2963.
- (139) Roland, T.; Léonard, J.; Hernandez Ramirez, G.; Méry, S.; Yurchenko, O.; Ludwigs, S.; Haacke, S. Sub-100 fs charge transfer in a novel donor-acceptor-donor triad organized in a smectic film. *Phys. Chem. Chem. Phys.* **2011**, *14*, 273.
- (140) Bu, L.; Guo, X.; Yu, B.; Fu, Y.; Qu, Y.; Xie, Z.; Yan, D.; Geng, Y.; Wang, F. Donor-acceptor liquid crystalline conjugated cooligomers for the preparation of films with the ideal morphology for bulk heterojunction solar cells. *Polymer* **2011**, *52*, 4253–4260.
- (141) Gao, B.-R.; Qu, J.-F.; Wang, Y.; Fu, Y.-Y.; Wang, L.; Chen, Q.-D.; Sun, H.-B.; Geng, Y.-H.; Wang, H.-Y.; Xie, Z.-Y. Femtosecond spectroscopic study of photoinduced charge separation and recombination in the donor-acceptor co-oligomers for solar cells. *J. Phys. Chem. C* **2013**, *117*, 4836–4843.
- (142) Bu, L.; Guo, X.; Yu, B.; Qu, Y.; Xie, Z.; Yan, D.; Geng, Y.; Wang, F. Monodisperse co-oligomer approach toward nanostructured films with alternating donor-acceptor lamellae. *J. Am. Chem. Soc.* **2009**, *131*, 13242–13243.
- (143) Qu, J.; Gao, B.; Tian, H.; Zhang, X.; Wang, Y.; Xie, Z.; Wang, H.; Geng, Y.; Wang, F. Donor-spacer-acceptor monodisperse conjugated co-oligomers for efficient single-molecule photovoltaic cells based on non-fullerene acceptors. *J. Mater. Chem. A* **2014**, *41*, 1086–1097.
- (144) Schwartz, P.-O.; Biniék, L.; Zaborova, E.; Heinrich, B.; Brinkmann, M.; Leclerc, N.; Méry,

- S. Perylenediimide-based donor–acceptor dyads and triads: impact of molecular architecture on self-assembling properties. *J. Am. Chem. Soc.* **2014**, *136*, 5981–5992.
- (145) Min, S.-Y.; Kim, T.-S.; Lee, Y.; Cho, H.; Xu, W.; Lee, T.-W. Organic nanowire fabrication and device applications. *Small* **2014**, *11*, 45–62.
- (146) Briseno, A. L.; Mannsfeld, S. C. B.; Jenekhe, S. A.; Bao, Z.; Xia, Y. Introducing organic nanowire transistors. *Mater. Today* **2008**, *11*, 38–47.
- (147) Zhang, C.; Yan, Y.; Sheng Zhao, Y.; Yao, J. Synthesis and applications of organic nanorods, nanowires and nanotubes. *Annu. Rep. Prog. Chem., Sect. C: Phys. Chem.* **2013**, *109*, 211.
- (148) Berson, S.; De Bettignies, R.; Bailly, S.; Guillerez, S. Poly(3-hexylthiophene) fibers for photovoltaic applications. *Adv. Funct. Mater.* **2007**, *17*, 1377–1384.
- (149) Xin, H.; Kim, F. S.; Jenekhe, S. A. Highly efficient solar cells based on poly(3-butylthiophene) nanowires. *J. Am. Chem. Soc.* **2008**, *130*, 5424–5425.
- (150) Wicklein, A.; Ghosh, S.; Sommer, M.; Würthner, F.; Thelakkat, M. Self-assembly of semiconductor organogelator nanowires for photoinduced charge separation. *ACS Nano* **2009**, *3*, 1107–1114.
- (151) Tian, L.; Szilluweit, R.; Marty, R.; Bertschi, L.; Zerson, M.; Spitzner, E.-C.; Magerle, R.; Frauenrath, H. Development of a robust supramolecular method to prepare well-defined nanofibrils from conjugated molecules. *Chem. Sci.* **2012**, *3*, 1512.
- (152) Marty, R.; Szilluweit, R.; Sánchez-Ferrer, A.; Bolisetty, S.; Adamcik, J.; Mezzenga, R.; Spitzner, E.-C.; Feifer, M.; Steinmann, S. N.; Corminboeuf, C.; et al. Hierarchically structured microfibers of “single stack” perylene bisimide and quaterthiophene nanowires. *ACS Nano* **2013**, *7*, 8498–8508.
- (153) Tian, L.; Hafner, R.; Brauer, J. C.; Rolland, D.; Hartmann, L.; Szilluweit, R.; Schaer, M.; Sienkiewicz, A.; Banerji, N.; Sidler, K.; et al. Light-induced generation of high charge carrier density in organic nanowires. *In preparation*.
- (154) Murphy, A. R.; Fréchet, J. M. J. Organic semiconducting oligomers for use in thin film transistors. *Chem. Rev.* **2007**, *107*, 1066–1096.
- (155) Gebers, J.; Rolland, D.; Marty, R.; Suárez, S.; Cervini, L.; Scopelliti, R.; Brauer, J. C.; Frauenrath, H. Solubility and crystallizability: facile access to functionalized π -conjugated compounds with chlorendylimide protecting groups. *Chem. Eur. J.* **2015**, *21*, 1542–1553.
- (156) Kreyes, A.; Mourran, A.; Hong, Z.; Wang, J.; Möller, M.; Gholamrezaie, F.; Roelofs, W. S. C.; de Leeuw, D. M.; Ziener, U. Predictability of thermal and electrical properties of end-capped oligothiophenes by a simple bulkiness parameter. *Chem. Mater.* **2013**, *25*, 2128–2136.
- (157) Ellinger, S.; Ziener, U.; Thewalt, U.; Landfester, K.; Möller, M. Synthesis and self-

- organization of α,ω -substituted oligothiophenes with long, branched alkyl substituents. *Chem. Mater.* **2007**, *19*, 1070–1075.
- (158) Kreyes, A.; Amirkhani, M.; Lieberwirth, I.; Mauer, R.; Laquai, F.; Landfester, K.; Ziener, U. The longest β -unsubstituted oligothiophenes and their self-assembly in solution. *Chem. Mater.* **2010**, *22*, 6453–6458.
- (159) González-Rodríguez, D.; Schenning, A. P. H. J. Hydrogen-bonded supramolecular π -functional materials. *Chem. Mater.* **2011**, *23*, 310–325.
- (160) Vadehra, G. S.; Wall, B. D.; Diegelmann, S. R.; Tovar, J. D. On-resin dimerization incorporates a diverse array of π -conjugated functionality within aqueous self-assembling peptide backbones. *Chem. Commun.* **2010**, *46*, 3947.
- (161) Stone, D. A.; Hsu, L.; Stupp, S. I. Self-assembling quinquethiophene–oligopeptide hydrogelators. *Soft Matter* **2009**, *5*, 1990.
- (162) Kawano, S.-I.; Fujita, N.; Shinkai, S. Quater-, quinque-, and sexithiophene organogelators: unique thermochromism and heating-free sol-gel phase transition. *Chem. Eur. J.* **2005**, *11*, 4735–4742.
- (163) Klok, H.-A.; Rösler, A.; Götz, G.; Mena-Osteritz, E.; Bäuerle, P. Synthesis of a silk-inspired peptide-oligothiophene conjugate. *Org. Biomol. Chem.* **2004**, *2*, 3541.
- (164) Schillinger, E.-K.; Mena-Osteritz, E.; Hentschel, J.; Börner, H. G.; Bäuerle, P. Oligothiophene versus β -sheet peptide: synthesis and self-assembly of an organic semiconductor-peptide hybrid. *Adv. Mater.* **2009**, *21*, 1562–1567.
- (165) Murphy, A. R.; Chang, P. C.; VanDyke, P.; Liu, J.; Fréchet, J. M. J.; Subramanian, V.; DeLongchamp, D. M.; Sambasivan, S.; Fischer, D. A.; Lin, E. K. Self-assembly, molecular ordering, and charge mobility in solution-processed ultrathin oligothiophene films. *Chem. Mater.* **2005**, *17*, 6033–6041.
- (166) Nelson, G. L.; Kinson, P. L.; Quinn, C. B. Fire retardant polymers. *Annual Review of Materials Science* **1974**, *4*, 391–414.
- (167) Ungnade, H. E.; McBee, E. T. The chemistry of perchlorocyclopentenes and cyclopentadienes. *Chem. Rev.* **1958**, *58*, 249–320.
- (168) Wall, B. D.; Diegelmann, S. R.; Zhang, S.; Dawidczyk, T. J.; Wilson, W. L.; Katz, H. E.; Mao, H.-Q.; Tovar, J. D. Aligned macroscopic domains of optoelectronic nanostructures prepared via shear-flow assembly of peptide hydrogels. *Adv. Mater.* **2011**, *23*, 5009–5014.
- (169) Spitzner, E.-C.; Riesch, C.; Szilluweit, R.; Tian, L.; Frauenrath, H.; Magerle, R. Multi-set point intermittent contact (MUSIC) mode atomic force microscopy of oligothiophene fibrils. *ACS Macro Lett.* **2012**, *1*, 380–383.
- (170) Głowacki, E. D.; Irimia-Vladu, M.; Bauer, S.; Sariciftci, N. S. Hydrogen-bonds in molecular solids – from biological systems to organic electronics. *J. Mater. Chem. B*

- 2013**, *1*, 3742.
- (171) Moore, J. S.; Stupp, S. I. Room-Temperature Polyesterification. *Macromolecules* **1990**, *23*, 65–70.
- (172) Havinga, E. E.; Rotte, I.; Meijer, E. W.; Hoeve, Ten, W.; Wynberg, H. Spectra and electrical-properties of soluble partially alkyl-substituted oligomers of thiophene up to 11 rings. *Synthetic Met.* **1991**, *41*, 473–478.
- (173) Bäuerle, P. The synthesis of oligothiophenes. In *Handbook of Oligo- and Polythiophenes*; Wiley-VCH Verlag GmbH, 2007; pp. 89–181.
- (174) Becker, R. S.; Seixas de Melo, J.; Macanita, A. L.; Elisei, F. Comprehensive investigation of the solution photophysics and theoretical aspects of oligothiophenes of 1-7 rings. *Pure Appl. Chem.* **1995**, *67*, 9–16.
- (175) Moulin, E.; Cid, J.-J.; Giuseppone, N. Advances in supramolecular electronics - from randomly self-assembled nanostructures to addressable self-organized interconnects. *Adv. Mater.* **2013**, *25*, 477–487.
- (176) Kim, F. S.; Ren, G.; Jenekhe, S. A. One-dimensional nanostructures of π -conjugated molecular systems: assembly, properties, and applications from photovoltaics, sensors, and nanophotonics to nanoelectronics. *Chem. Mater.* **2011**, *23*, 682–732.
- (177) Hasegawa, M.; Iyoda, M. Conducting supramolecular nanofibers and nanorods. *Chem. Soc. Rev.* **2010**, *39*, 2420.
- (178) Xiao, S.; Tang, J.; Beetz, T.; Guo, X.; Tremblay, N.; Siegrist, T.; Zhu, Y.; Steigerwald, M.; Nuckolls, C. Transferring self-assembled, nanoscale cables into electrical devices. *J. Am. Chem. Soc.* **2006**, *128*, 10700–10701.
- (179) Che, Y.; Gross, D. E.; Huang, H.; Yang, D.; Yang, X.; Discekici, E.; Xue, Z.; Zhao, H.; Moore, J. S.; Zang, L. Diffusion-controlled detection of trinitrotoluene: interior nanoporous structure and low highest occupied molecular orbital level of building blocks enhance selectivity and sensitivity. *J. Am. Chem. Soc.* **2012**, *134*, 4978–4982.
- (180) Che, Y.; Yang, X.; Loser, S.; Zang, L. Expedient vapor probing of organic amines using fluorescent nanofibers fabricated from an n-type organic semiconductor. *Nano Lett.* **2008**, *8*, 2219–2223.
- (181) Liu, H.; Kameoka, J.; Czaplewski, D. A.; Craighead, H. G. Polymeric nanowire chemical sensor. *Nano Lett.* **2004**, *4*, 671–675.
- (182) Aleshin, A. N. Polymer nanofibers and nanotubes: charge transport and device applications. *Audio, Transactions of the IRE Professional Group on* **2007**, –.
- (183) Noy, A.; Miller, A. E.; Klare, J. E.; Weeks, B. L.; Woods, B. W.; DeYoreo, J. J. Fabrication of luminescent nanostructures and polymer nanowires using dip-pen nanolithography. *Nano Lett.* **2002**, *2*, 109–112.

- (184) Martin, C. Membrane-based synthesis of nanomaterials. *Chem. Mater.* **1996**, *8*, 1739–1746.
- (185) Lee, J. I.; Cho, S. H.; Park, S.-M.; Kim, J. K.; Kim, J. K.; Yu, J.-W.; Kim, Y. C.; Russell, T. P. Highly aligned ultrahigh density arrays of conducting polymer nanorods using block copolymer templates. *Nano Lett.* **2008**, *8*, 2315–2320.
- (186) Yoon, H.; Chang, M.; Jang, J. Formation of 1D poly(3,4-ethylenedioxythiophene) nanomaterials in reverse microemulsions and their application to chemical sensors. *Adv. Funct. Mater.* **2007**, *17*, 431–436.
- (187) Chen, J.-Y.; Kuo, C.-C.; Lai, C.-S.; Chen, W.-C.; Chen, H.-L. Manipulation on the morphology and electrical properties of aligned electrospun nanofibers of poly(3-hexylthiophene) for field-effect transistor applications. *Macromolecules* **2011**, *44*, 2883–2892.
- (188) Lee, S. W.; Lee, H. J.; Choi, J. H.; Koh, W. G.; Myoung, J. M.; Hur, J. H.; Park, J. J.; Cho, J. H.; Jeong, U. Periodic array of polyelectrolyte-gated organic transistors from electrospun poly(3-hexylthiophene) nanofibers. *Nano Lett.* **2010**, *10*, 347–351.
- (189) Kuo, C.-C.; Wang, C.-T.; Chen, W.-C. Highly-aligned electrospun luminescent nanofibers prepared from polyfluorene/PMMA Blends: fabrication, morphology, photophysical properties and sensory applications. *Macromol. Mater. Eng.* **2008**, *293*, 999–1008.
- (190) Kim, D. H.; Lee, D. Y.; Lee, H. S.; Lee, W. H.; Kim, Y. H.; Han, J. I.; Cho, K. High-mobility organic transistors based on single-crystalline microribbons of triisopropylsilylethynyl pentacene via solution-phase self-assembly. *Adv. Mater.* **2007**, *19*, 678–682.
- (191) Briseno, A. L.; Mannsfeld, S. C. B.; Lu, X.; Xiong, Y.; Jenekhe, S. A.; Bao, Z.; Xia, Y. Fabrication of field-effect transistors from hexathiapentacene single-crystal nanowires. *Nano Lett.* **2007**, *7*, 668–675.
- (192) Sun, Y.; Tan, L.; Jiang, S.; Qian, H.; Wang, Z.; Yan, D.; Di, C.; Wang, Y.; Wu, W.; Yu, G.; et al. High-performance transistor based on individual single-crystalline micrometer wire of perylo[1,12-b,c,d]thiophene. *J. Am. Chem. Soc.* **2007**, *129*, 1882–1883.
- (193) Schwab, A. D.; Smith, D. E.; Bond-Watts, B.; Johnston, D. E.; Hone, J.; Johnson, A. T.; de Paula, J. C.; Smith, W. F. Photoconductivity of self-assembled porphyrin nanorods. *Nano Lett.* **2004**, *4*, 1261–1265.
- (194) Lee, C. C.; Grenier, C.; Meijer, E. W.; Schenning, A. P. H. J. Preparation and characterization of helical self-assembled nanofibers. *Chem. Soc. Rev.* **2009**, *38*, 671–683.
- (195) Bernevig, B. A.; Hughes, T. L.; Zhang, S. C. Quantum spin Hall effect and topological phase transition in HgTe quantum wells. *Science* **2006**, *314*, 1757–1761.
- (196) Faramarzi, V.; Niess, F.; Moulin, E.; Maaloum, M.; Dayen, J.-F.; Beaufrand, J.-B.; Zanettini, S.; Doudin, B.; Giuseppone, N. Light-triggered self-construction of

- supramolecular organic nanowires as metallic interconnects. **2012**, 1–6.
- (197) Kim, S. H.; Parquette, J. R. A model for the controlled assembly of semiconductor peptides. *Nanoscale* **2012**, *4*, 6940.
- (198) Marty, R.; Nigon, R.; Leite, D.; Frauenrath, H. Two-fold odd–even effect in self-assembled nanowires from oligopeptide-polymer-substituted perylene bisimides. *J. Am. Chem. Soc.* **2014**, *136*, 3919–3927.
- (199) Gebers, J.; Hartmann, L.; Ozen, B.; Schaer, M.; Suárez, S.; Bugnon, P.; Scopelliti, R.; Steinrück, H.-G.; Konovalov, O.; Magerl, A.; et al. Crystal structure, thin film morphology, and OFET performance of a hydrogen-bonded quaterthiophene. *In preparation*.
- (200) Piris, J.; Dykstra, T. E.; Bakulin, A. A.; Loosdrecht, P. H. M. V.; Knulst, W.; Trinh, M. T.; Schins, J. M.; Siebbeles, L. D. A. Photogeneration and ultrafast dynamics of excitons and charges in P3HT/PCBM blends. *J. Phys. Chem. C* **2009**, *113*, 14500–14506.
- (201) Zhang, W.; Hu, R.; Li, D.; Huo, M.-M.; Ai, X.-C.; Zhang, J.-P. Primary dynamics of exciton and charge photogeneration in solvent vapor annealed P3HT/PCBM films. *J. Phys. Chem. C* **2012**, *116*, 4298–4310.
- (202) Hu, R.; Zhang, W.; Fu, L.-M.; Zhang, J.-P.; Ai, X.-C. Spectroelectrochemical characterization of anionic and cationic polarons in poly(3-hexylthiophene)/fullerene blend. Effects of morphology and interface. *Synthetic Met.* **2013**, *169*, 41–47.
- (203) Sheng, C. X.; Tong, M.; Singh, S.; Vardeny, Z. Experimental determination of the charge/neutral branching ratio η in the photoexcitation of π -conjugated polymers by broadband ultrafast spectroscopy. *Phys. Rev. B* **2007**, *75*, 085206.
- (204) Panzer, M. J.; Frisbie, C. D. High carrier density and metallic conductivity in poly(3-hexylthiophene) achieved by electrostatic charge injection. *Adv. Funct. Mater.* **2006**, *16*, 1051–1056.
- (205) Lee, K.; Cho, S.; Heum Park, S.; Heeger, A. J.; Lee, C.-W.; Lee, S.-H. Metallic transport in polyaniline. *Nature* **2006**, *441*, 65–68.
- (206) Ye, J.; Craciun, M. F.; Koshino, M.; Russo, S.; Inoue, S.; Yuan, H.; Shimotani, H.; Morpurgo, A. F.; Iwasa, Y. Accessing the transport properties of graphene and its multilayers at high carrier density. *Proc Natl Acad Sci U S A* **2011**, *108*, 13002–13006.
- (207) Haddon, R. C. Electronic structure, conductivity and superconductivity of alkali metal doped C60. *Acc. Chem. Res.* **1992**, *25*, 127–133.
- (208) Xie, W.; Liu, F.; Shi, S.; Ruden, P. P.; Frisbie, C. D. Charge density dependent two-channel conduction in organic electric double layer transistors (EDLTs). *Adv. Mater.* **2014**, *26*, 2527–2532.
- (209) Tanaka, T.; Chatani, Y.; Tadokoro, H. Crystal structure of polyisobutylene. *J. Polym. Sci.: Polym. Phys. Ed.* **1974**, *12*, 515–531.

- (210) Sunde, M.; Serpell, L. C.; Bartlam, M.; Fraser, P. E.; Pepys, M. B.; Blake, C. C. Common core structure of amyloid fibrils by synchrotron X-ray diffraction. *J Mol Biol* **1997**, *273*, 729–739.
- (211) Greenwood, N. N.; Earnshaw, A. Chemistry of the elements; 2nd ed.; Butterworth-Heinemann Ltd.: Oxford, UK, 1997.
- (212) Kasha, M.; Rawls, H. R.; El-Byoumi, A. M. The exciton model in molecular spectroscopy. *Pure Appl. Chem.* **1965**, *11*, 371–392.
- (213) Berova, N.; Bari, L. D.; Pescitelli, G. Application of electronic circular dichroism in configurational and conformational analysis of organic compounds. *Chem. Soc. Rev.* **2007**, *36*, 914.
- (214) Brustolin, F.; Surin, M.; Lemaure, V.; Romanazzi, G.; Sun, Q.; Cornil, J.; Lazzaroni, R.; Sommerdijk, N. A. J. M.; Leclère, P.; Meijer, E. W. The self-assembly of amphiphilic oligothiophenes: hydrogen bonding and poly(glutamate) complexation. *Bull. Chem. Soc. Jpn.* **2007**, *80*, 1703–1715.
- (215) Krimm, S.; Bandekar, J. Normal mode spectrum of the parallel-chain beta-sheet. *Biopolymers* **1988**, *27*, 909–921.
- (216) Bandekar, J.; Krimm, S. Vibrational spectroscopy of L-valyl-glycyl-glycine, a parallel-chain beta-structure. *Biopolymers* **1988**, *27*, 885–908.
- (217) Fichou, D.; Xu, B.; Horowitz, G.; Garnier, F. Generation of stabilized polarons and bipolarons on extended model thiophene oligomers. *Synthetic Met.* **1991**, *41*, 463–469.
- (218) Fichou, D.; Horowitz, G.; Garnier, F. Polaron and bipolaron formation on isolated-model thiophene oligomers in solution. *Synthetic Met.* **1990**, *39*, 125–131.
- (219) Fichou, D.; Horowitz, G.; Xu, B.; Garnier, F. Stoichiometric control of the successive generation of the radical cation and dication of extended α -conjugated oligothiophenes: a quantitative model for doped polythiophene. *Synthetic Met.* **1990**, *39*, 243–259.
- (220) Hotta, S.; Waragai, K. Solid-state absorption-spectroscopy of alkyl-substituted oligothiophenes. *Journal of Physical Chemistry* **1993**, *97*, 7427–7434.
- (221) Emmi, S. S.; D'Angelantonio, M.; Beggiato, G.; Poggi, G.; Geri, A.; Pietropaolo, D.; Zotti, G. The generation and spectral characterization of oligothiophenes radical cations. A pulse radiolysis investigation. *Radiat Phys Chem Oxf Engl 1993* **1999**, *54*, 263–270.
- (222) Nakanishi, H.; Sumi, N.; Ueno, S.; Takimiya, K.; Aso, Y.; Otsubo, T.; Komaguchi, K.; Shiotani, M.; Ohta, N. Spectral properties of the longest oligothiophenes in the oxidation states. *Synthetic Met.* **2001**, *119*, 413–414.
- (223) Beljonne, D.; Cornil, J.; Sirringhaus, H.; Brown, P. J.; Shkunov, M.; Friend, R. H.; Bredas, J. L. Optical signature of delocalized polarons in conjugated polymers. *Adv. Funct.*

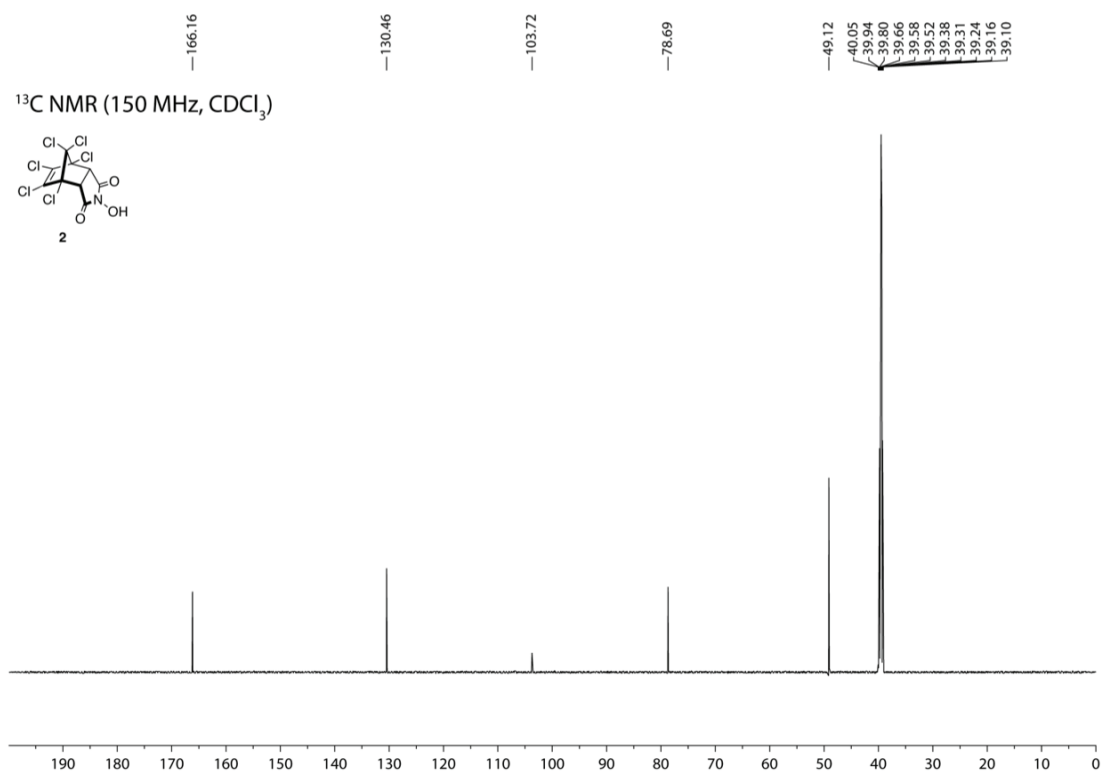
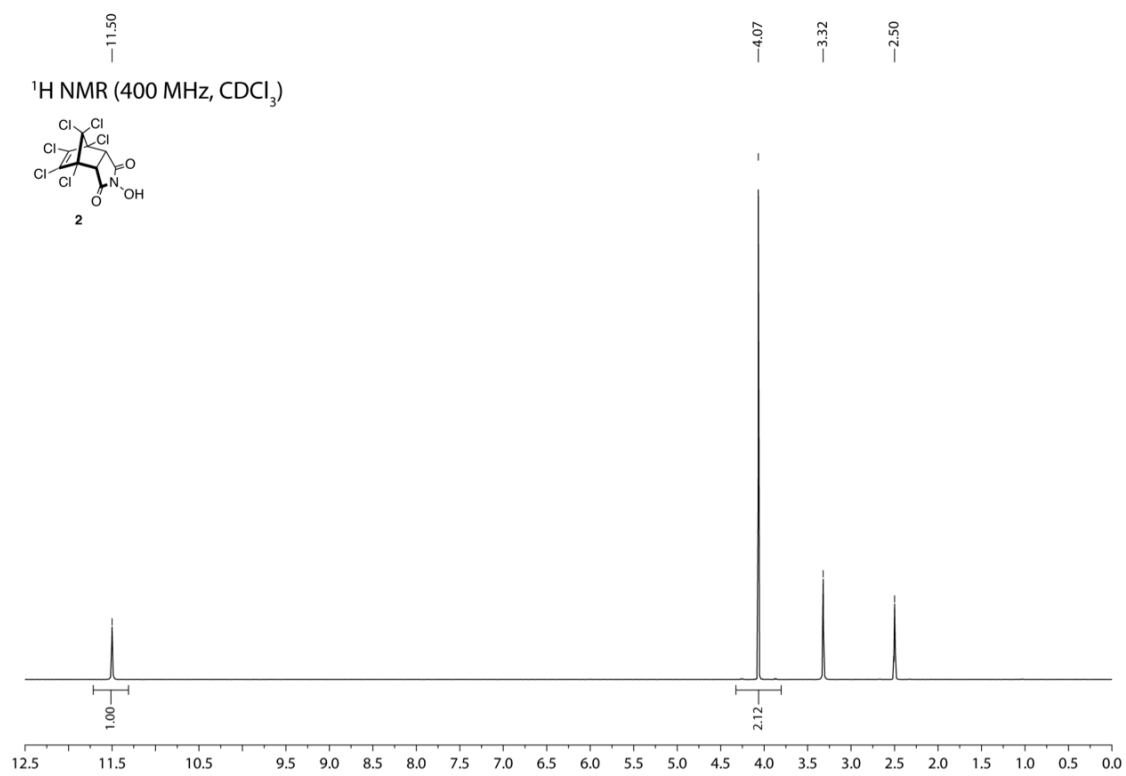
- Mater.* **2001**, *11*, 229–234.
- (224) Wintgens, V.; Valat, P.; Garnier, F. Photochemical generation of radical cations from thiophene oligomers. *Journal of Physical Chemistry* **1994**, *98*, 228–232.
- (225) Richtol, H. H.; Fitzgerald, E. A., Jr; Wuelfing, P., Jr. Photochemical oxidation of some substituted aromatic amines in chloroform. *Journal of Physical Chemistry* **1971**, *75*, 2737–2741.
- (226) Nicolai, H. T.; Kuik, M.; Wetzelaer, G. A. H.; de Boer, B.; Campbell, C.; Risko, C.; Bredas, J. L.; Blom, P. W. M. Unification of trap-limited electron transport in semiconducting polymers. *Nat. Mater.* **2012**, *11*, 882–887.
- (227) Fernández, G.; Sánchez, L.; Veldman, D.; Wienk, M. M.; Atienza, C.; Guldi, D. M.; Janssen, R. A. J.; Martin, N. Tetrafullerene conjugates for all-organic photovoltaics. *J. Org. Chem.* **2008**, *73*, 3189–3196.
- (228) Nishizawa, T.; Tajima, K.; Hashimoto, K. Supramolecular formation of fibrous nanostructure in donor-acceptor dyad film. *J. Mater. Chem.* **2007**, *17*, 2440.
- (229) Kelber, J.; Bock, H.; Thiebaut, O.; Grelet, E.; Langhals, H. Room-temperature columnar liquid-crystalline perylene imido-diester by a homogeneous one-pot imidification-esterification of perylene-3,4,9,10-tetracarboxylic dianhydride. *Eur. J. Org. Chem.* **2011**, 707–712.
- (230) Xue, C.; Sun, R.; Annab, R.; Abadi, D.; Jin, S. Perylene monoanhydride diester: a versatile intermediate for the synthesis of unsymmetrically substituted perylene tetracarboxylic derivatives. *Tetrahedron Lett.* **2009**, *50*, 853–856.
- (231) Croisier, E.; Liang, S.; Schweizer, T.; Balog, S.; cacute, M. M.; Snellings, R.; Cugnoni, J. E. L.; Michaud, V. E. R.; Frauenrath, H. A toolbox of oligopeptide-modified polymers for tailored elastomers. *Nature Communications* **2014**, *5*, 1–10.
- (232) Biniek, L.; Schwartz, P.-O.; Zaborova, E.; Heinrich, B.; Leclerc, N.; Méry, S.; Brinkmann, M. Zipper-like molecular packing of donor-acceptor conjugated co-oligomers based on perylenediimide. *J. Mater. Chem. C* **2015**, 1–8.
- (233) Morel, D. L.; Ghosh, A. K.; Feng, T.; Stogryn, E. L.; Purwin, P. E.; Shaw, R. F.; Fishman, C. High-efficiency organic solar cells. *Appl. Phys. Lett.* **1978**, *32*, 495.
- (234) Ghosh, A. K.; Feng, T. Merocyanine organic solar cells. *J. Appl. Phys.* **1978**, *49*, 5982.

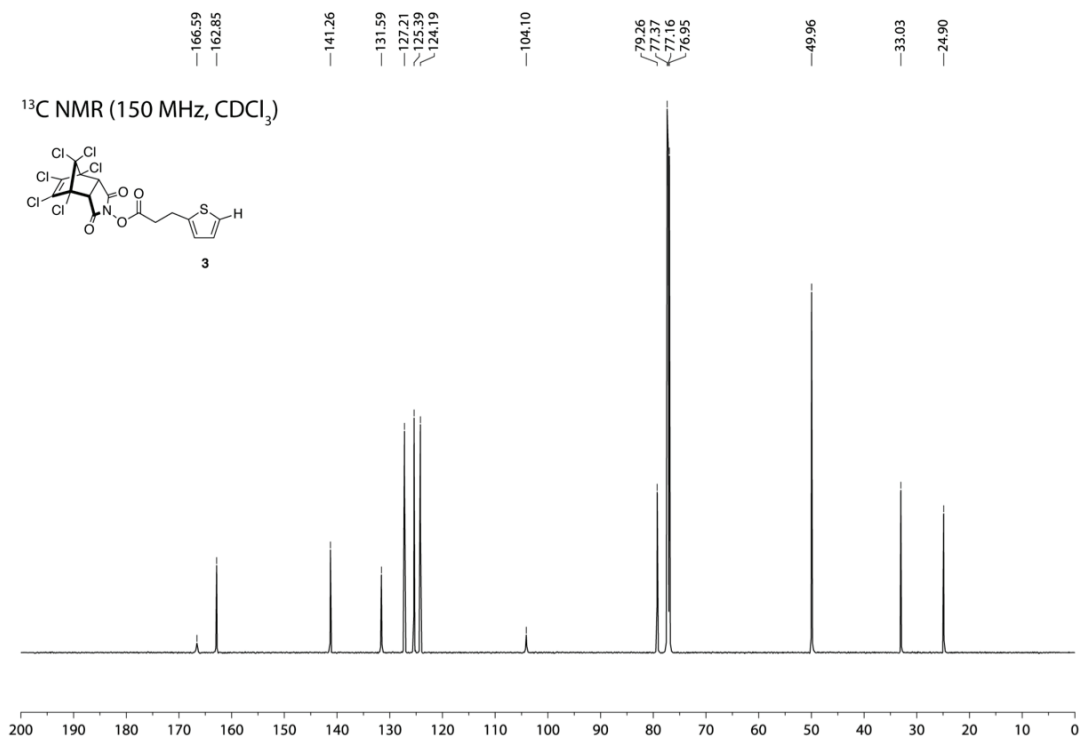
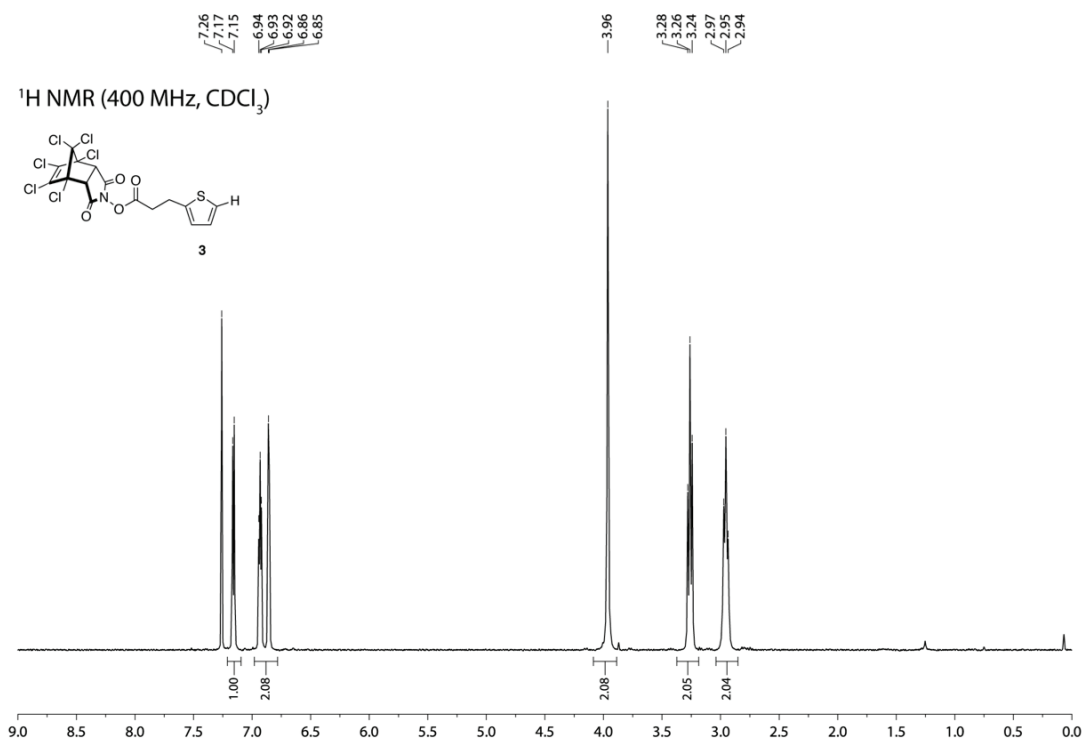
Appendix

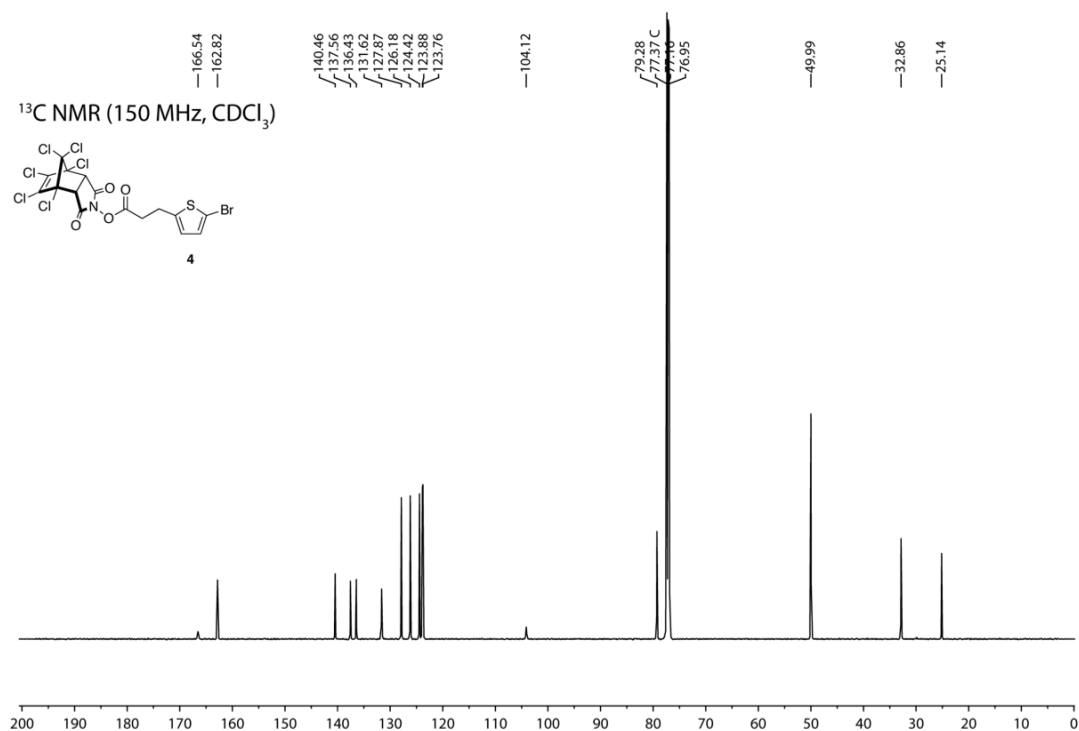
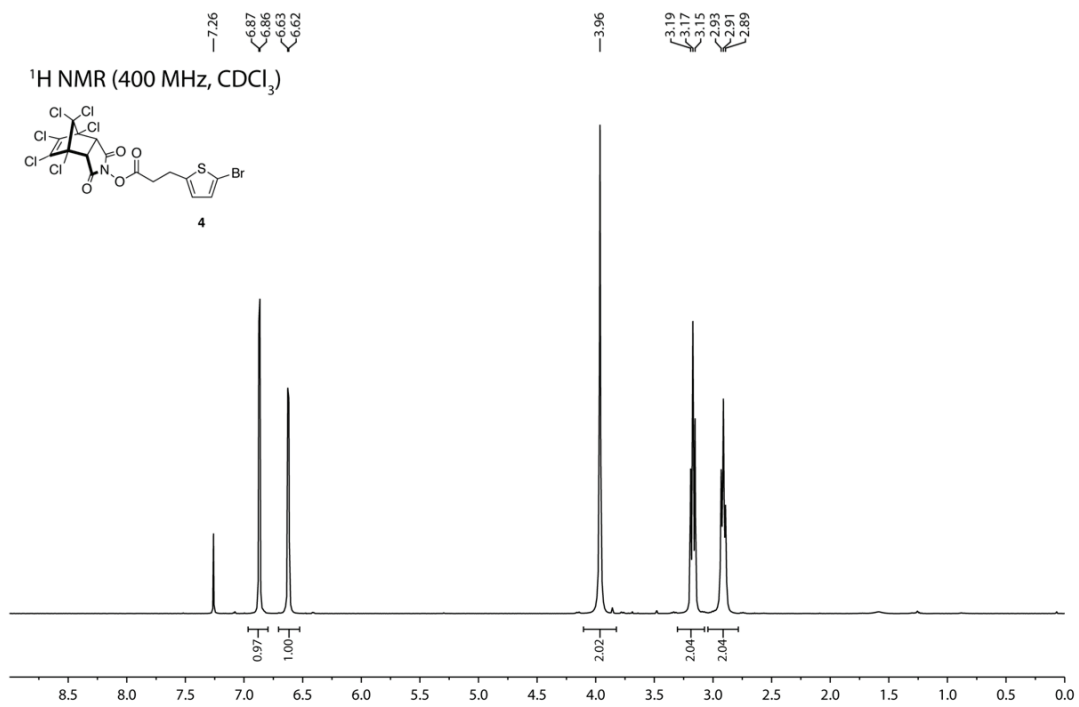


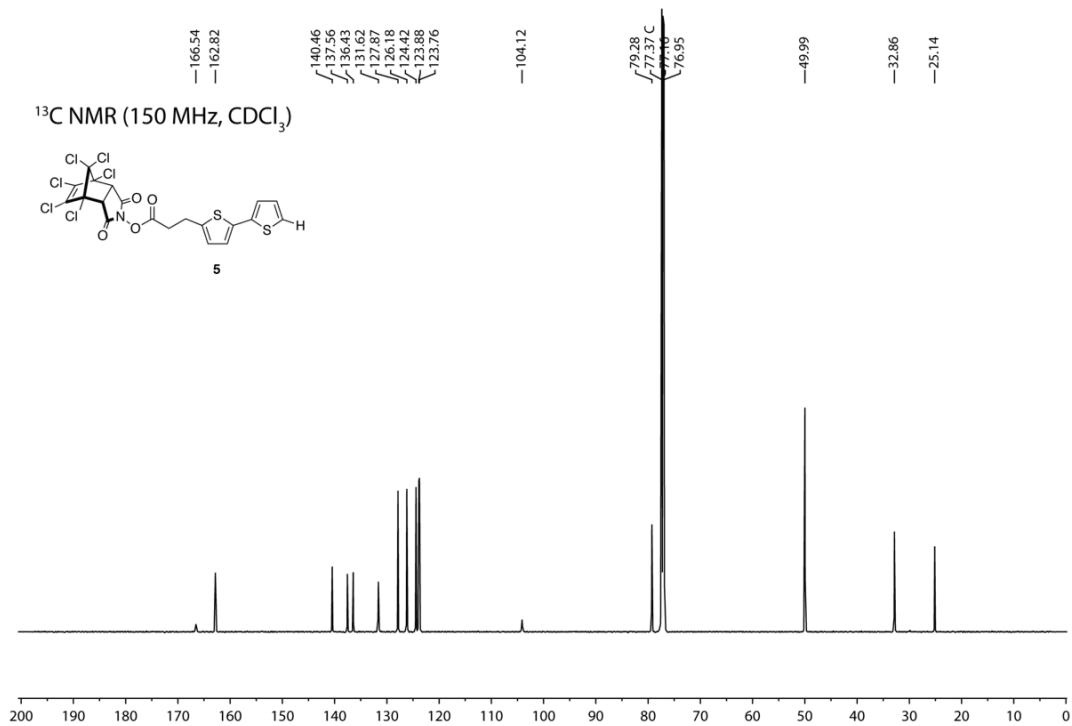
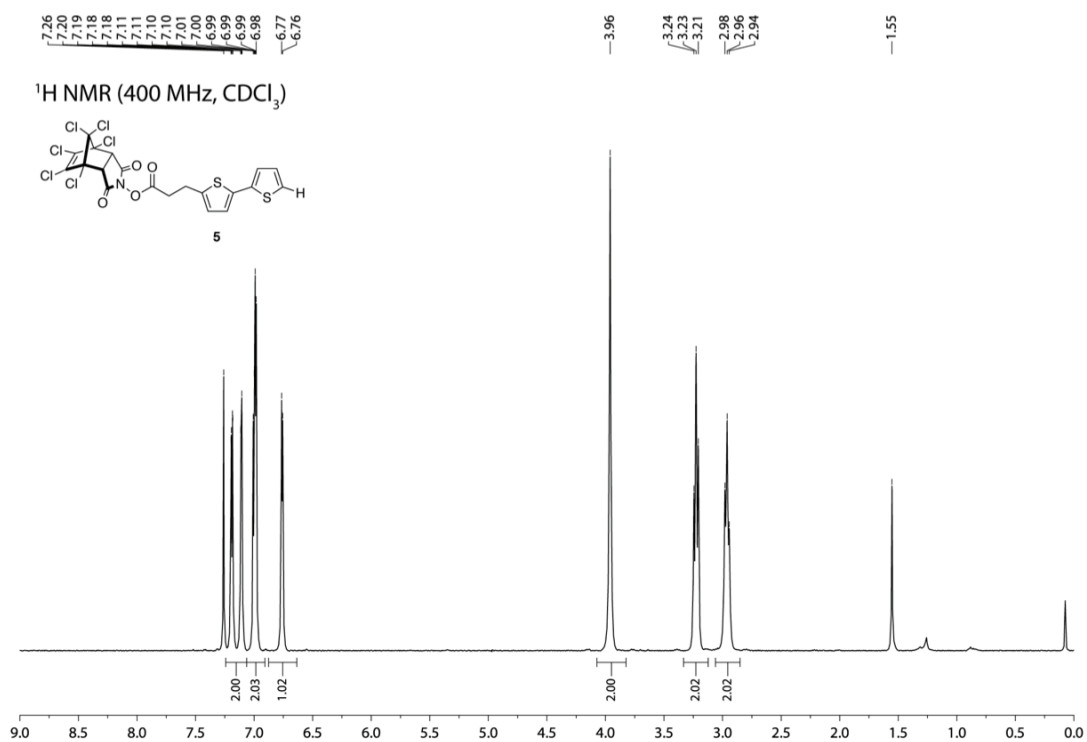
8 Appendix

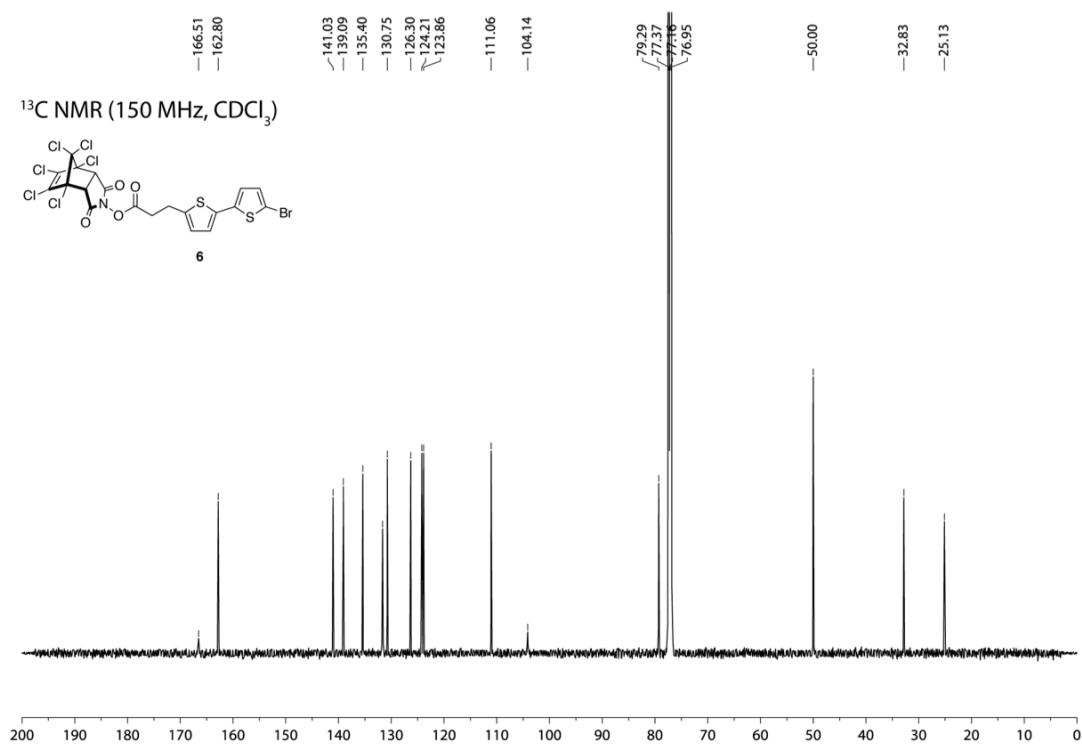
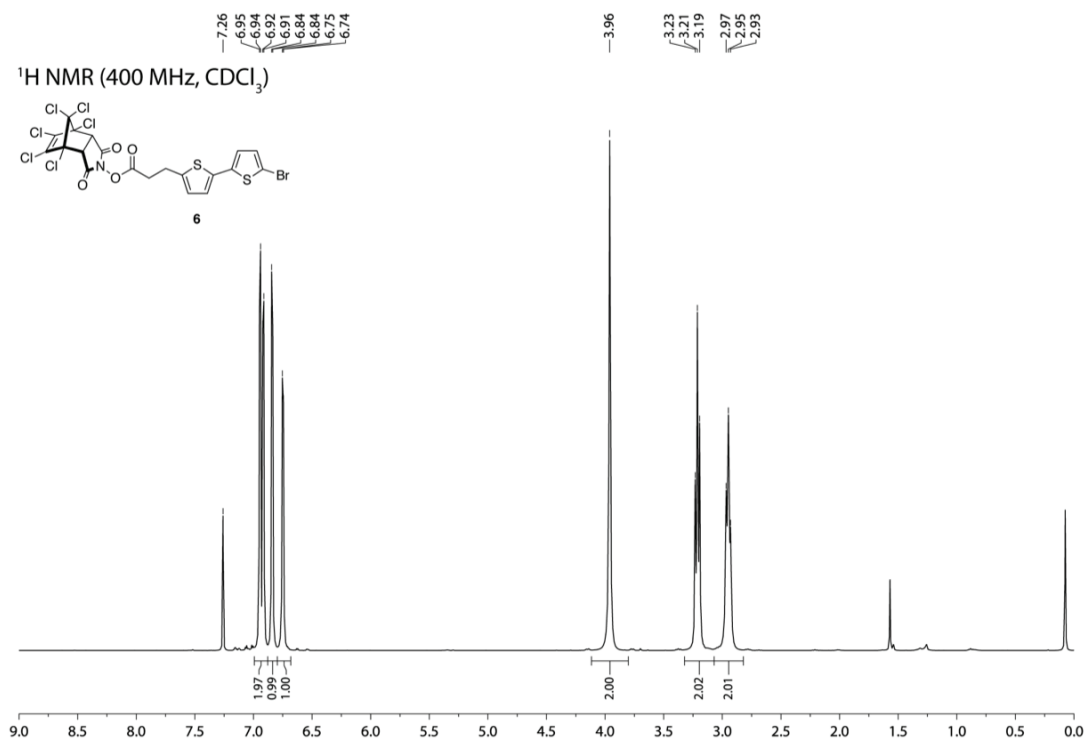
8.1 Spectral Data for Synthesized Compounds

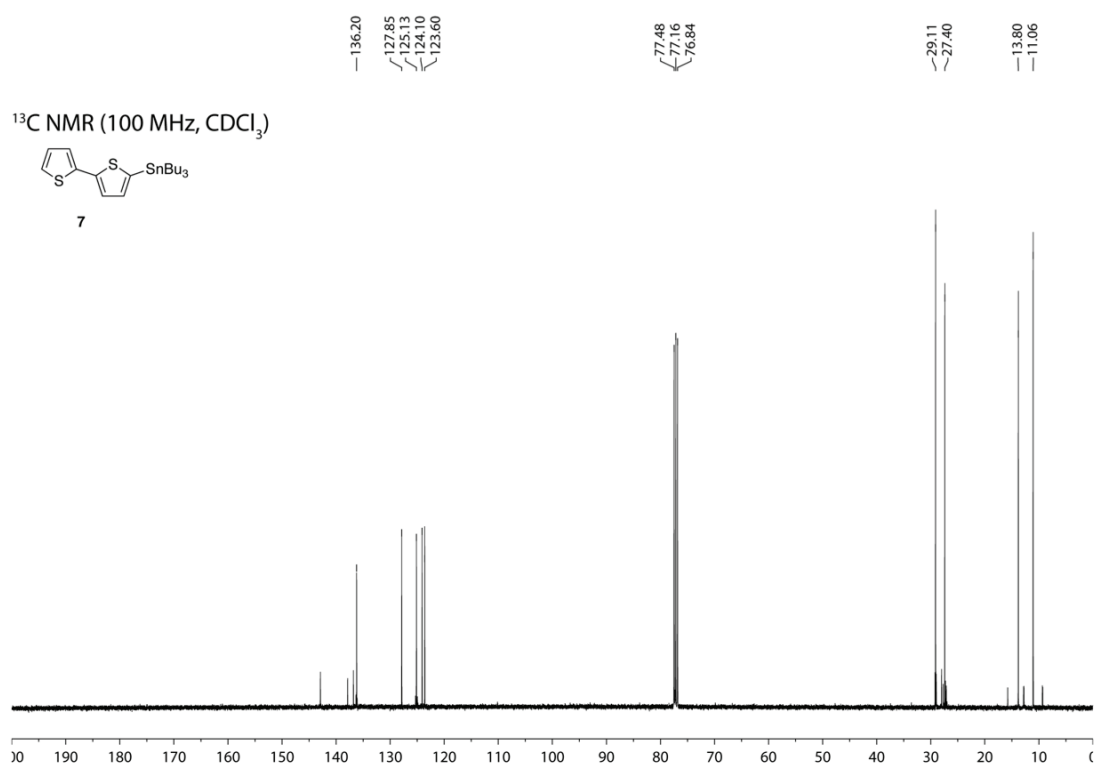
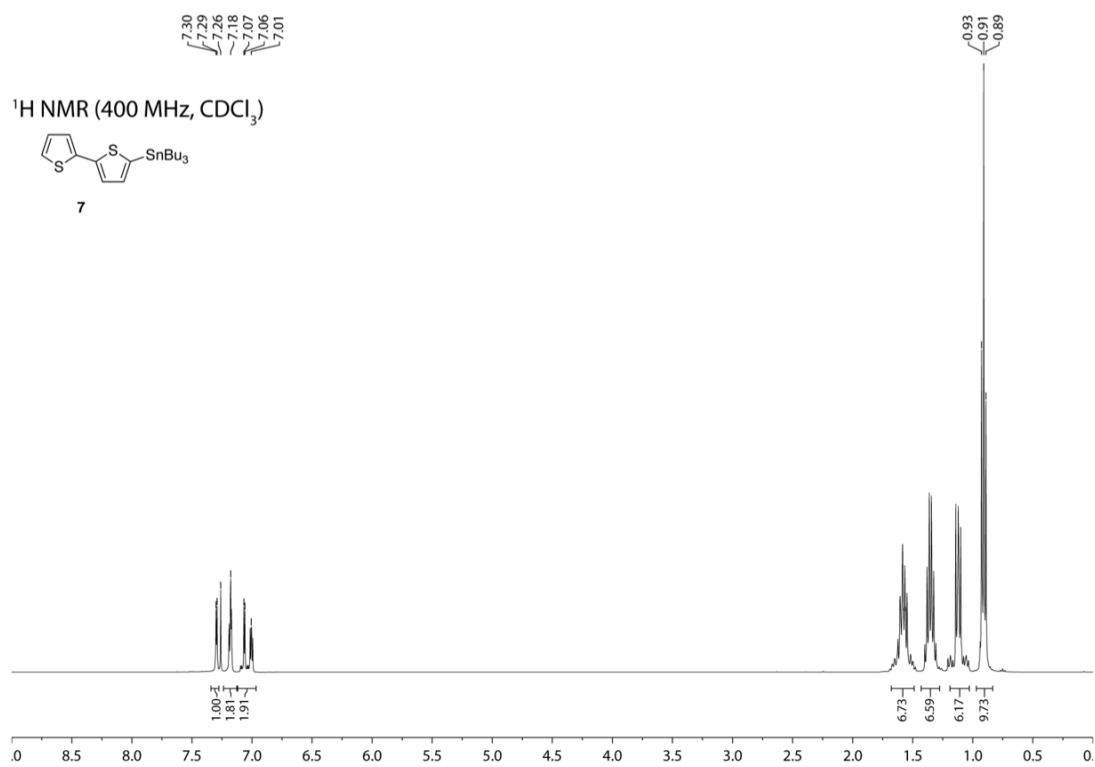


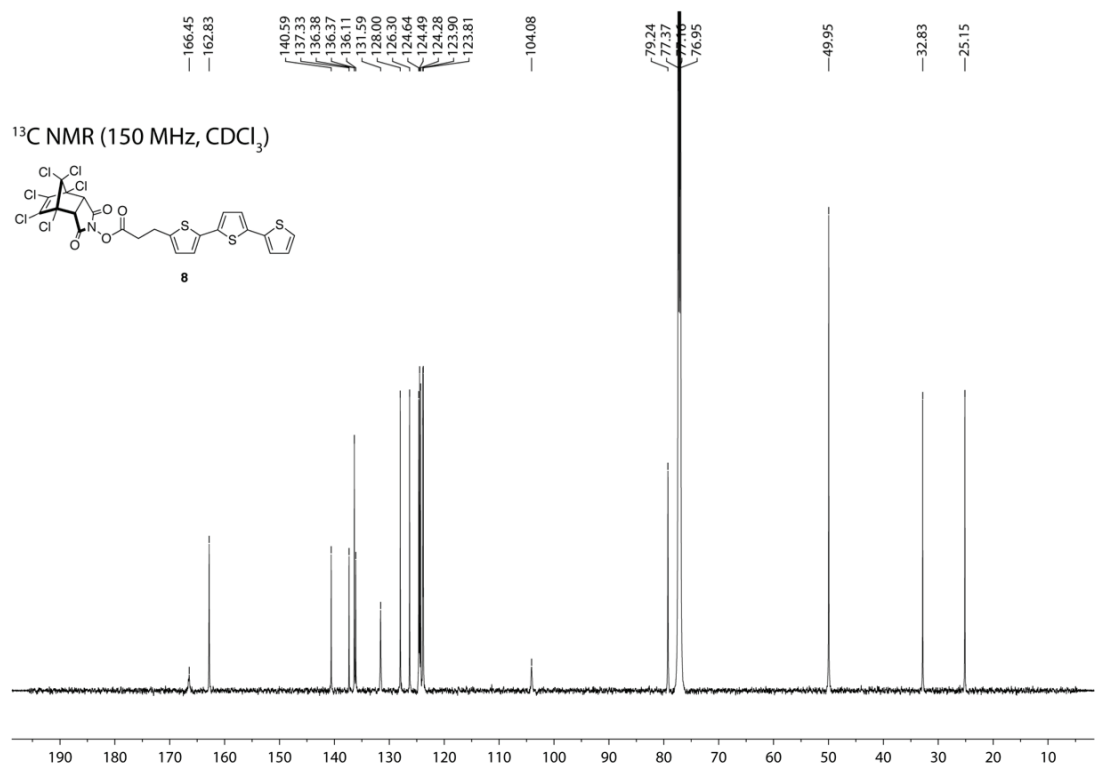
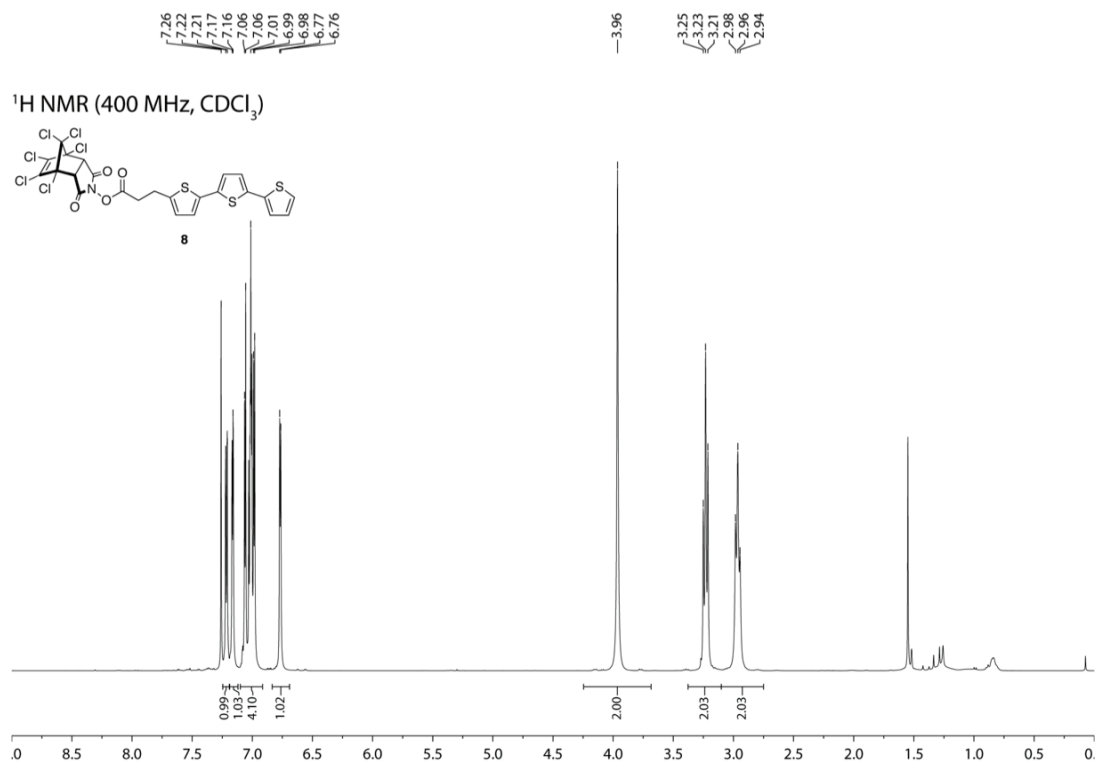


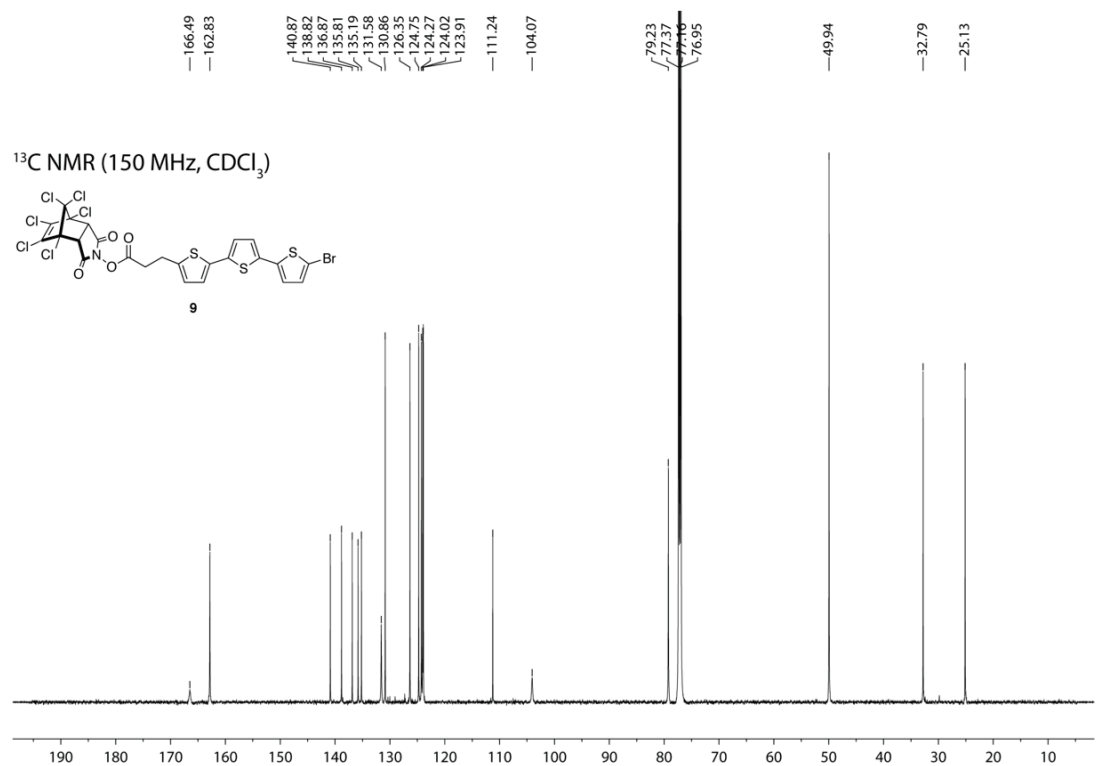
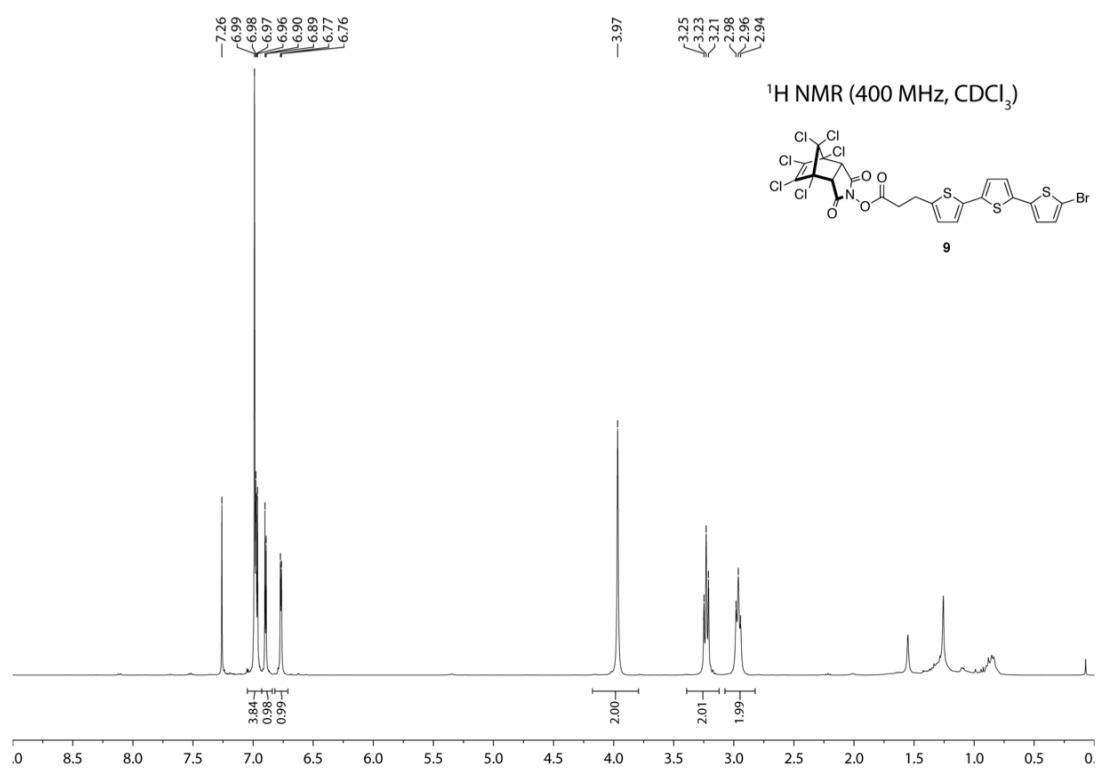


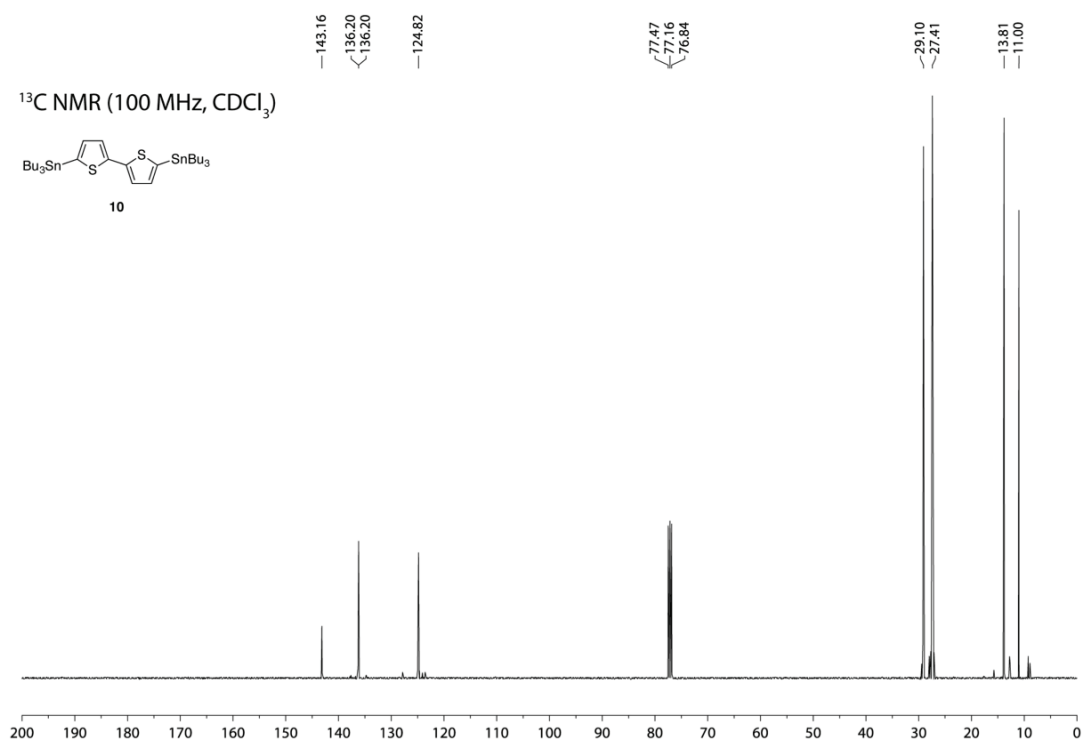
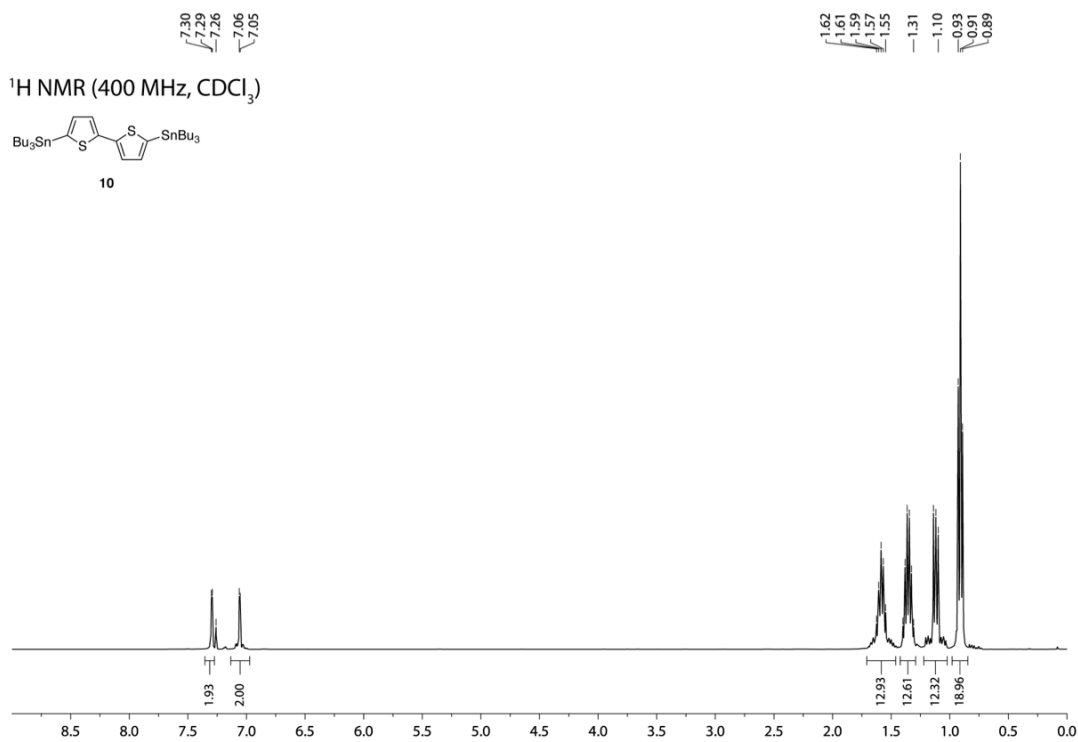


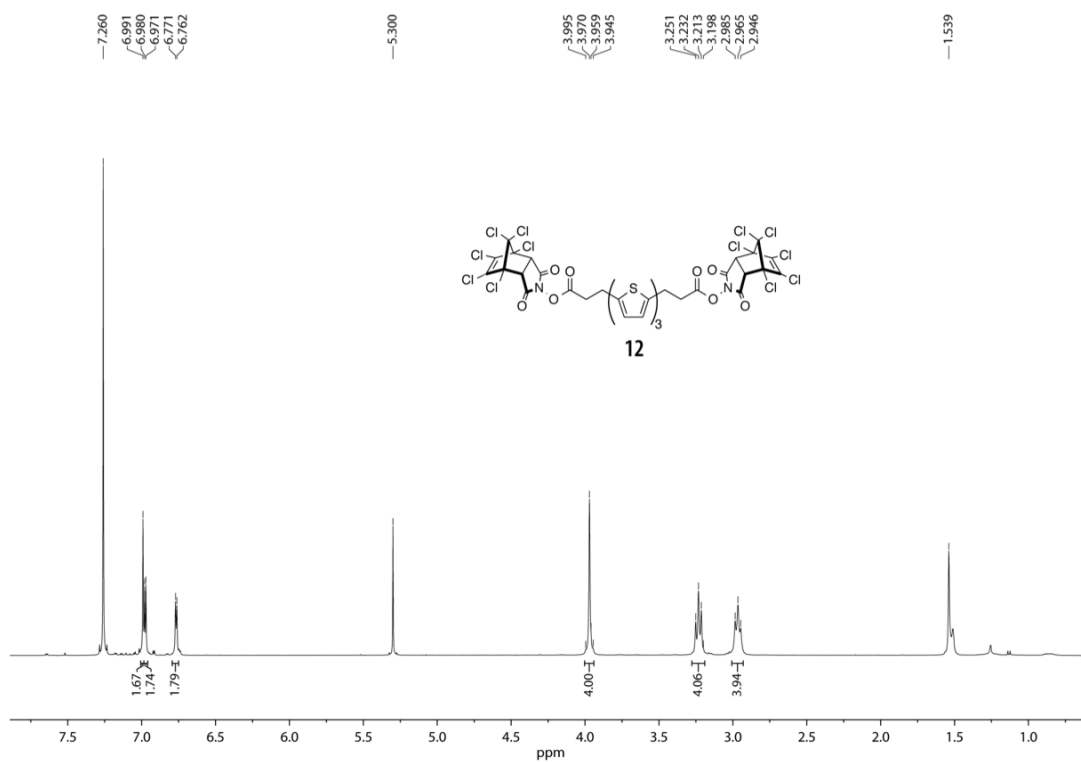


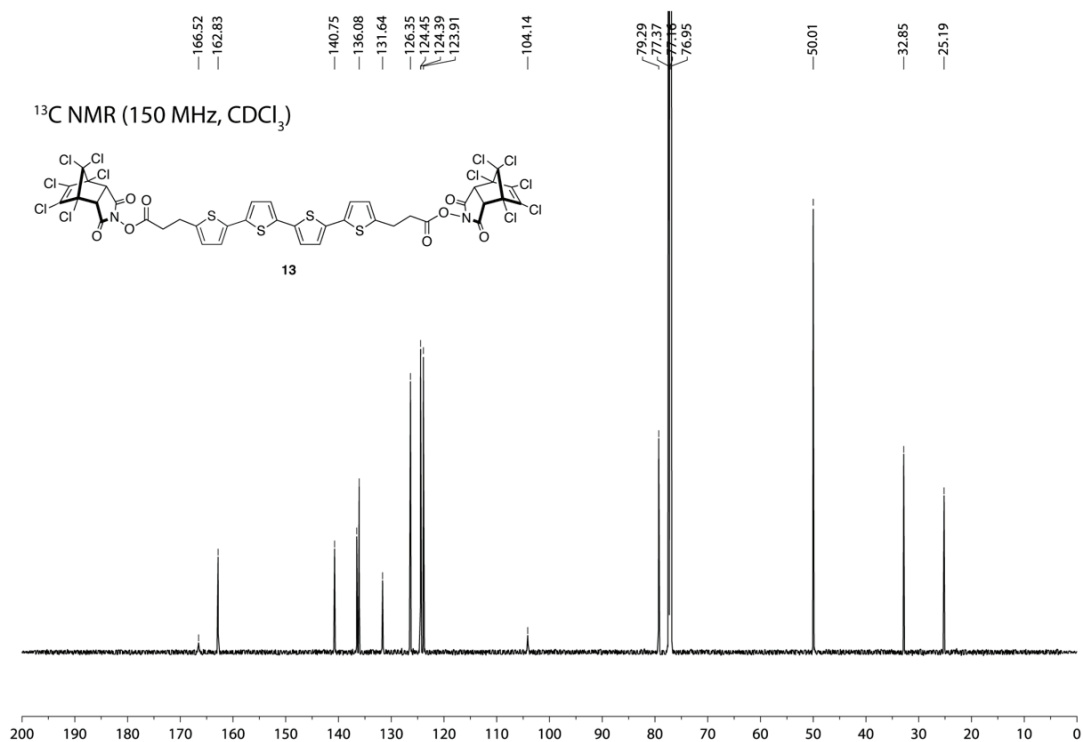
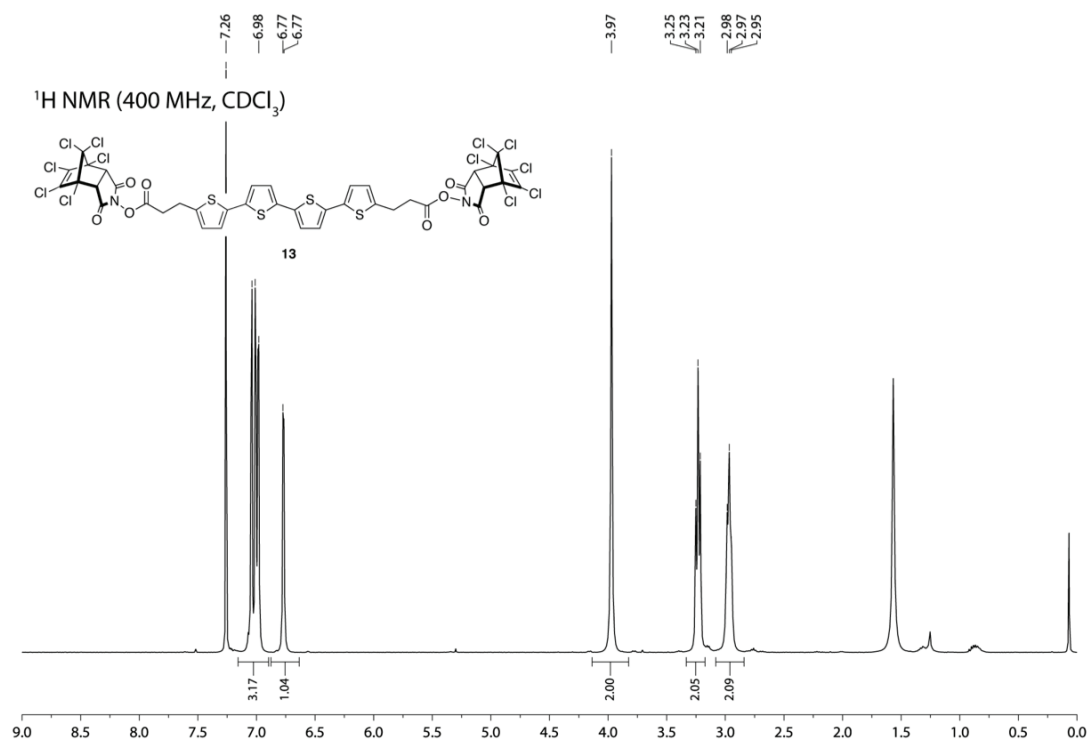


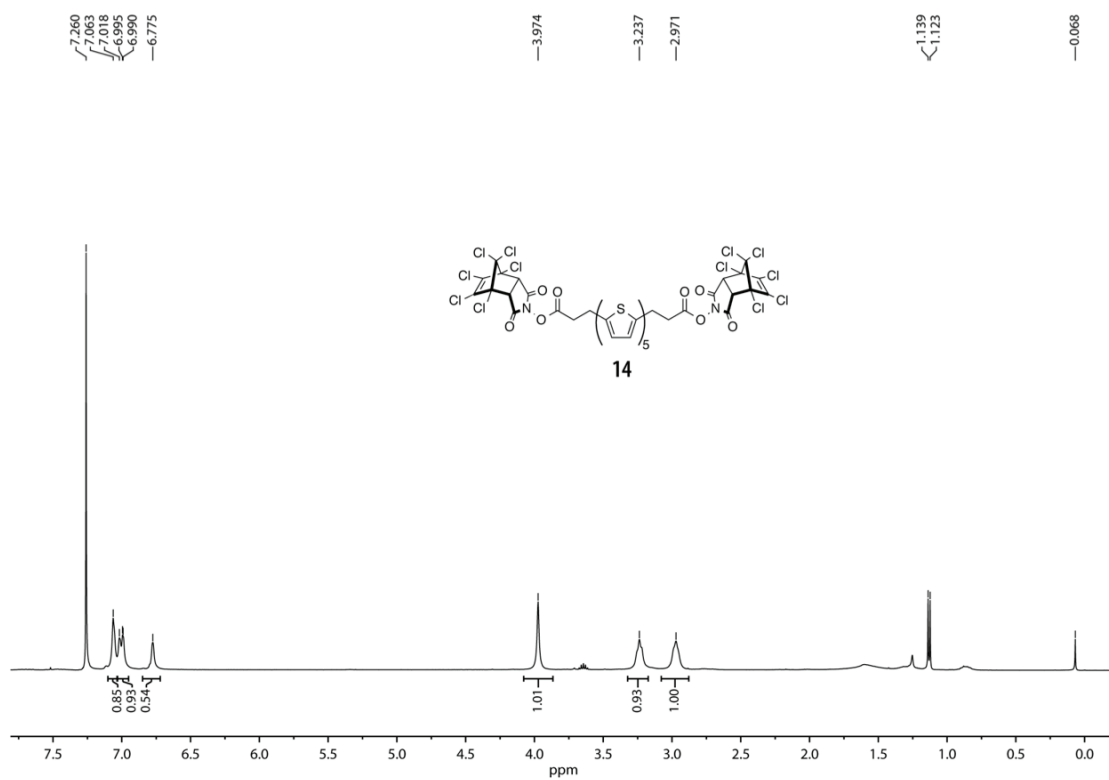


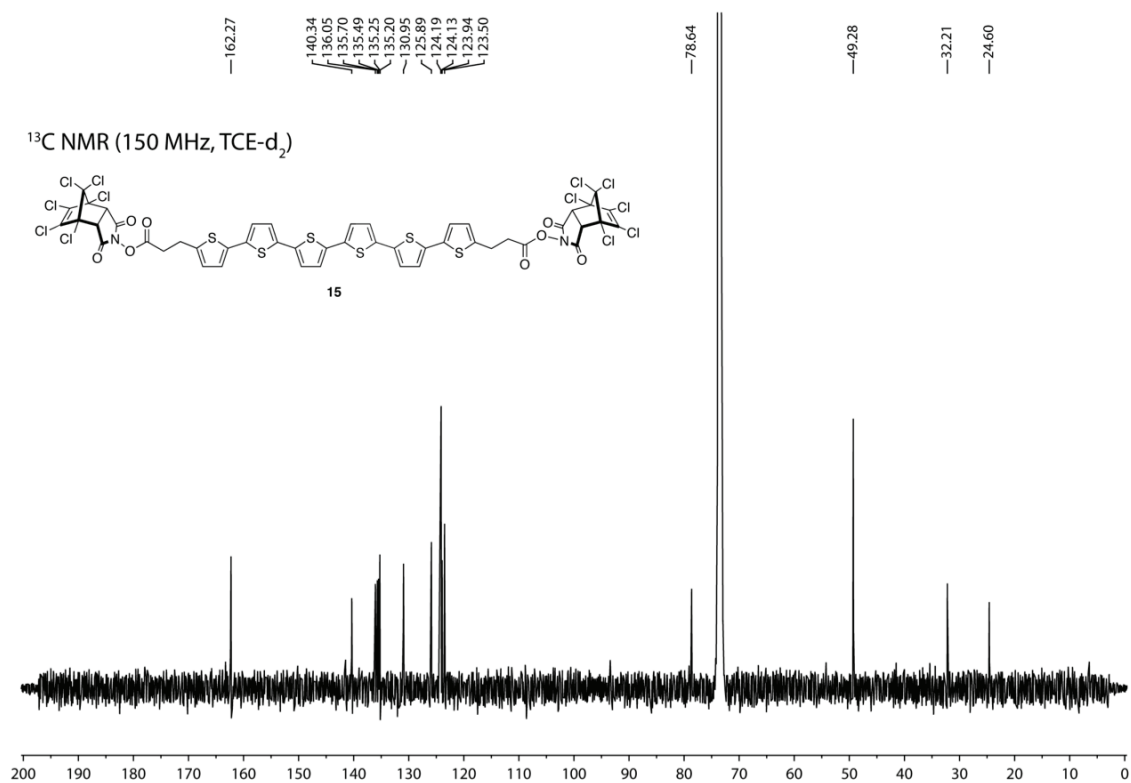
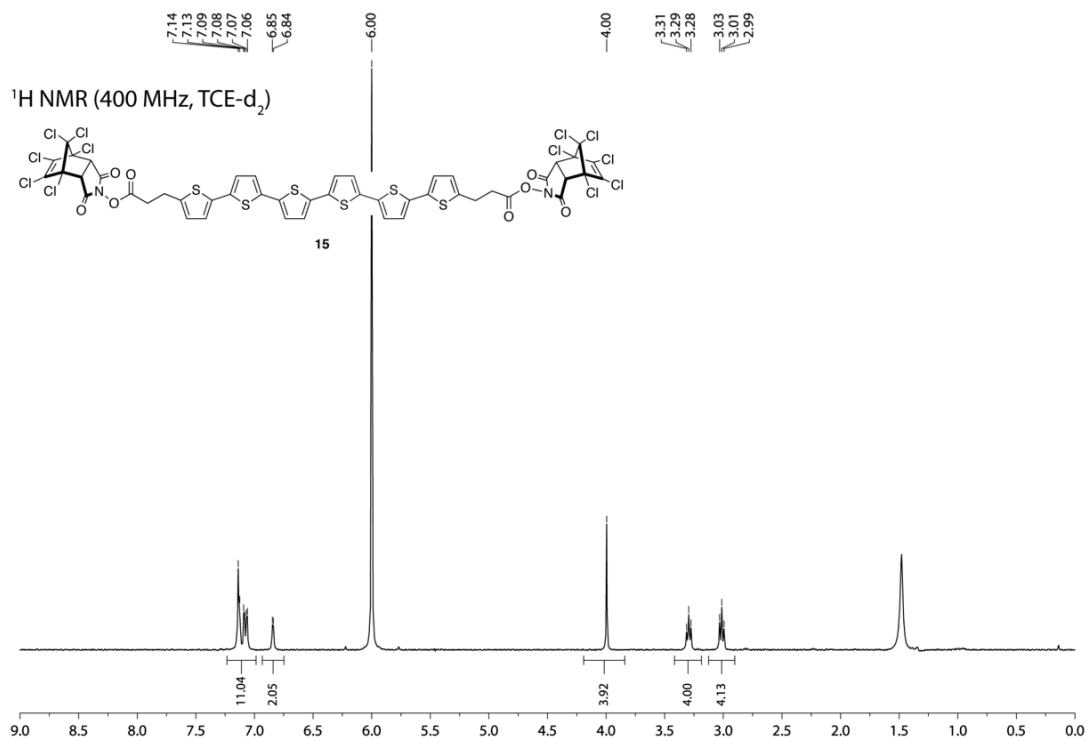


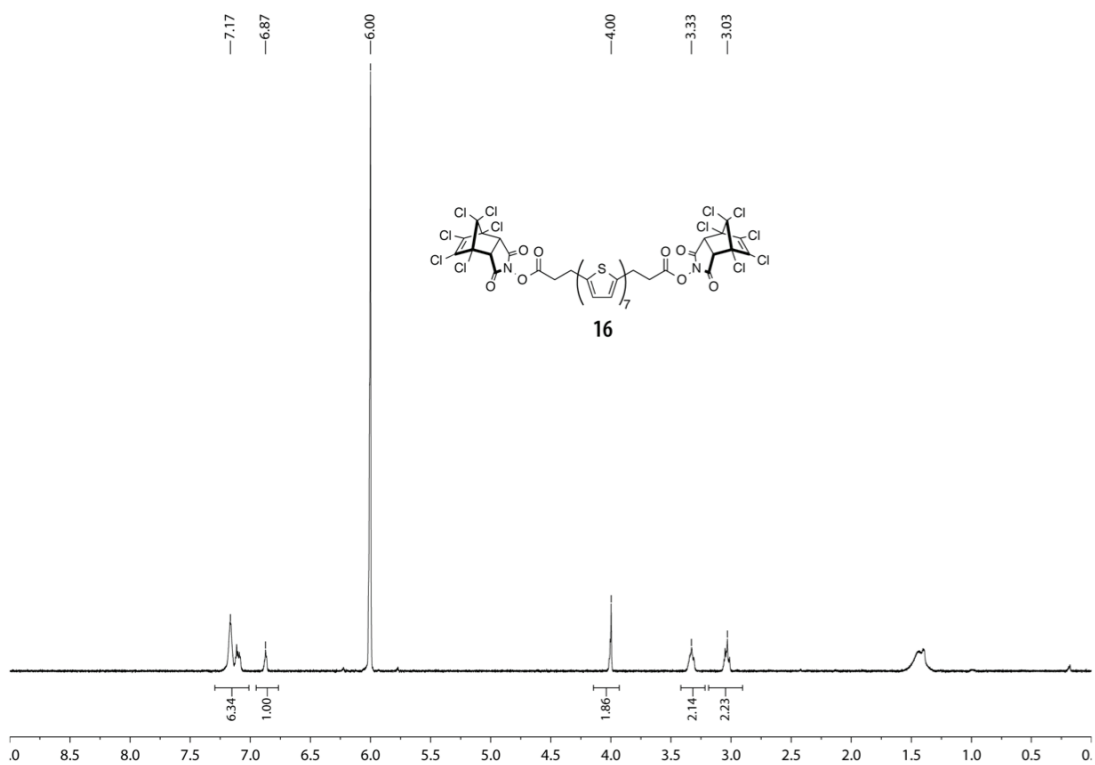






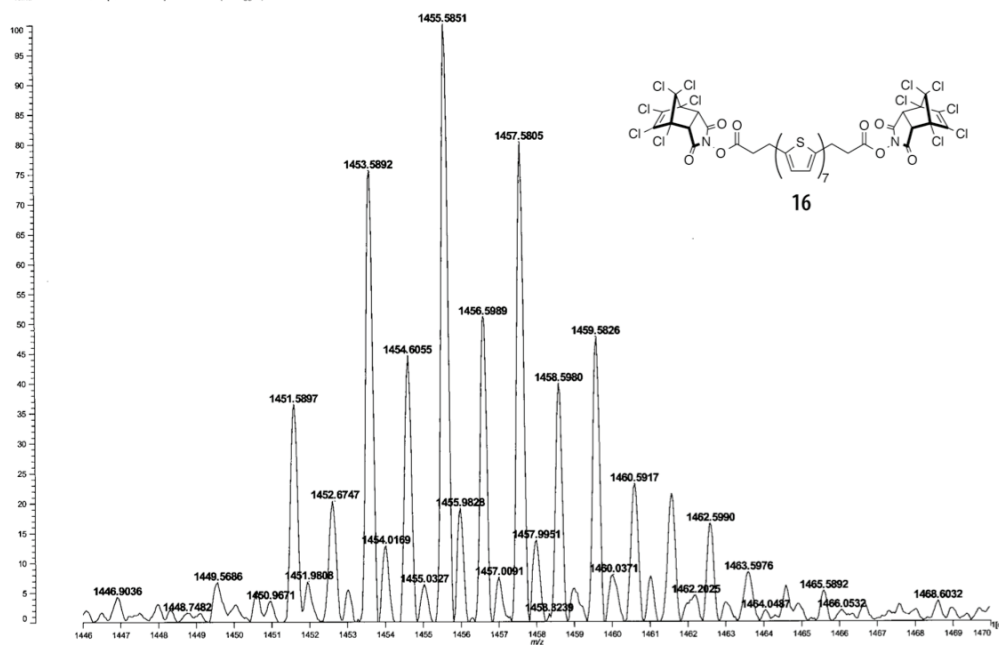


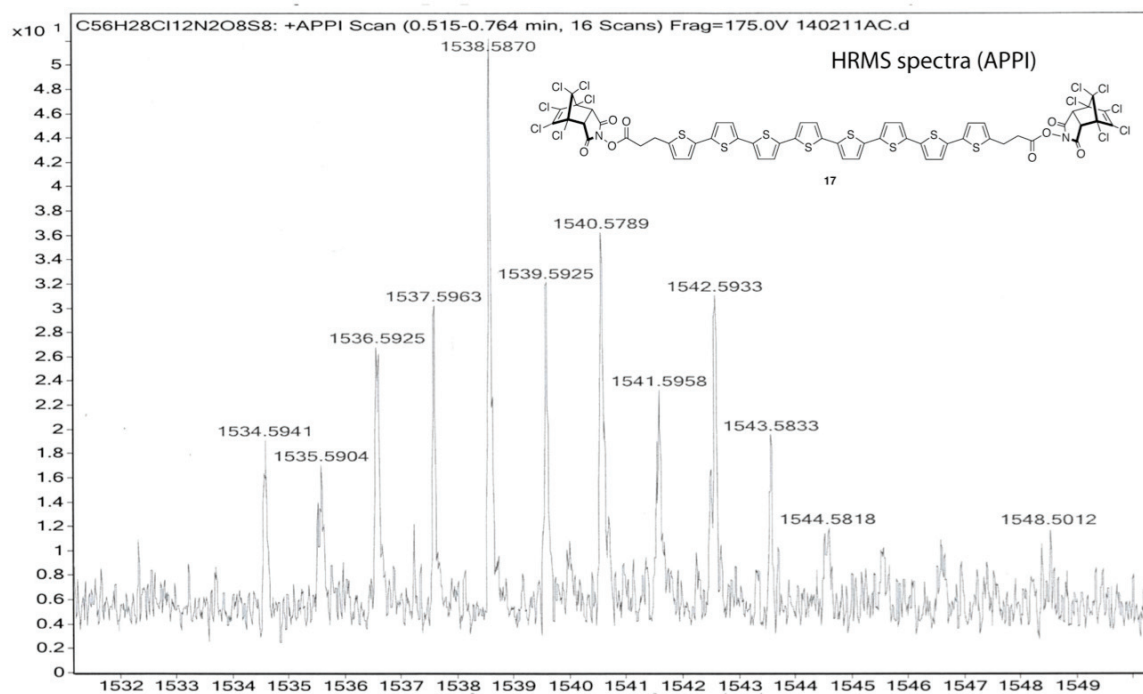
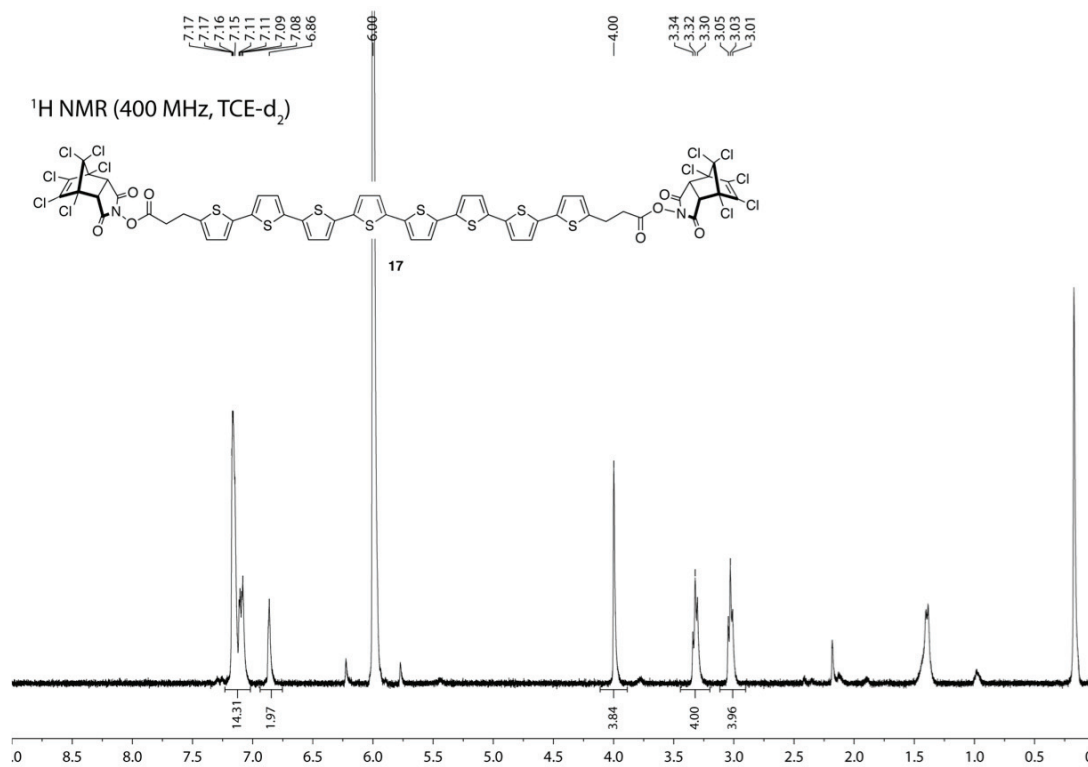


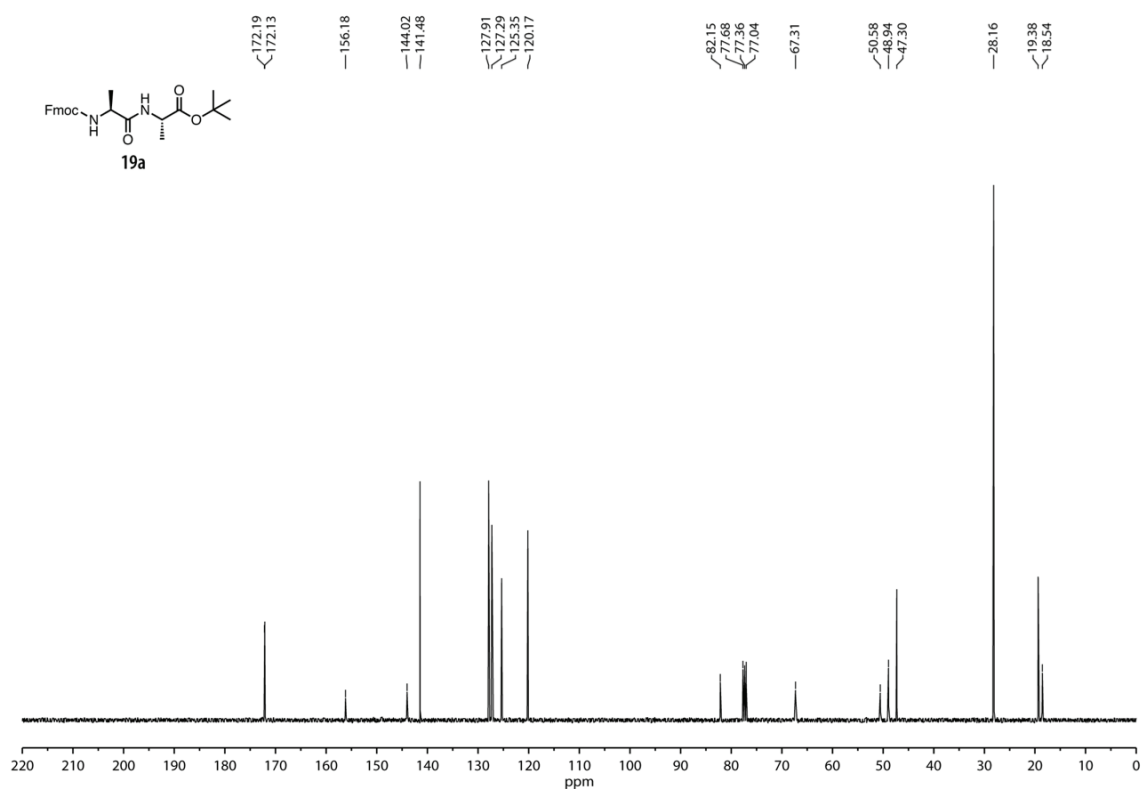
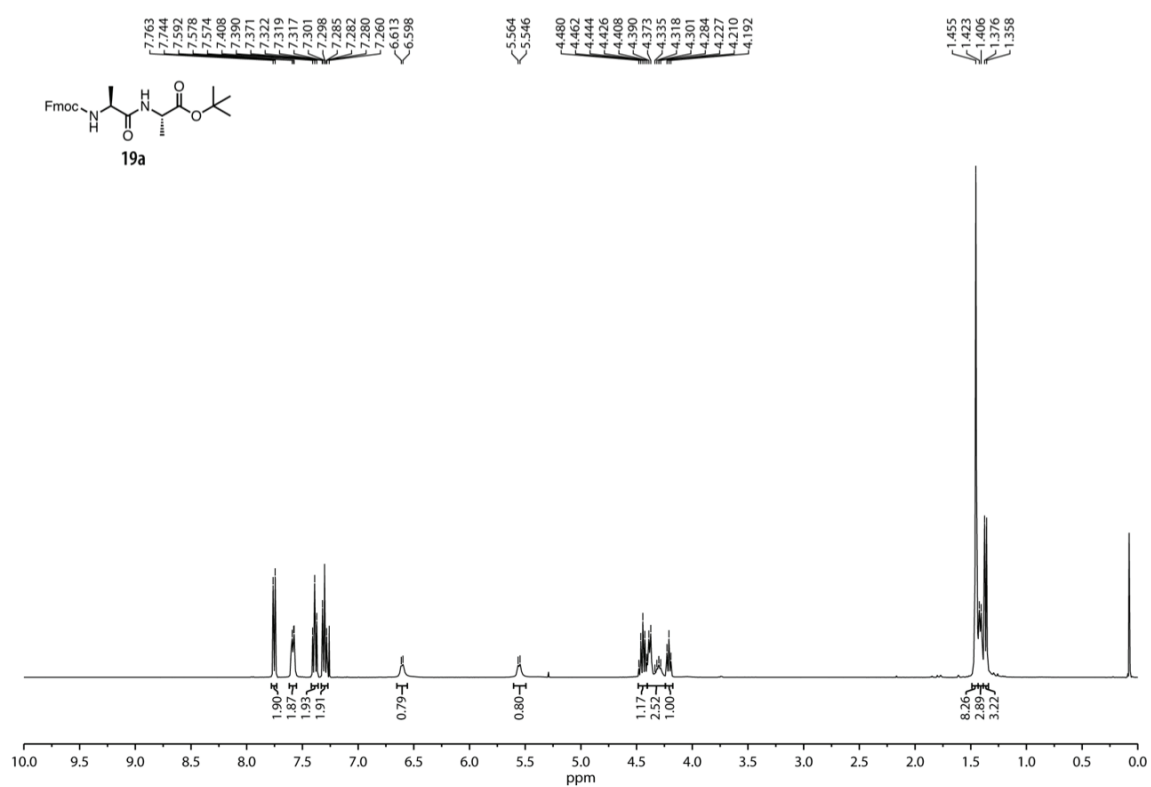


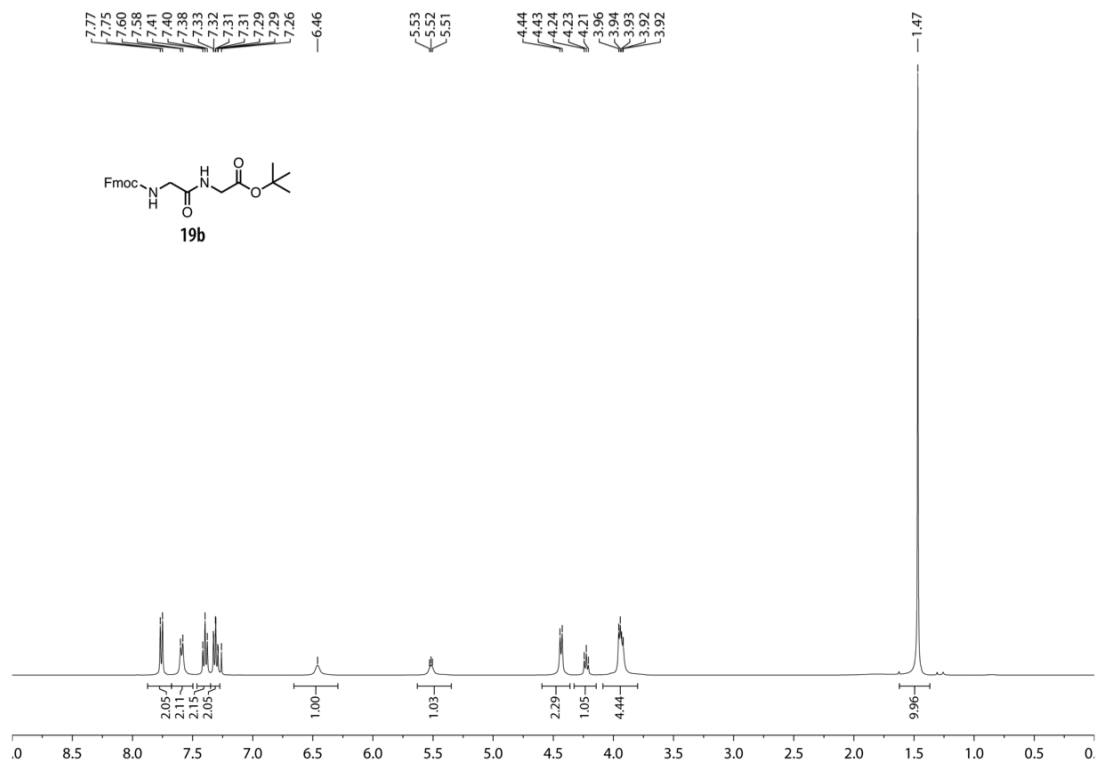
Date: Routine\150312\LC16_CMAA_REF_000213.q 12 Mar 2015 15:03 Cal: ref150312PE1500 12 Mar 2015 14:58
Shimadzu Biotech Avnra QP10plus 3.3.3.20090916: Mode reflecton, Power 138, Bias/kv: 1.5, @ 1000 (bin 123)

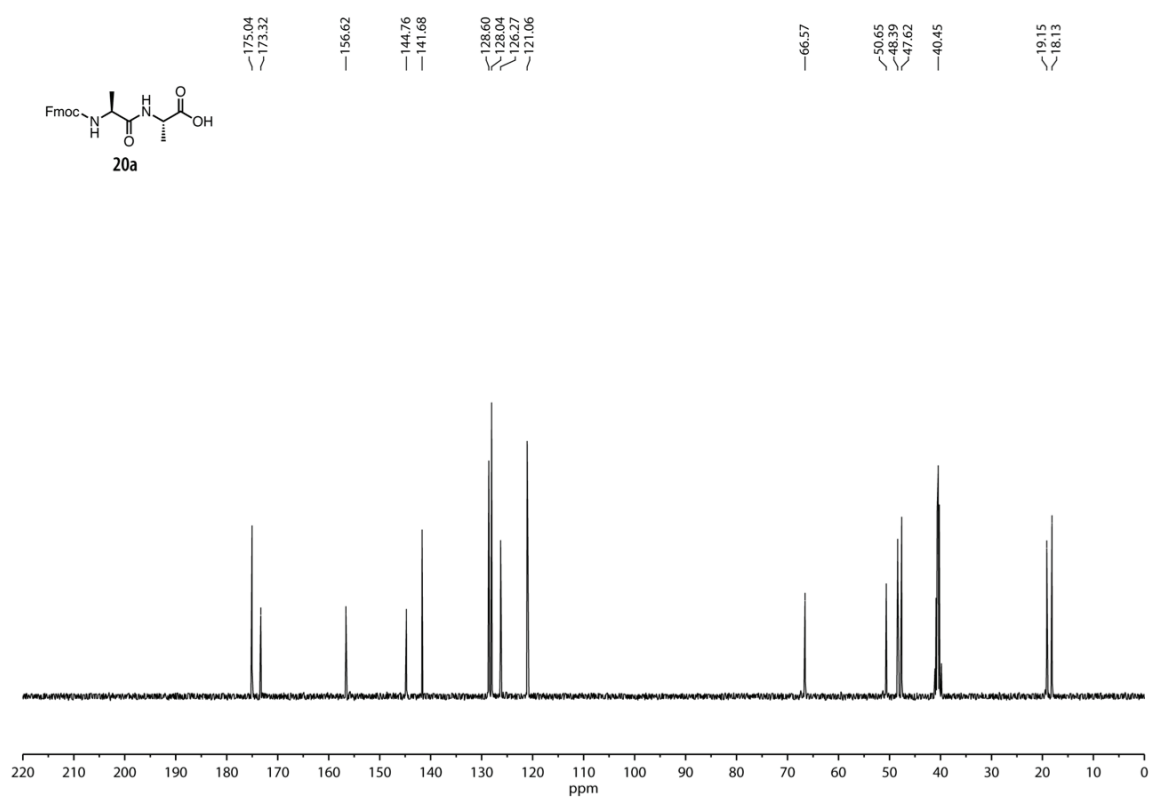
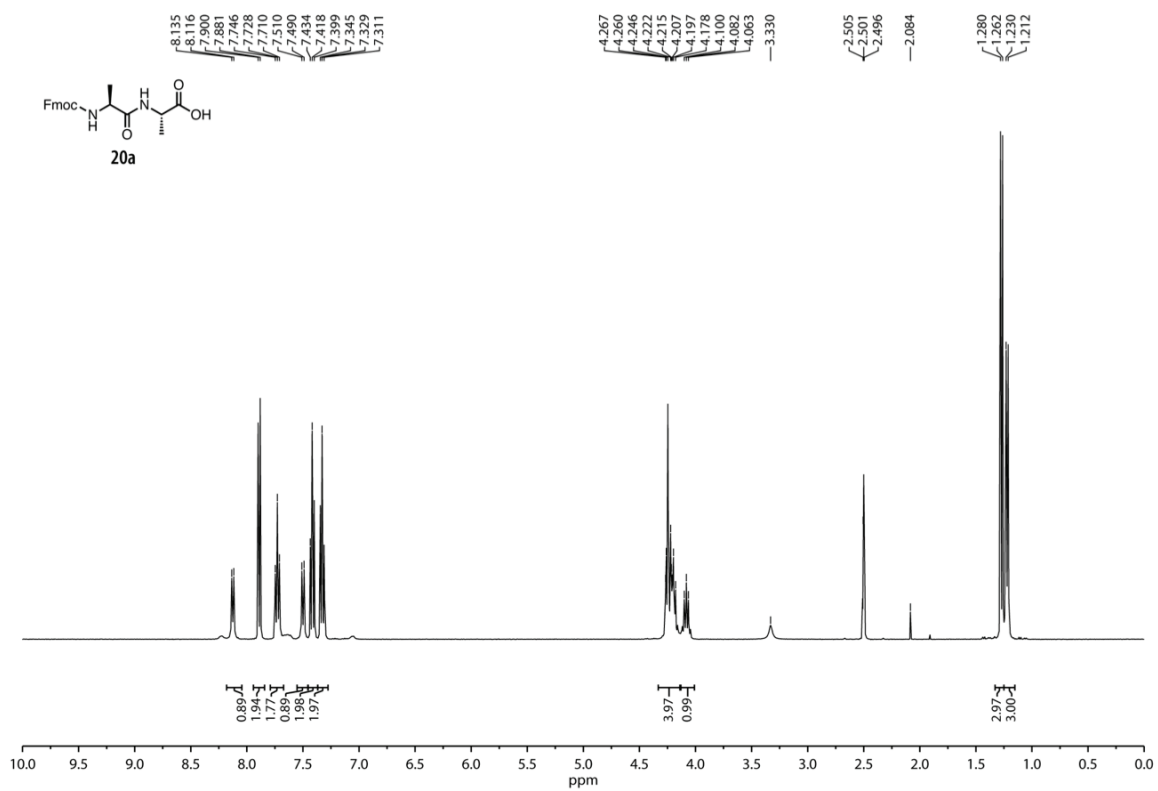
%Int. 163 mV(eum= 7527 mV) Profiles 1-48: (48 Tagged) Smooth Sv-G1 2 -Baseline 16

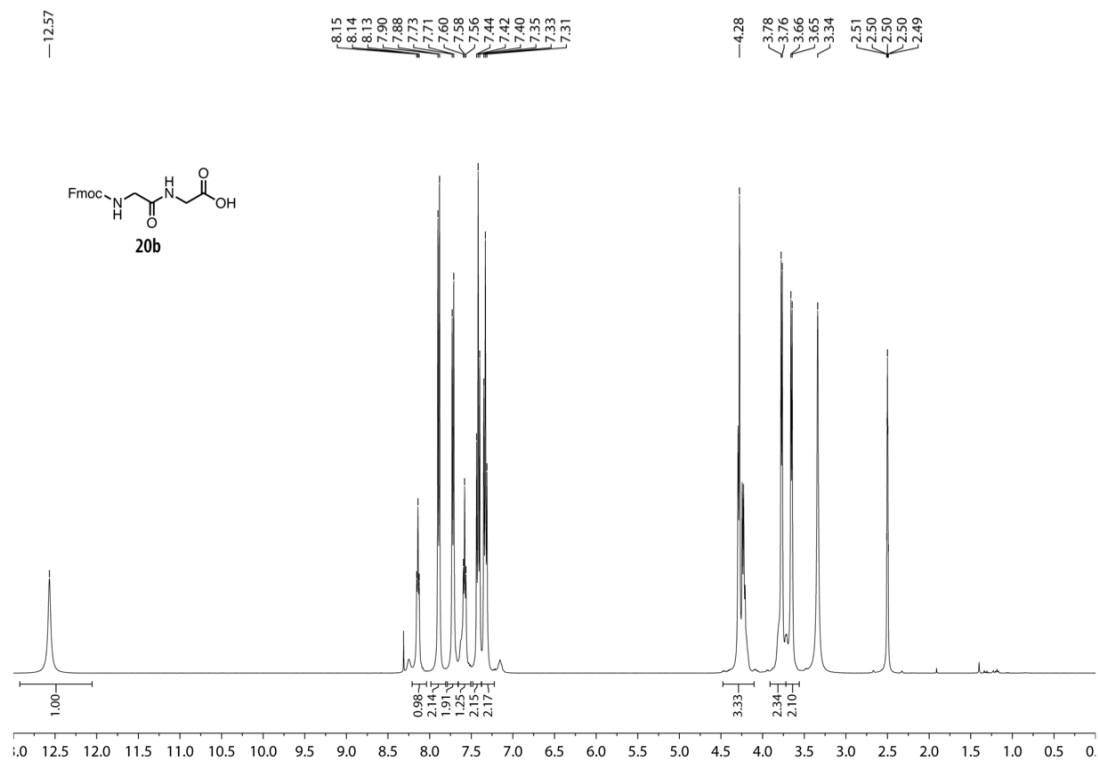


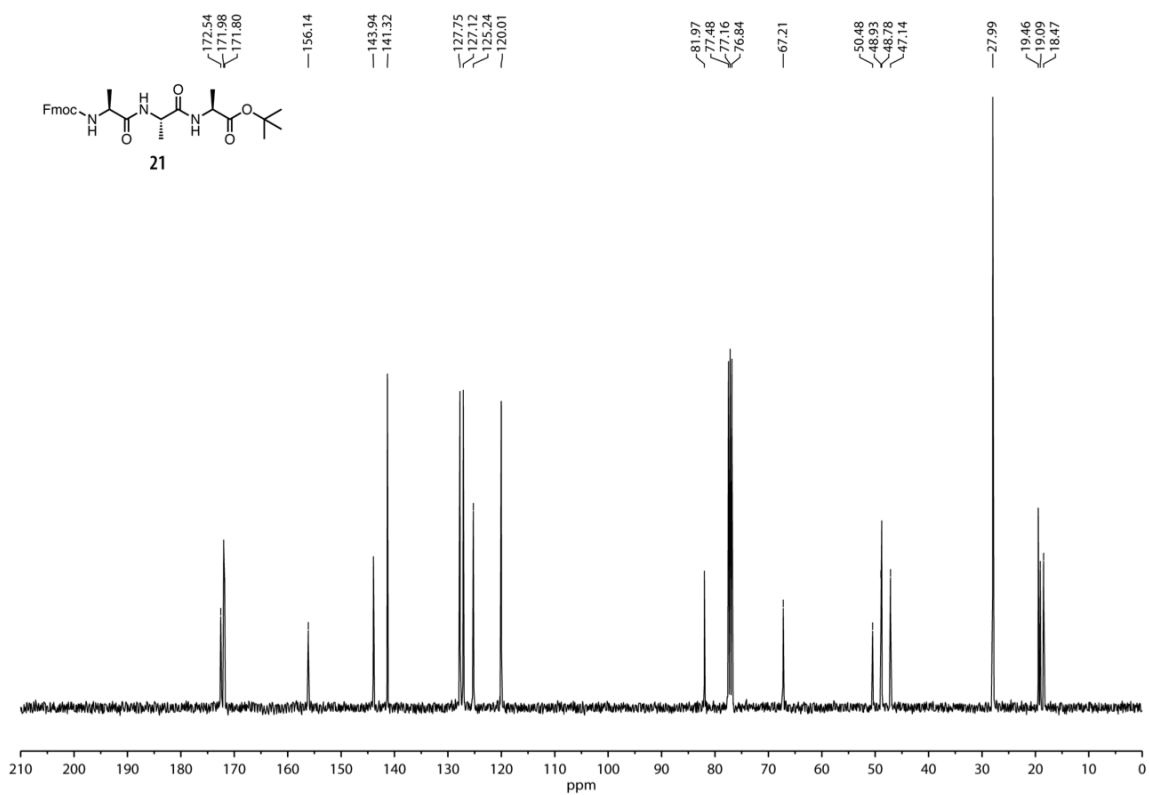
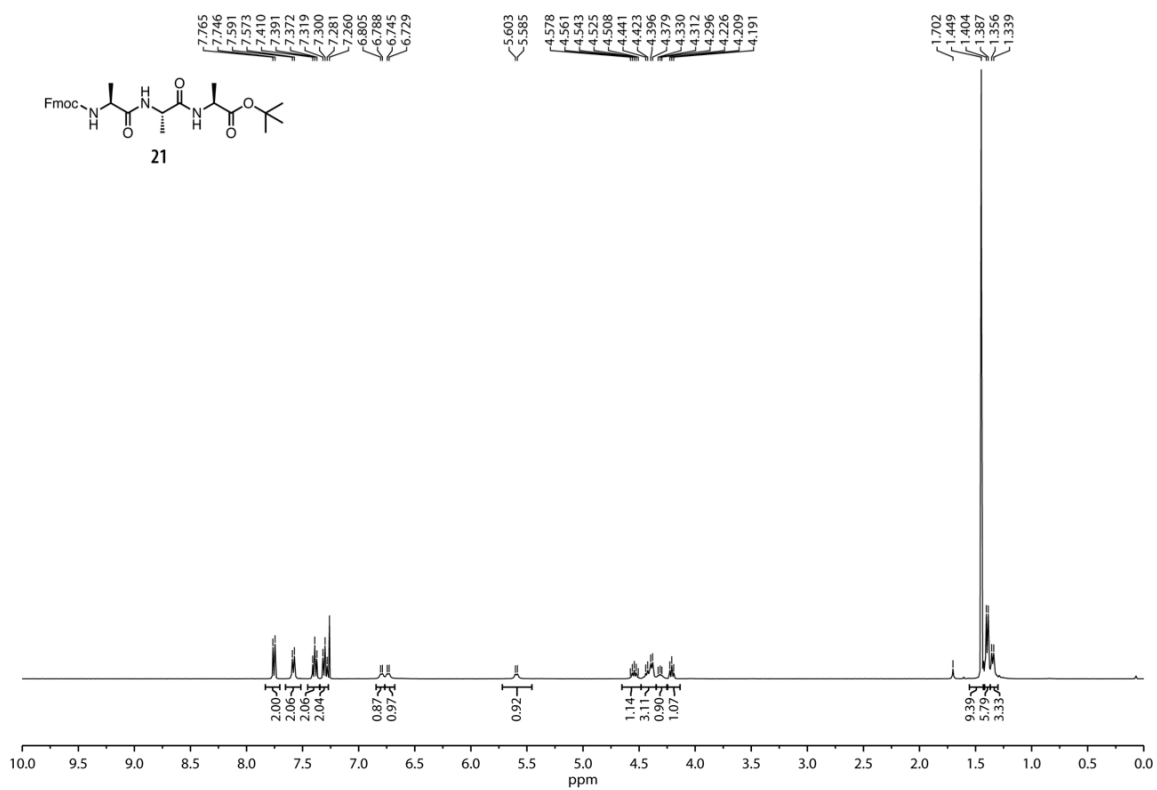


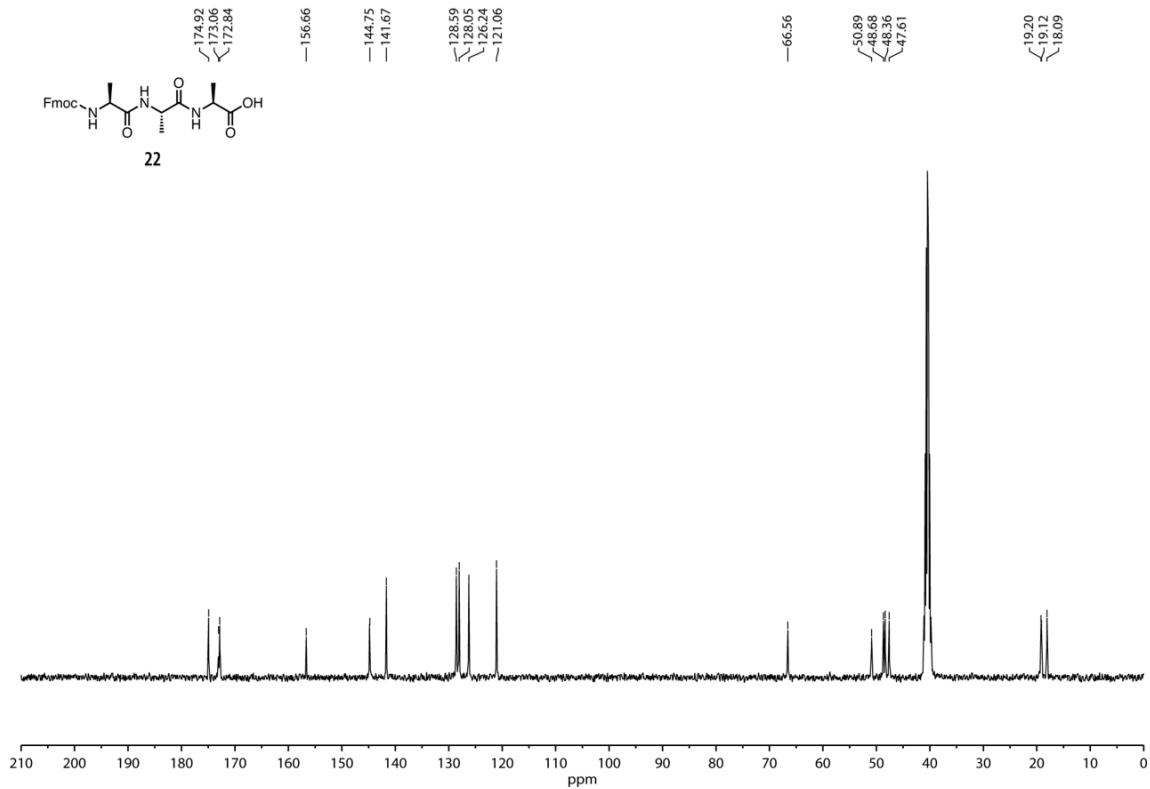
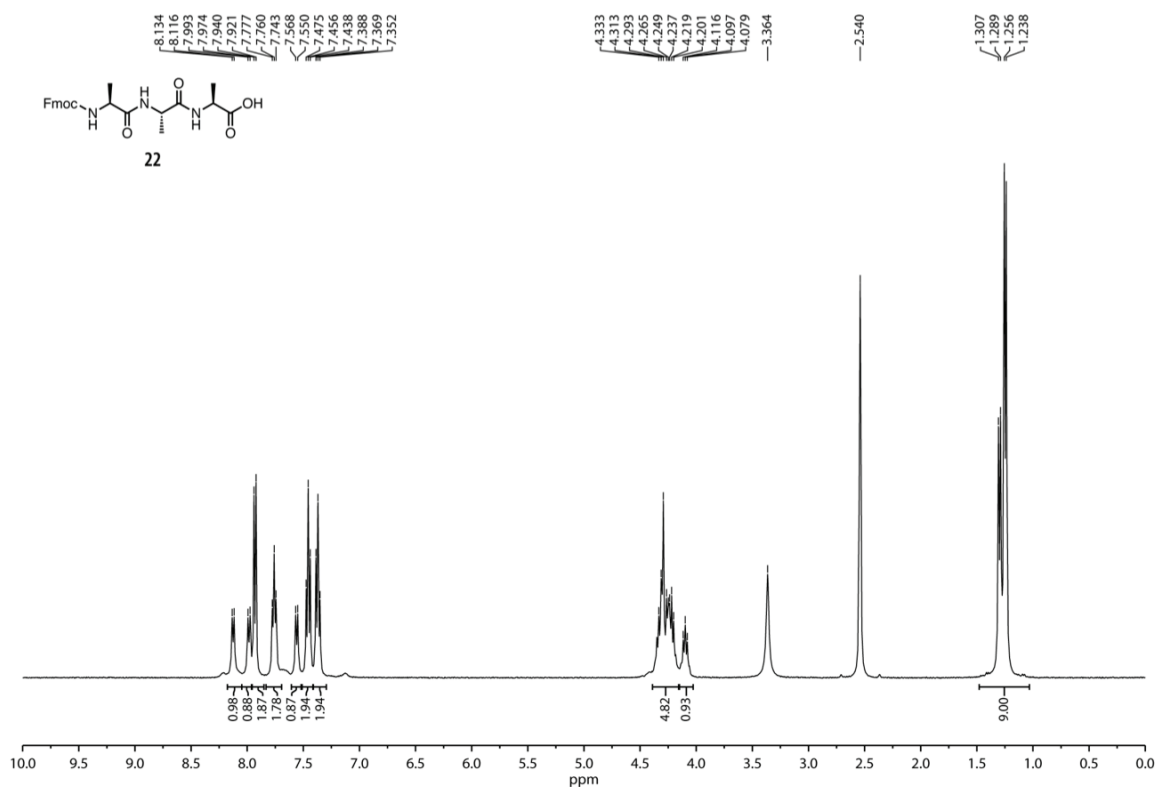


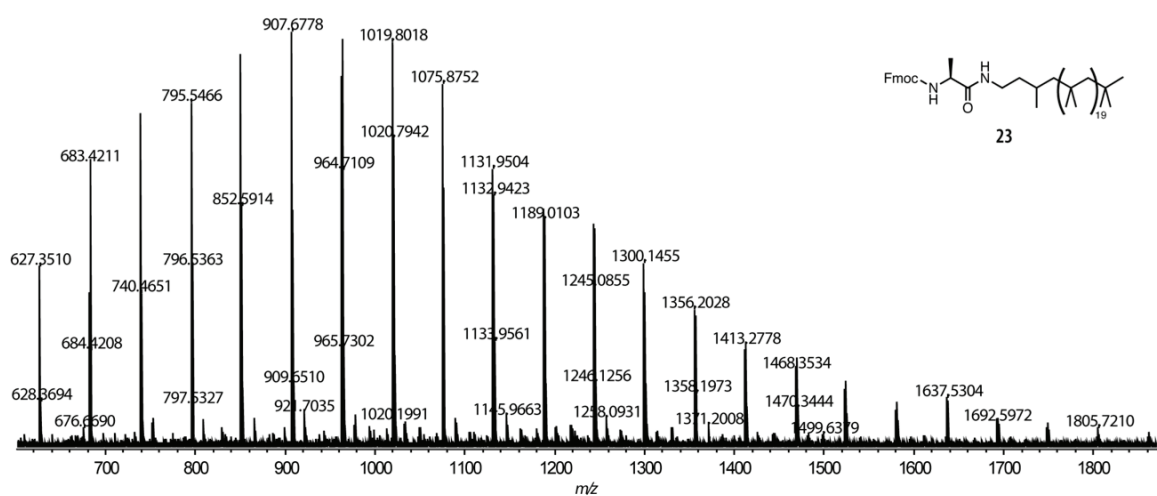
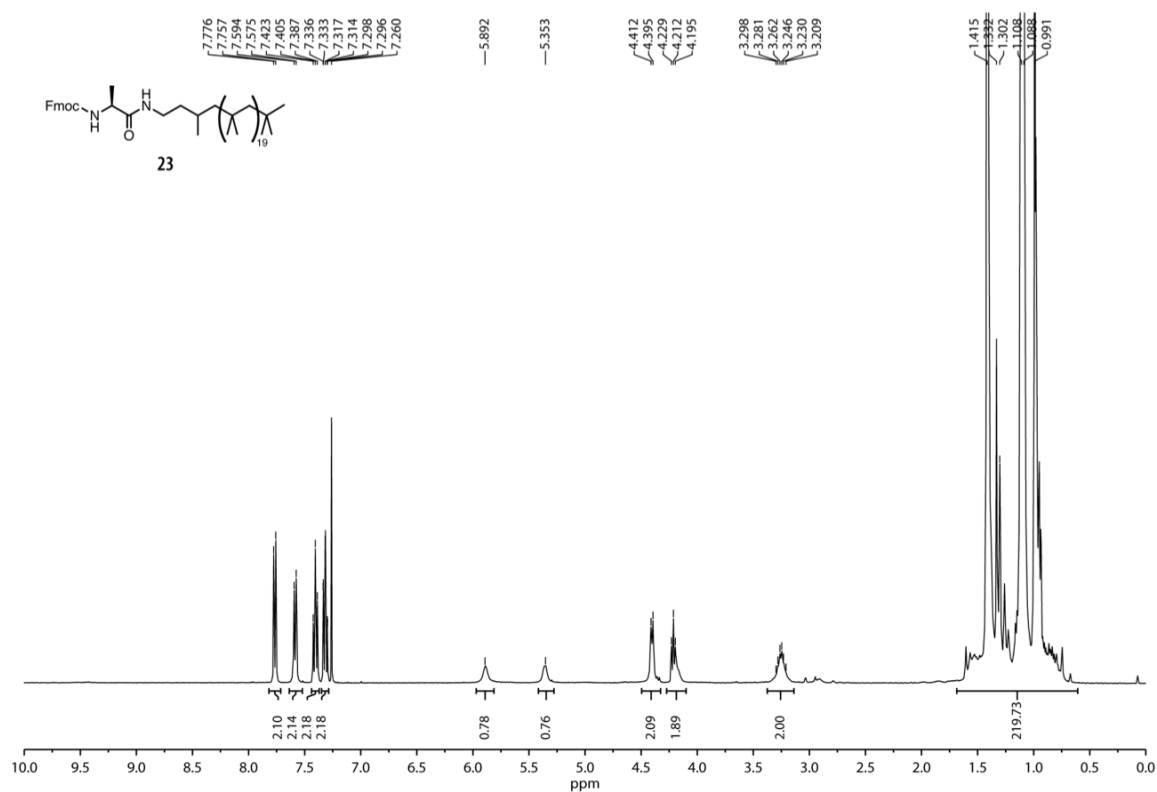


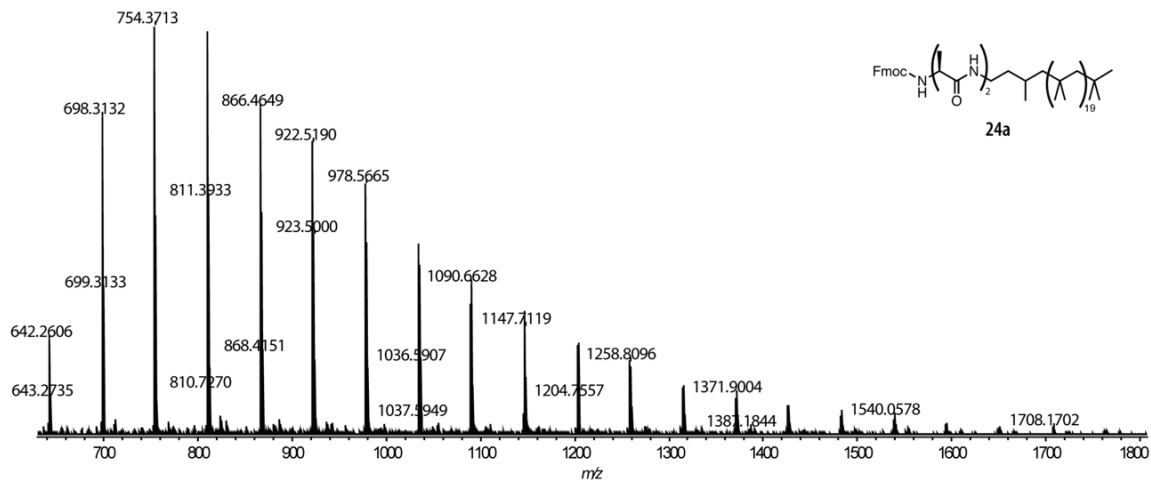
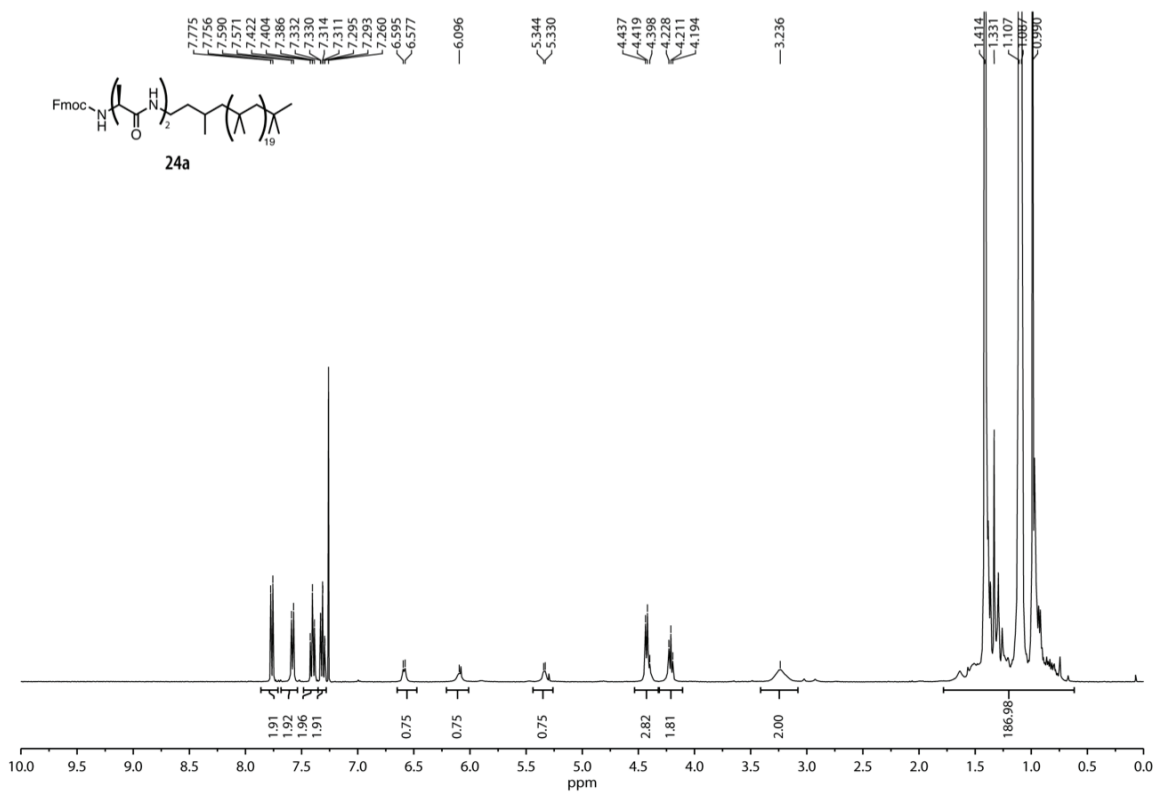


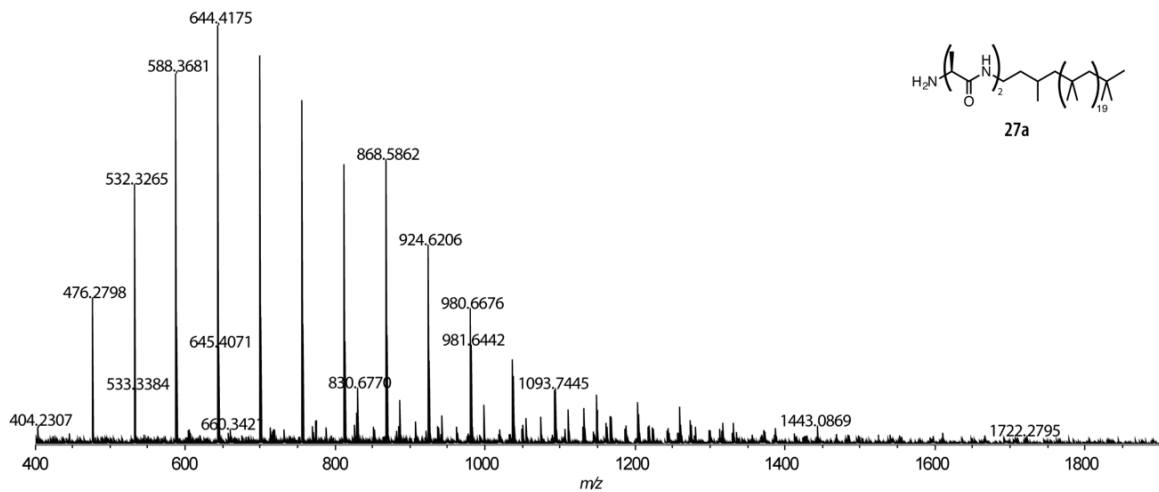
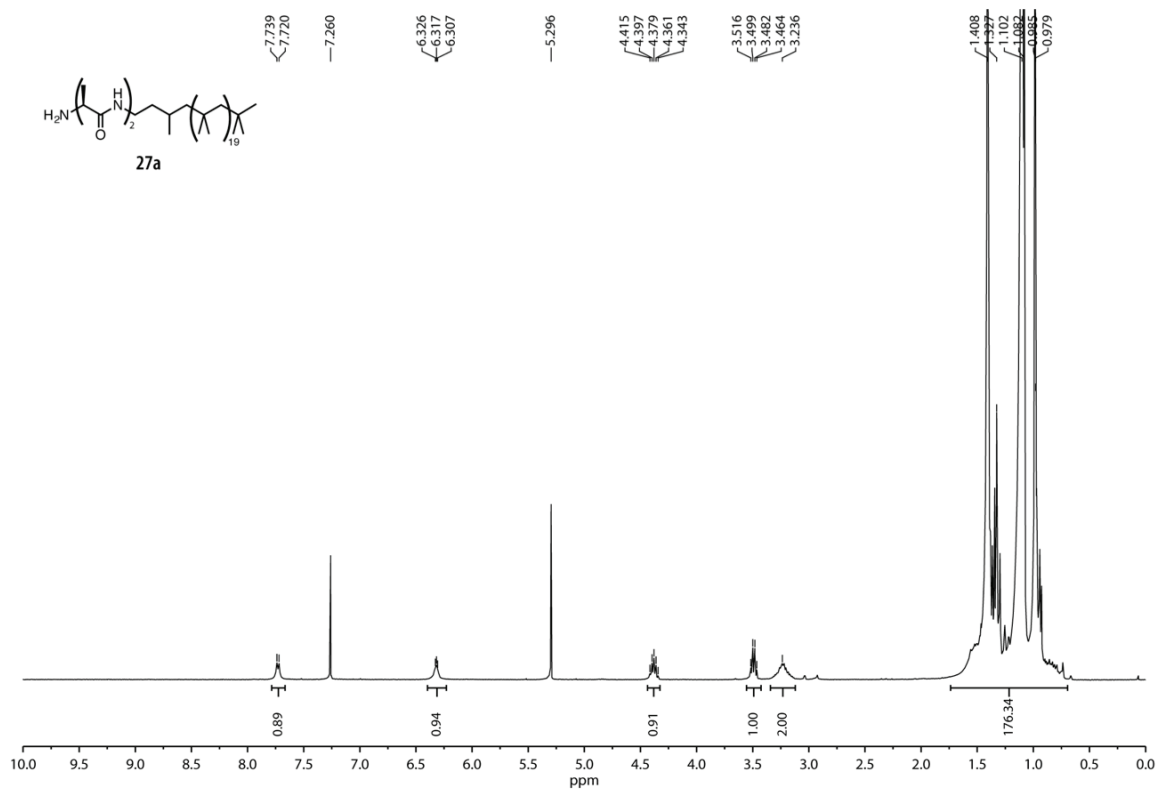


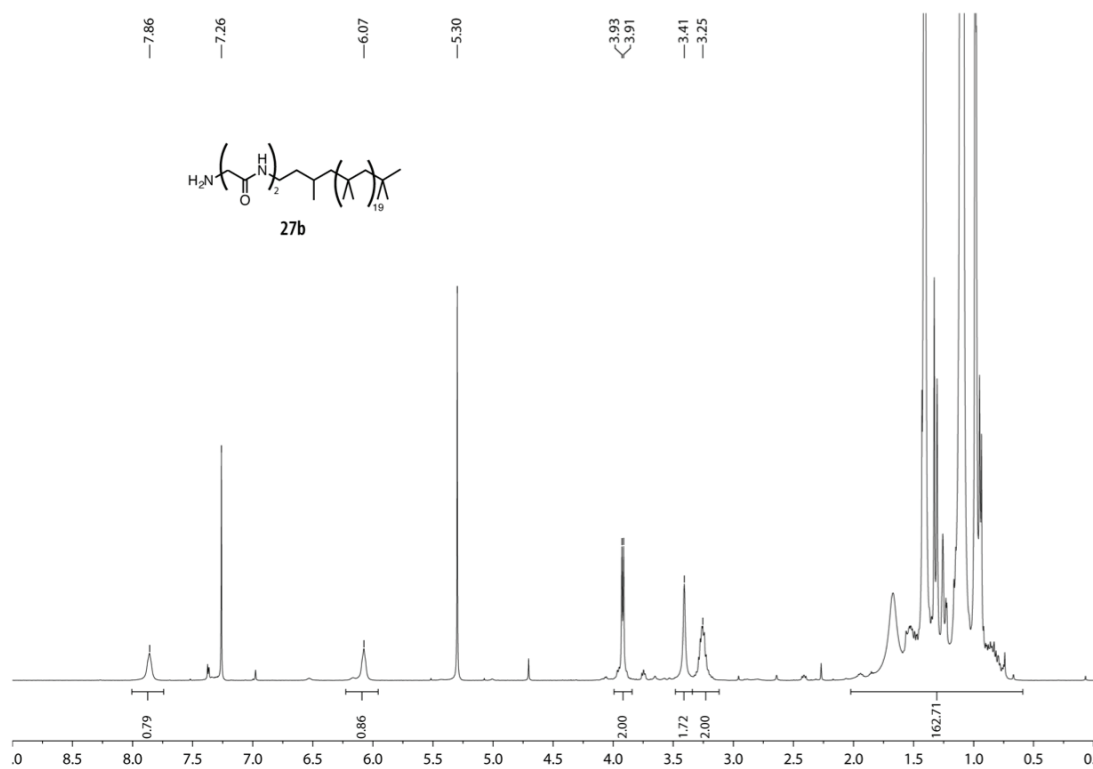


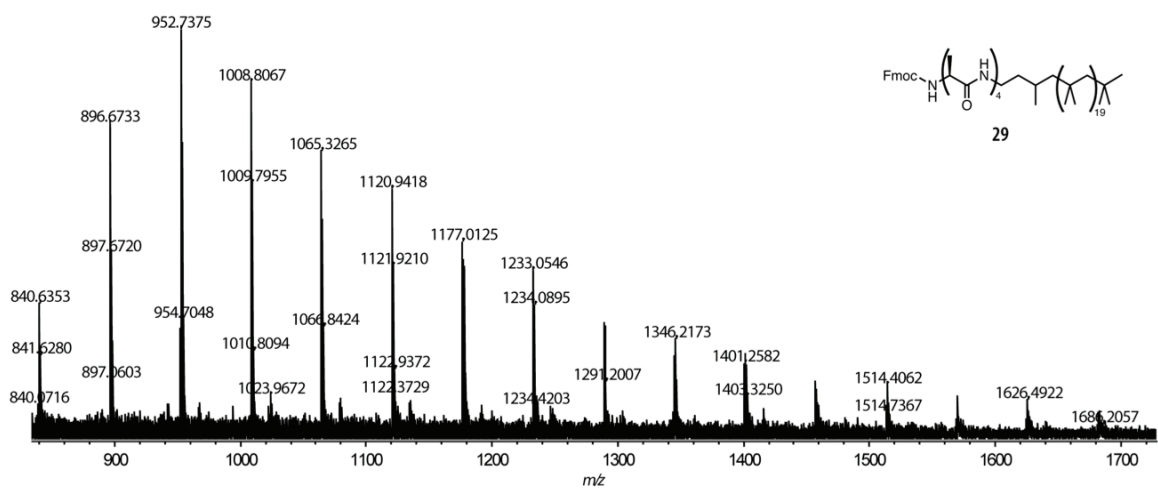
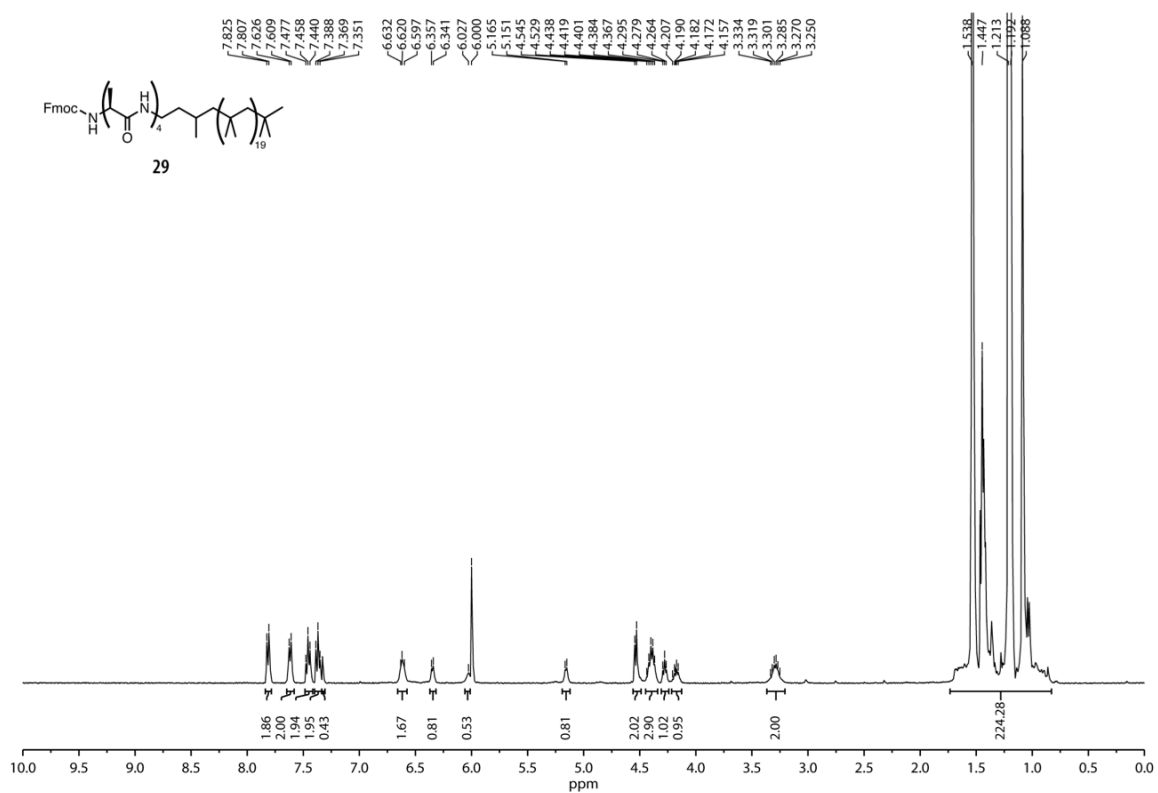


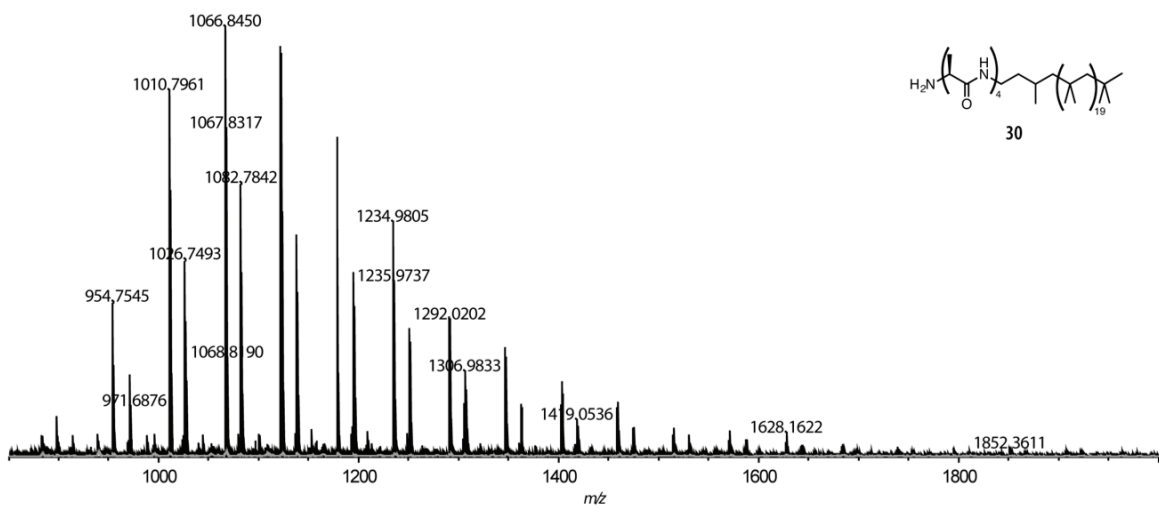
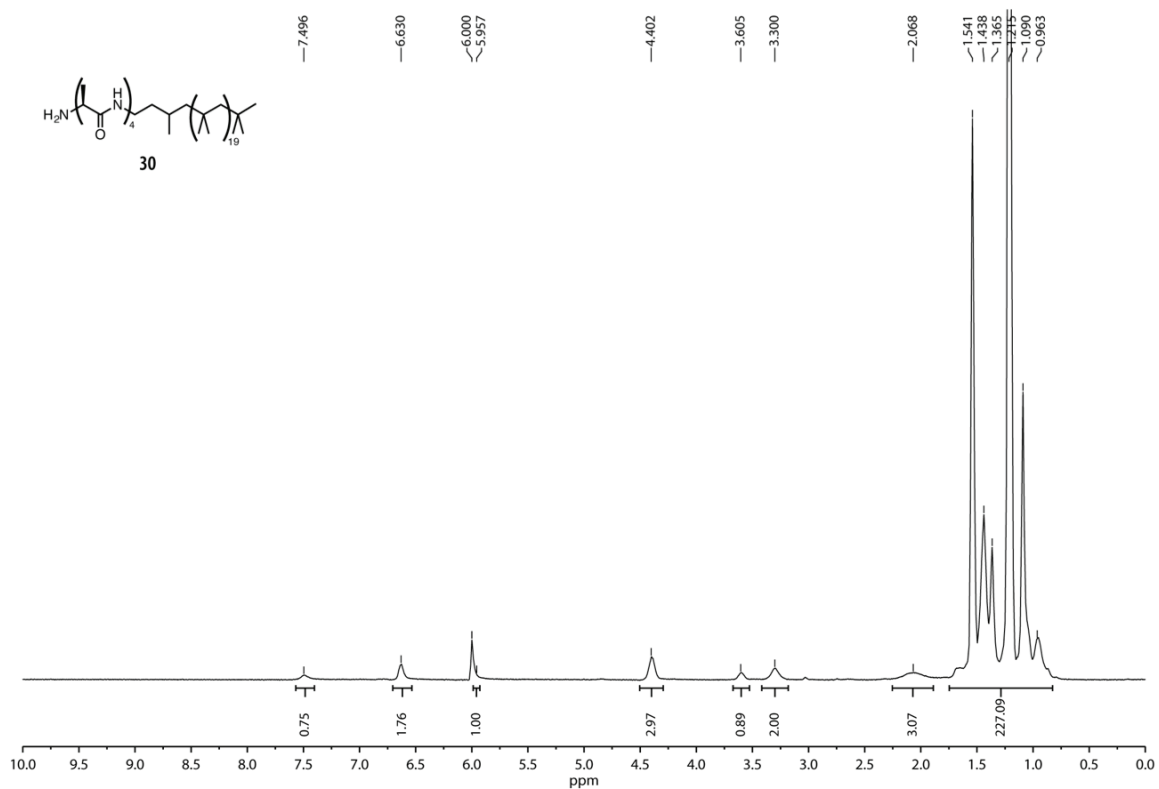


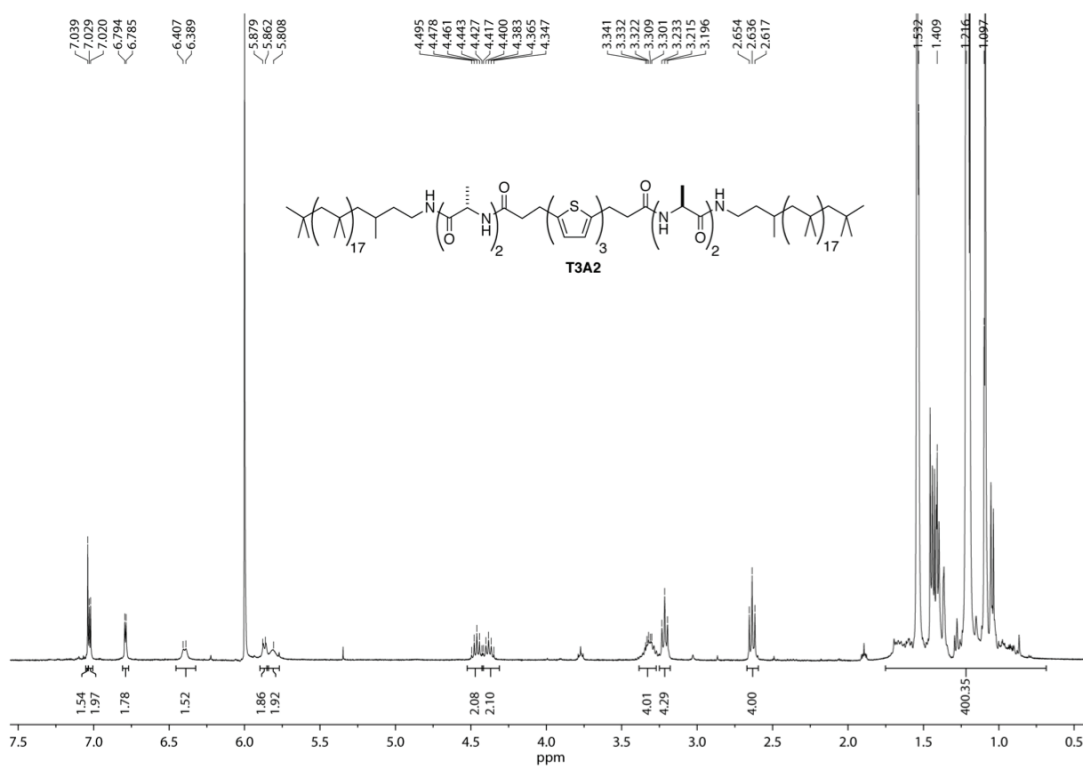
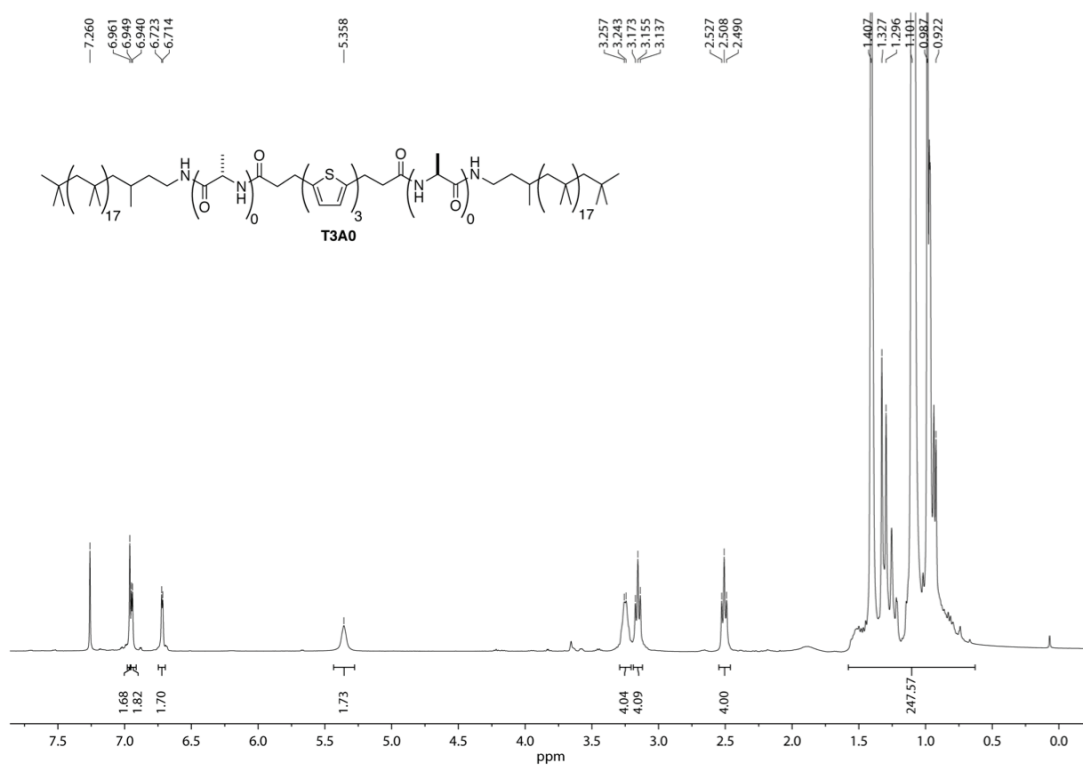


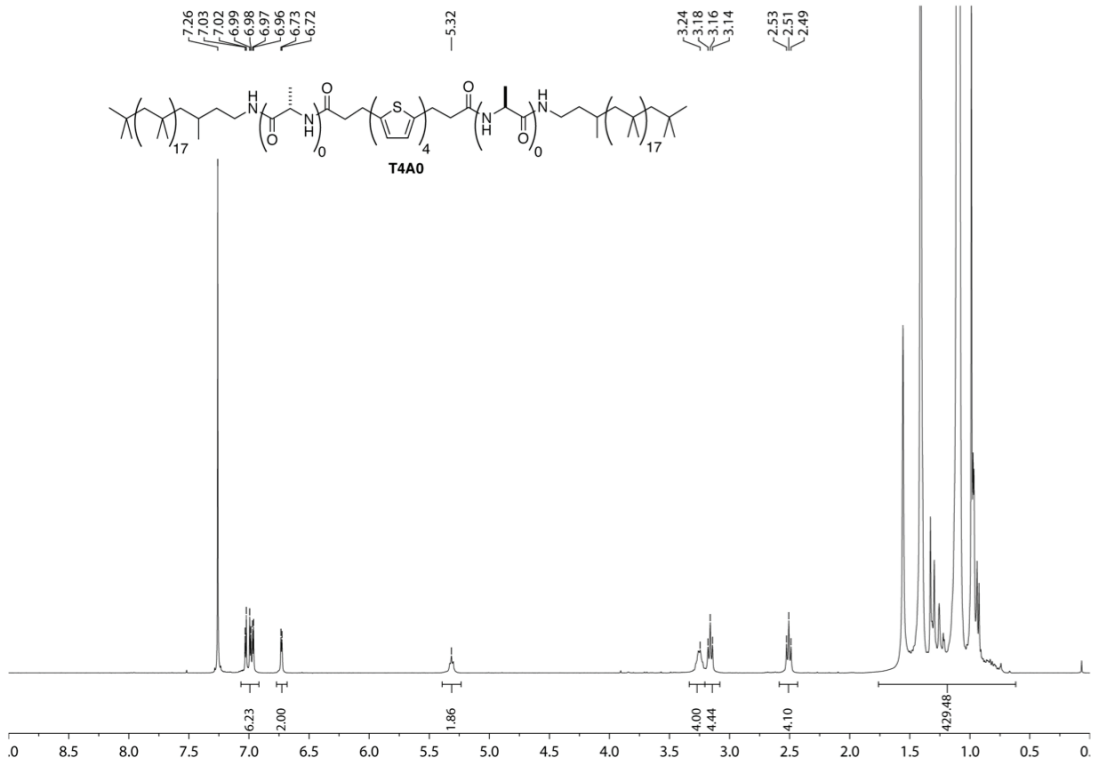






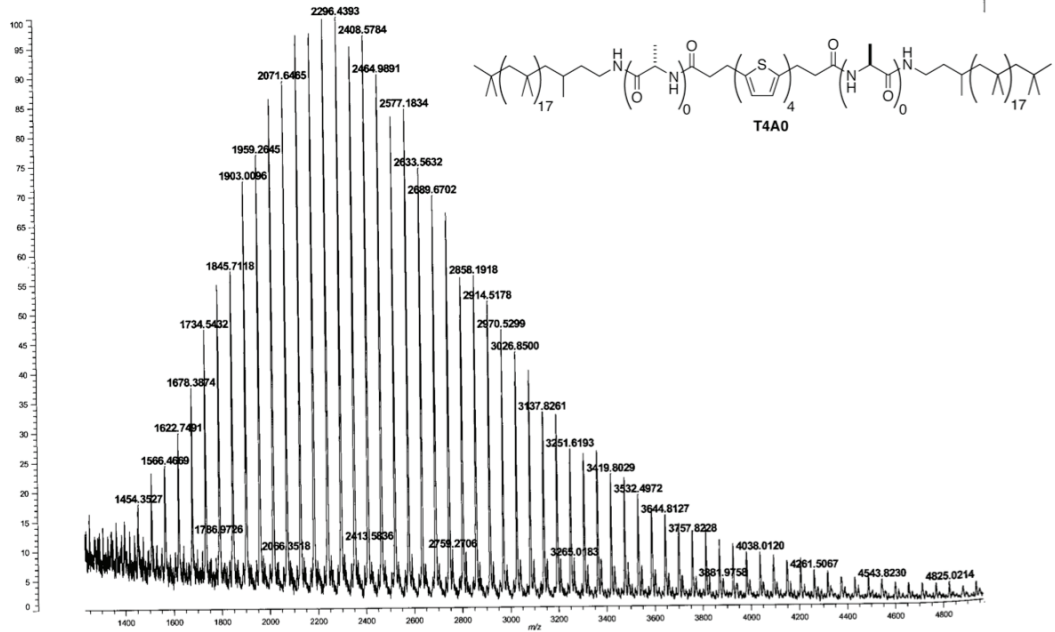


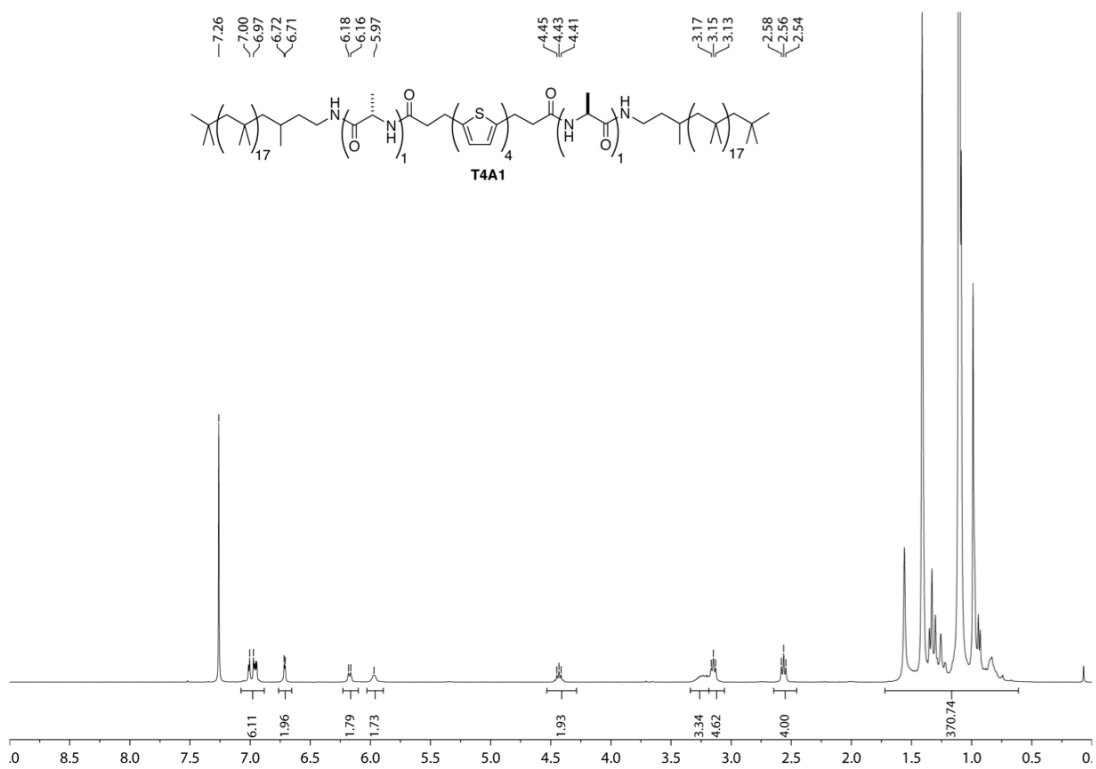




Data: Routine\130319\DER05_DCTS_LN1_0002_003 15 Mar 2013 15:55 Cal: L1-130305_P03000 5 Mar 2013 16:50
 Shimadzu Biotek Austria GmbH plus 2.3.3.20080316 Model: Inerts, Power: 118, F.Ext.: @ 4500 (bin 117)

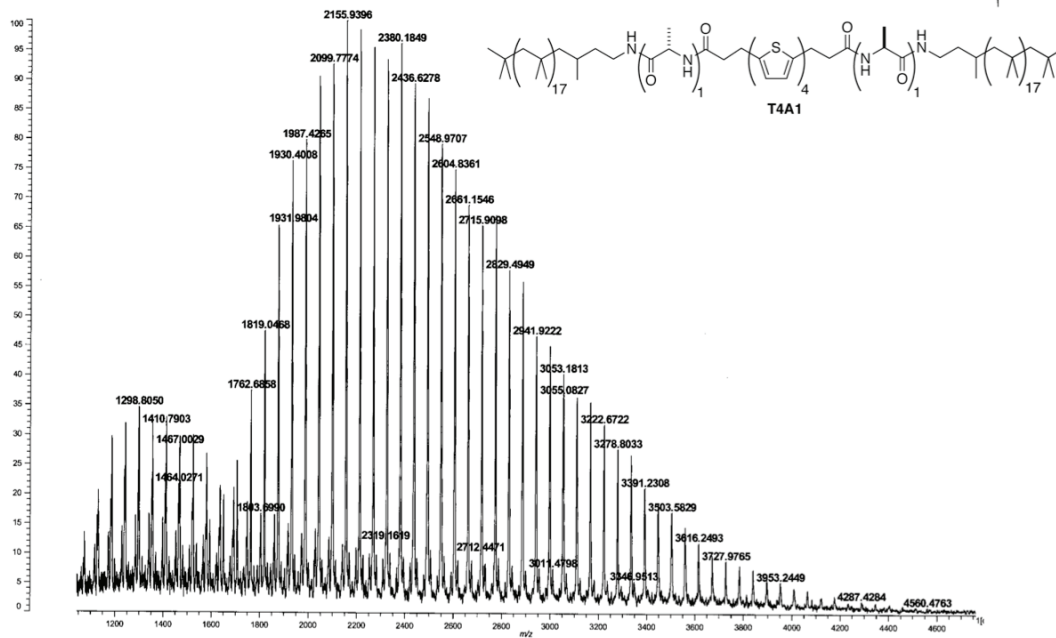
%Int. 20 ml/min=2297 mV, Profiles 1-115 (115 Tagged) Smooth Av 10

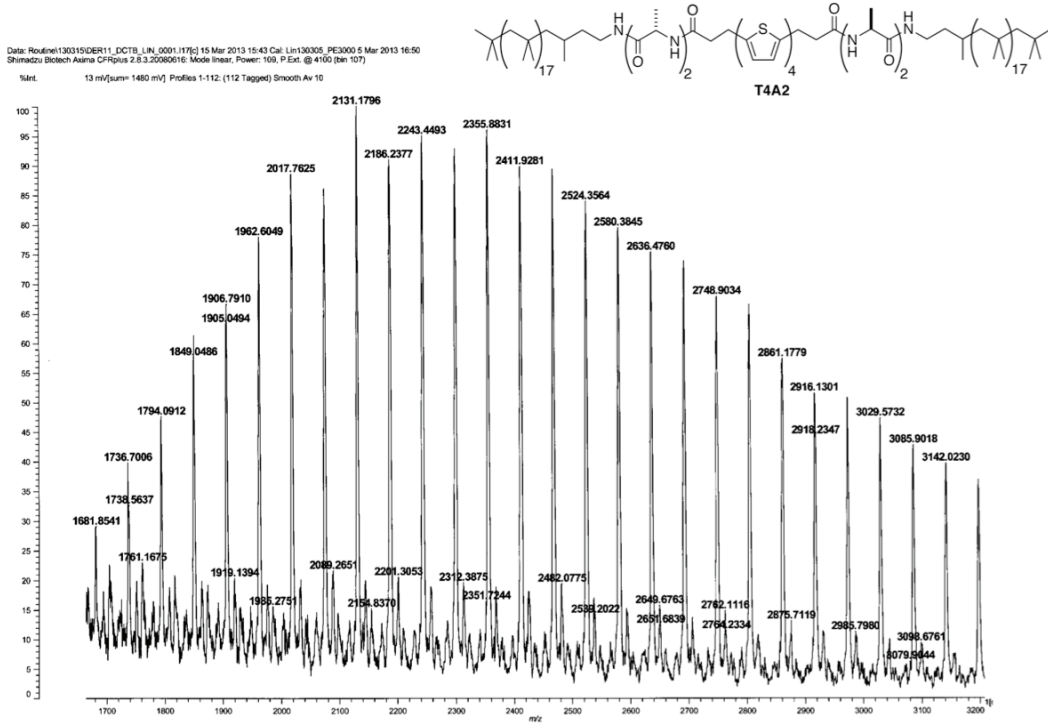
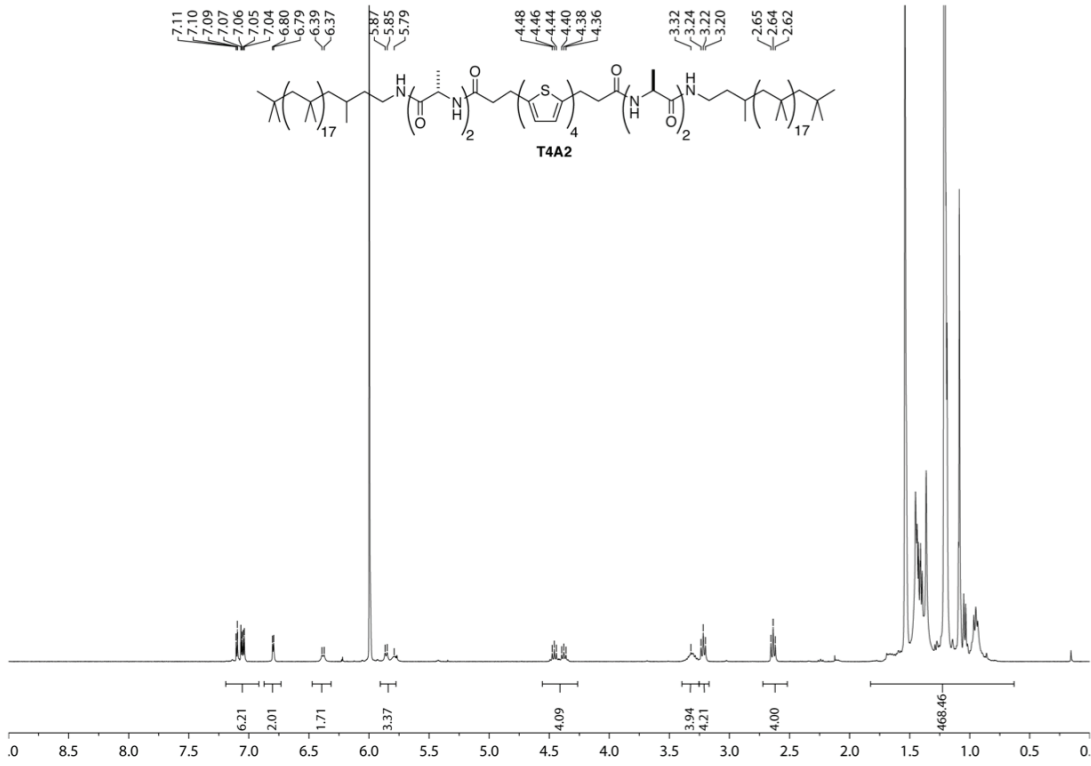


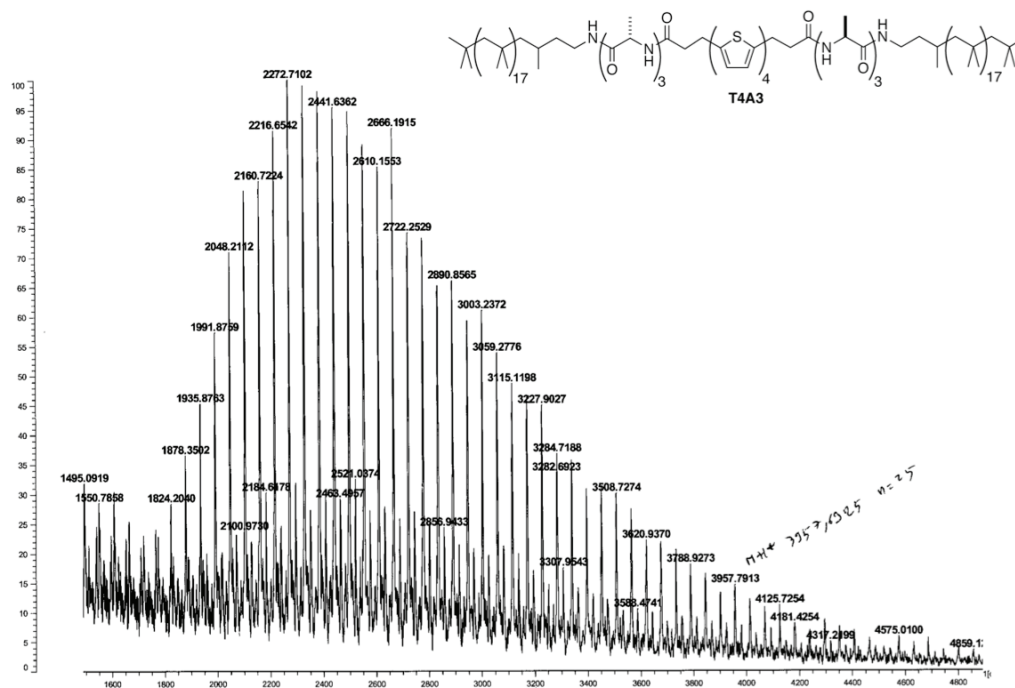
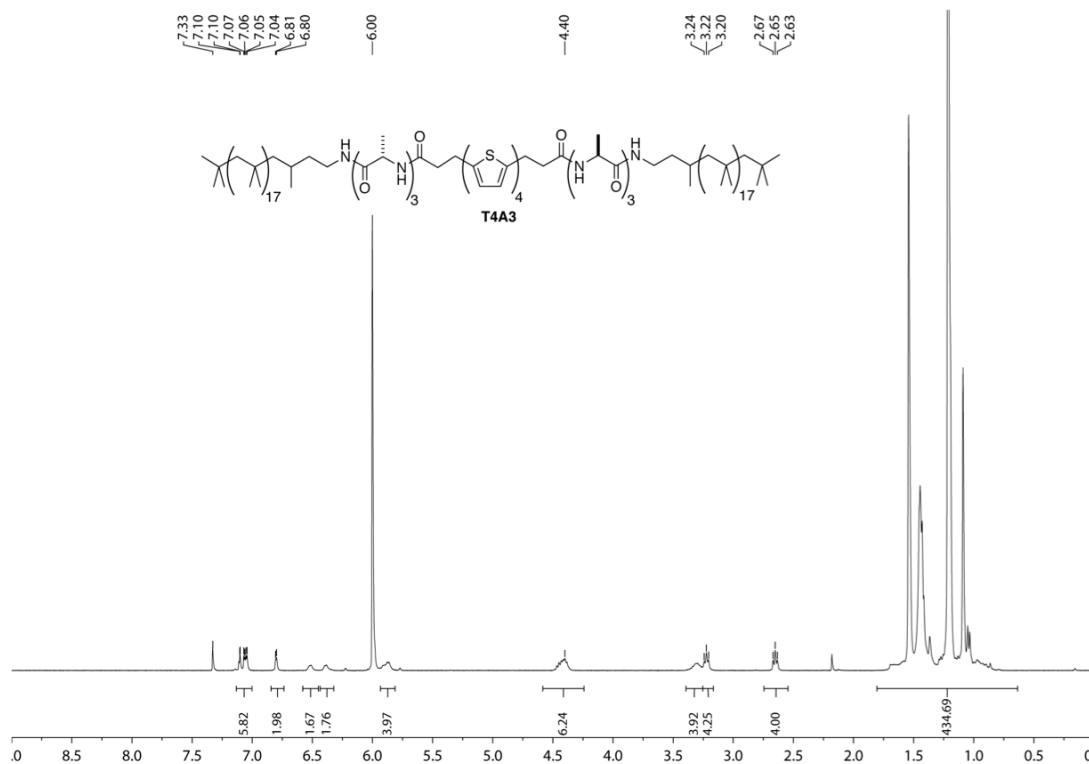


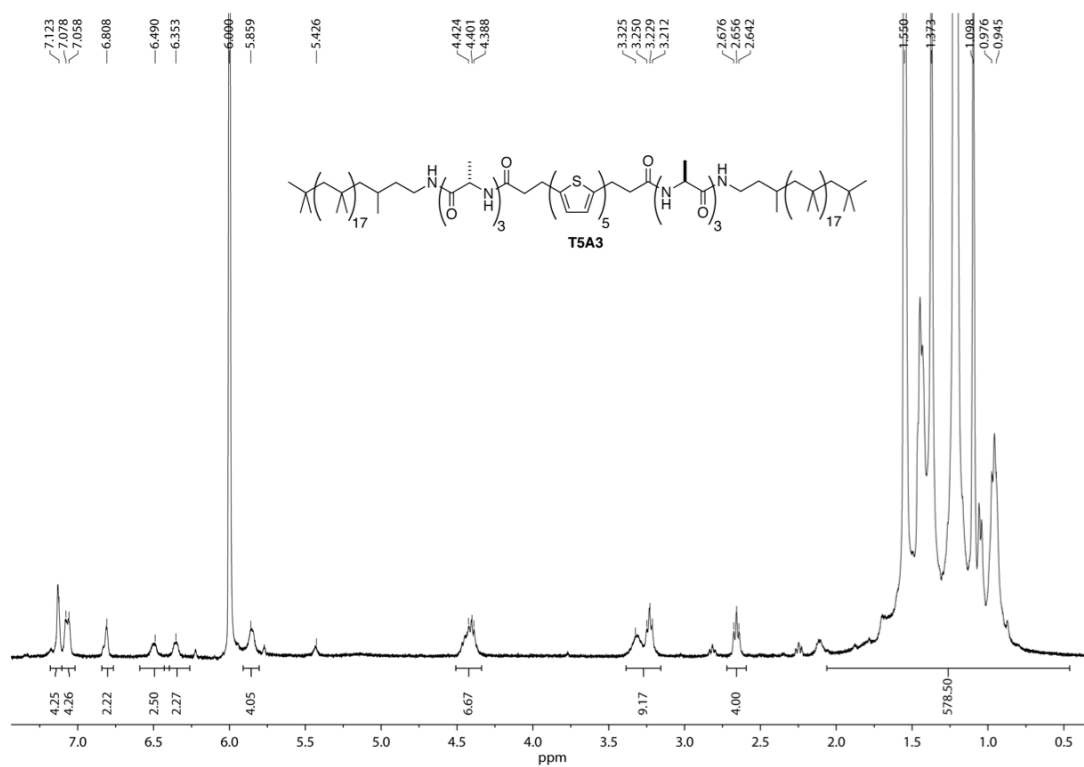
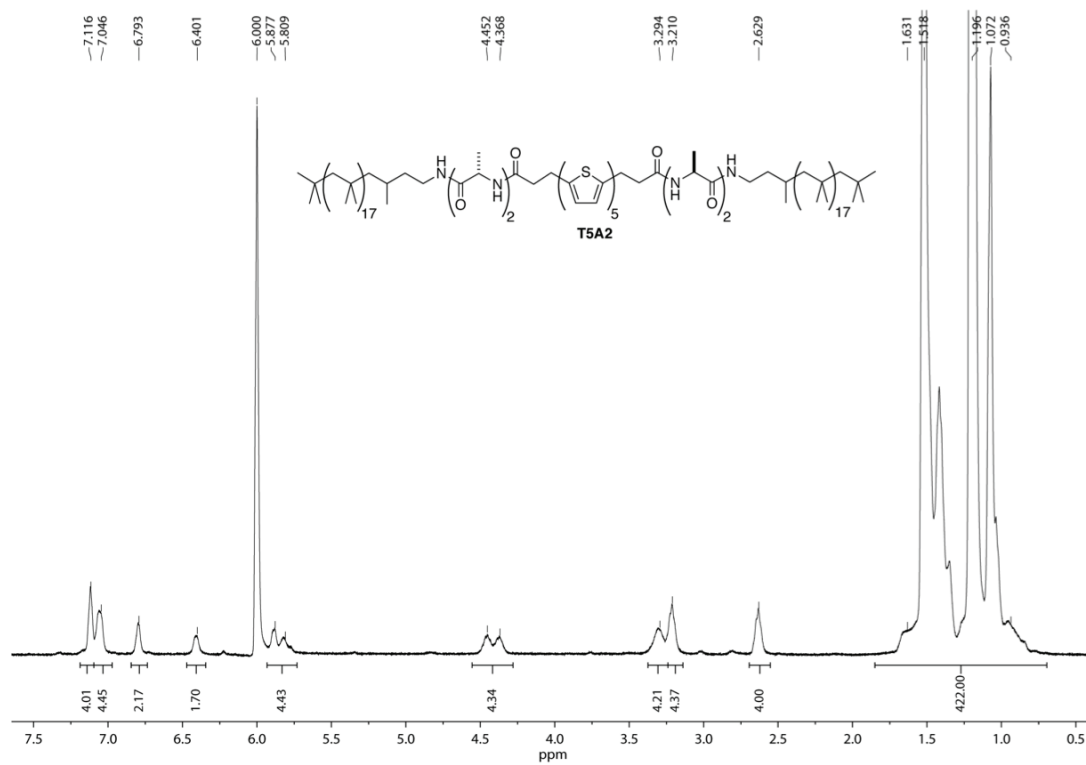
Date: Roadrel1362191ER204_DCTB_LIN_0001 (246) 15 Mar 2013 16:45 Cal: Lin100395_PC3000 5 Mar 2013 16:50
 Shimadzu Biotach Axima CFXplus 2.8.3.2009016: Mode: Free; Power: 100; P.Eat.: 4; 430 (bin 107)

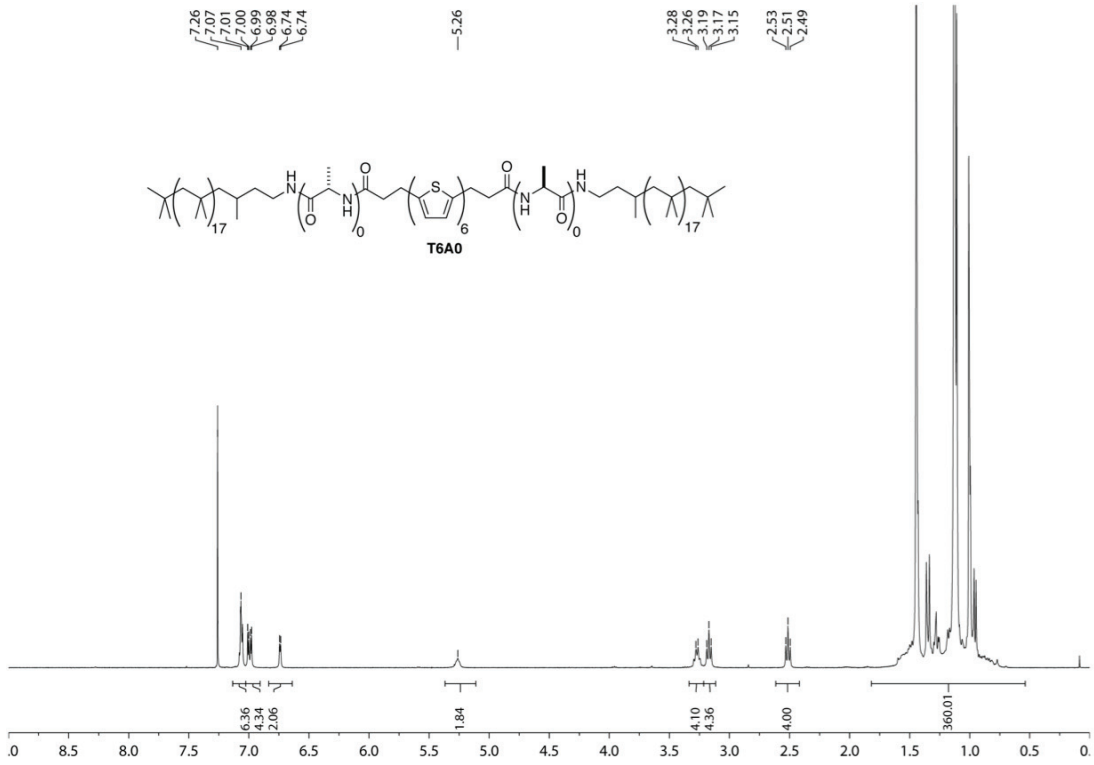
%Int. 24 mV(sum=2961 mV) Profiles 1-123: (123 Tagged) Smooth Av 10





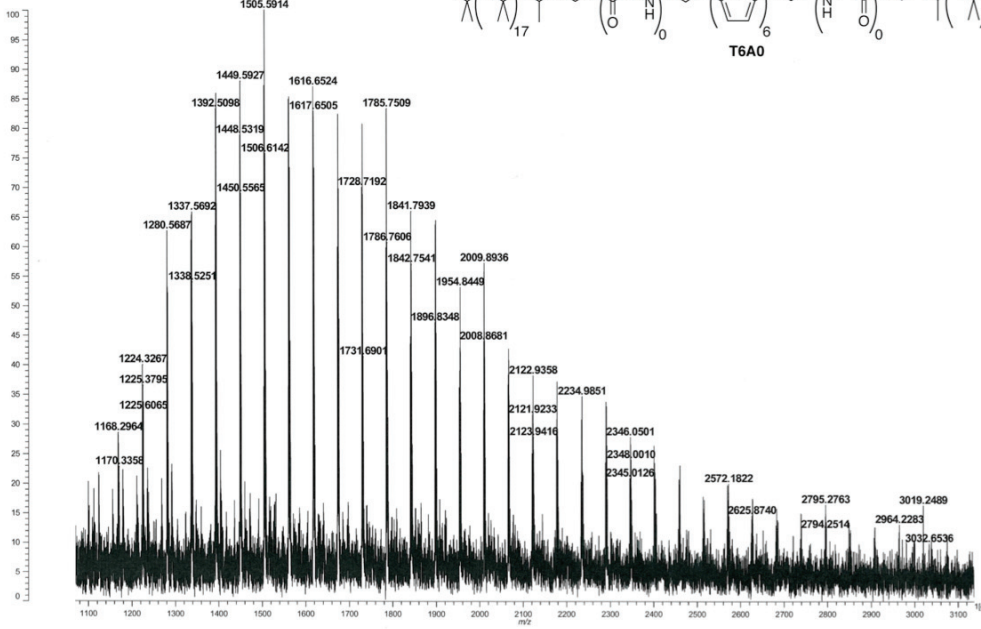


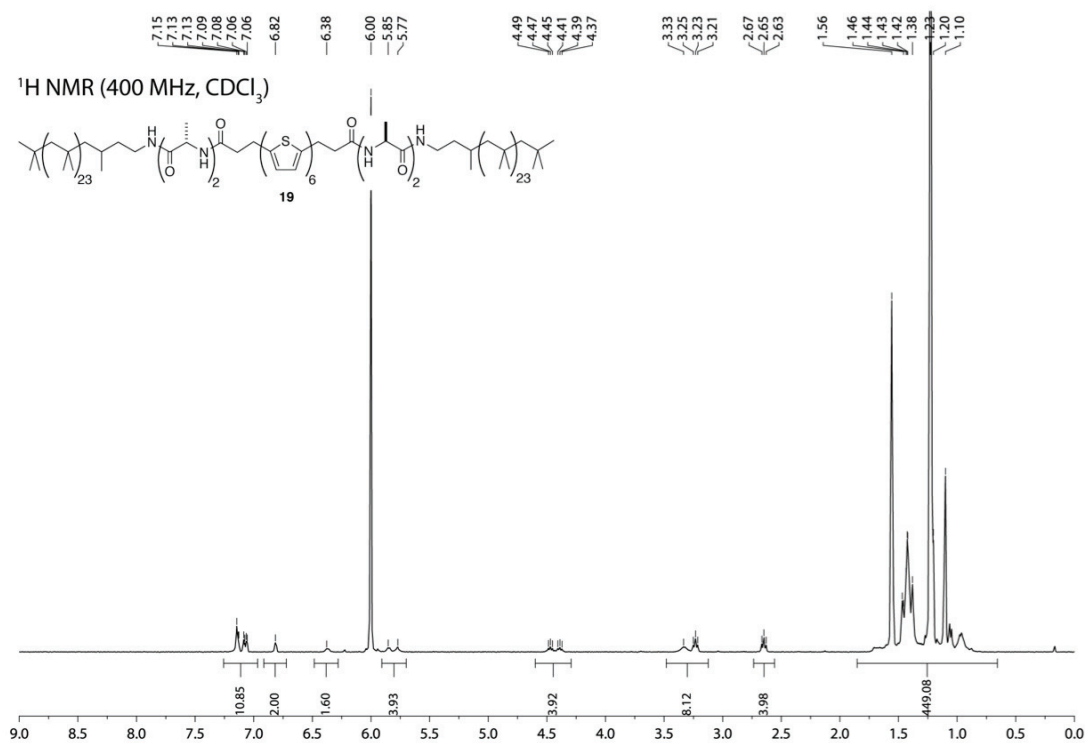




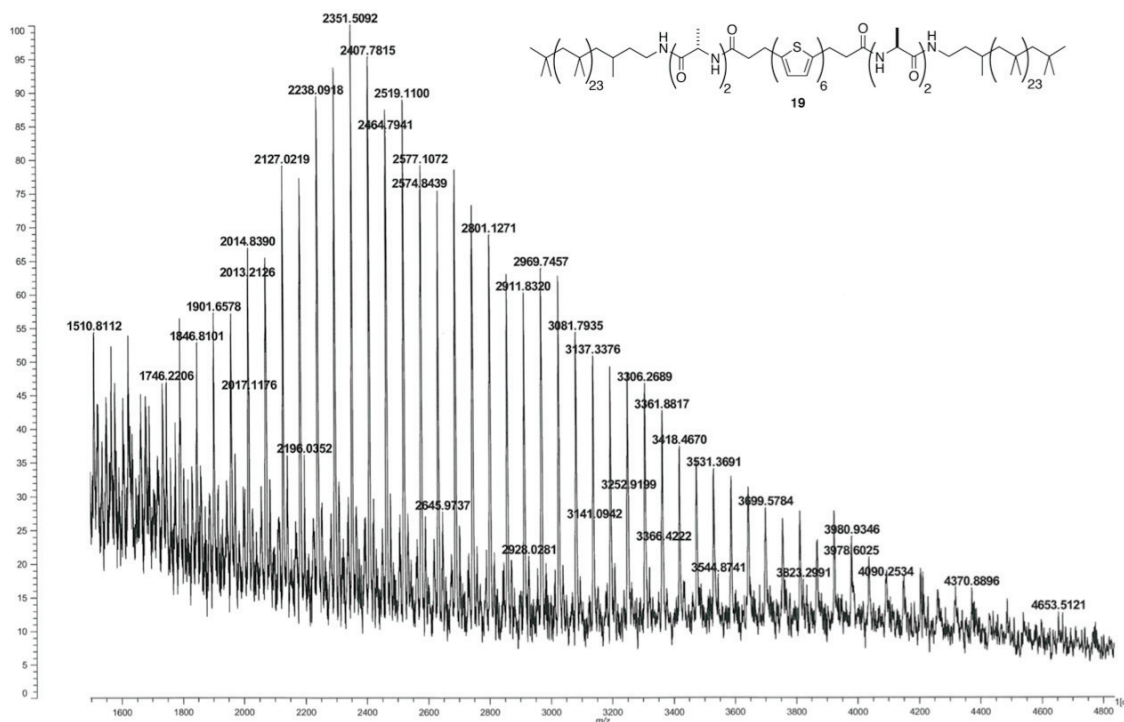
Date: Routine140404DR390_DCTE_F03032.E2[6] 4 Apr 2014 10:51 Cal: ref140404PE3800 4 Apr 2014 10:25
 Shimadzu Biotech Axima CFRplus 2.8.3.20080616: Mode reflecton, Power: 145, Blanket, P.Ext. @ 2000 (bin 166)

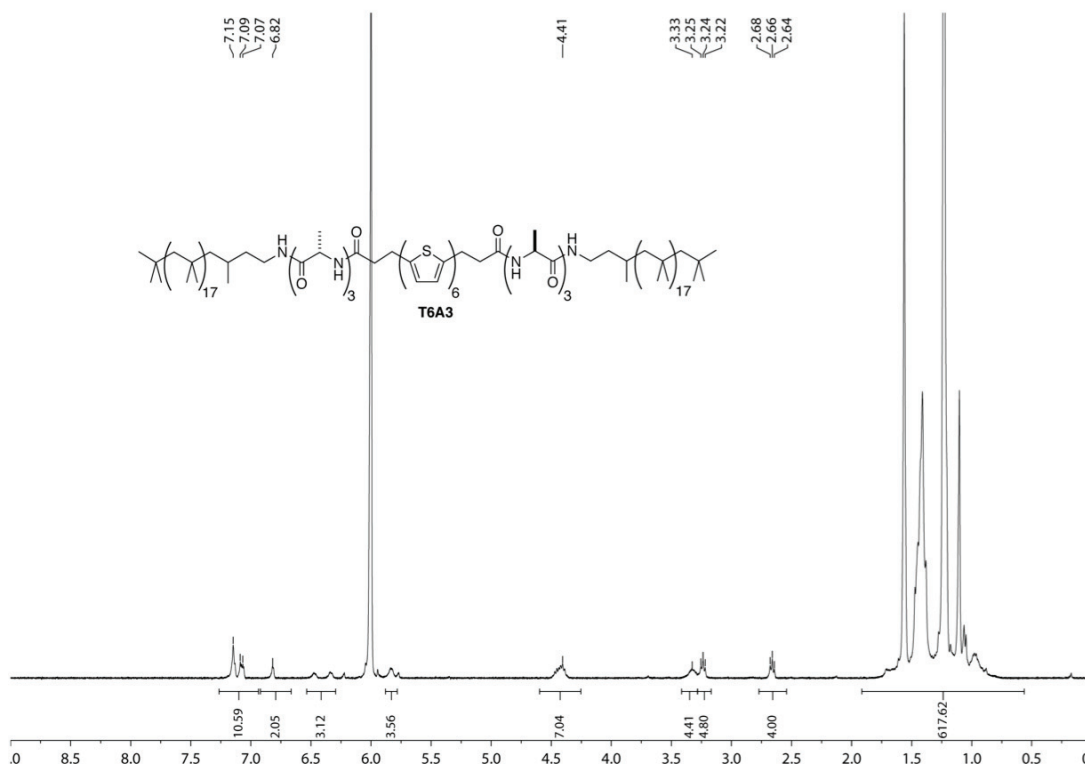
%Int. 18 mV(sum= 2118 mV) Profiles 1-120: (120 Tagged) Smooth Sv-Gl 2





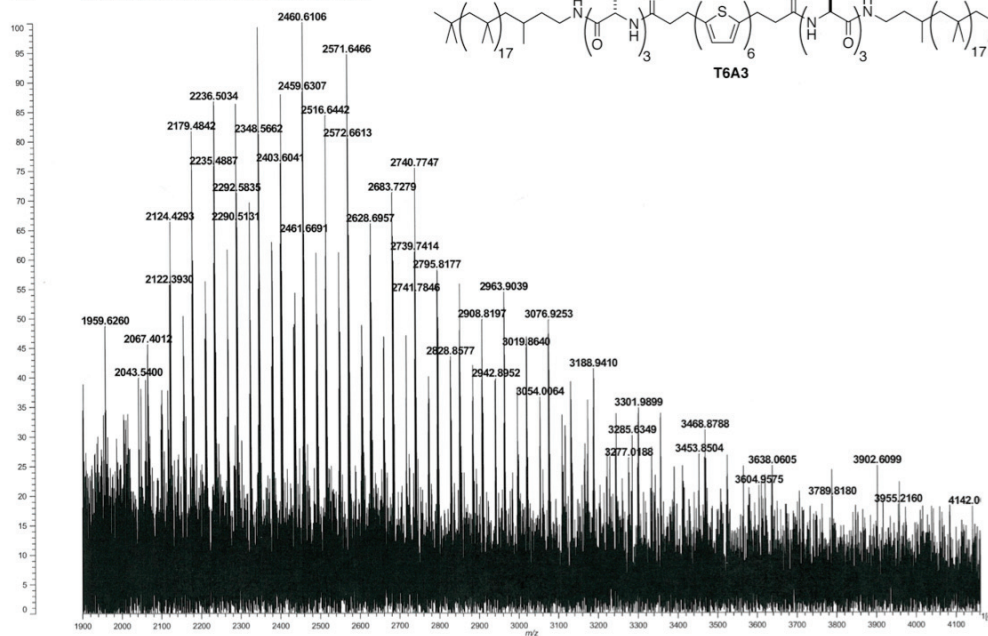
MS spectra (APPI)

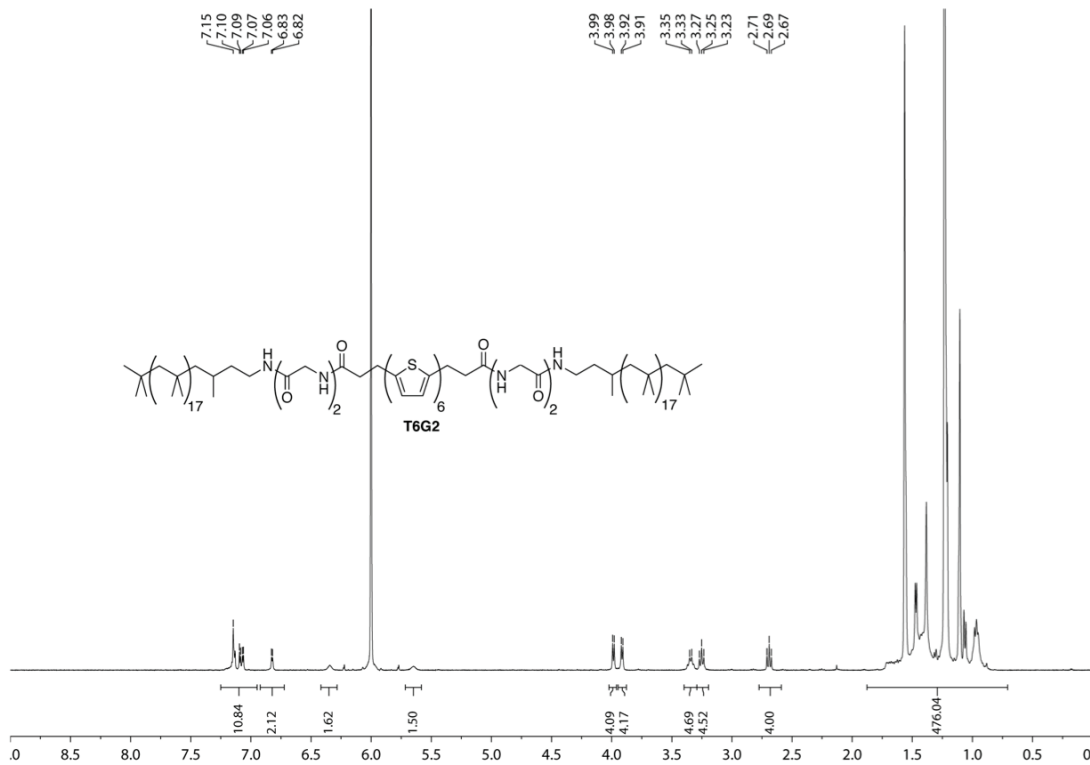




Data: Routine\140920\DRM9_CHCA_0001.H1 [1] 30 Sep 2014 11:59 Cal: ml40920PE200 30 Sep 2014 11:27 Shimadzu Biotech Avimsa CFXplus 2.8.3.20060616: Mode reflectron, Power: 135, Blanked, P.Ext. @ 3500 (bin 182)

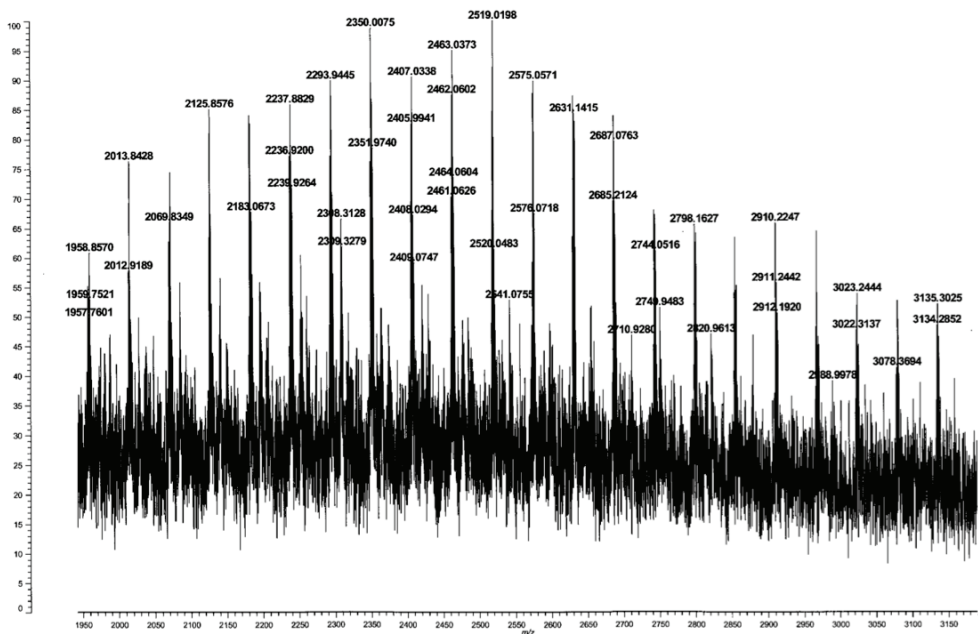
%Int. 15 mV[sum=2404 mV] Profiles 1-163; (163 Tagged) Smooth Sv-G1 2 -Baseline 16

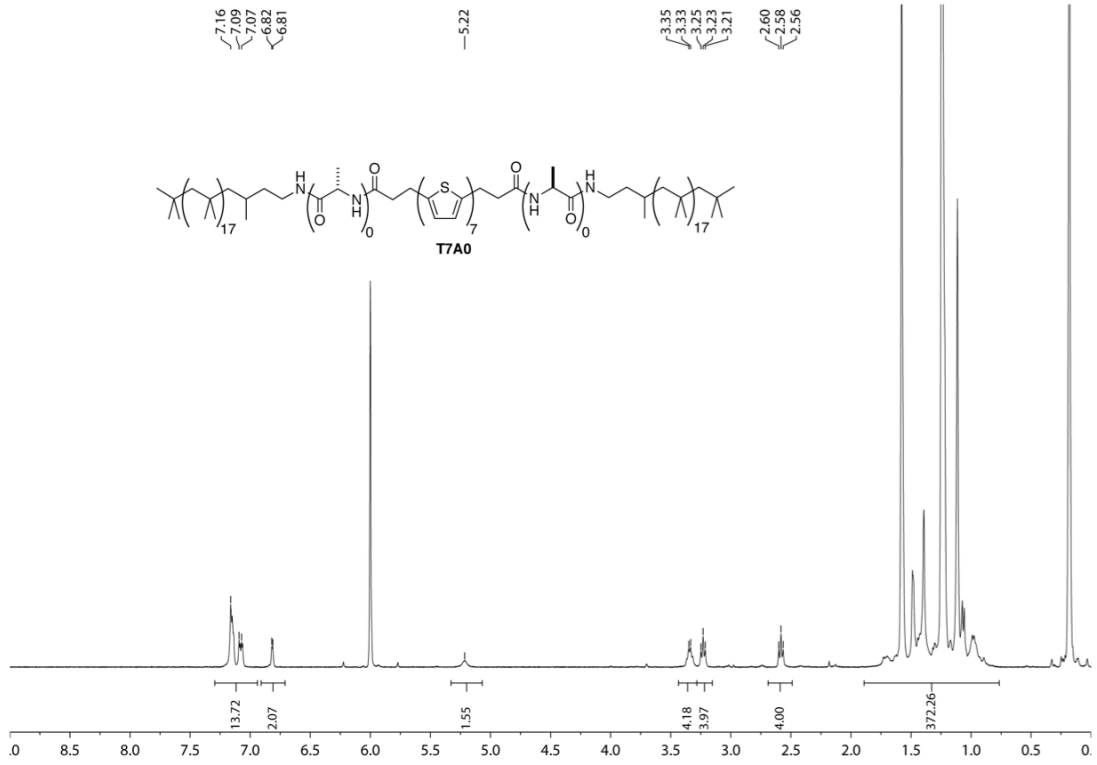




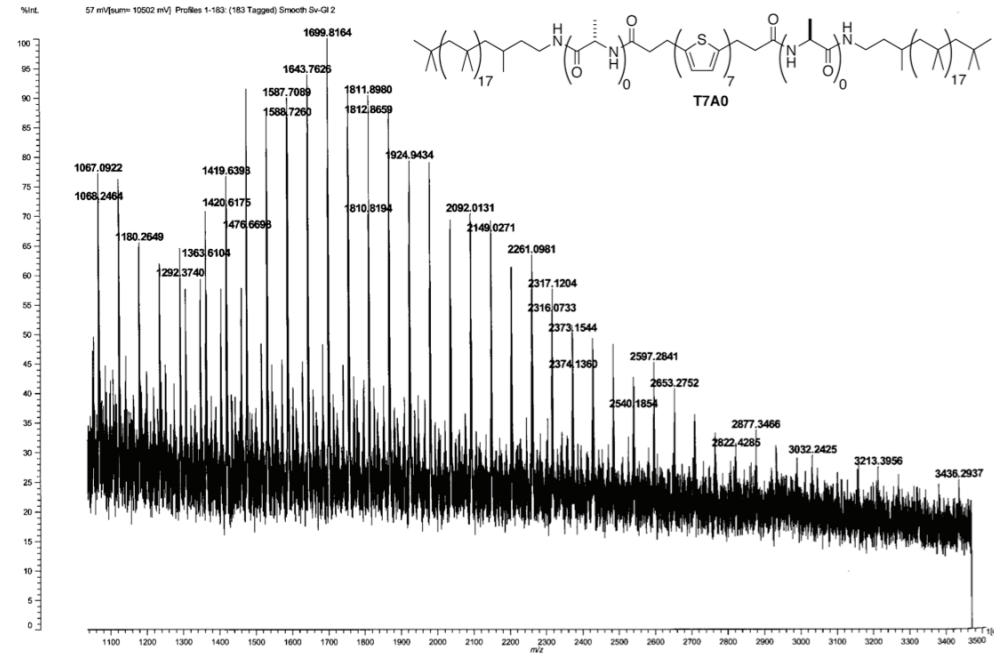
Date: Routine15031240355_DCTB_REF_0003.L2[2] 12 Mar 2015 15:34 Cal: ref150312PE3700 12 Mar 2015 15:27
 Shimadzu Biotech Axima CP Rikis 2.3.3 20080616: Mode reflectron, Power: 135, Blanked, P.Ext. @ 3700 (bin 187)

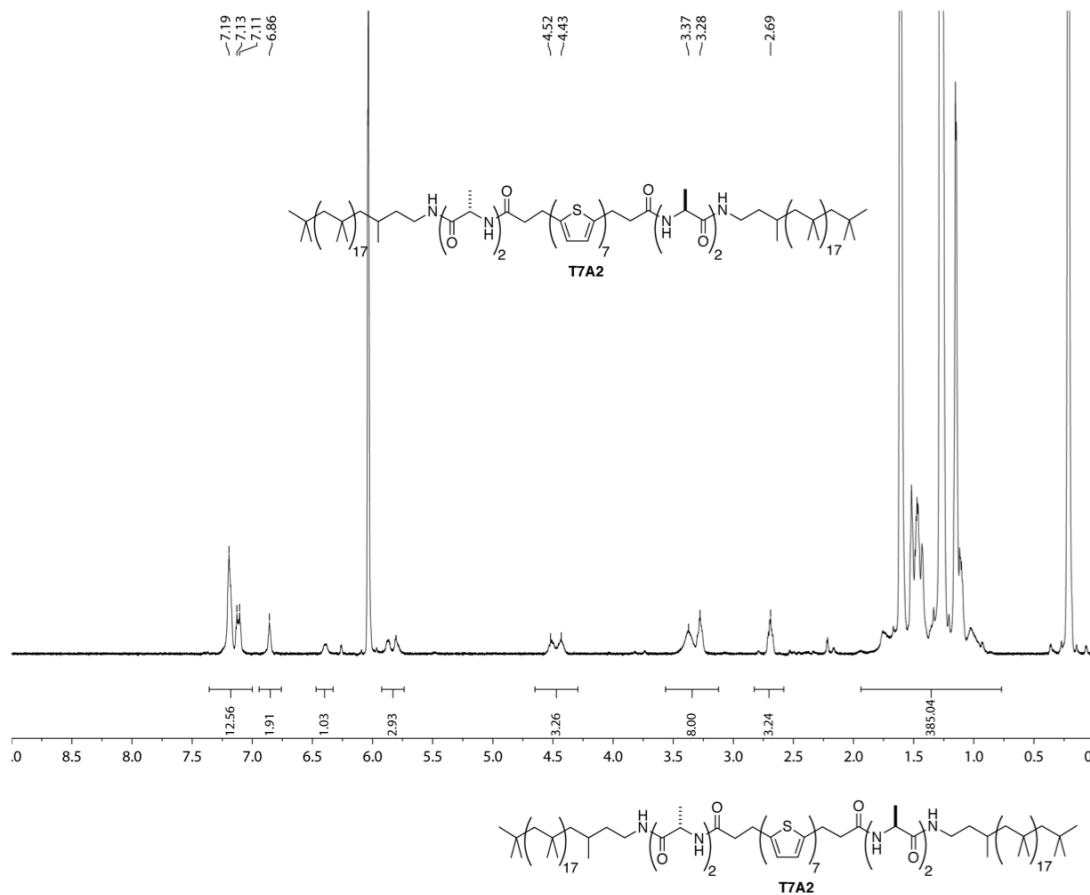
6.6 mV[sum= 1232 mV] Profiles 1-189: (189 Tagged) Smooth Sv-G1 2



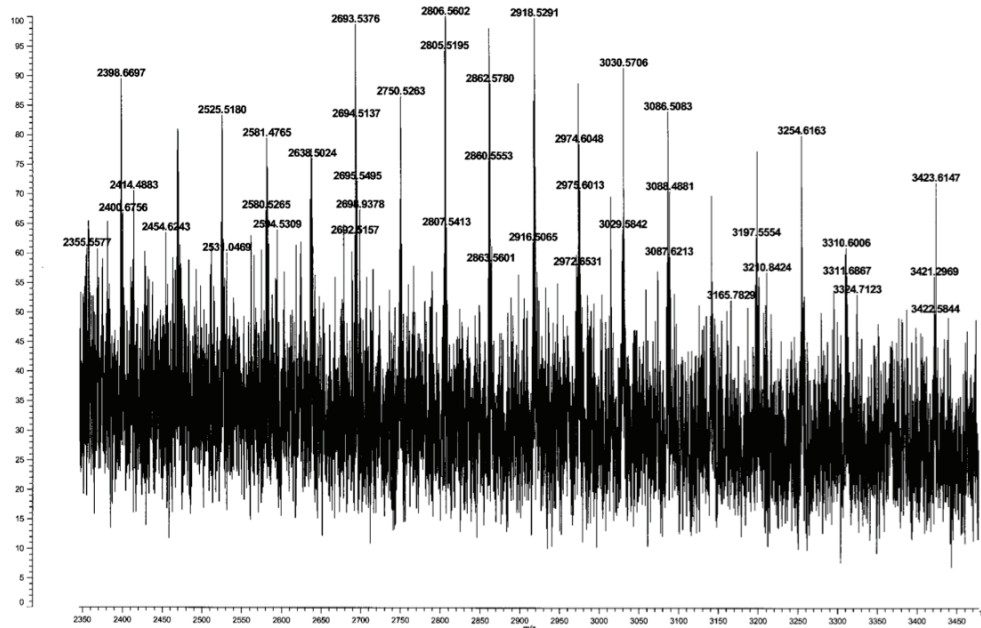


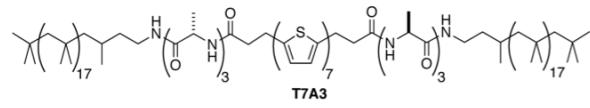
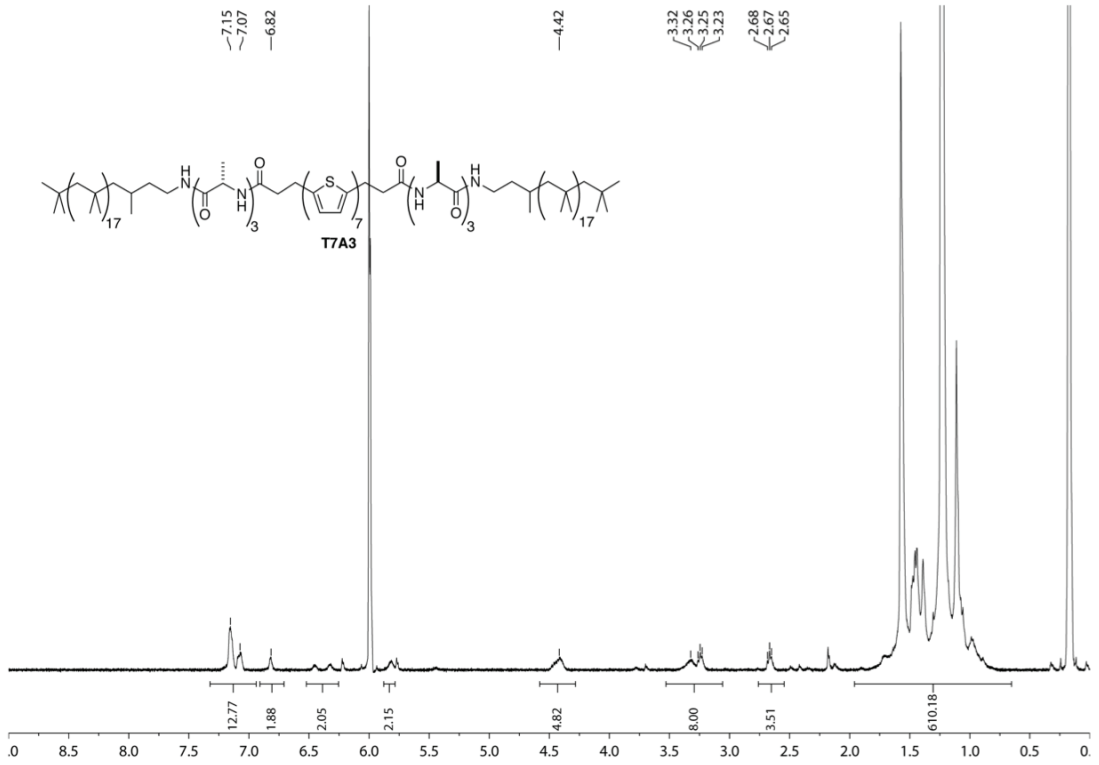
Data: Routine140404LC20_DCTB_P0001 F6(1) 4 Apr 2014 10:57 Cal: ref140404E3800 4 Apr 2014 10:25
 Shimadzu Biotech Avimsi CTRplus 2.8.3.2008016: Mode:reflectron; Power: 147; Blanked; P1.C4; @ 2900 (bin 196)



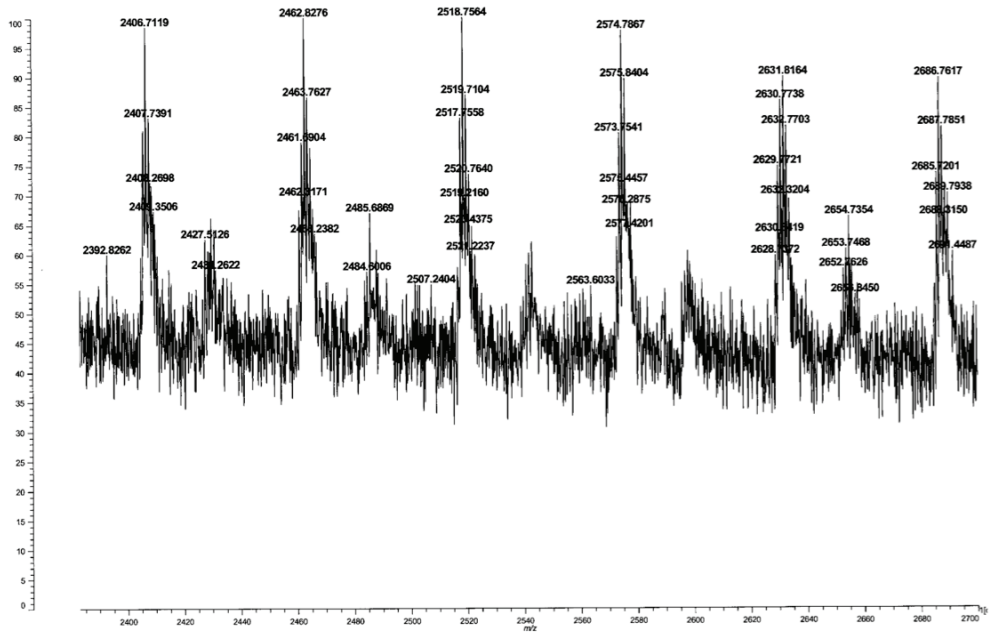


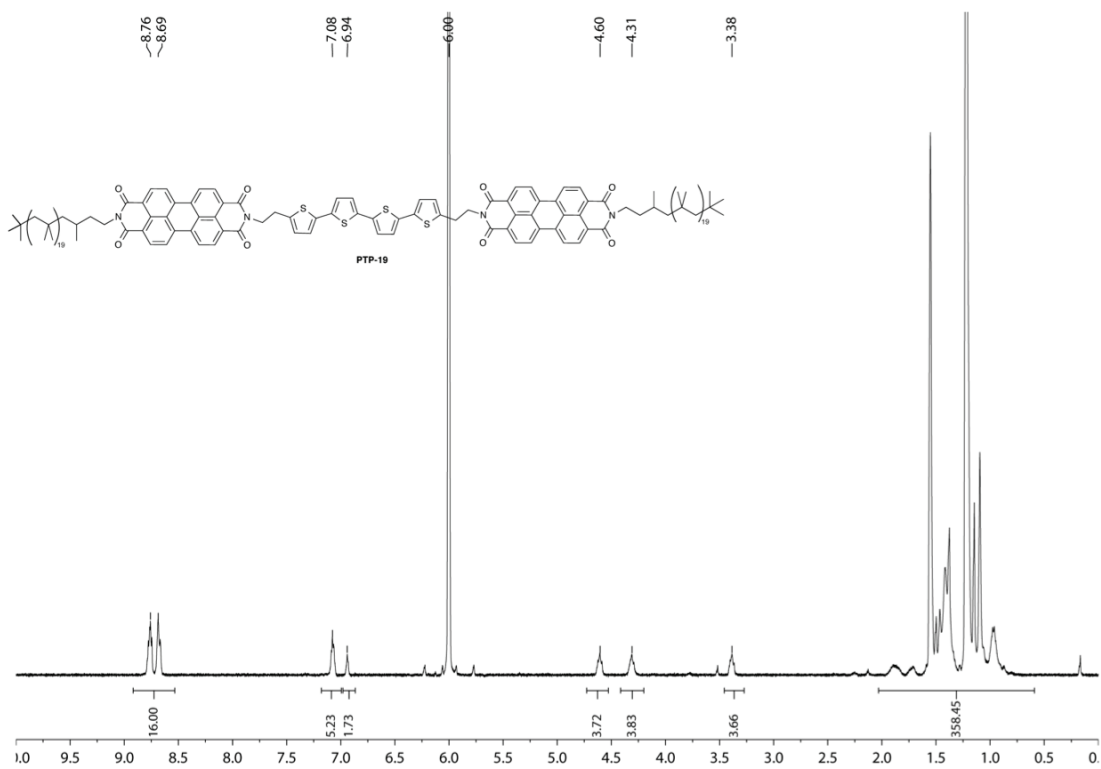
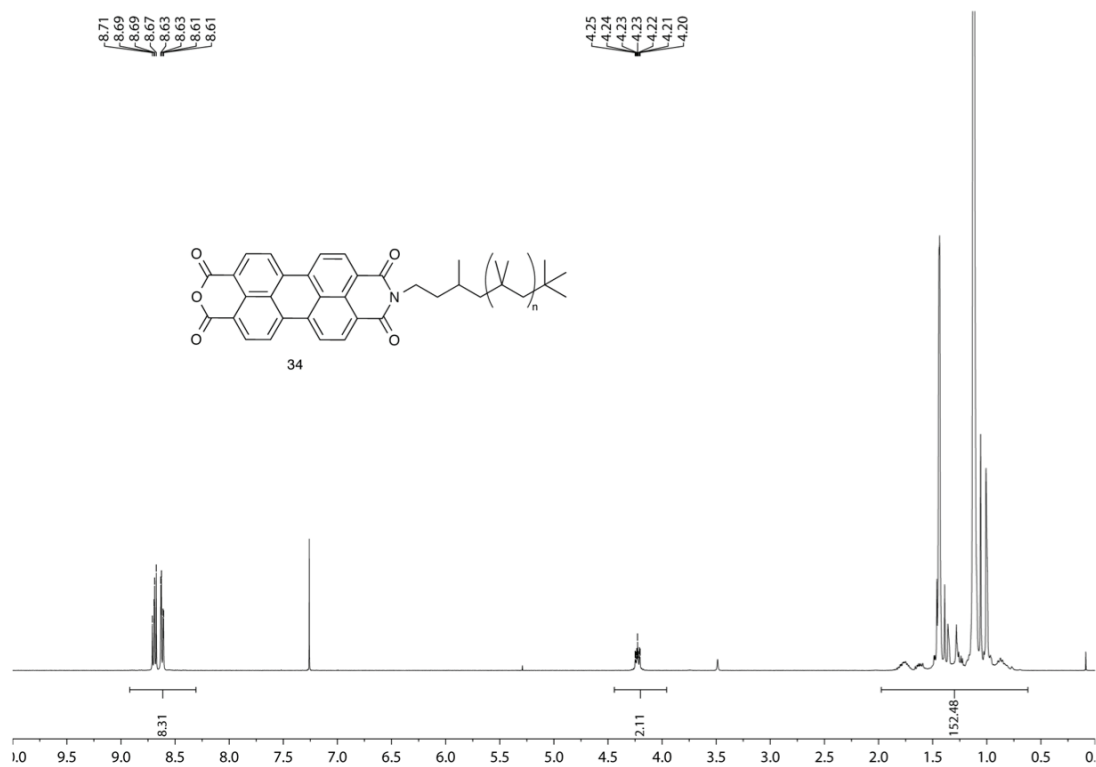
Data: Routine\140404\LC23_DHB_Pe0001.F101 4 Apr 2014 11:09 Cal: ref140404PE3800 4 Apr 2014 10:25
 Shimadzu Biotech Axima CF-Rplus 2.8.3.20080616. Mode: reflectron. Power: 132. Blanket. P.Ext. @ 2500 (bin 154)
 10 mV (sum= 766 nV) Profiles 28-102; (75 Tagged) Smooth Sv-GI 2





Data: Routine140404DR380A_DCTB_PE0001 E7[3] 4 Apr 2014 10:27 Cal: ms140404PE3800 4 Apr 2014 10:25
 Shimadzu Biotech Axima CFFplus 2.8.3.20080616: Mode reflectron, Power: 132, Blanket, P.Ext. @ 2500 (bin 154)
 %Int. 29 mV(umv= 6379 mV) Profiles 1-185: (185 Tagged) Smooth Srv-GI 2





8.2 Curriculum Vitae

Education

- 2009 – 2015: **Doctorate (PhD)** in Material Science
Ecole Polytechnique Fédérale de Lausanne (EPFL), Switzerland
Laboratory of Macromolecular and Organic Materials (LMOM)
- 2008 – 2009: **Master of Science (MSc.)** in Chemistry
Eidgenössische Technische Hochschule Zürich (ETHZ), Switzerland.
- 2004 – 2009: **Bachelor of Science (BSc.)** and **MSc.** in General Sciences and Chemistry
Ecole Polytechnique, Paris, France

Teaching Experience

- 2010 – 2014: Supervision of seven student projects in the laboratory of Prof. H. Frauenrath.
- 2011 – 2014: Teaching assistant for the course “Organic Electronic Materials – Synthesis, Properties, and Applications” given by Prof. H. Frauenrath: Preparation and teaching of parts of the course & exercise supervision

Language Skills

- **French** Mother tongue
- **English** Fluent written and spoken level
- **German** B2
- **Japanese** A2

May 1st, 1984 – France

French Nationality

8.3 List of Publications

Publications (peer-reviewed)

“Solubility and Crystallizability: Facile Access to Functionalized π -Conjugated Compounds with Chlorendylimide Protecting Groups” Gebers, J.; Rolland, D.; Marty, R.; Suarez, S.; Cervini, L.; Scopelliti, R.; Brauer, J.; Frauenrath, H. *Chem. Eur. J.* **2014**, *20*, 1.

“Coordination-Driven Self-Assembly of PEO-Functionalized Perylene Bisimides: Supramolecular Diversity from a Limited Set of Molecular Building Blocks” Gebers, J.; Rolland, D.; Frauenrath, H. *Angew. Chem. Int. Ed.* **2009**, *48*, 4480.

Publications (in preparation)

“Light-induced generation of high charge carrier density in organic nanowires” Tian, L.; Hafner, R.; Brauer, J.; Rolland, D.; Hartmann, L.; Szilluweit, R.; Schear, M.; Sienkiewicz, A.; Banerji, N.; Sidler, K.; Brugger, J.; Spitzner, E.; Bremond, E.; Wu, S.; Corminboeuf, C.; Frauenrath, H.

“Charge Generation and Recombination in an n-p-n Triad Forming Lamellar Phases” Rolland, D.; Brauer, J.; Hartmann, L.; Biniek, L.; Binkmann, M.; Banerji, N.; Frauenrath, H.

Talks and Poster Presentations

“Long-lived Charge Carriers in Oligothiophene Nanowires” Rolland, D.; Frauenrath, H.; **2014**, Oral contribution at the SCS Fall Meeting, ETHZ, Zürich, Switzerland.

“Charge Separation in an n-p-n Triad Forming Lamellar Structures” Rolland, D.; Brauer, J.; Hartmann, L.; Binkmann, M.; Banerji, N.; Frauenrath, H. **2014**, Oral contribution at the SPIE Optics & Photonics, San Diego, USA.

“Long-lived Charge Carriers in Oligothiophene Nanowires” Rolland, D.; Frauenrath, H. **2014**, Poster presentation at the ICOE, Modena, Italy.

“An n-p-n Triad Designed and Studied Toward Organic Photovoltaics” Rolland, D.; Brauer, J.; Hartmann, L.; Binkmann, M.; Banerji, N.; Frauenrath, H. **2014**, Oral contribution at the E-MRS Spring Meeting, Lille, France.

“An n-p-n Triad Designed Toward Organic Photovoltaics” Rolland, D.; Brauer, J.; Hartmann, L.; Binkmann, M.; Banerji, N.; Frauenrath, H. **2014**, Poster presentation at the MRS Spring Meeting, San Francisco, USA.

“An n-p-n Triad Designed for Organic Photovoltaics” Rolland, D.; Brauer, J.; Hartmann, L.; Banerji, N.; Frauenrath, H. **2013**, Poster presentation at the CECAM Workshop: Structure-Property Relationships of Molecular Precursors to Organic Electronics, EPFL, Lausanne, Switzerland.

“Nanostructured Materials for Organic Photovoltaics” Rolland, D.; Brauer, J.; Hartmann, L.; Banerji, N.; Frauenrath, H. **2013**, Poster presentation at the ECME, Imperial College, London, UK.

“Nanostructured Materials for Organic Photovoltaics” Rolland, D.; Banerji, Liang, S.; N.; Sanchez-Ferrer, A.; Mezzenga, R.; Frauenrath, H. **2012**, Poster presentation at the SCS Fall Meeting, ETHZ, Zürich, Switzerland.

“Nanostructured Materials Containing Organic Semiconductors” Rolland, D.; Frauenrath, H. **2011**, Poster presentations at the Conference Electronic Properties of π -conjugated Materials II, University of Würzburg, Würzburg, Germany, at the SCS Fall Meeting, EPFL, and at the 5th EDMX Research Day, EPFL, Lausanne, Switzerland.

“Towards Polymer Materials Containing Oligothiophene Segments” Rolland, D.; Frauenrath, H. **2010**, Poster presentations at the SCS Fall Meeting, ETHZ, Zürich, Switzerland.